NASA Contractor Report 195340

Investigation of Moving Belt Radiator Technology Issues

W. Peter Teagan and Jerry L. Aguilar
Arthur D. Little, Inc.
Cambridge, Massachusetts

June 1994

Prepared for
Lewis Research Center
Under Contract NAS3–24650

National Aeronautics and
Space Administration

Table of Contents

List of Figures

List of Tables

1.0 Summary of MBR Testing and Evaluation

This report details the analysis and testing of the Moving Belt Radiator (MBR) technology development. The work was completed under a task order contract with NASA Lewis Research Center. Six tasks were assigned that included analysis and testing of the various components and aspects of a MBR system.

The MBR system provides a means of dissipating excess heat from a large system such as a space based nuclear power system. The MBR, in order to be competitive with alternative technologies, would be paired with systems that require the dissipation of a large amount of heat. A MBR system consists of a belt, interface heat exchanger (IHX), and a drive system. The MBR continuously passes through the IHX where it is heated up by the excess heat and then is exposed to space where the heat is radiated. Figure 1 shows the MBR concept. Several types of MBRs can be developed. These variations include a solid belt radiator (SBR), liquid belt radiator (LBR), and a hybrid belt radiator (HBR). Further descriptions of these variations are provided in Section 2.0.

These tasks were, in the order presented in this report:

- Scalability Analysis--The model that was in previous work (see Reference 1) to predict the size and performance of a LBR. Several performance parameters were varied to determine the parasitic losses and the overall performance. Three cases were defined and studied to determine which of the design parameters most greatly affected the final performance of the LBR.

- Belt Dynamic Analysis--This task provided a preliminary study of belt dynamics by using software developed at Arthur D. Little (the software was developed under this same task). The title of the computer program is Belt Radiator Simulation Program (BERS). The software was used to determine potential failure modes for the belt and to examine the stability of a full scale belt. Additionally, the effects of external forces were examined to determine which of these forces should be included in the analysis. Since the primary application for a MBR would be on a spacecraft, the effects of spacecraft maneuvers were also modeled and possible failure modes associated with this application were identified. Several methods of controlling the belt are proposed. In order to improve the belts resistance to the failure modes that were identified, several options such as increasing the rotational speed of the belt, were examined and should provide the required improvements.

- Small Scale Table Top Dynamic Testing--A series of preliminary tests were conducted on a small belt to examine the shape when the belt is rotated. The tests were conducted with the belt in the horizontal and the vertical orientations. The belt was also modeled using the BERS computer code to provide a means of verifying the computer code. The effects of perturbation to a rotating belt were included in the testing.

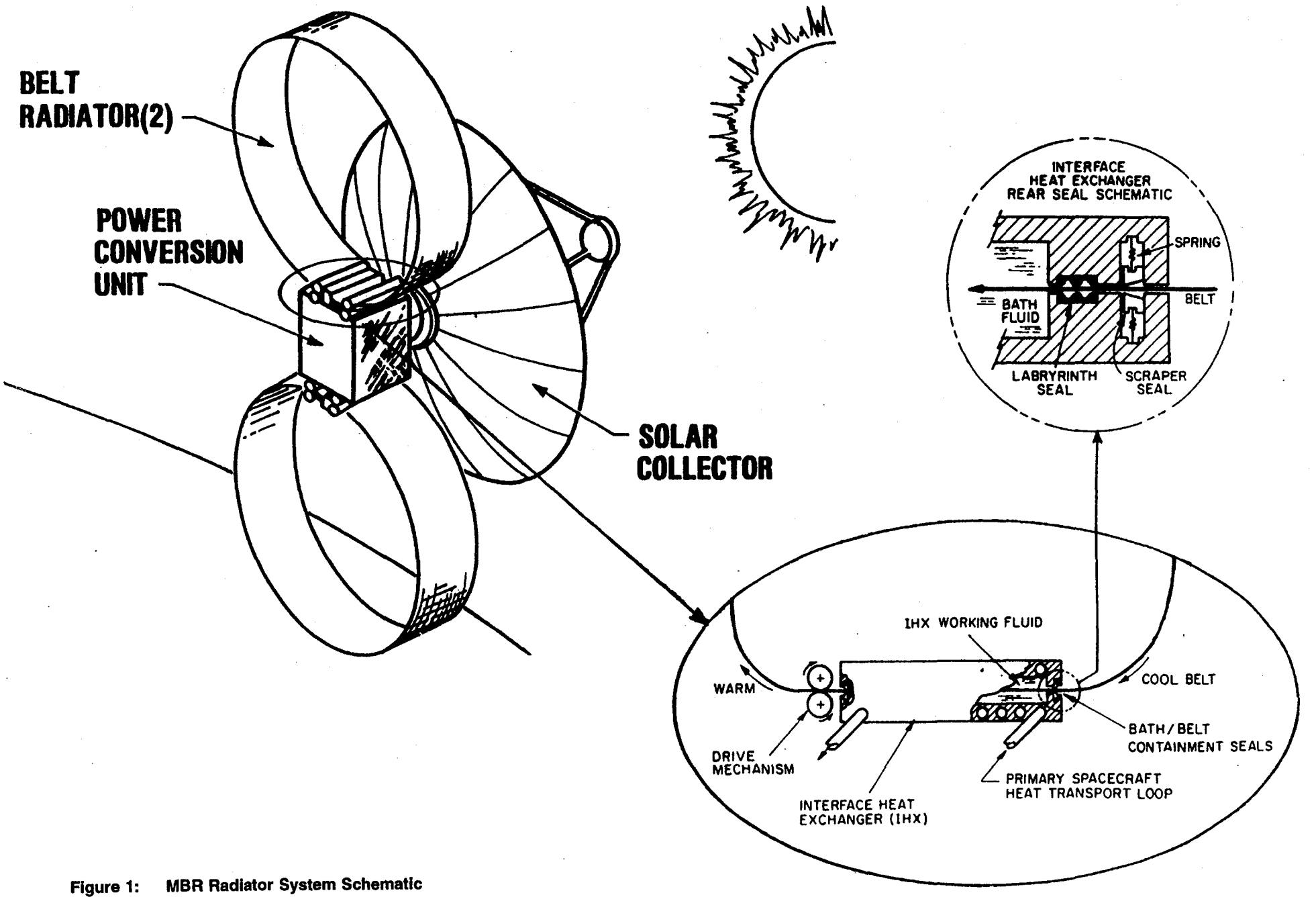

Figure 1: MBR Radiator System Schematic

- KC-135 Microgravity Testing--Several belts made of different materials and thicknesses were tested aboard NASA's KC-135 reduced gravity test bed. In this task, only the dynamics were tested. No IHX components were included. Additionally, deployment of the belt was tested by releasing the belt from a stowed configuration while the KC-135 was in reduced gravity. The belt was shown to deploy into a circular shape when the proper materials and thicknesses were used.

- Materials Evaluation--Several materials that were considered as potential candidates for use as belts in a MBR system were tested to determine their properties. The properties of interest were those that were required for the BERS program. This database can, therefore, be used to conduct further evaluations with actual belt materials using BERS. The primary material parameters that were of interest were the stiffness and damping of the belts. The testing was conducted using an Instron tensile testing system. The effects of cycling the belt from a stretched to unstretched conditions were also considered. Belts made of meshes were included in the test matrix. The mesh belts are considered for the LBR systems.

- IHX Testing--A series of tests were conducted to determine the heat exchanger effectiveness when gallium is used as the IHX fluid. This was accomplished by using a continuous belt that was drawn through an IHX and measuring the heat rejection capacity and drag forces. Also, included in this test, a composite belt such as could be used for a HBR was constructed. The belt used a paraffin as the phase change material that is sealed in the belt. The general thermal characteristics were measured for the composite belt.

- Liquid Bath Containment--The objective of this task was to demonstrate that a seal design could be developed that would contain the IHX fluid while not imposing high parasitic requirements. The experimental apparatus that was used in the IHX testing was also used for these tests. Therefore, the drag forces due to the IHX were measured and were found to be relatively unrelated to the velocity of the belt through the IHX. A variety of seals were tested. These included clearance and scraper seals. The effectiveness of IHX end and side seals were evaluated to determine the optimum configuration for the containment of the IHX fluid. The drag forces were compared to a model that was also developed under this task.

2.0 Introduction

2.1 MBR Background

As part of ongoing work with NASA Lewis Research Center since 1982, Arthur D. Little, Inc. has been developing the Moving Belt Radiator (MBR) System concept for use on spacecraft. In this concept, shown in Figure 1, a belt is drawn through an interface heat exchanger (IHX) containing a low vapor pressure working fluid which functions as the heat sink for the power generation or environmental conditioning system. The moving belt passes through the IHX where it is heated by the hot fluid, then as the belt travels through space it radiates the energy to the background environment.

Previous work, described in Reference 1 shows that appropriate MBR configurations have major advantages for use in space missions with substantial heat rejection requirements including:

- An ability to stow a 200 MW radiator in the shuttle bay;
- Relatively simple deployment from a stowed position;
- Weight of one fifth to one third that of heat pipe or pumped fluid configurations;
- Favorable survivability characteristics against both natural environment and hostile threats.

These attributes could both enhance and enable future NASA and Department of Defense (DOD) missions as their thermal heat rejection needs increase in the future.

2.1.1 Moving Belt Radiator System Options

This effort initially focussed on liquid belt radiators (LBR) wherein a meniscus of the IHX fluid is formed on a mesh structure, the belt. This concept resulted in excellent heat transfer characteristics in the IHX and could take advantage of the heat of fusion of the IHX liquid (tin, lithium, etc.). A second option is the solid belt radiator (SBR) concept which consists of a flat solid belt being drawn through a heat exchanger, the heat exchanger being either a liquid bath or a solid to solid contact. The SBR has the advantage over the LBR in that no free liquid surface is exposed to space. Increased attention has focussed on a unique hybrid belt radiator (HBR) design that retains the excellent heat transfer characteristics of the LBR in the IHX yet does not result in a free liquid surface exposed to space. Additionally, it increases the thermal capacity over that of a SBR concept. The HBR consists of a phase change material that is encased within the belt. Again the belt is drawn through a heat exchanger, liquid bath or solid-solid contact, then radiates the thermal energy to space. The three concepts, LBR, SBR, and HBR, are collectively referred to as the MBR system.

Several modes of MBR deployment have been assessed and their impacts on stowability, deployment, and system weight evaluated. These include:

- Using lightweight, extendable, boom structures to establish the shape and movement of the belt. The shape would be similar to that of a conveyor belt.
- Taking advantage of the zero gravity environment and centrifugal forces such that the belt is self-deployed into a hoop structure.

Figure 2 depicts both of these options. The extendable boom system would provide better control of the belt and more accurate positioning. This option would, however, be heavier and require a larger belt due to the reduced view factor from the belt surface to space.

The alternative, and preferred, configuration does not use any deployment structure and is predicted to produce a circular shape. If a circular shape is formed then the best view factor is also achieved. Both of these advantages decrease the system weight. The disadvantage to the self-deployed configuration is that the dynamics are very difficult to predict and testing must be conducted in a reduced gravity and vacuum environment.

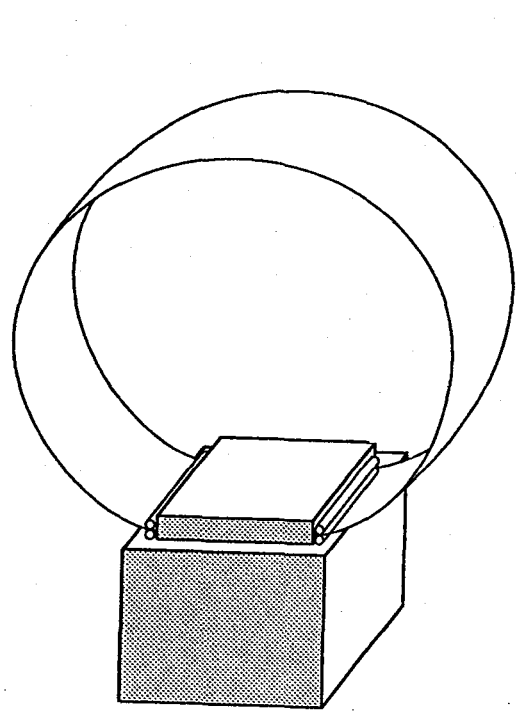

a. No Support Structure, Self-Deployed

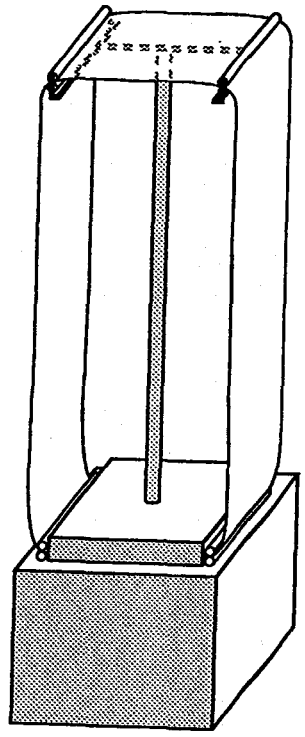

b. Using Extendable Boom

Figure 2: Deployment Concepts

2.2 Tasks Completed

Under the NASA Contract NAS3-24650 six separate tasks were completed. These included:

- Task 1: Belt Dynamic Analysis;
- Task 2: Liquid Bath Containment;
- Task 3: MBR Scalability Analysis;
- Task 4: Properties of MBR Materials and Physical Study of MBR Dynamics;
- Task 6: Interface Heat Exchanger - Heat Transfer Tests; and
- Task 15: MBR Reduced Gravity Dynamics Testing.

Under the contract other options were included but were not exercised. These are listed in Appendix A. Following are descriptions of the work completed for each task.

2.2.1 Task 1: Belt Dynamic Analysis

Task 1 was an initial study of belt dynamics and dynamic control. The principal objective of this investigation was to gain an initial understanding of the way a rotating belt would behave under various dynamic situations. The secondary objective was the study of potential control strategies to reduce unwanted motion.

The approach taken to address this task included the following steps:

- Classify the belt dynamics according to the source of disturbance: spacecraft motion or external influences (e.g. Coriolis acceleration), with major emphasis on the dynamics caused by the former.
- Develop an understanding of the dynamic behavior of the belt for spacecraft translation and rotation along each of the three axes.
- Develop the tools and estimates of the belt properties to study the belt response to the various types of spacecraft motion.
- Define the criteria for unacceptable belt performance for each type of motion studied.
- Develop an understanding of the spacecraft accelerations which will cause unacceptable belt motion.
- Identify the potential options for controlling the unacceptable belt motion.

The principal tool developed to study the belt motion was a computer program which can simulate belt motion. The program can analyze various types of motion and conditions such as:

- In-plane belt motion caused by spacecraft translation along the two axes within the belt plane (x-axis and y-axis);
- Rotation around the third axis (z-axis, i.e. belt axis);
- Options to study both elastic and inelastic belts; and
- Options to study one-phase and two-phase belt designs.

The study concentrated primarily on the in-plane motion of the belt because:

- A detailed study of the out-of-plane motion would require significantly more complex computation algorithms. These algorithms should be developed in later phases of MBR development.
- Belt speed, which is an important design parameter to be considered in the baseline study, will primarily affect the in-plane motion.

An initial insight into the out-of-plane and the in-plane motion was gained from this study and is described in Section 4.1.

2.2.2 Task 2: Liquid Bath Containment

Task 2 considered liquid bath containment for the moving belt radiator concept. Of interest were sealing systems for the belt/bath interface and the drag associated with the belt passing through the bath container. This work identified sealing systems for both the liquid belt and "hybrid belt" system. A 1/10 scale model of the radiator bath/belt was constructed to investigate different sealing geometries for different belt designs, working fluids and belt velocities. This work is described in Section 6.2

2.2.3 Task 3: MBR Scalability Analysis

Task 3 considered MBR design scalability and relationships between certain performance parameters which tend to limit system size. The information was derived from an analytical model developed under other tasks associated with this contract. The model was modified to reflect new design information and then used to create the formal computer code used in this study. Design constraints were established and applied to the results of the parametric study to determine maximum scalability of five different systems. In addition, the overall scalability of a "hybrid belt" system was considered. This work is described in detail in Section 3.0.

2.2.4 Task 4: Properties of MBR Materials and Physical Study of MBR Dynamics

The Task 4 work can be divided into two areas:

1. Materials Properties Tests (see Section 5.0).
2. Rotating Loop Dynamics Tests (see Section 4.2).

Figure 3 summarizes the work of this task. In Task 4, stretching and bending properties of MBR materials were studied to characterize the dynamic properties of a MBR. This information is necessary to revise and improve the dynamic belt model of Task 1. The Task 1 computer model benefits from the knowledge gained in the materials tests of this task. In addition to studying MBR materials, Task 4 analyzed the response of a revolving belt to various inputs using a physical model of the MBR. This was done primarily to verify the results of the Task 1 computer simulation.

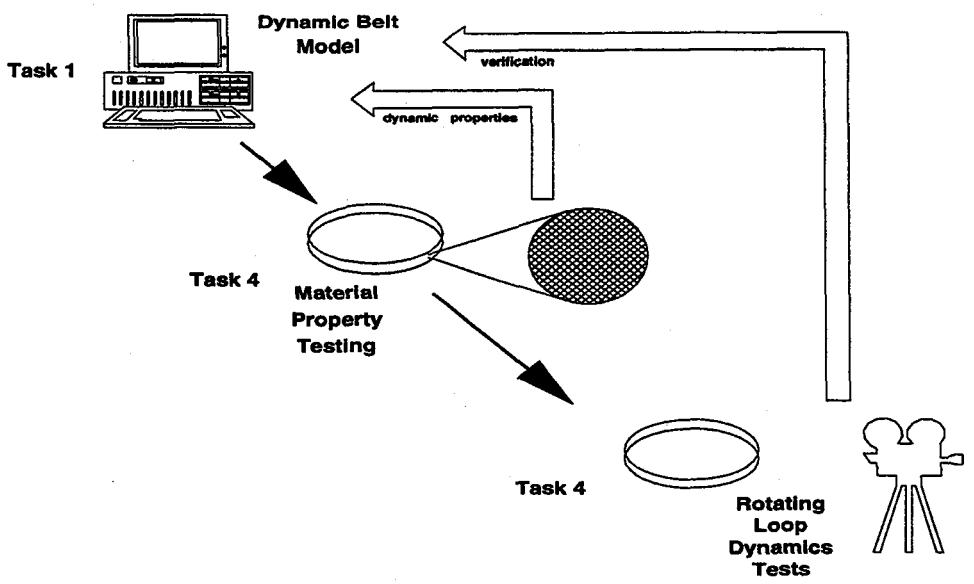

Figure 3: Rotating Loop Dynamic Tests

2.2.5 Task 6: Interface Heat Exchanger - Heat Transfer Tests

One of the key design features of a hybrid belt radiator influencing performance and reliability is the IHX. This subsystem, shown in Figure 1, is where heat is transferred from the primary heat rejection loop to the belt radiator. The use of gallium as a heat transfer fluid in the IHX has several significant advantages including:

- Low vapor pressure over a temperature range from 303 K (86°F) to over 750 K (890°F), making its use appropriate for both low and high temperature radiators (gallium has an extremely wide range of temperature in the liquid state).
- Poor wetting or non-wetting of most materials by gallium facilitates sealing the material within the IHX.
- High heat transfer characteristics which result in negligible temperature drops from the primary heat transfer loop to the moving belt, thereby reducing radiator size for a fixed primary heat transfer loop temperature level.
- Low viscosity reduces viscous drag losses to negligible levels.

Due to the compelling advantages of gallium as an IHX heat transfer fluid, all testing in this task focussed on the use of this material.

The HBR system can utilize either a solid moving belt structure or a belt structure containing a heat of fusion material. One such structure consists of a "sandwich" arrangement with heat of fusion material contained between solid outer surfaces. The major advantage of including heat of fusion material within the belt structure is that much lower belt speeds can be utilized (as compared to a solid belt). Lower speeds result in improved sealing, structural, and dynamic requirements. Belt thicknesses can be reduced with associated unit area weight benefits.

The Task 6 activity (discussed in Sectin 6.1) provided further experimental data on the design and operation of HBR systems by:

- Performing bench top level experiments utilizing a small IHX, compliant seals, gallium as a heat transfer fluid, and a continuous belt made of Teflon. Steady state heat transfer and viscous drag effects were examined over a temperature range of 310 K to 333 K (98°F to 140°F).
- Fabricating hybrid belt structures using aluminum, stainless steel, and Teflon sheath materials and paraffin as the heat of fusion material. Hybrid belt samples were subjected to heat up and cool down cycles to verify the impact of heat of fusion material on the thermal characteristics.

2.2.6 Task 15: MBR Reduced Gravity Dynamics Testing

The primary purpose of this task was the demonstration of the dynamic behavior of a MBR in a reduced gravity environment. This task consisted of designing and building a test apparatus which was flown on NASA's KC-135 reduced gravity test bed. The experiment was flown five times with each flight lasting approximately 2 hours. During each flight approximately 30 parabolas were completed with each parabola providing about 20 seconds of near microgravity.

The belts tested were either 3 or 4 foot in diameter and were made from a variety of materials. The remaining variables included: angular velocity, initial conditions, and perturbations to the belt. The data collected included acceleration levels in three axes, qualitative descriptions of the belt performance, and visual records (video and 16 mm film). This work is discussed in Section 4.4.

3.0 Scalability Analysis

Following is the approach, results, and conclusions from the Scalability Analysis completed under Task 3. During this task only Liquid Belt Radiators (LBR) were evaluated.

3.1 Analytical Approach

3.1.1 Improvements in the Analytical Model

A number of modifications were made to the analytic model (discussed in Reference 1) in order to more accurately predict the sizing and performance of the LBR system. Prior calculations were based on a linearized energy balance equation formulated in terms of the maximum belt radiating temperature. To improve the accuracy of the model, a closed form solution to the energy balance equation was employed. The effect of seal loading on parasitic power was analyzed and accounted for in the calculations. More accurate heat exchanger heat transfer coefficients were also incorporated into the program. Revised system mass scaling coefficients were also considered in order to arrive at a more accurate value for total system mass. In addition to these modifications, a view factor algorithm was added to allow different fractions of the inner belt surface to view the cold background of space. These improvements yielded a more accurate model of the actual system.

3.1.2 Analytical Model Assumptions

In order to make the analysis more tractable, a number of assumptions were made. Each is summarized below:

1. Screen mass effects were ignored. This is equivalent to assuming that the entire belt structure is composed of the working fluid.
2. Wetting conditions and stable menisci were assumed to exist for all belt/fluid combinations.
3. The IHX size was limited only by the radiator working fluid. For all analyses, the log mean temperature difference (LMTD) between the intermediate coolant loop and the working fluid was fixed at 50 K (90 R).
4. All heat rejection loads were assumed to be dissipated through two LBR belts, as indicated in the results.
5. The LBR is assumed to operate in low earth orbit with a characteristic background temperature of 250 K (450 R).
6. The IHX gap thickness (distance between the belt surface and the heat exchanger heat transfer plate) was configured to be dependent upon the working fluid under consideration. For organic materials the gap thickness was set at 0.635 cm (0.25 in) and 0.318 cm (0.125 in) for the liquid metals.

3.2 Task Methodology

3.2.1 Critical Design Parameters/Variables

As previously mentioned, an analytical model developed in prior LBR design work was used to evaluate overall system scalability. The analytical model was formulated into a computer program to evaluate the effect of a number of variables on key system performance parameters. A flowchart describing the LBR design algorithm is shown in Figure 4. The performance parameters defined below and summarized in Table 1 were central to the entire analysis and represented the primary limitations on system scalability.

Table 1: Performance Parameter Constraints

Single-Sided Area	Qualitative assessment based on manufacturability and Shuttle Stowability
Belt Velocity	≤ 5 m/s (16.4 ft/s)
Parasitic Power	< 1.5% Thermal Load
System Specific	< 5 kg/m^2 (1 lbm/ft^2)
Evaporative Loss Rate	<10% Belt Mass Per Year

Belt Velocity: Belt velocity is a function of thermal load, belt thickness, and aspect ratio. Only experimental testing can firmly establish upper limits on acceptable belt velocities as a function of working fluid and seal designs. It appears, however, that requirements for fluid containment and long seal life will necessitate limiting belt velocities to less than 5 m/s (16.4 ft/s).

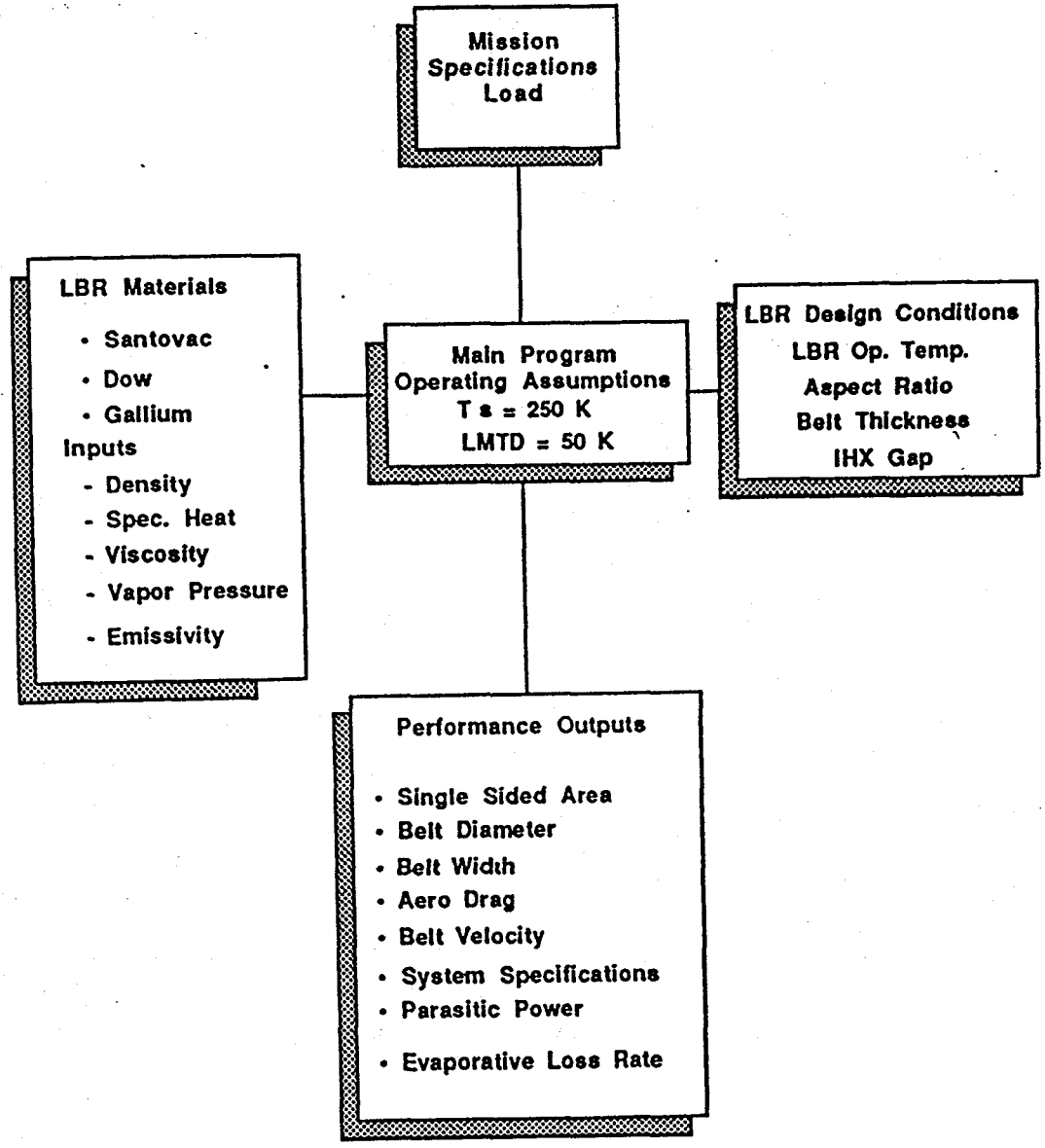

Figure 4: MBR Design Program Information Flows

Single Sided Area: The area of the LBR is directly related to thermal load. This parameter is constrained in part by the launch vehicle, and must be examined from a qualitative viewpoint when assessing the impact of increased size on manufacturability and deployment in space.

Parasitic Power: Parasitic power is a function of the square of the belt velocity, the viscosity of the working fluid, and the width of the belt. High levels of parasitic power require additional primary power generation (with increased heat rejection loads) and also create excessive wear on the drive mechanisms. For the purposes of this analyses an upper limit on parasitic power of 1.5% of the thermal load was assumed.

System Specific Mass: Current heat pipe radiator technology is defined to have a system specific mass of approximately 5 kg/m^2 (1 lbm/ft^2). In order for the LBR to provide a credible technology alternative, only systems having a specific mass of less than 5 kg/m^2 (1 lbm/ft^2) were considered to have merit.

Evaporative Loss Rate: Evaporative loss of working fluid material is not only a long term LBR reliability issue, but a concern with regard to ancillary equipment contamination integrity and life. As operating temperature and mission thermal loads increase, evaporative losses will become critical for a variety of candidate working fluids. For this reason, all liquid belt radiator designs were subject to the constraint that evaporative loss rates must be less than 10% of the mass of the belt itself over a period of a year.

A major portion of the information used in the program was dependent upon the choice of a particular working fluid. These constraints included the density, specific heat, heat of fusion, viscosity, emissivity, and vapor pressure. The LBR operating temperature was also dependent upon the thermo-physical properties of belt fluid used.

3.2.2 System Scaling Variables

As described in Section 3.3, load, aspect ratio, and belt thickness are considered key design variables. A more detailed discussion of major variables affecting LBR system scaling is presented below.

Thermal Load: The thermal load is taken to be the power radiated to space by the liquid belt. Values for thermal load ranged from 75 kW to 200 MW.

LBR Working Fluid: The working fluid is carried by the belt into space where it radiates its heat. The five working fluids selected for consideration in this study included Santovac 6, Reference 2 polydimethlysiloxane (Me_2), lithium, tin, and gallium. Of the five materials, only tin and lithium operate in a phase change mode.

Belt Thickness: Liquid belt thickness is limited by system mass and mechanical constraints. Belt thickness varied between 0.508 mm (0.020 in) and 2.54 mm (0.100 in).

LBR Operating Temperature: LBR operating temperature depends upon the working fluid used. Santovac has an operating temperature of 300 to 330 K (80 to 135°F), Me_2 operates at 340 to 370 K (153 to 207°F), lithium at 453 K (356°F), tin at 505 K (450°F), and gallium at 700 to 800 K (800 to 980°F).

Aspect Ratio: The aspect ratio, defined as the ratio of the belt diameter to the belt width, significantly impacts system size and belt dynamics. Aspect ratios varied from 2 to 8 in this study.

3.2.3 Definition of Test Cases

The majority of the LBR scalability and performance analyses are based on the results of three cases in which load, aspect ratio, and belt thickness are treated as independent variables. Specifying these three variables and the properties of the working fluid enables the equations of the analytical model to be solved for the performance parameters outlined in Table 1. It should be noted that additional insights into LBR scalability may also be obtained by considering belt width and belt velocity as independent variables.

The individual cases are summarized below:

- Case 1: Performance Parameters versus Operating Temperature:

These evaluations considered the effect of operating temperature on the LBR system load when belt thickness and the aspect ratio were fixed. In this case an aspect ratio of 4 was used with a belt thickness of 0.508 mm (0.020 in). The following operating temperatures were considered in the analyses.

1. Low temperature heat rejection at approximately 350 K (171°F) utilizing Santovac and the Dow Corning Me_2 oils. This would correspond to the need to dissipate heat from power electronics or low temperature power cycles such as the baseline Brayton design.
2. Intermediate temperature, 453 K (356°F), heat rejection system utilizing a phase change material such as lithium. This operating temperature corresponds to several power systems under consideration, such as the Stirling power cycle.
3. High temperature heat rejection systems utilizing both a phase change tin radiator (505 K, 450°F) and sensible gallium radiator (700 to 800 K, 800 to 980°F). These LBR operating temperatures correspond to high temperature Brayton and Rankine cycles, as well as thermoelectric systems being developed for the advanced nuclear space power systems.

- Case 2: LBR Performance Parameters versus Belt Thickness:

For the heat rejection temperatures given in Case 1 the effect of variable belt thickness on LBR system scalability was considered. An aspect ratio of 4 was used. The temperature was also held constant while belt thickness varied from 0.013 to 0.254 cm (0.005 to 0.100 in).

- Case 3: LBR Performance Parameters versus Aspect Ratio:

This case is similar to Case 2, with the exception that the aspect ratio is the independent variable, for a particular belt thickness and operating temperature.

3.3 System Scalability Results

3.3.1 Case 1 Evaluations

The results of the Case 1 evaluations are presented in Figure 5. With Santovac 6 and Me_2, the ability to reject higher thermal loads is limited by the relatively high viscosity of these two materials and resulting large parasitic power. On the other hand due to the low viscosity and latent heat capacity of tin and lithium, increased thermal rejection is possible. With these materials belt velocity will limit scalability before parasitic power becomes a constraint. Tin can accommodate power levels of approximately 50 MW, while lithium can operate at a significantly higher power level. Gallium operating in the sensible mode can reject heat up to 5 MW. As with other LBR systems using low viscosity liquid metals, belt velocity constrains the maximum power rejected by the gallium LBR, assuming launch vehicle stowability limitations are not considered.

Figure 6 depicts the scalability of the LBR for these same materials when shuttle cargo bay size limitations (i.e. belt width) are considered. As can be seen in the figure, latent tin and lithium LBR's, due to their low viscosity, are constrained by the required belt width. The maximum heat rejection level consistent with belt width limits is shown for lithium and tin having emissivities of 0.1 and 0.3. For Santovac 6 and Me_2, parasitic power constraints limits system scalability; while with the sensible gallium, belt velocity is the limiting factor.

3.3.2 Performance Parameter Relationships and Trends Identified in Case 2 and 3 Evaluations

For all the materials considered, belt thickness and speed had the most significant impact on overall system performance. Aspect ratio had a comparatively minor effect on system scalability and performance, although appropriate variation of this parameter can lessen stowable volume constraints. High belt speeds yield LBR systems with high power rejection levels, but at the expense of increased parasitic power and bath sealing difficulties. Thicker belts also result in more massive systems with lower specific power. A trade off therefore exists between belt thickness and belt speed which depends on the belt fluid used and the system load.

The results of the Case 2 analysis are displayed in Figures 7, 8, and 9. These graphs illustrate how belt thickness affects both belt speed and in turn parasitic power levels. As shown in Figure 7 higher belt speeds using Santovac working fluid result in high parasitic power levels. Therefore, for viscous fluids (principally organic materials), increased belt thicknesses should be utilized in order to keep belt speed and parasitic power low.

Figures 8 and 9 illustrate the effect of belt thickness on belt velocity and parasitic power levels of a lithium radiator rejecting 1 MW, 5 MW, and 10 MW of thermal energy. As is shown in the figure, increasing belt thickness greatly decreases parasitic power levels.

In Figure 10, the Case 3 results indicate relatively small effect of aspect ratio variation on belt velocity. For large systems with stowable volume constraints, this insensitivity can be used to decrease overall system size (belt width) and thereby increase power rejection capabilities. As shown for the 10 MW lithium radiator, increasing the aspect ratio by a factor of 4 increases the belt velocity by a factor of 2. Since the principle size-limiting

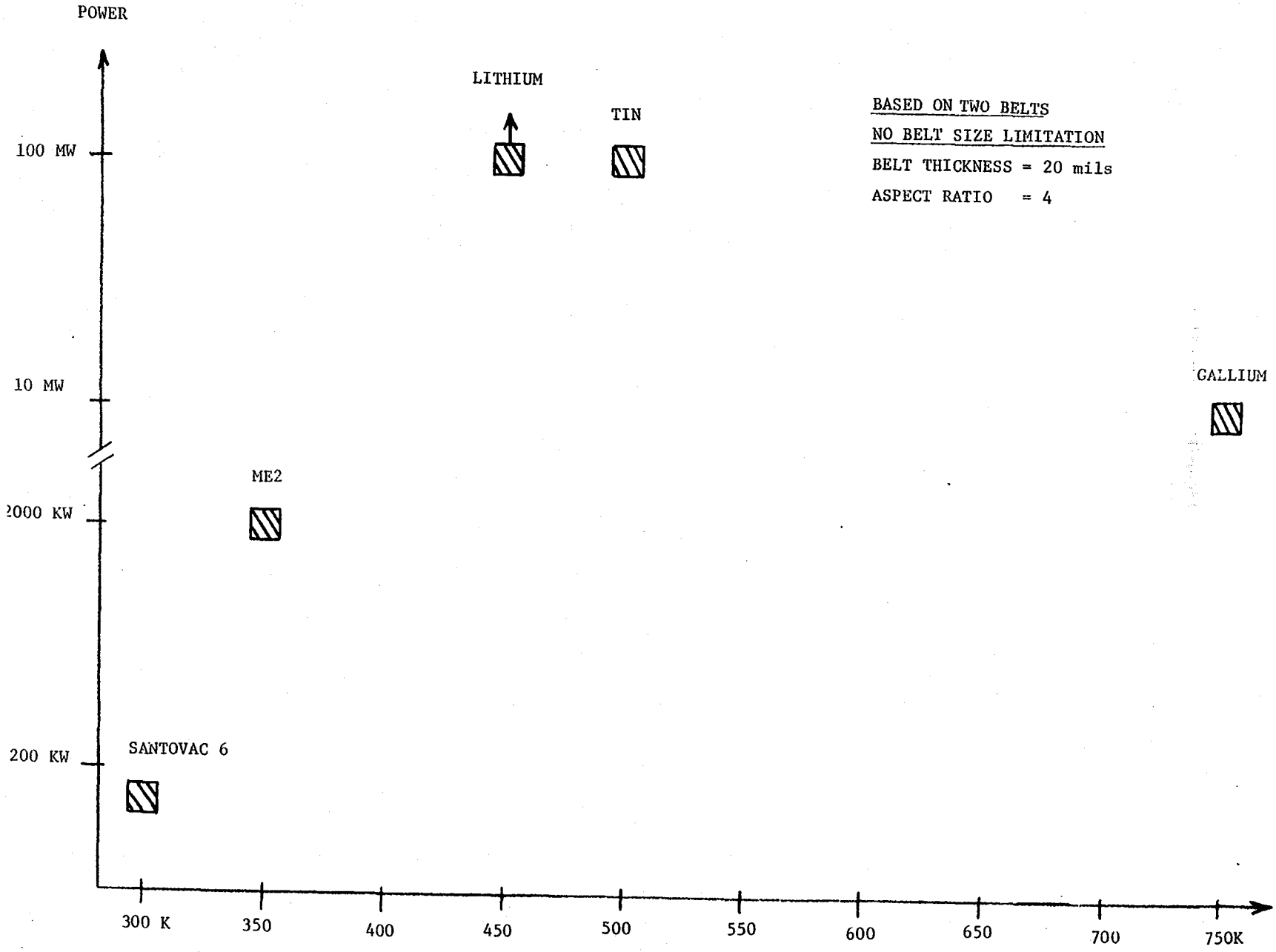

Figure 5: Results of Case 1 Evaluations

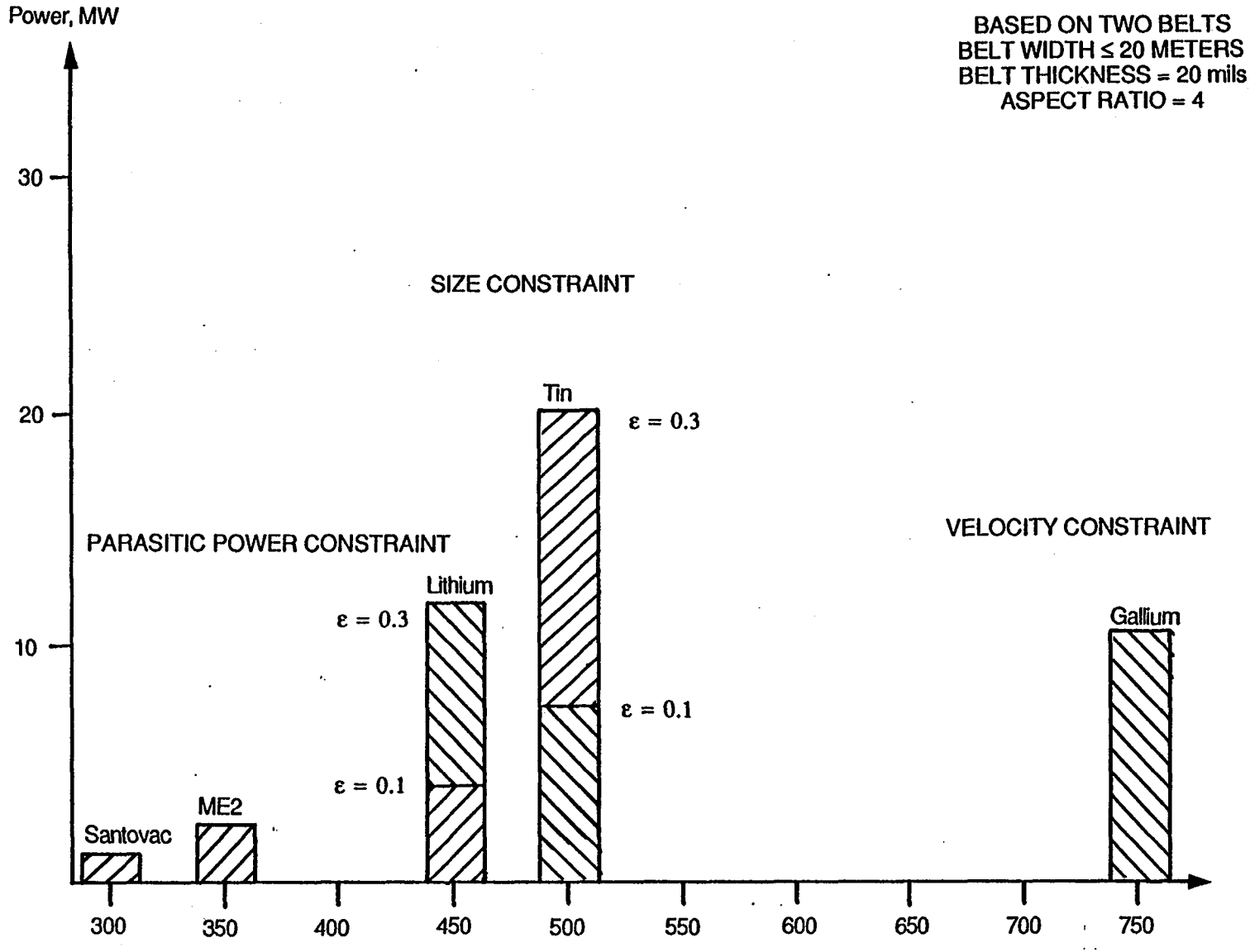

Figure 6: Case 1 Results Showing Various Operating Constraints

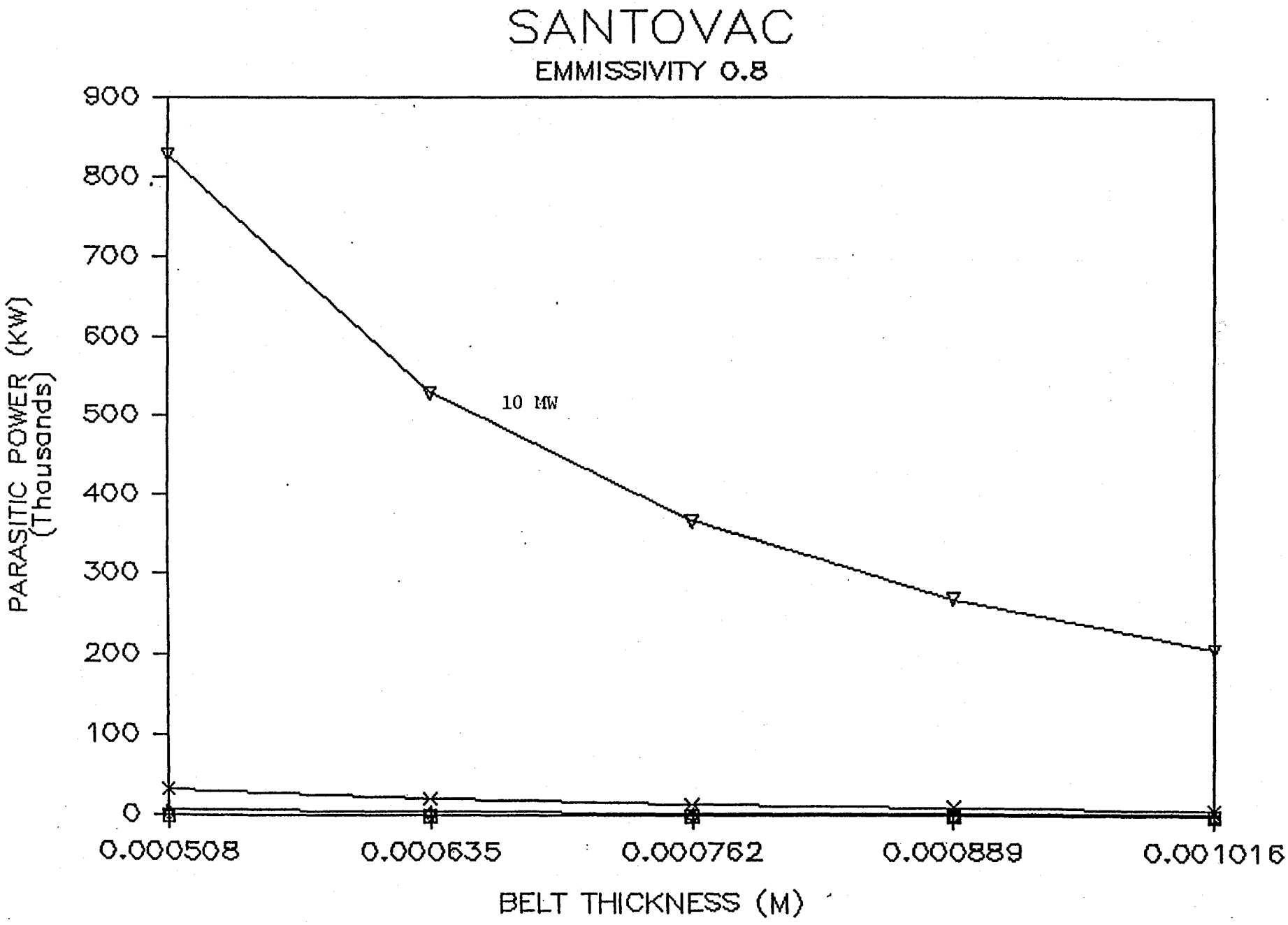

Figure 7: **Parasitic Power vs. Belt Thickness for Santovac 6**

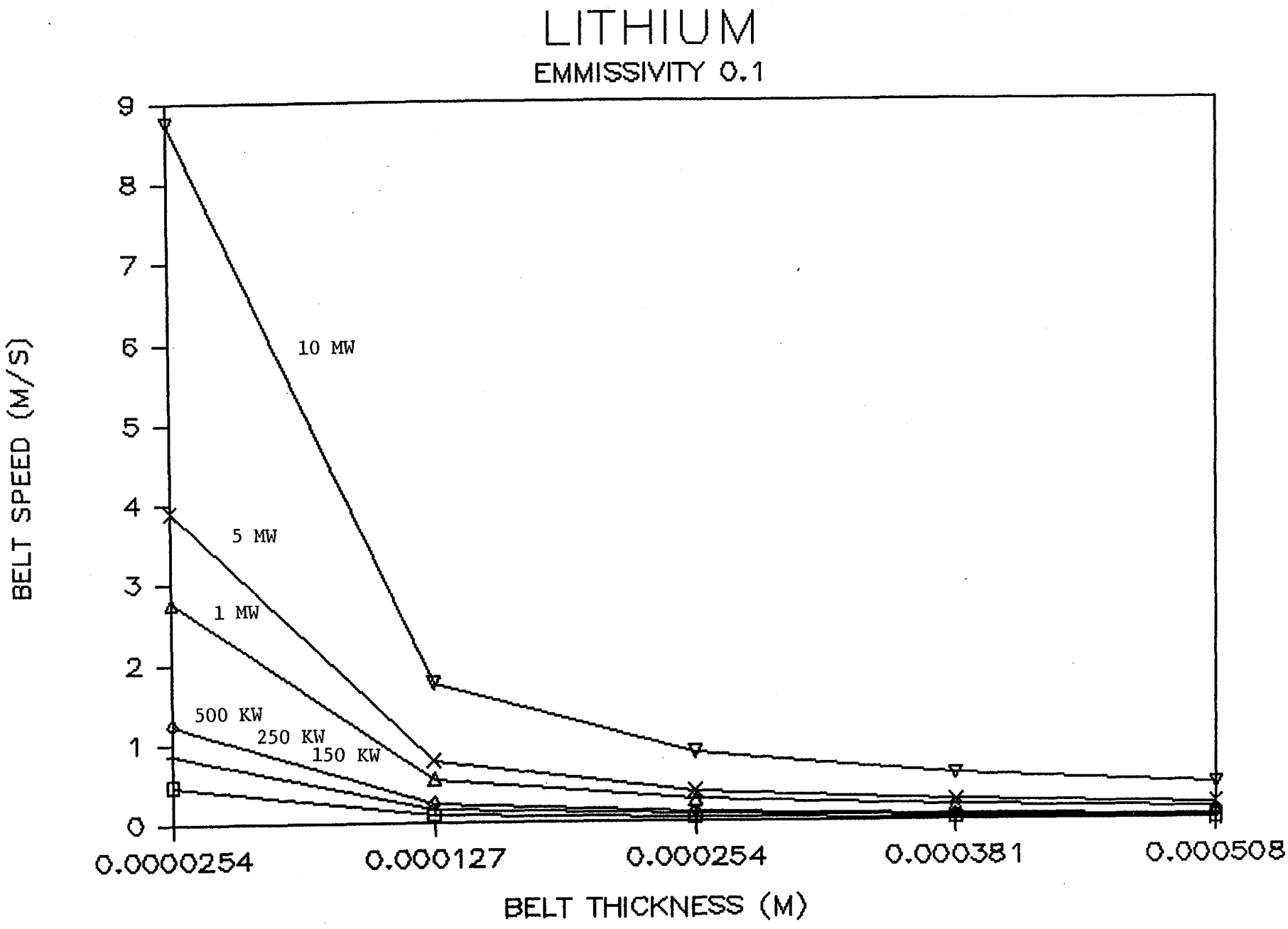

Figure 8: **Belt Speed vs. Belt Thickness for $\varepsilon = 1$ Molten Lithium**

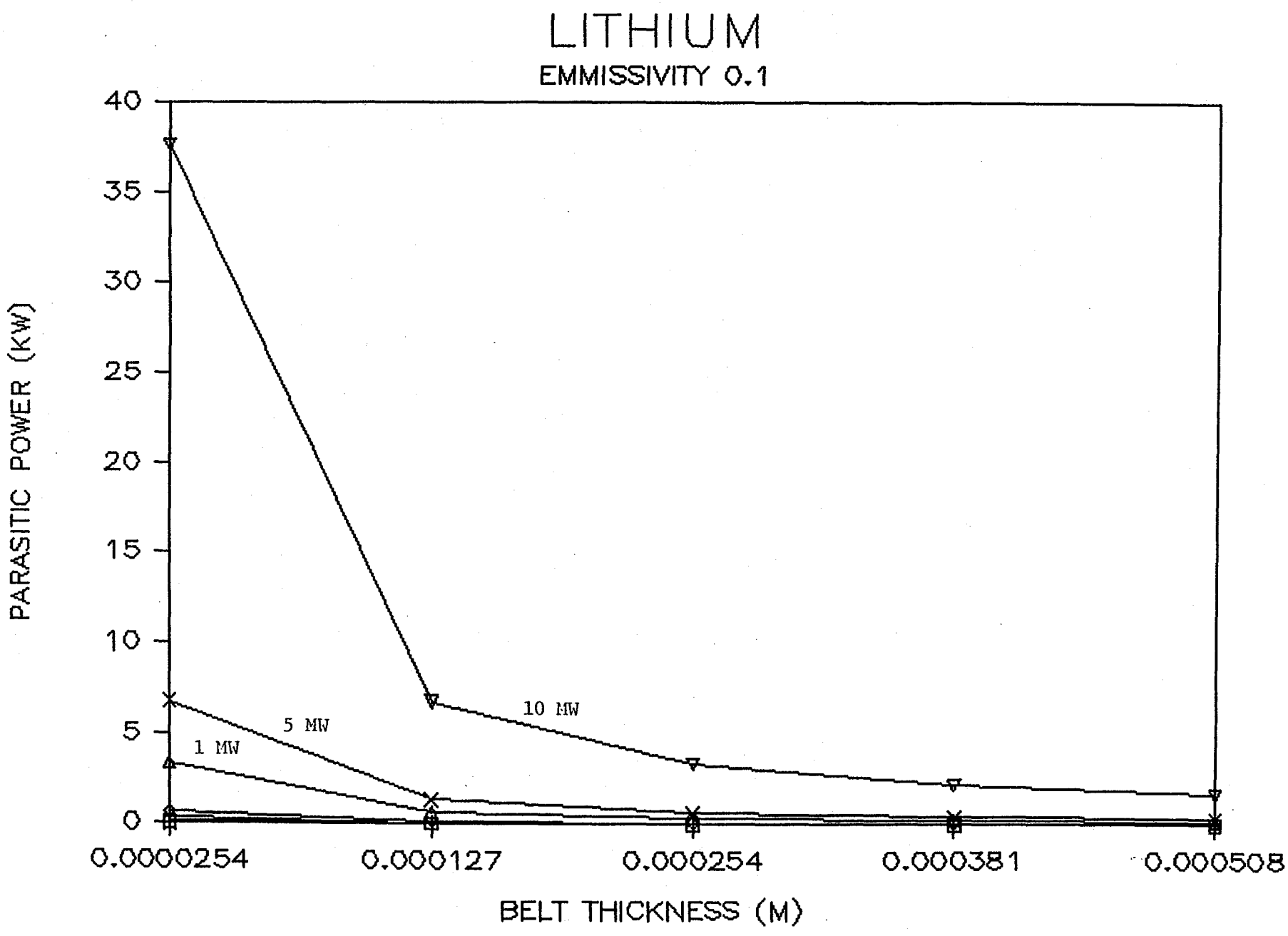

Figure 9: **Parasitic Power vs. Belt Thickness for $\varepsilon = 0.1$ Molten Lithium**

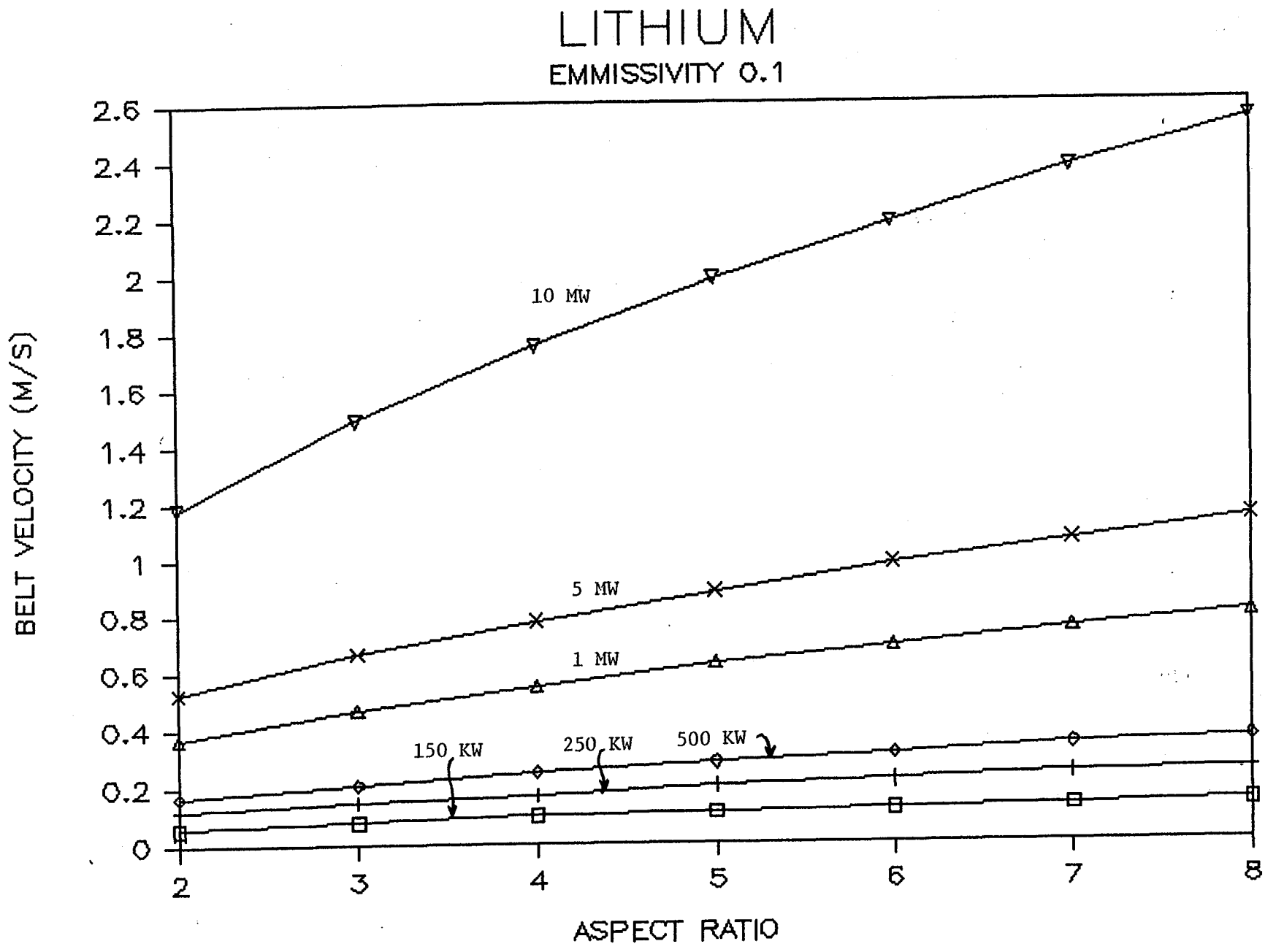

Figure 10: Case 3 Results for Molton Lithium

constraint for the liquid metals operating in the latent mode is maximum belt width, aspect ratio could be substantially increased before the maximum belt velocity constraint or decreased radiative area become a critical issue.

The effect of increased belt thickness on system heat rejection capability and specific power is illustrated in Figure 11. This graph is based on Me_2 operating in the sensible mode with a belt speed of 4.81 m/s (15.8 ft/s). Power levels are shown for belt thickness varying from 0.508 mm (0.020 in) to 2.54 mm (0.100 in). This demonstrates that power levels significantly in excess of 2 MW can be obtained with organic fluids if belt thickness on the order of 2.54 mm (0.100 in) are practical. It should be noted that independent of the belt fluid, thermal rejection levels can be significantly increased with increased belt thickness, although at the expense of system specific power.

Figure 12 portrays the significant effect increased belt speed has on total heat rejected. The graph is shown for tin with an emissivity of 0.1, and a belt thickness of 0.508 mm (0.020 in). Increasing belt speed is a means of scale up for LBR's using low viscosity liquid metals. However, LBR's using organic belt fluids must maintain low velocities due to their high viscosity and parasitic power constraints.

3.3.3 Comparison of LBR Scalability with Heat Pipe Technology

Figure 13 depicts the performance of the LBR compared with standard heat pipe technology. The specific power of approximately 10 kg/kW (22 lbm/kW) for heat pipe radiators, is based on a heat pipe operating temperature of 355 K (180°F). The comparison in Figure 13 is based on LBR using Me_2 operating at 355 K (180°F) and with a belt speed of 4.81 m/s (15.8 ft/s). It should be noted that a maximum heat rejection level of 4 MW was obtained by fixing belt speed at a high value and considering belt thickness and area as variables. As shown by the graph, specific power increases slightly with increasing power rejected by a single LBR unit. In practice, however, this effect will not be a factor for very large power rejection systems, since such systems will most likely be composed of smaller, more "optimally" sized LBR modules.

3.3.4 Hybrid Belt Analysis

In general, the most advantageous belt radiator would utilize a combination of a phase change material with a high emissivity belt structure. Thus, the hybrid radiator would feature the high heat capacity of liquid metals and the high emissivity of the organics. Figure 14 displays levels of heat rejection that are possible with a belt consisting of a hypothetical material having half the heat of fusion of lithium ($\approx$ 300 kJ/kg) and an emissivity equal to Me_2 (0.8). For a 0.05 cm (0.020 in) belt under these conditions, substantial heat rejection levels are possible. As shown by Figure 14, 200 MW can be rejected for a material having an operating temperature of 750 K (891°F). At a substantially lower temperature of 350 K (171°F), a significant rejection load of 10 MW is still possible. Since these thermal loads are significantly in excess of most mission requirements, the HBR shows great promise. It also has the advantage that no free liquid surface is exposed to space, thus eliminating possible contamination problems.

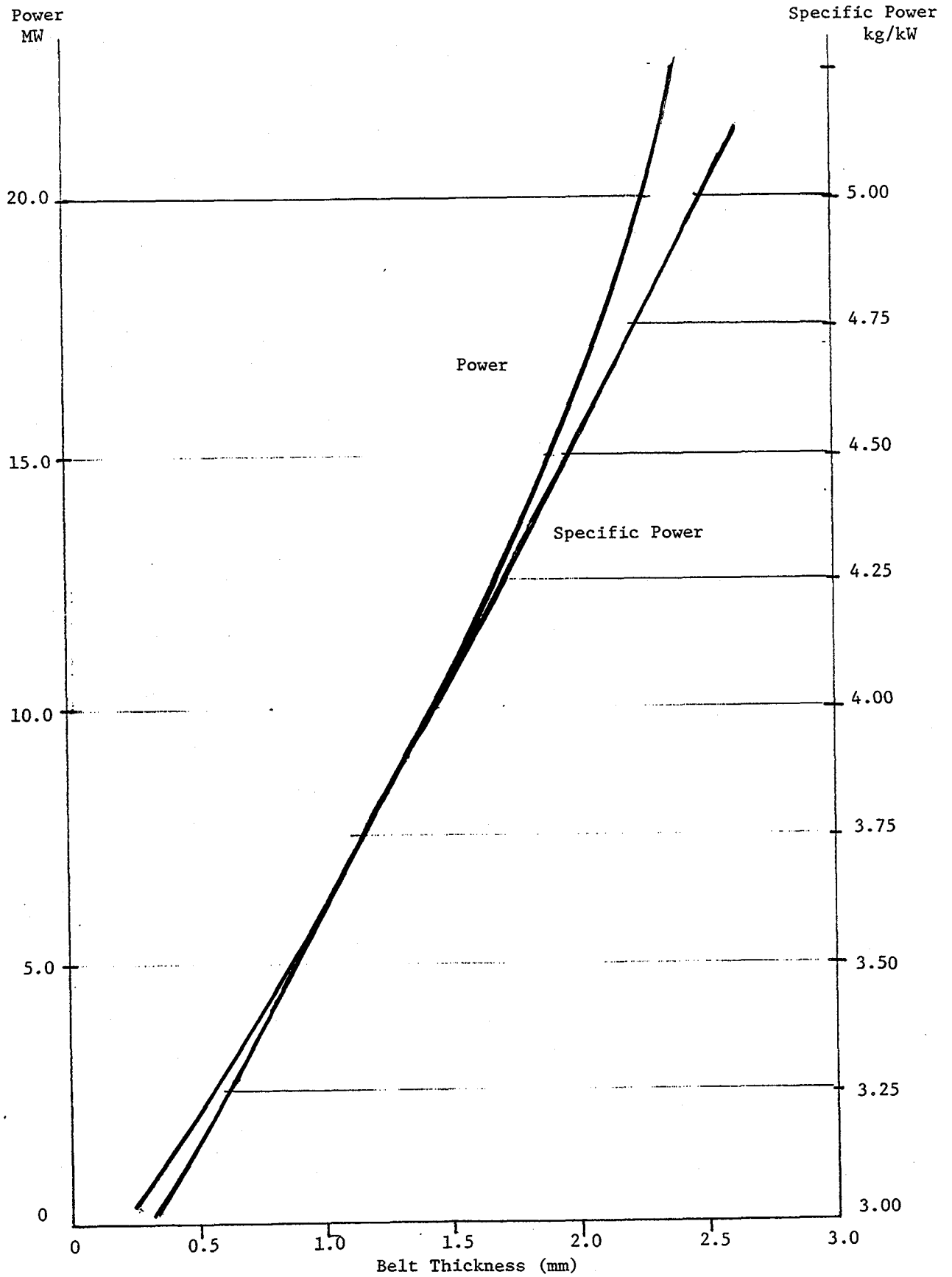

Figure 11: Effect of Increased Belt Thickness on Heat Rejection and Specific Power

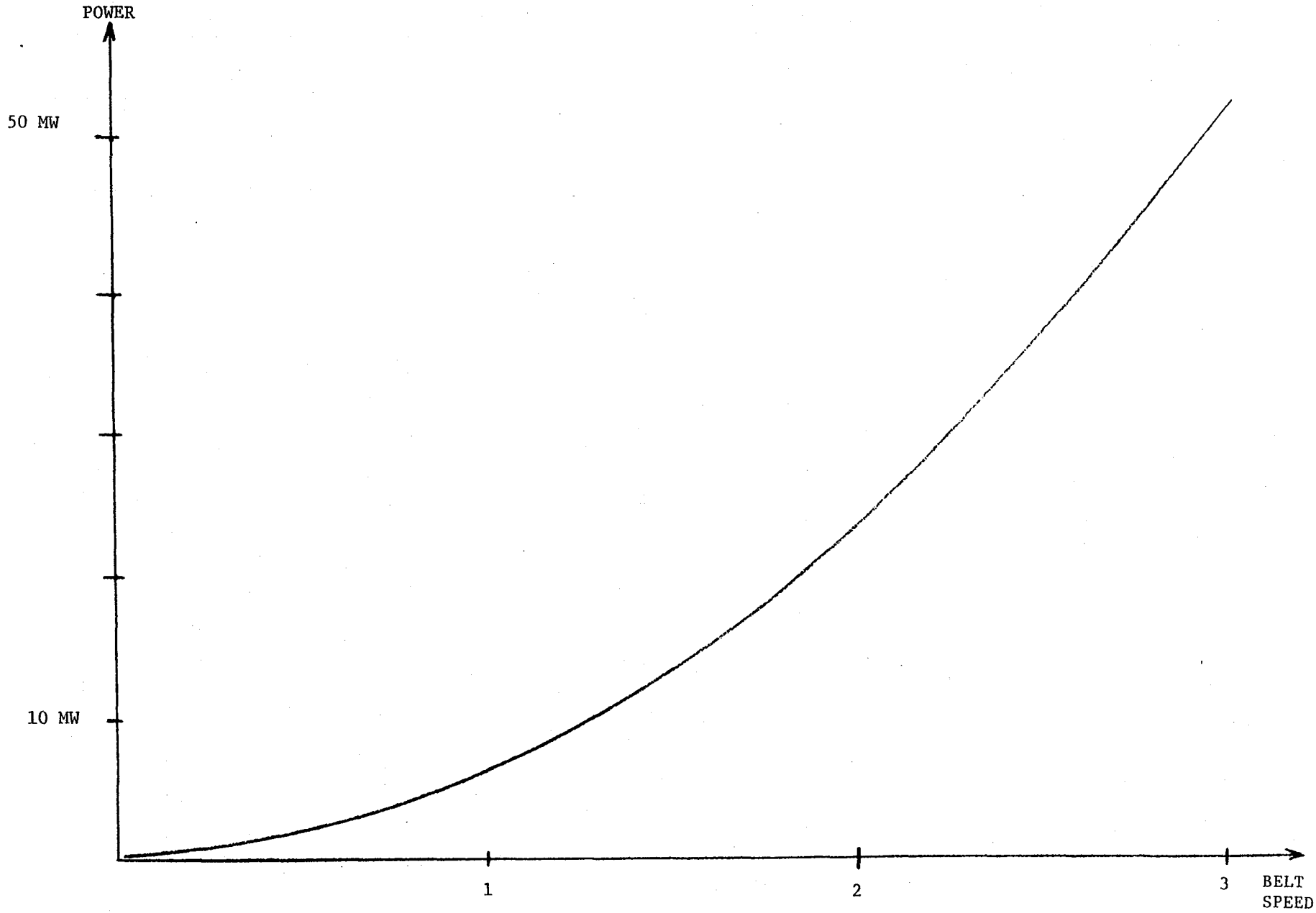

Figure 12: Effect of Belt Speed on LBR Heat Rejection Level

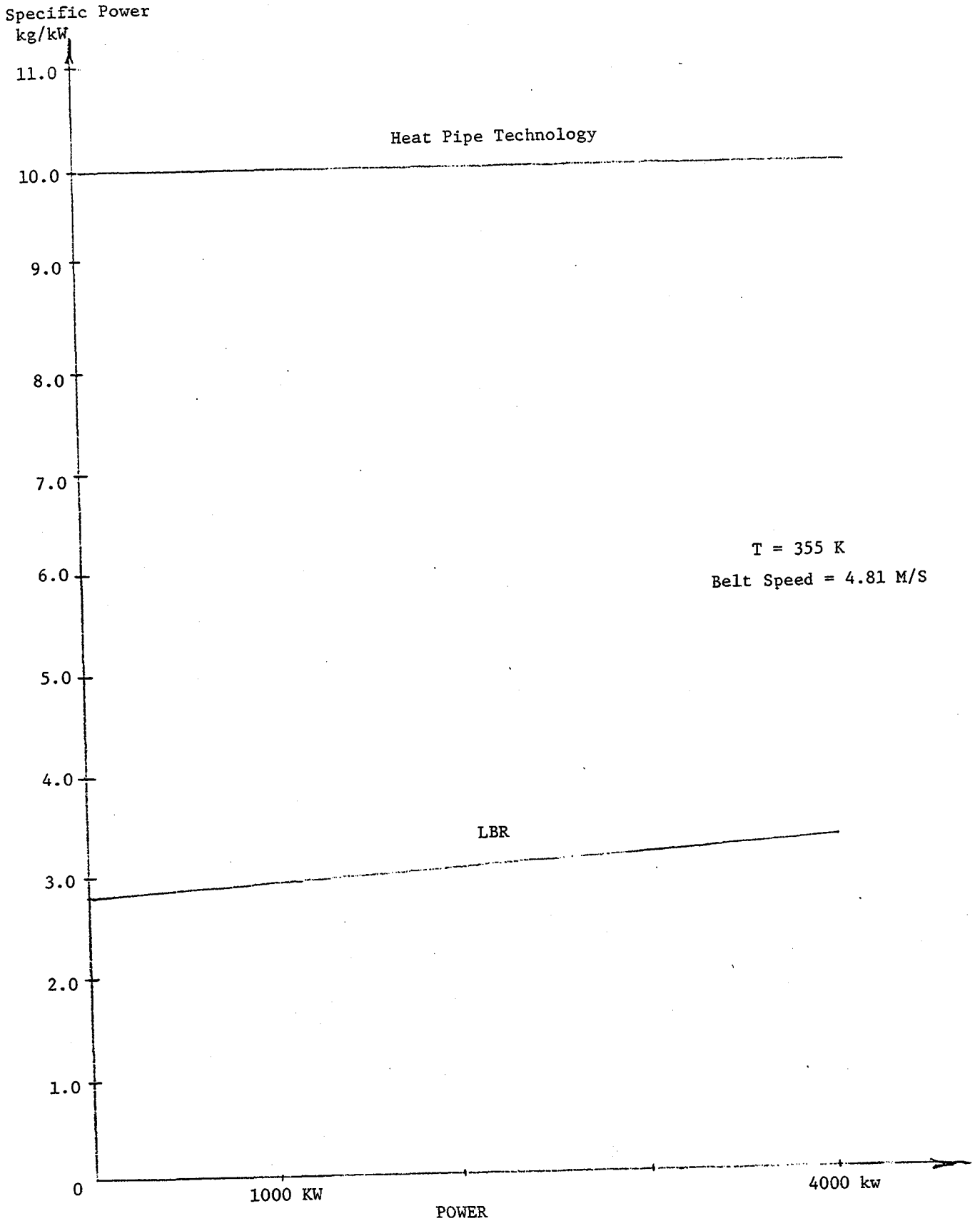

Figure 13: Comparison of Me2 LBR with Heat Pipe Technology

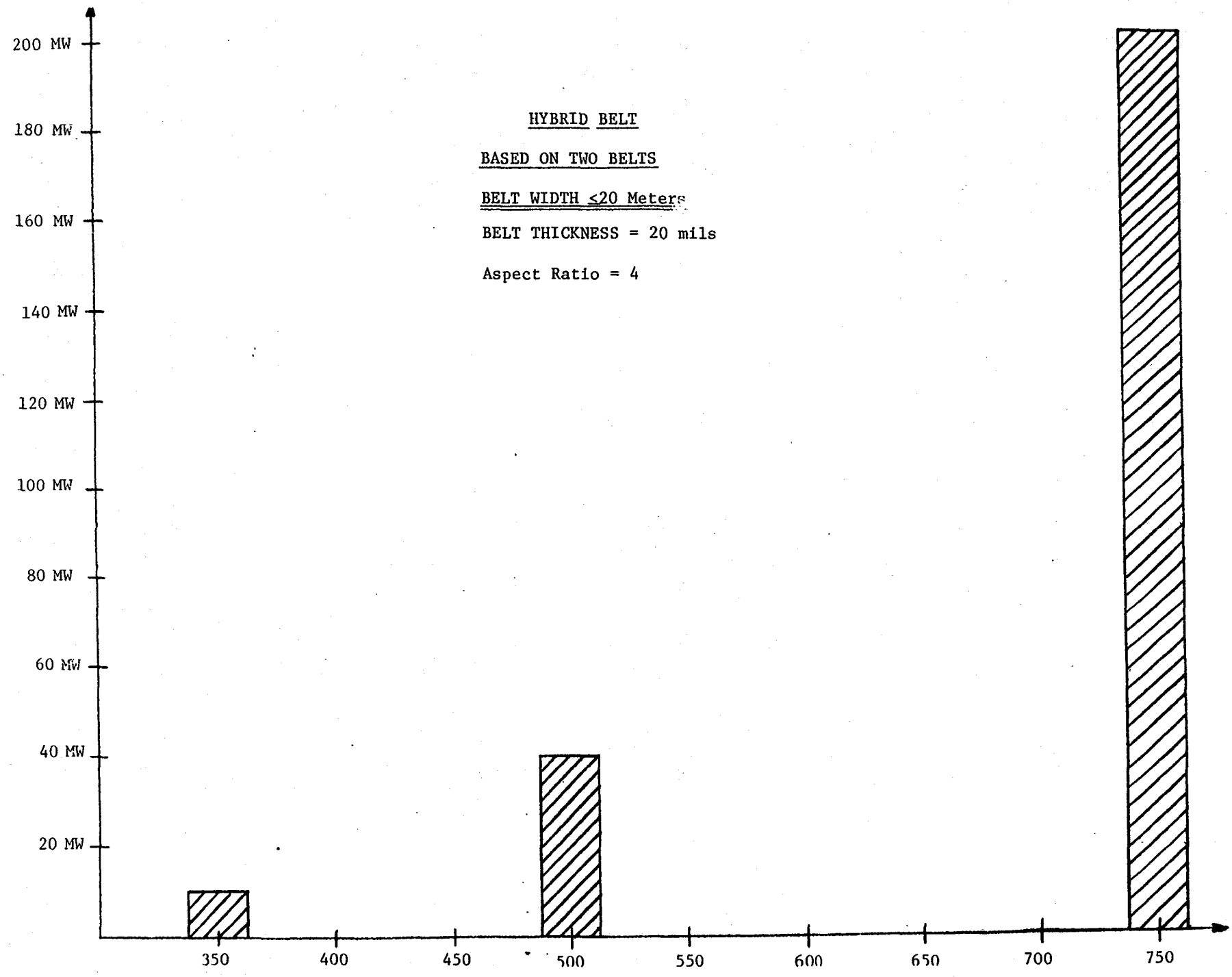

Figure 14: , Hybrid Belt Heat Rejection Performanc

3.4 Conclusions

Overall LBR system scalability is largely dependent on the working fluid chosen. The most scalable systems use phase change liquid metals and are more limited by stowable volume than parasitic power or belt velocity. Even when physical size constraints exist, power rejection levels of up to 20 MW can easily be obtained with phase change liquid metals. The most scalable system in this category is tin, since it operates in the latent mode at a temperature of 500 K (441°F). Liquid metals are also attractive due to their low viscosity, resulting in low parasitic power requirements as compared with organic materials.

Organic materials operating in the sensible mode such as Santovac 6 or Me_2 are limited primarily by parasitic power. The viscosity of oils is approximately two to three orders of magnitude higher than that of liquid metals. For this reason, systems based on organic fluids are only scalable to power rejection levels of 75 to 300 kW. Even if parasitic power constraints are relaxed slightly, the system size will still be constrained by high belt speeds due to the low heat capacity of organic fluids. The most desirable feature of organics is their high emissivity compared with those of liquid metals.

The optimal system would combine the equivalent high heat capacity of liquid metals operating in the latent mode with the high emissivity of organic fluids. Such a hybrid system would utilize a belt composed of a phase change material surrounded by, or coated with, a material of high emissivity. A potential hybrid system could feature gallium as the IHX fluid. If hybrid belt manufacturing hurdles could be solved, power rejection levels significantly in excess of 20 MW could be readily obtained for a single module.

4.0 Dynamic Analysis and Testing

The dynamics of a MBR system were evaluated using software developed specifically for a MBR (Task 1), conducting small scale table top experiments (Task 4), and by conducting experiments aboard NASA's KC-135 reduced gravity test bed (Task 15). Following are the descriptions of the analysis, computer model development, and experimental procedures.

4.1 Computer Modeling of MBR System

4.1.1 Dynamic Model

This section discusses the analysis and computer model developed to understand the dynamics of the belt.

4.1.1.1 Steady-State Motion

As shown in Figure 15, the steady-state shape of the belt will be cylindrical[1] and all elements in force equilibrium. Thus, for a segment of length dx, a force balance in the radial direction yields:

[1] This does not take into account (i) any tension force caused by an imbalance between the centrifugal force and gravitational force (important for a large belt circulating in the radial direction), (ii) variation in belt properties due to liquid phase change and (iii) the effects of Coriolis acceleration. These are discussed later.

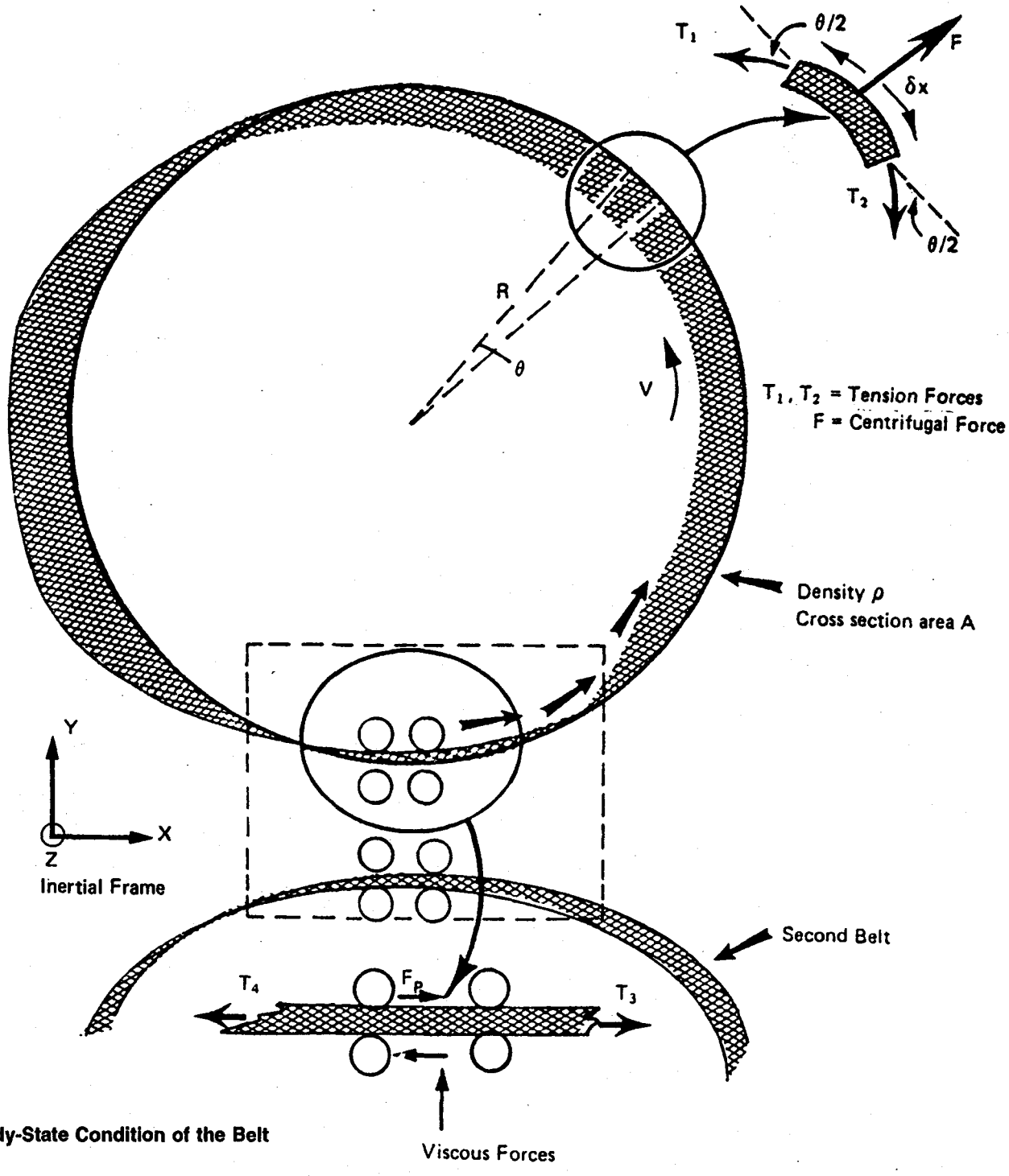

Figure 15: Steady-State Condition of the Belt

$$F = T_1 \sin\frac{\theta}{2} + T_2 \sin\frac{\theta}{2}$$

Where F is the centrifugal force on the element defined as:

$$dF = \rho A dx \frac{V^2}{R}$$

A = Belt Cross Sectional Area

If no tangential acceleration is assumed, a force balance in the tangential direction yields:

$$T_1 \cos\frac{\theta}{2} = T_2 \cos\frac{\theta}{2}$$

or $T_1 = T_2 = T$

substituting

$$\theta = \frac{dx}{R}$$

and assuming

$$\sin\theta \approx \theta$$

we finally obtain:

$$T = \rho A V^2$$

indicating the tension in the belt is proportional to mass per unit length velocity squared.

In an ideal system with no damping or tension, the forces acting at the rollers will be zero since T_3 will equal T_4. Thus, the belt will continue spinning at velocity V. In reality, however, viscous drag forces and variations in belt tension are present in the belt length between the rollers. These are compensated by the roller drive.

4.1.1.2 Dynamic Response Issues

As mentioned earlier, the objective of the dynamic analysis is to study the response of a belt to external effects and spacecraft generated forces. These forces can generate in-plane or out-of-plane motion of the belt as discussed next.

4.1.1.2.1 External Effects

Two of the external effects to be considered are:

- The acceleration generated by gravity/centrifugal force imbalance; and
- The Coriolis acceleration effects.

4.1.1.2.1.1 The force imbalance

The acceleration generated by the imbalance between gravitational and centrifugal forces is depicted in Figure 16. The center of gravity (cg) of the spacecraft/belt system is assumed to lie in the spacecraft. If we assume that the spacecraft is in a circular orbit with a radius r_{cg} from the center of earth, then from the force balance, centrifugal equals gravitational force:

$$M\omega^2 r_{cg} = MM_e G/r_{cg}^2 \tag{1}$$

Where

M = mass of the system;
M_e = mass of the earth (6.0×10^{24} kg, 1.3×10^{25} lbm);
G = gravitational constant (6.67×10^{-20} km^3/kg-s^2, 1.1×10^{-9} ft^3/lbm-s^2); and
ω = angular velocity of spacecraft.

From Equation (1),

$$\omega^2 = M_e G/r_{cg}^3 \tag{2}$$

Now, Point A on the belt will also rotate around earth at the same angular velocity ω; however, since Point A is at radius r_a, which may not be the same as radius of the center of gravity (r_{cg}), the gravitational force will not cancel the centrifugal force. For $r_a > r_{cg}$, the centrifugal force will be higher than the gravitational force. The reverse will be true for $r_a < r_{cg}$. The acceleration due to this imbalance, a_i will be:

$$a_i = \omega^2 r_a - M_e G/r_a^2 \tag{3}$$

Substituting the value of ω from equation (2) and rearranging

$$a_i = \frac{M_e G}{r_a^2}\left[\left(\frac{r_a}{r_{cg}}\right)^3 - 1\right] \tag{4}$$

For typical values of r_a, r_{cg}, M_e and G, the value of a_i is indeed quite small, as shown in Table 2. Thus this effect need only be considered for very large belts.

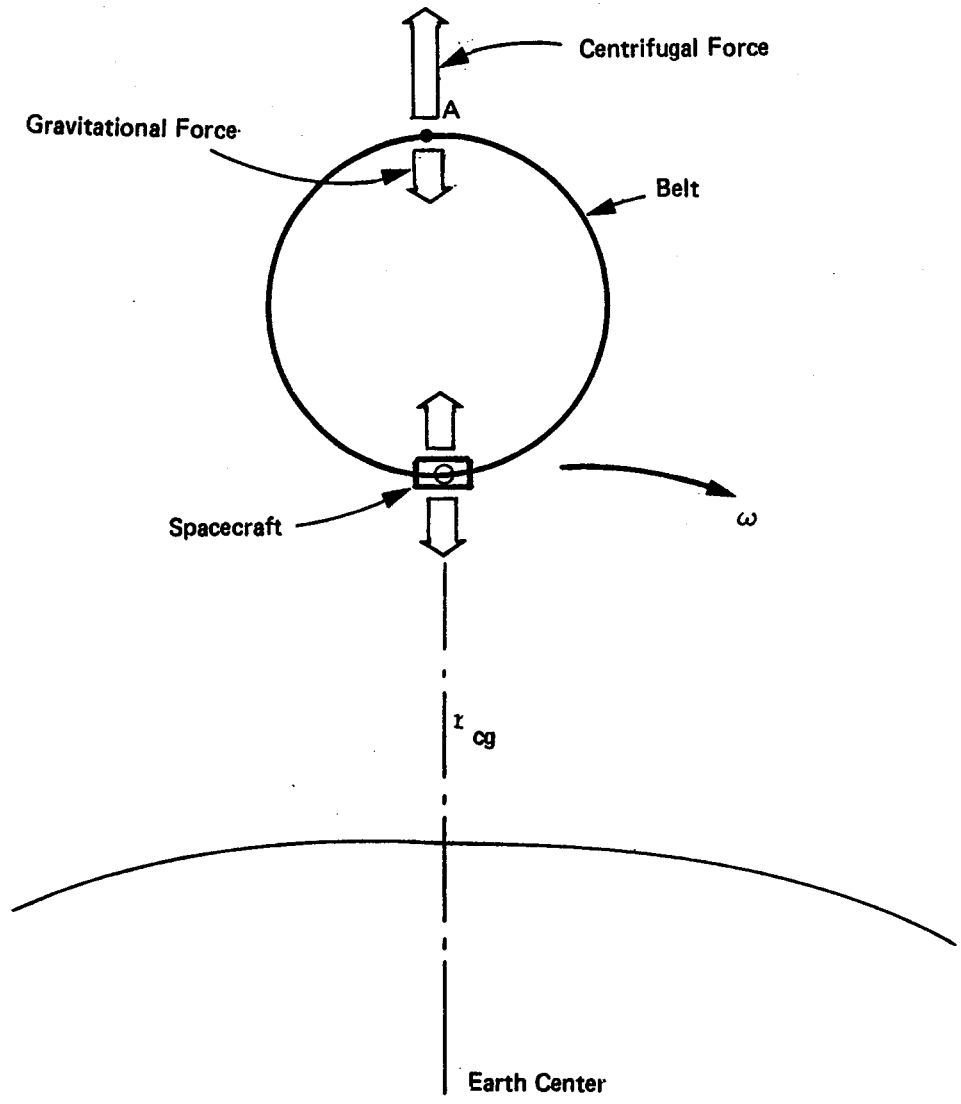

Figure 16: An Imbalance in Centrifugal and Gravitational Forces

Table 2: Typical Orbit Parameters for LEO

Variable	Variable Description	Value
r_{cg}	Spacecraft orbital radius; corresponds to a circular equatorial orbit of approximately 282 km (176 mi)	6660 km (10656 mi)
P	Orbital period; corresponds to a circular equatorial orbit of approximately 282 km (176 mi)	90 min
ω_s	Angular velocity of spacecraft	1.16×10^{-3}/s
r_b	Belt radius	6 m
r_a	Maximium belt orbital raduis ($r_a = r_{cg} + r_b$)	6660.006 km
a_i	Imbalance acceleration	2.4×10^{-8} km/s^2
V_{rel}	Belt tangential velocity	0.001 km/s
a_{cor}	Coriolis acceleration	2.32×10^{-6} km/s^2
a_c	Centripetal acceleration due to belt rotation	1.67×10^{-4} km/s^2
a_c/a_i	Ratio of centripetal to accelerations	6958
a_c/a_{cor}	Ratio of to coriolis acceleration	72

4.1.1.2.1.2 The Coriolis acceleration

Coriolis acceleration (a_c) will exist any time a point within a rotating frame of reference has a relative velocity with respect to the frame of reference. This acceleration is defined as:

$$a_c = 2\,\omega \times V_{rel}$$

where ω is the angular velocity of the frame with respect to the inertial frame and V_{rel} is the relative velocity.

Now, every point in the belt has a relative velocity with respect to the spacecraft which is rotating around earth. Assuming spacecraft rotation once every hour and V_{rel} equal to 1 m/sec, the magnitude of the Coriolis acceleration is 0.00232 m/sec^2 (0.00761 ft/s^2). For a belt with radius 6.49 m, the centripetal acceleration on belt is 0.167 m/sec^2 (0.547 ft/s^2), which is 72 times the Coriolis acceleration. Thus, the effects of the Coriolis acceleration can be neglected in the initial analysis.

4.1.1.2.2 Spacecraft Motion

The spacecraft can translate or rotate along any of the three axes shown in Figure 17. Also, it can execute a motion which includes any combination of these. This initial investigation was restricted to uncoupled motions.

It is important to make a distinction between vibrations and gross deformations. A relatively small motion of the spacecraft can set up vibrations in the belt. For example, a motion in the y-direction can start bending vibrations in the belt, as shown in Figure 18 (a). A study of these vibrations, their modes, frequencies and damping constants, is useful while preparing a final design of the belt. At this stage, however, it may be more important to study the gross deformation of the belt due to large displacements of spacecraft such as those shown in Figures 17 (b) and (c).

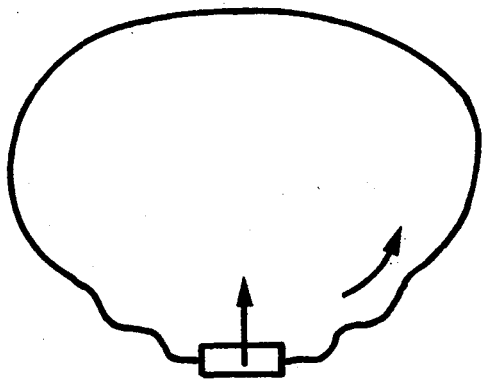

(a) In-plane Bending Vibrations in Belt Due to Small Displacement of Spacecraft Along Y Direction

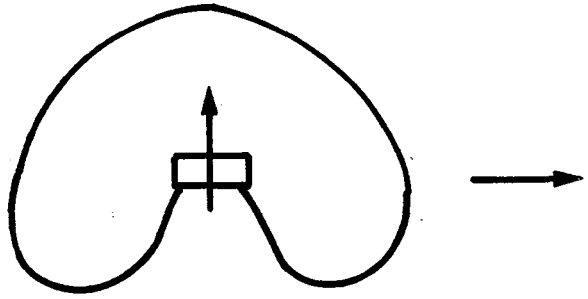

(b) Gross Deformation of Belt Due to Large Displacement of Spacecraft Along Y Direction

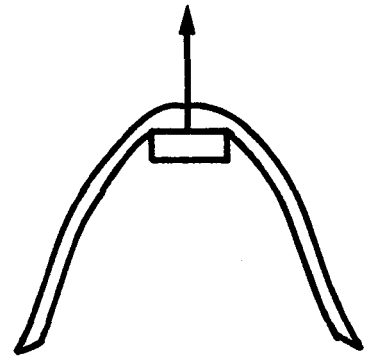

(c) Belt Failure

Figure 17: Vibration and Gross Deformation in Belt Due to Y Direction Translation of Spacecraft

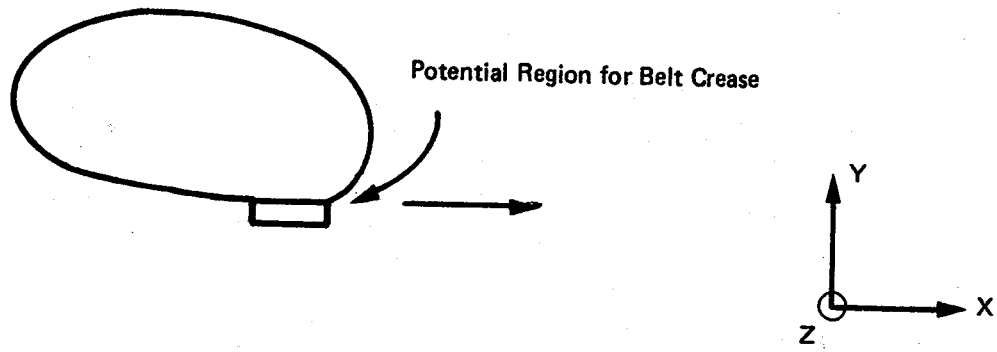

(a) Translation Along X Axis

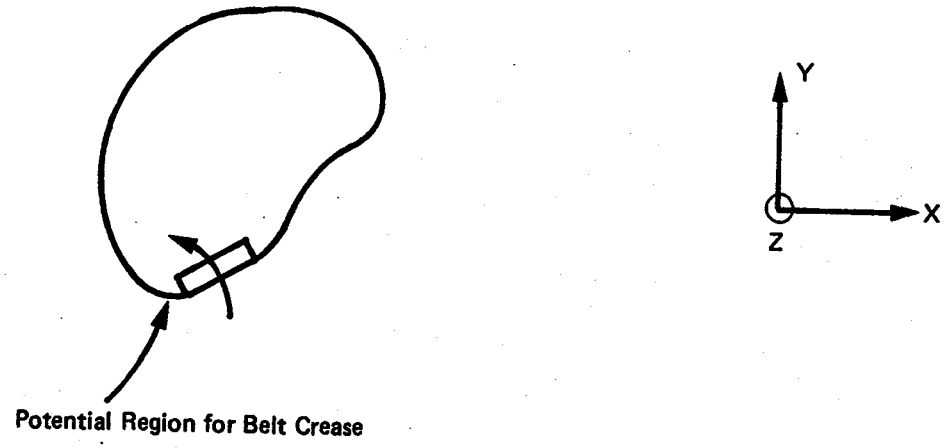

(b) Rotation Around Z Axis

(For translation along Y axis, see Figure 2.3 (b).)

Figure 18: Gross Deformation in Belt Due to In-Plane Motion of Spacecraft

Such deformations can cause a permanent crease in the belt or harm its structural integrity. If this can happen while the spacecraft is executing a maneuver the feasibility of the whole concept will be in jeopardy. The same cannot be said about the vibrations in a belt. They may lead to certain temporary performance deterioration, but generally not to a system failure. Thus, the emphasis is on studying the gross deformations.

We next make qualitative observations about gross deformation in a belt due to spacecraft motions, i.e. translation along and rotation about the three axes.

4.1.1.2.2.1 In-plane motion

The translation of a spacecraft along the x- and y-axes and rotation around the z-axis will produce in-plane belt motion. This motion is less complex to analyze than the out-of-plane motion produced by the other three types of spacecraft motion. As discussed above, translation along the y-axis will produce motion such as that shown in Figure 17. A large acceleration along the x-axis will produce a belt shape as shown in Figure 19 (a) leading to a crease type failure near entry or exit from the spacecraft. Rotation around the z-axis will still produce in-plane motion of the belt, but now the danger will be a crease type failure at the spacecraft entry or exit, or belt wrapping on itself (see Figure 18 (b)).

A computer program has been developed to understand the in-plane motion of the the program is discussed in Section 4.1.1.3.

4.1.1.2.2.2 Out-of-plane motion

As discussed earlier, the out-of-plane motion has not been analyzed in any depth. However, some observations about this can be made:

- The motion of the spacecraft along the z-axis will produce a somewhat complicated response in the belt.
- The belt will resist motion because of inertia and that will in effect produce a shear force and torque along its x-axis near the spacecraft entry and exit points. This will cause a twist in the belt and, potentially, a damaging crease, as shown in Figure 19 (a)..

That torque (T) on the belt near the spacecraft can be expressed as:

$$T = M_b Z R_b$$

Where

M_b = Belt mass
R_b = Belt radius
Z = Belt cg acceleration along z-axis

If the torque needed to cause permanent damage (τ_c) is known, the critical value of acceleration can be calculated from:

$$Z_{critical} = \frac{T_c}{M_b R_b} \qquad (5)$$

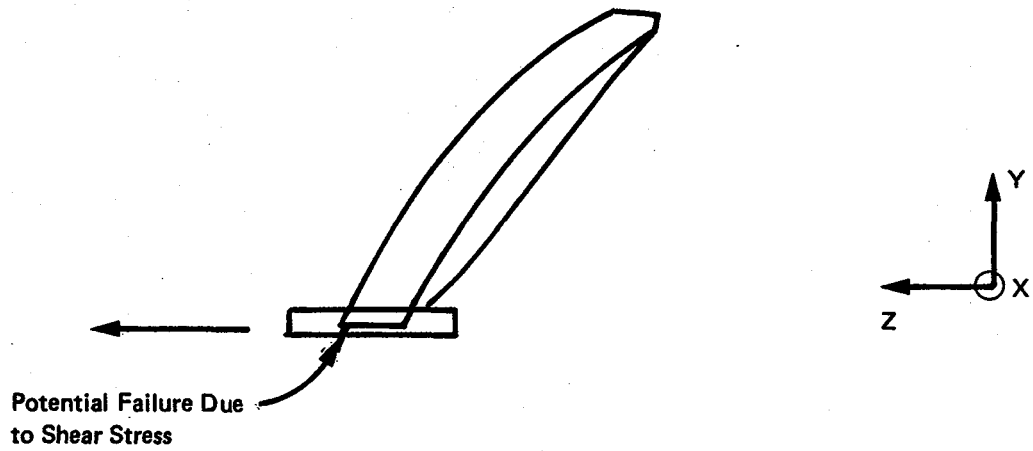

(a) Acceleration Along Z Axis

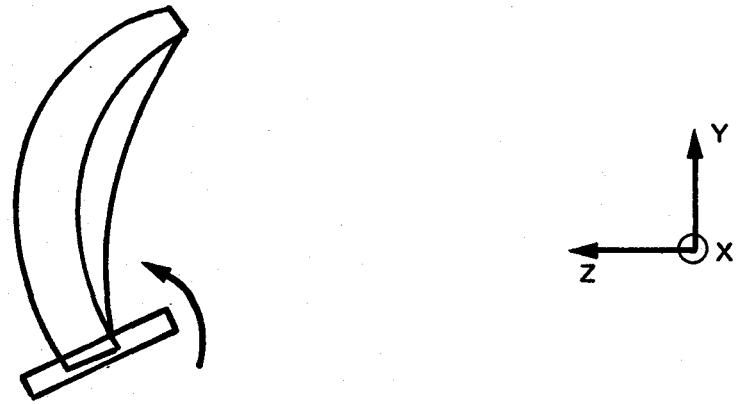

(b) Rotation Along X Axis

Figure 19: Gross Deformation in Belt Due to Out-of-Plane Motion of the Spacecraft

As long as the spacecraft motion keeps belt cg acceleration under this value, the belt will not be damaged. Laboratory data on belt compliance in twist and torque required to cause permanent damage are needed to obtain acceleration threshold along the z-axis.

However, to get a very rough estimate on critical z-axis acceleration, we made the following assumptions:

- The belt fails in twist because the peak shear stress in the belt at the belt edges exceeds shear yield limit.
- Shear stress at any location in the belt is proportional to its distance from belt mid-line.

Then, the following equation holds true:

$$T_c = 0.667\tau_y \frac{w^2}{2} t \qquad (6)$$

Where

τ_y= shear yield limit
w = belt width
t = belt thickness.

For an aluminum belt with a thickness of 0.25 mm (0.01 in), width of 3.3 m (10.8 ft), radius of 6.0 m, and a mass of 84 kg (185 lbm). Shear strength for aluminum is in the 62 MN/m^2 to 331 MN/m^2 (9000 psi to 48,000 psi), with a mean of 196 MN/m^2 (28,500 psi).

$T_c = 3.5 \text{ X } 10^5$ N-m

$Z_{critical} = 347$ m/sec^2 = 35 g

This is a very rough estimate based on an assumption that the "weakest link in the chain" in the z-axis acceleration mode is shear failure at the belt outer edge near spacecraft entry or exit. Another possibility is that the belt will get tangled at a much lower acceleration level. However, this analysis indicates that the belt can take substantial acceleration levels along the z-direction. This is important to note when the in-plane acceleration levels are examined.

The rotational acceleration about the x-axis will produce an effect on the belt similar to that produced by the translational acceleration along the z-axis (see Figure 19 (b)). The torque created by such motion on the belt at spacecraft entry-exit points will be:

$$\tau = \alpha I_{AA} \qquad (7)$$

$$I_{AA} = \frac{m_b}{2}\left(R_b^2 + \frac{w_b^2}{6}\right) + m_b R_b^2$$

where

I_{AA} = belt moment of inertia along an axis passing through spacecraft and parallel to the x-axis.

If the critical torque level is assumed to be 3.5×10^5, and I_{AA} to be 4612 kg-m^2, peak angular acceleration along the x-direction is:

$$\alpha = 3.5\,(10^5)/4612 = 76 \text{ rad/sec}^2$$

This high acceleration level indicates that the belt will fail because of some other mode (e.g., getting tangled) prior to failure due to shear stress when the spacecraft is rotated about the x-axis.

Finally, the rotation of the spacecraft along the y-axis produces a complex response in the belt, particularly if the rotational acceleration is significant. The failure mode in this case could be buckling on the belt sides. Some laboratory tests are needed to determine buckling limits of the belt and hence the critical acceleration levels. Our engineering judgment is, however, that the belt will be able to take relatively large rotational acceleration levels about the y-axis.

4.1.1.3 Dynamic Model of In-Plane Motion

While selecting the best way of modeling the in-plane motion of the belt, various options were considered.

Early in the project it was decided not to attempt to develop a distributed closed-form model of the belt. Lallman of Langley Research Center has performed a detailed analysis of vibration characteristics of a steadily rotating slender ring (see Reference 3). As it is, this analysis is very complex. The MBR incorporates additional complications of (*i*) constraints to the motion due to travel inside the spacecraft and (*ii*) nonlinear characteristics of a two-phase belt. These would make any search for a closed form solution prohibitively complicated, and very likely, futile.

Thus, we decided, instead, to use a lumped parameter approximation. Figure 20 shows the lumped parameter representation of the MBR for investigating the in-plane motion. As can be seen, the belt is divided into lumped masses connected by:

- Linear springs and dampers representing belt elasticity and damping in the tension/compression mode.
- Rotational springs and dampers representing belt stiffness and damping in the bending mode.

The dynamic equations of motion of the belt are a collection of equations of motion for each lumped mass in the x- and y-directions, i.e.:

$$\ddot{X}_i = \Sigma \frac{F_{xi}}{M_i} \tag{8}$$

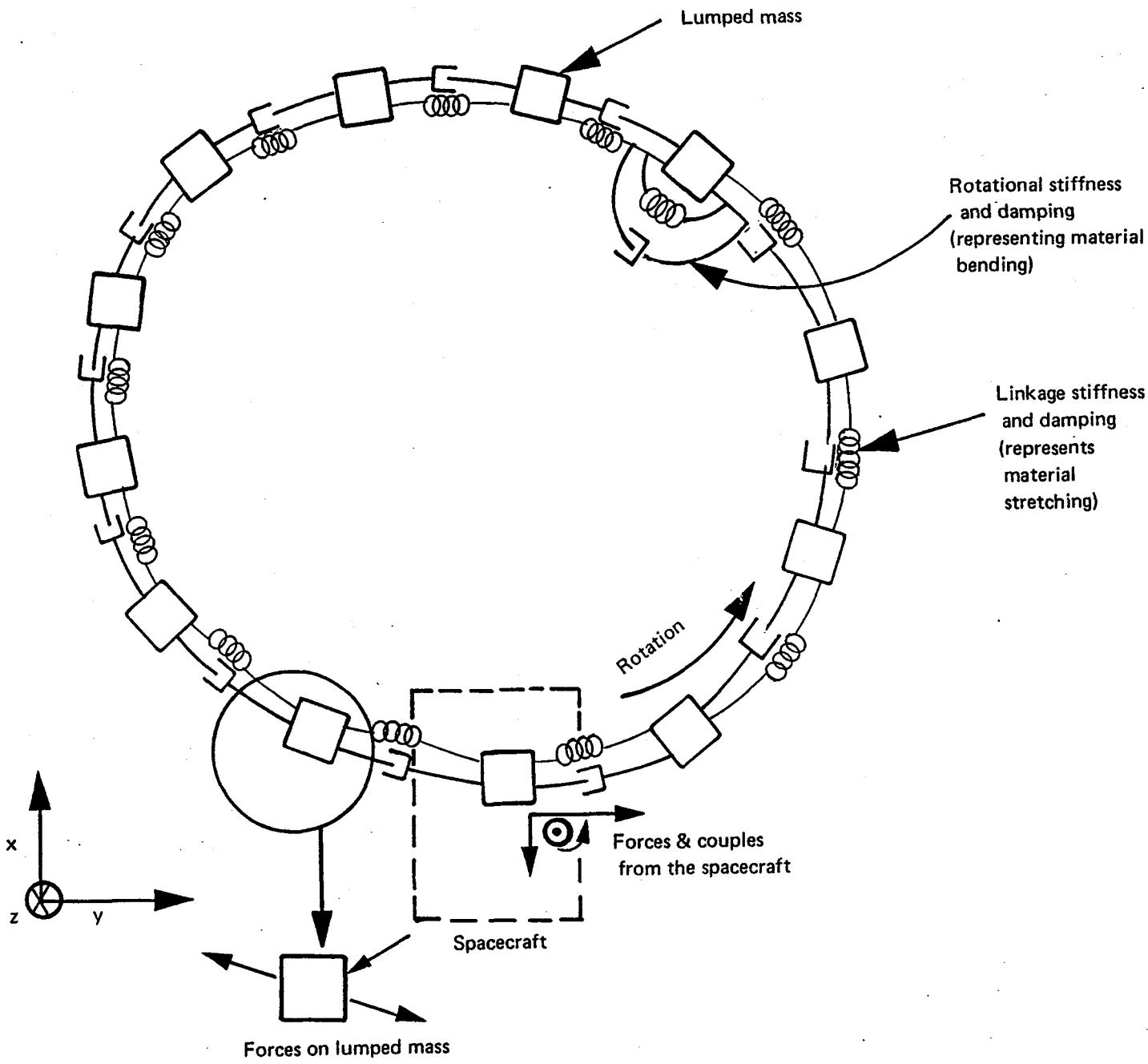

Figure 20: Lumped-Parameter Representative of the LBR Belt for Investigation In-Plane Vibration Modes

$$\ddot{Y}_i = \Sigma \frac{F_{yi}}{M_i} \tag{9}$$

Where ΣF_{xi} and ΣF_{yi} are summations of the x- and y-direction components of forces acting on the ith mass.

M_i = mass of the ith mass

$\ddot{X}_i$ = x-direction acceleration of the ith mass

$\ddot{Y}_i$ = y-direction acceleration of the ith mass

Note that all displacements, velocities and accelerations are referenced to the inertial frame.

The forces on the masses can arise from the bending of linear springs and dampers (shown in Figure 20) or from the spacecraft. The spacecraft provides forces necessary to impart a velocity to the belt so that it can perform its function as a radiator. Additional forces are imparted when the spacecraft moves (beyond its steady rotation around earth). The spacecraft imparted forces, however, depend on the detailed designs of bath and drive mechanism which are not yet finalized. In the model developed, we bypassed the problem of having to specify the forces that would act on the belt inside the spacecraft by assuming that the spacecraft imposes displacement and velocity constraints on the part of the belt inside the spacecraft, with forces assumed to be such that these constraints are observed.

The forces acting on the lumped masses are as shown in Figure 21. The forces acting on a lumped mass are:

$$F_{ki} = k_i(d_i - l_i) \qquad for\, d_i > l_i$$

$$= 0 \qquad for\, d_i \le l_i \tag{10}$$

where

l_i = initial length of link i,
k_i = linear stiffness (elasticity) of link i,
F_{ki} = linear stiffness force in link i, and
d_i = stretched length of link i.

$$d_i = \sqrt{(X_{i+1} - X_i)^2 + (Y_{i+1} - Y_i)^2} \tag{11}$$

where

X_i = x-coordinate of mass i
Y_i = y-coordinate of mass i

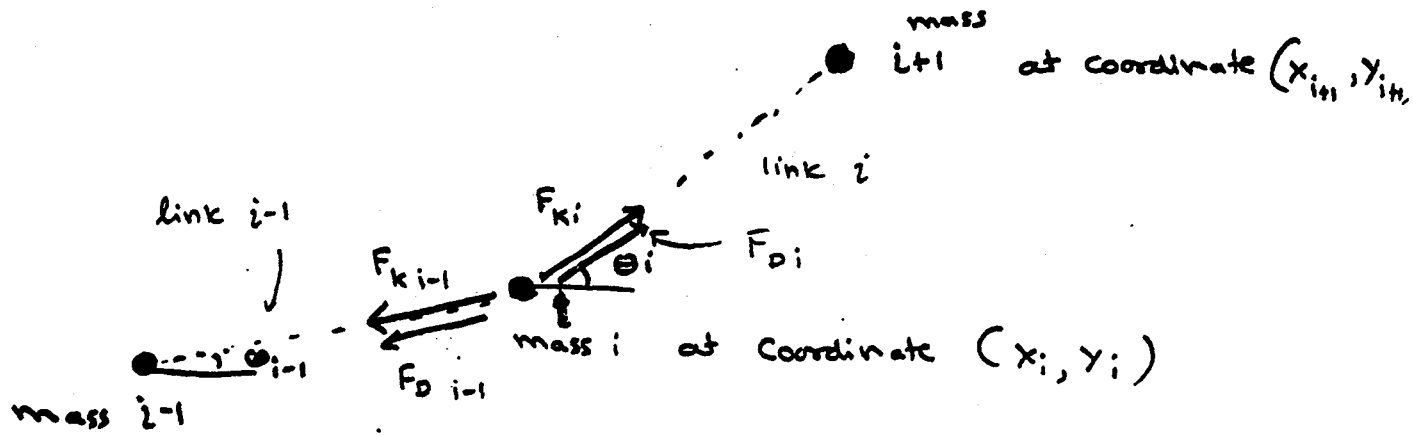

(a) Forces from belt stretching

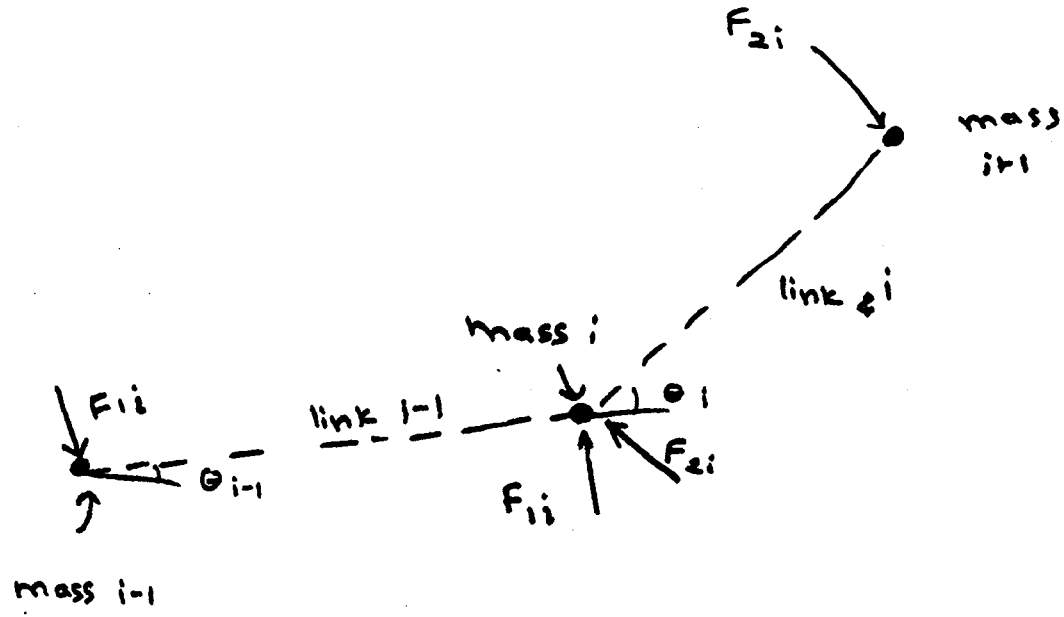

(b) Forces from belt bending

Figure 21: Forces Acting on Lumped Masses

$$k_i = \frac{E_t A}{l_i} \tag{12}$$

where

E_t = belt modulus of elasticity in tension
A = cross-sectional area of the belt

Similarly, the damping force in link i, F_{Di}, is given by

$$F_{Di} = \frac{V_i B}{l} \tag{13}$$

where

B = damping coefficient of the belt in tension
V_i = velocity of link i

$$V_i = (V_{xi+1} - V_{xi})\cos\theta_i + (V_{yi+1} - V_{yi})\sin\theta_i \tag{14}$$

where

V_{xi} = x-direction velocity of mass i
V_{yi} = y-direction velocity of mass i

$$B = 2\pi\eta\sqrt{AE_t\mu} \tag{15}$$

where

η = damping ratio of first natural frequency in stretching
μ = linear mass density of belt.

Similarly, the forces acting on the lumped masses due to belt bending are given by:

$$F_{1i} = (K_{li}\psi_i + B_{li}\psi_i)/d_{i-1} \tag{16}$$

$$F_{2i} = (k_{li}\psi_i + B_{li}\psi_i)/d_i \tag{17}$$

$$\psi_i = \theta_i - \theta_{i-1} \tag{18}$$

$$k_{li} = \frac{E_b I}{l_i} \tag{19}$$

$$B_{li} = \frac{B_l}{l_i} \tag{20}$$

where

k_{li} = belt bending stiffness at mass ι
B_l = belt bending damping coefficient
ψ_i = bending angle
E_b = modulus of elasticity in bending
I = belt section modulus
B_l = damping coefficient for one meter long belt in bending

Also, for a belt made out of a mesh,

$$B_l = \frac{4Br_f}{3\pi} \tag{21}$$

where

r_f = wire radius

The forces given by equations (10), (13), (16) and (17) are broken into x and y components and added together so that mass accelerations in the x- and y-directions can be obtained using equations (8) and (9).

The constraints imposed by the spacecraft are shown in Figure 22.

For every mass inside the spacecraft,

$$\ddot{X}_i = \ddot{X}_s - 2Vsin(\Omega)\dot{\Omega} - \ddot{\Omega}X_{bi}\sin(\Omega) - \dot{\Omega}^2 X_{bi}\sin(\Omega) \tag{22}$$

$$\dot{X}_i = \dot{X}_s + V\cos(\Omega) - X_{bi}\sin(\Omega)\dot{\Omega} \tag{23}$$

$$X_i = X_s + X_{bi}\cos(\Omega) \tag{24}$$

$$\ddot{Y}_i = \ddot{Y}_s + 2V\cos(\Omega)\dot{\Omega} + \ddot{\Omega}X_{bi}\cos(\Omega) - \dot{\Omega}^2 X_{bi}\sin(\Omega) \tag{25}$$

$$\dot{Y}_i = \dot{Y}_s + X_{bi}\cos(\Omega)\dot{\Omega} + V\sin(\Omega) \tag{26}$$

$$Y_i = Y_s - H + X_{bi}\sin(\Omega) \tag{27}$$

where

$\ddot{X}_i$ = acceleration along inertial x-axis for mass i
$\dot{X}_i$ = velocity along inertial x-axis for mass i
X_i = displacement along inertial x-axis for mass i
$\ddot{Y}_i$ = acceleration along inertial y-axis for mass i
$\dot{Y}_i$ = velocity along inertial y-axis for mass i

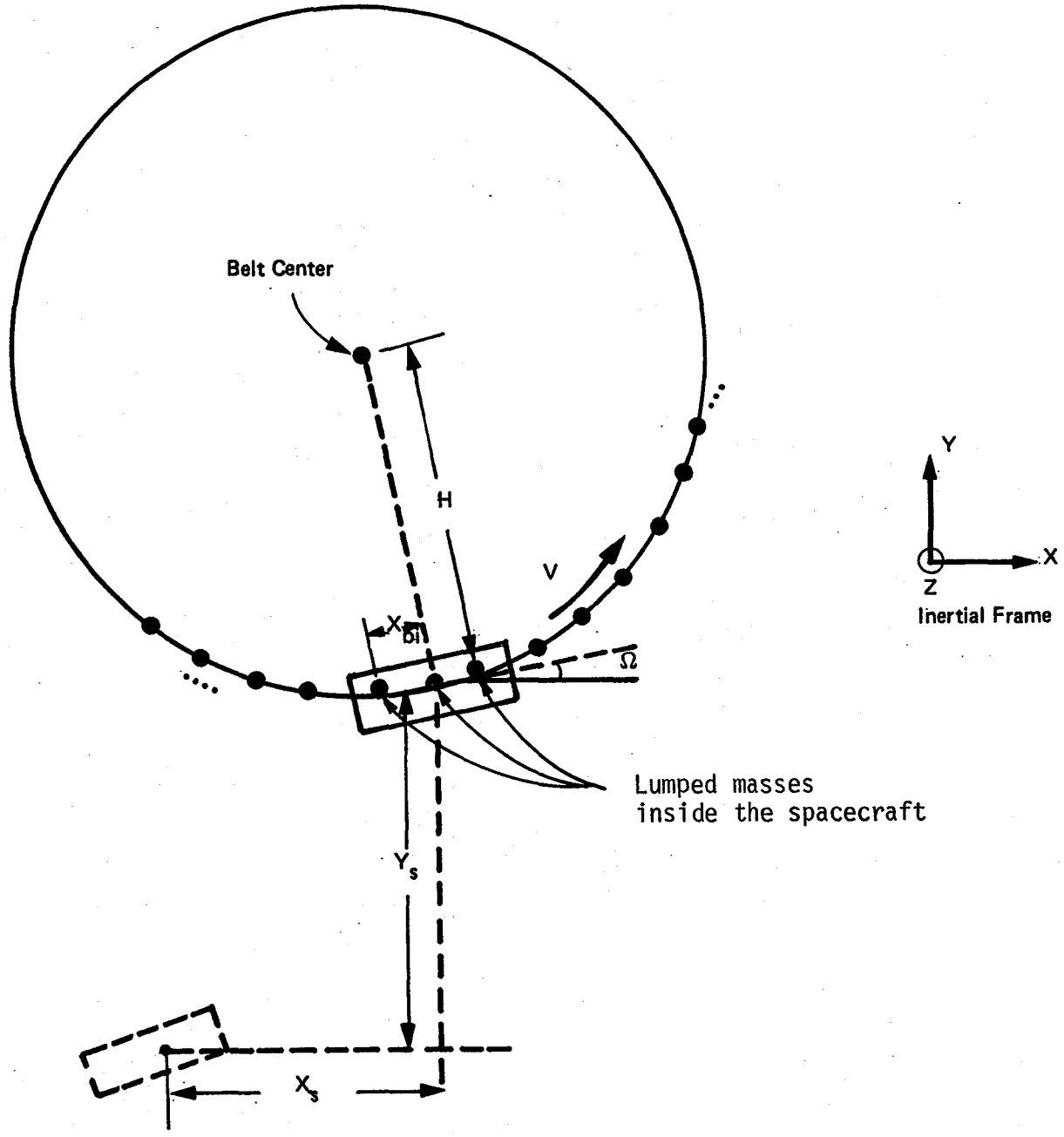

Figure 22: Spacecraft Motion in the Inertial Frame

Y_i = displacement along inertial y-axis for mass i
$\ddot{\omega}$ = spacecraft angular acceleration around inertial z-axis
$\dot{\omega}$ = spacecraft angular velocity around inertial z-axis
ω = spacecraft angular displacement around inertial z-axis
$\ddot{X}_s$ = spacecraft acceleration along inertial x-axis
$\dot{X}_s$ = spacecraft velocity along inertial x-axis
X_s = spacecraft displacement along inertial x-axis
$\ddot{Y}_s$ = spacecraft acceleration along inertial y-axis
$\dot{Y}_s$ = spacecraft velocity along inertial y-axis
Y_s = spacecraft displacement along inertial y-axis
X_{Bi} = distance of lumped mass i from spacecraft center
H = height of belt center above liquid bath inside spacecraft
V = belt velocity.

This model was coded and converted into a computer simulation which generates snapshots of the belt starting from an initial condition to any desired time subsequent to application of spacecraft motion.

At this point it should be noted that the belt designs under consideration incorporate materials which are quite inelastic. This causes a problem in performing computer simulations, since the time step required for calculations is quite small. Thus, a significant amount of computer time is needed to perform simulations. This issue was addressed by developing a model which assumes the belt to be made up of inelastic, rigid links connected with each other by hinges with bending stiffness and damping. This model, however, is quite complex and requires detailed information on forces acting on the belt while inside the spacecraft. Such forces cannot be provided while the designs of the heat exchanger and drive mechanism are under development. Therefore, this model was abandoned, at least temporarily, and continued using the model discussed above, which, while slow and time consuming, is appropriate for this stage of belt development.

4.1.1.3.1 Computer Program Summary

A computer program, titled Belt Radiator Simulation Program (BERS), was developed to simulate the in-plane dynamic performance of the belt radiator. This program incorporated the lumped-parameter model, described in the preceding subsection, and used a Runge-Kutta fourth order integration algorithm to generate plots of belt shape for a variety of belt parameters and spacecraft motions.

The input parameters for the program include:

- Number of lumped masses (N);
- Belt width (W);
- Belt drive length (2 max X_{Bi});
- Belt length, unstretched (Nl_i);
- Belt material density, mass per area (μ/W);

- Modulus of elasticity of belt material in tension (E_t);
- Modulus of elasticity of belt material in bending (E_b);
- Belt area of cross section (A);
- Belt section modulus (I);
- Damping ratio for first stretching vibration mode (η);
- Radius of mesh fibers, for screen type belt (r_f);
- Velocity of rotation (V)
- Spacecraft motion parameters (acceleration magnitude, direction, duration).

The output of the program can include, if desired, a printout of displacements, velocities and acceleration of any lumped mass, plus the forces acting on any mass. However, the preferred output includes plots, similar to those shown in Figure 23, of the belt shape at any time.

4.1.1.4 Belt Parameters

As an example, a glass fibre belt is considered to demonstrate the capabilities of the BERS Program. The belt is assumed to be composed of a square mesh screen made of twisted glass fibers covered with polyamide (nylon) plastic. The core glass fiber mesh gives added strength and stiffness to the screen and forms the matrix for the plastic covering. For the liquid-filled belt, only the mass of the belt is influenced by the liquid -- the stiffness characteristics are not.

From simple measurements and bench tests, we made the following estimates.

Wire diameter = 0.5 mm (0.02 inch)
Belt material density = 0.61 kg/m^2
Modulus of elasticity in tension = 4.13 x 10^9 N/m^2 (6 x 10^5 psi)
Modulus of elasticity in bending = 1.37 x 10^9 N/m^2 (2 x 10^5 psi)
No. of wires per meter = 394 (10 per inch)

For a design which has 3.3 m wide belt:

Total number of wires in belt cross section = 1300
Total area of cross section = 2.55 x 10^{-4} m^2
Belt cross section modulus = 4.34 x 10^{-12} m^4
Damping ratio for first stretching vibration mode = 1.0

Also, we assumed the velocity of rotation to be 1.0 m/s with a total belt length of 40.8 m.

One final note on belt parameters: the equations of damping provided in subsection 4.1.1.3 (Eqs. (15) and (20)), were developed assuming that the major source of damping in a flexing belt is the internal hysteresis (open area in a cyclic stress-strain loop). The natural internal hysteresis of the plastic is augmented by fiber reinforcement and/or the twisted fiber core. There is essentially no effect of environmental drag and the effect of liquid distortion (in LBR's) is believed to be a minor contributor to damping. The

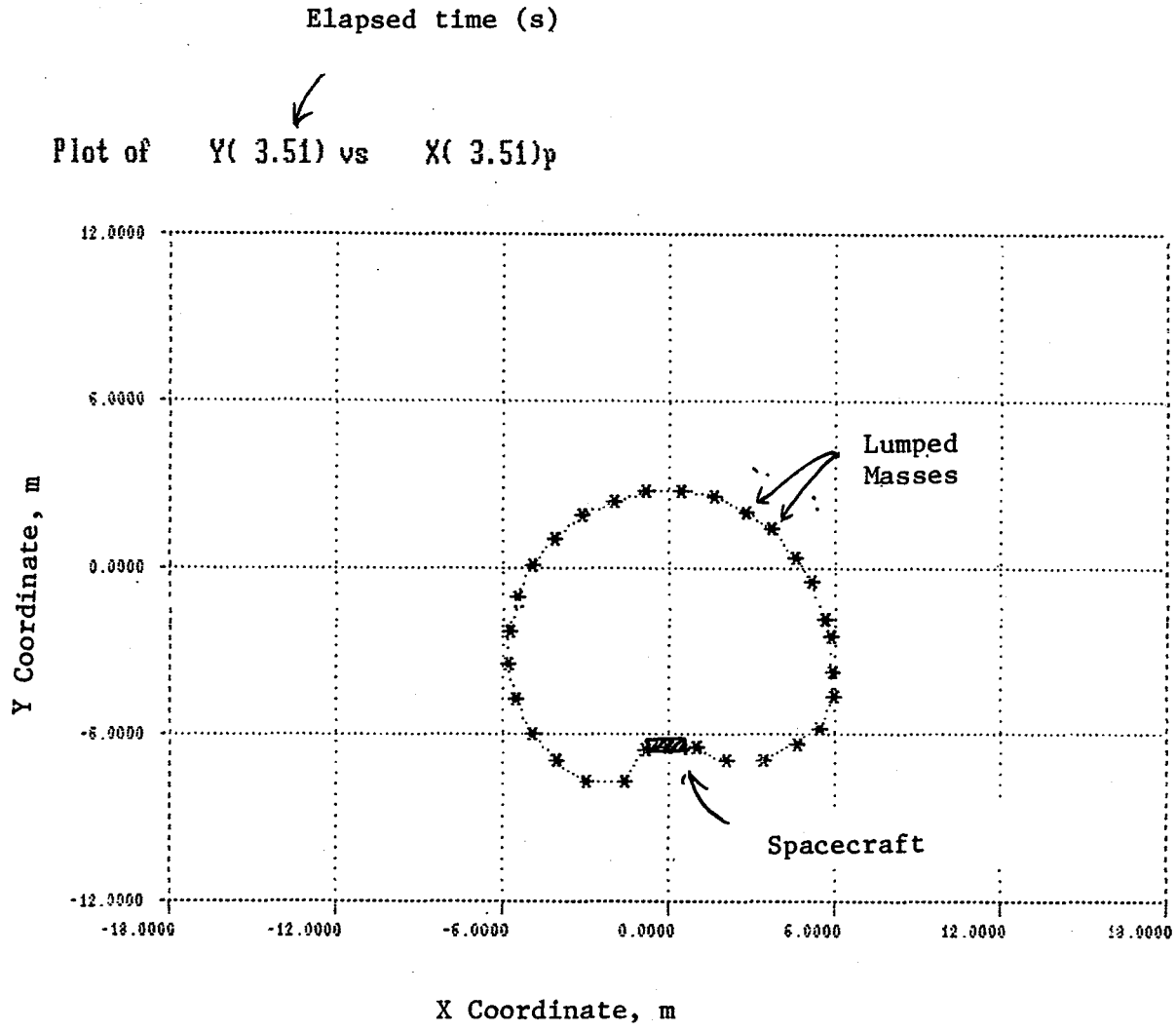

Axes: Spacecraft based (not inertial)

Acceleration: 0.5 m/s^2

Figure 23:- A Typical Belt Shape Plot Generated by the Computer Program BERS

damping force due hysteresis is not, in general, proportional to the rate of deformation in tension and bending (viscous damping); rather it depends on both the rate and amount of deformation.

In practical cases the damping is reasonably small. Therefore, we determined the "equivalent damping constant" in such a manner that with the system undergoing sinusoidal motion, the actual damping force does the same work per cycle as is represented by the equivalent damping constant. The equations of damping are the result of an analysis performed with such assumptions. In Task 4 we plan to perform tests to verify the validity of these assumptions and obtain more accurate estimates of damping.

4.1.2 Dynamic Analysis

This Section describes the results of simulations performed using the model discussed in the earlier section. Only the belt response to spacecraft motion is discussed since the effects of external influences are considered negligible (see subsection 4.1.1.2.1).

The major objective of the dynamic analysis was to determine the in-plane acceleration levels that the base design of the belt can withstand. As discussed earlier, the belt can fail in a variety of ways -- it can get tangled, develop a crease or deformation, or tear. We do not have enough data on spacecraft design or belt ties, to accurately predict its failure in any of these ways. The analysis presented in subsection 4.1.1.2.2 used some rough estimates of belt strength, but the intent there was to illustrate that the belt is likely to be able to withstand significant accelerations in those modes. No accurate prediction was attempted, unlike the objective in the study of the in-plane motion. Therefore, we have defined failure as the point when the belt touches itself or the spacecraft.

4.1.2.1 Belt Response to y-direction Motion

More effort was devoted to analying this motion than any other because two of the key design parameters, belt speed and bending stiffness, primarily affect the motion in this direction.

In order to gain an understanding of the level of acceleration which the belt is likely to withstand along the y-axis, we performed a simple calculation based on probable belt shape, shown in Figure 24.

The force from the spacecraft will lead to several changes in the belt from its equilibrium status. In Region I, the belt will develop a bump so that the upward force "F" from the spacecraft gets balanced by the downward force components of tension. The tension in the belt will, however, not remain uniform. This becomes apparent when the sides of the belt (Region II) are considered. The force required to accelerate the upper part of the belt will lead to a reduction in tension in the sides of the belt. Finally, the top part of the belt will flatten to provide the force required to accelerate the upper part of the belt. Corresponding to each of these effects is a threshold acceleration level.

If for Regions I we assume F to be the vertical force transmitted by the spacecraft to the belt in equilibrium.

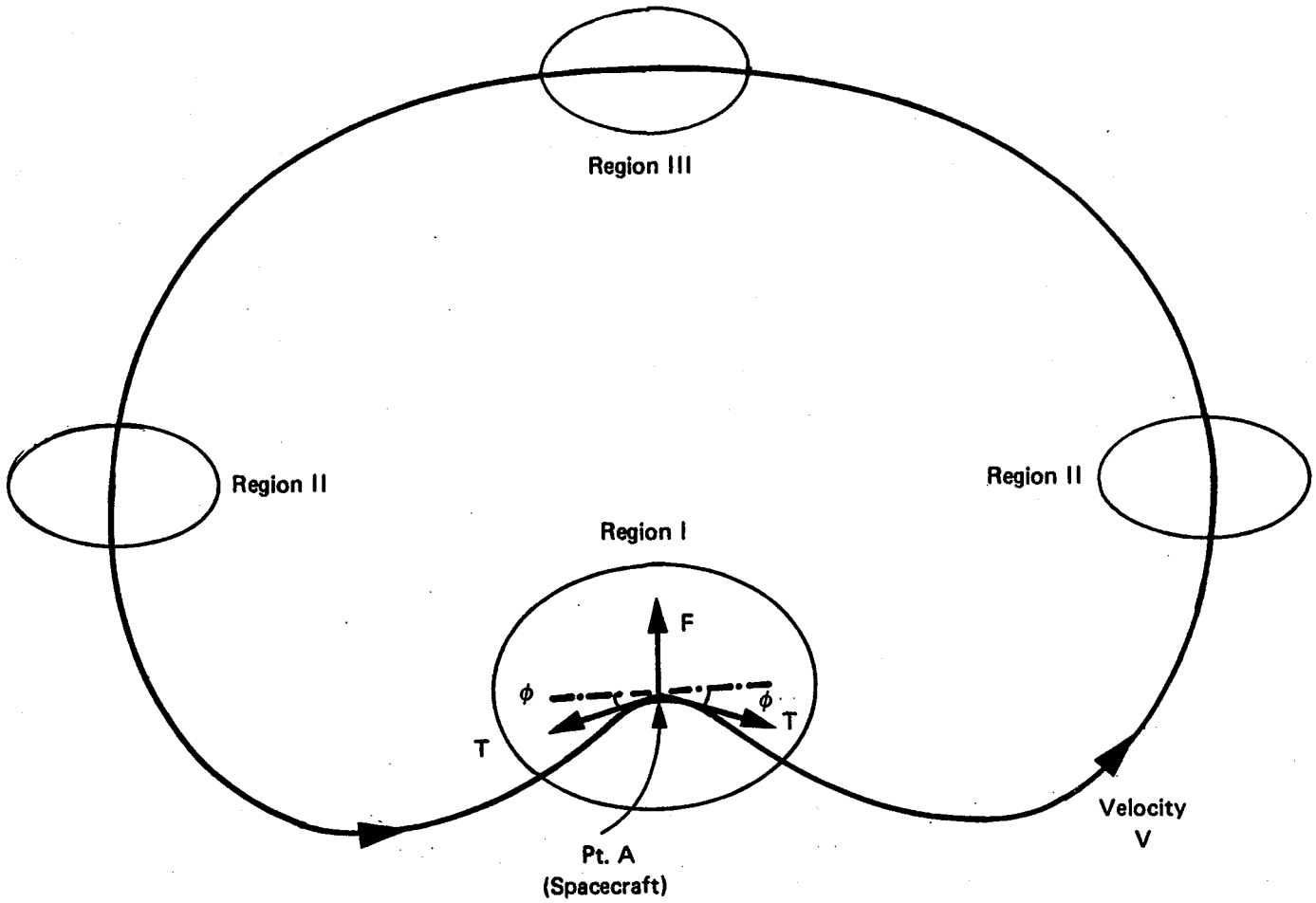

Figure 24: Probable Belt Shape Under Y Direction Acceleration of Spacecraft

Then,

$$F = a\mu l \tag{28}$$

where:

a = belt acceleration along y-axis (at equilibrium),
μ = linear mass density of belt, and
l = belt length.

Now, for point A to be in equilibrium in the y-direction,

$$F = 2T\sin\phi \tag{29}$$

where:

T = belt tension

However, from the discussion in subsection 4.1.1.1,

$$\begin{aligned} T &= \rho A V^2 \\ &= \mu V^2 \end{aligned} \tag{30}$$

(This is an approximation at best, because the belt tension will not be uniform.)

From Equations (28), (29) and (30)

$$a = \frac{2V^2\sin\phi}{l} \tag{31}$$

Now, at most Φ can be 90°. Then for $V = 1$ m/s and $l = 40.8$ m we get

$$\begin{aligned} a_{max} &= \frac{2V^2}{l} \\ &= 0.05 m/s^2 \end{aligned}$$

This is the level at which the top part of the belt will very likely touch the spacecraft, causing probable failure.

For

a = 0.01 m/s^2,
l = 40.8 m, and
V = 1 m/s,

we get,

$$\sin\Phi = 0.2$$
$$\text{or } \Phi = 12^\circ$$

which provides some degree of flexibility for belt deformation.

In Region II, the peak acceleration will be that which reduces the tension to zero. Thus,

$$2T = 0.5\,\mu l a_{max}$$

$$\begin{aligned} a_{max} &= 4T/\mu l \\ &= 4\mu V^2/\mu l \\ &= 4V^2/l \\ &= 0.1 \text{ m/s}^2 \end{aligned}$$

In Region III, the peak acceleration level will match centripetal acceleration. At that point, the belt will be completely flat on the top.

$$\begin{aligned} a_{max} &= V^2/R_b \\ &= 0.154 \text{ m/s}^2 \end{aligned}$$

These are, however, steady state values achieved after a transient period. Since the belt response is highly nonlinear (the belt cannot transmit any compressive force -- see Equation 10), we cannot tell if the belt can withstand the transients without resorting to using the computer simulation. Overall, however, it seems that the belt may be able to take only very small acceleration levels in the y-direction.

This, coupled with the fact that the belt is practically inelastic, causes a problem in performing simulations. Due to the inelasticity of the belt, we have to use very small time steps in the computer runs, typically about 0.0005 seconds. And, at acceleration levels of 0.01 m/s^2, the acceleration has to be applied to the belt for at least a few seconds (say 10) before there is any displacement. A simulation of 10 seconds will involve 20,000 time steps, making it quite lengthy and expensive. (As mentioned earlier, our attempt to bypass this problem by developing a rigid link model did not work because the belt drive mechanism is not yet designed.) Therefore, we decided to use a "Compliant" belt for gaining an initial understanding of the belt dynamics with the response of the "Inelastic" belt simulated only for some key cases.[2] The "Compliant" belt is assumed to have a modulus of elasticity of 4.13 X 10^6 N/m^2. For this belt, we can employ a much more affordable time step of 0.015 seconds. As can be seen from earlier calculations, the ability of the belt to take the y-axis acceleration seems to be independent of its elasticity.

A large number of simulation runs were made to study the belt response to both steady state and impulse type accelerations in the y-direction. The belt will experience a steady-state acceleration if the spacecraft is undergoing a deliberate maneuver lasting over long periods, while it will experience an impulse type acceleration (e.g. docking of another spacecraft).

[2] In any case, until we get more accurate estimates of damping in Task 4, any simulation of even the inelastic belt will be somewhat inaccurate.

From the results of the simulation we found that the belt cannot withstand a steady-state acceleration of even 0.01 m/s^2 (about 0.001g) in the y-direction without a failure (i.e., touching itself and/or the spacecraft). Figure 25 shows the shapes of the belt without any spacecraft acceleration and that with 0.01 m/s^2 acceleration at around 35 seconds into the acceleration phase. The shortening of distance between lumped masses in Figure 25 (b) is indicative of the belt losing its tension and crumpling.

The stiffness of the belt can be increased by increasing its rotational speed and/or by increasing the bending stiffness.

Figure 26 shows the effect of increasing the bending stiffness by a factor of 10^4. As can be seen, the belt shape remains perfectly circular, for 0.01 m/s^2 acceleration in the y-direction. However, if the acceleration level is raised to 0.1 m/s^2, even this belt deforms and eventually fails at around 25 seconds.

Increasing the bending stiffness by a factor of 1000 makes the belt withstand the acceleration level of 0.01 m/s^2 for at least 40 seconds, as shown in Figure 27 (a). However, the belt gets significantly deformed. If the acceleration is increased to 0.1 m/s^2, the belt fails at around 15 seconds, as shown in Figure 27 (b).

The effect of increasing the belt speed on its response is evident in Figure 28, which shows the belt shape without any acceleration (a) and with 0.01 m/s^2 vertical acceleration (b) at 40 seconds after the acceleration begins. As can be seen, the belt seems to be able to withstand this acceleration level quite well. Figure 28 (c) shows the effect of increasing acceleration level to 0.1 m/s^2. As can be seen, the belt is not able to withstand that level of acceleration.

One final simulation, shown in Figure 29, represents what happens to the belt at a very high acceleration level, equal to 10 m/s^2 (about 1-g). As can be seen, the belt collapses on the spacecraft.

The belt performance envelope for steady-state acceleration in the y-direction is shown in Figure 30. This plot can be employed in developing preliminary designs for the belt given the acceleration levels it is expected to withstand.

For studying the belt response to an impulse type acceleration, we applied an acceleration waveform shown in Figure 31 (a) in the y-direction. The belt could withstand this acceleration nicely, as evidenced by its near steady-state shape 20 seconds after the impulse was applied.

At this point, a simulation was run with the inelastic belt to double-check the assertion that belt elasticity does not affect its gross response to spacecraft motion in the y-direction. The inelastic belt can also withstand the 1-g impulse as shown in Figure 31 (c).

To summarize, the belt response in the y-direction, the belt design, as assumed, can withstand only very small constant acceleration levels, unless the bending stiffness or belt speed is increased substantially. It can, however, withstand substantial impulse type acceleration levels which last only a very short time.

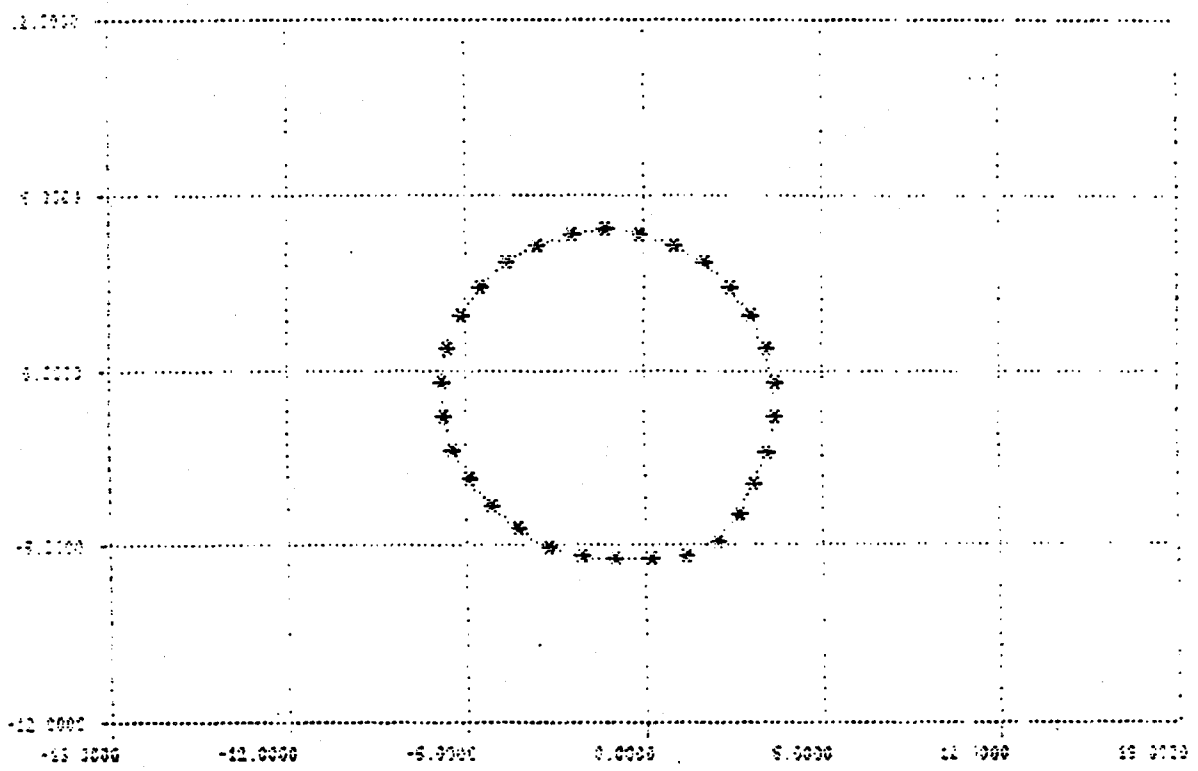

(a) No acceleration

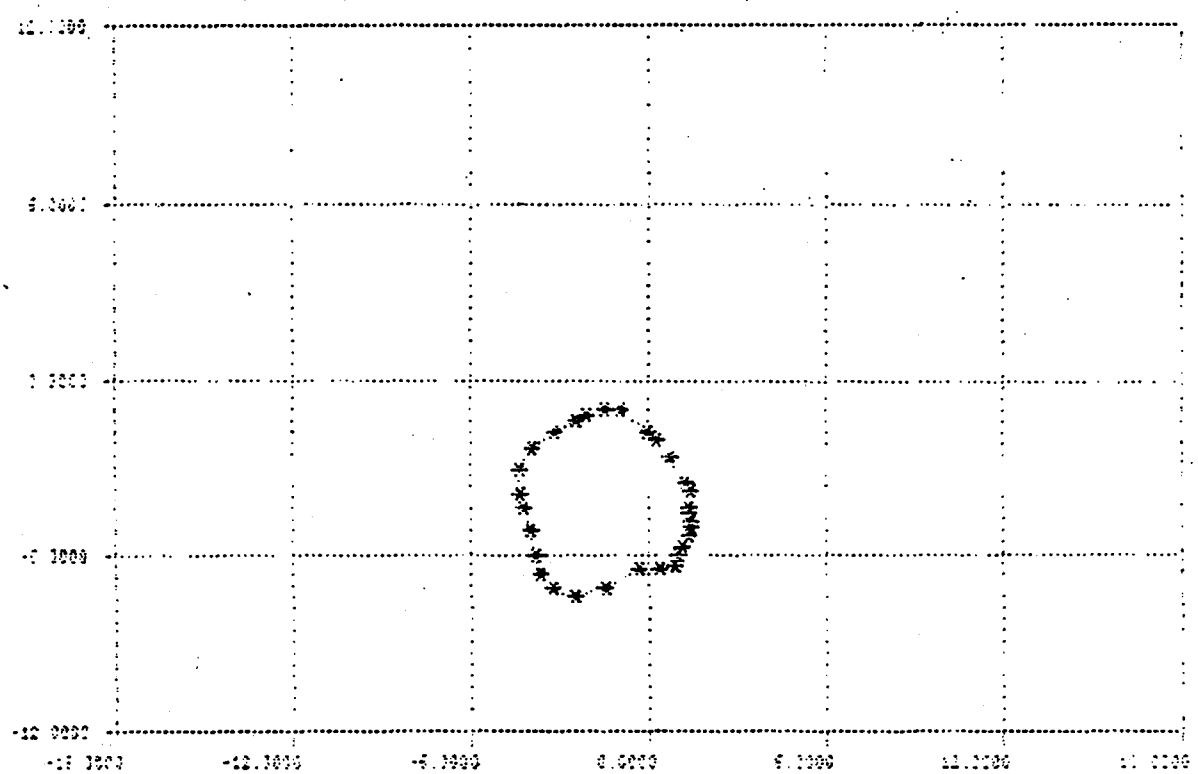

(b) Acceleration level: 0.01 m/s^2

Figure 25: The Belt response to a Constant Acceleration in the Y Direction

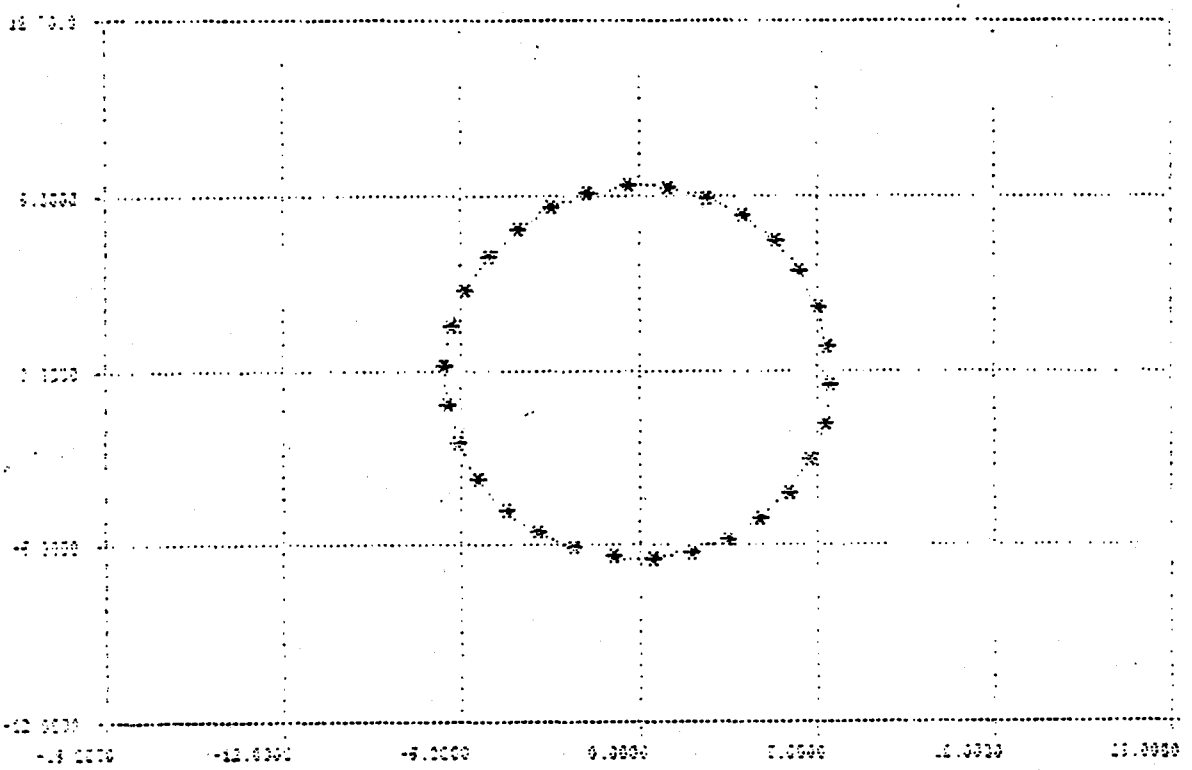

(a) Acceleration level: 0.01 m/s^2

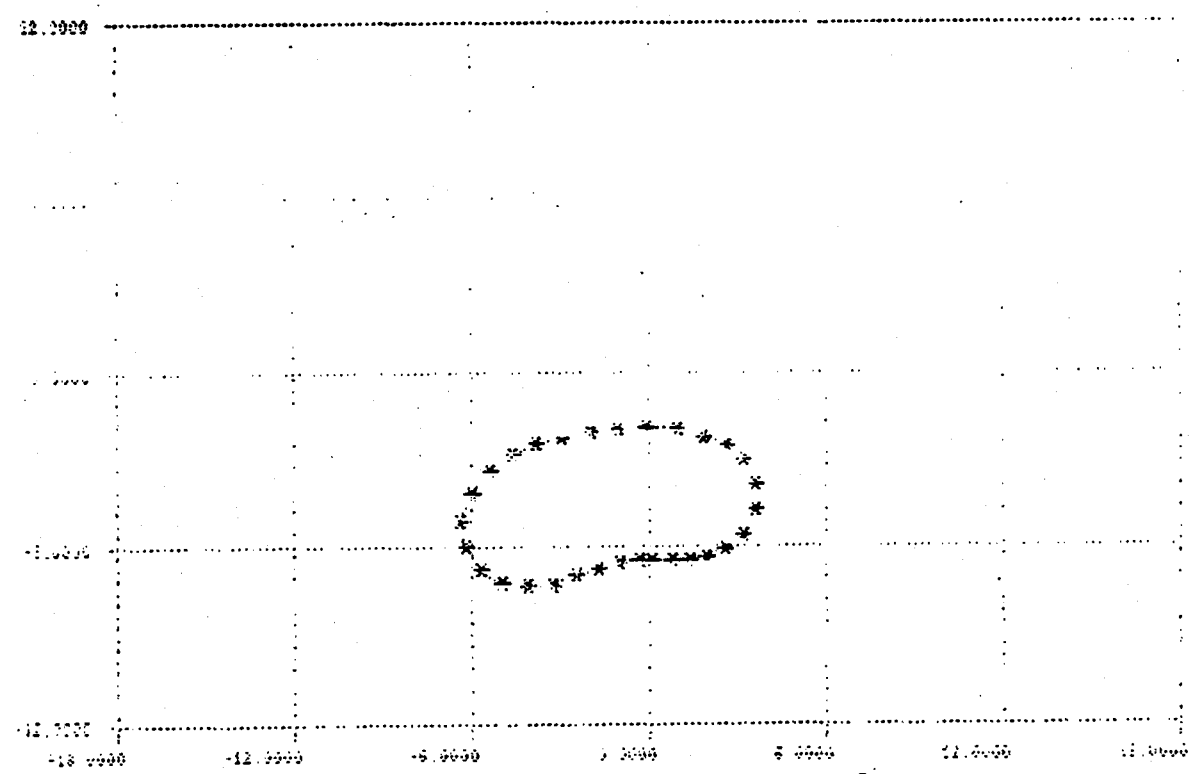

(b) Acceleration level: 0.1 m/s^2

Figure 26: The Effect of Increasing Bending Stiffness by a Factor of 10,000 on the Belt Response to a Constant Acceleration in the Y Direction

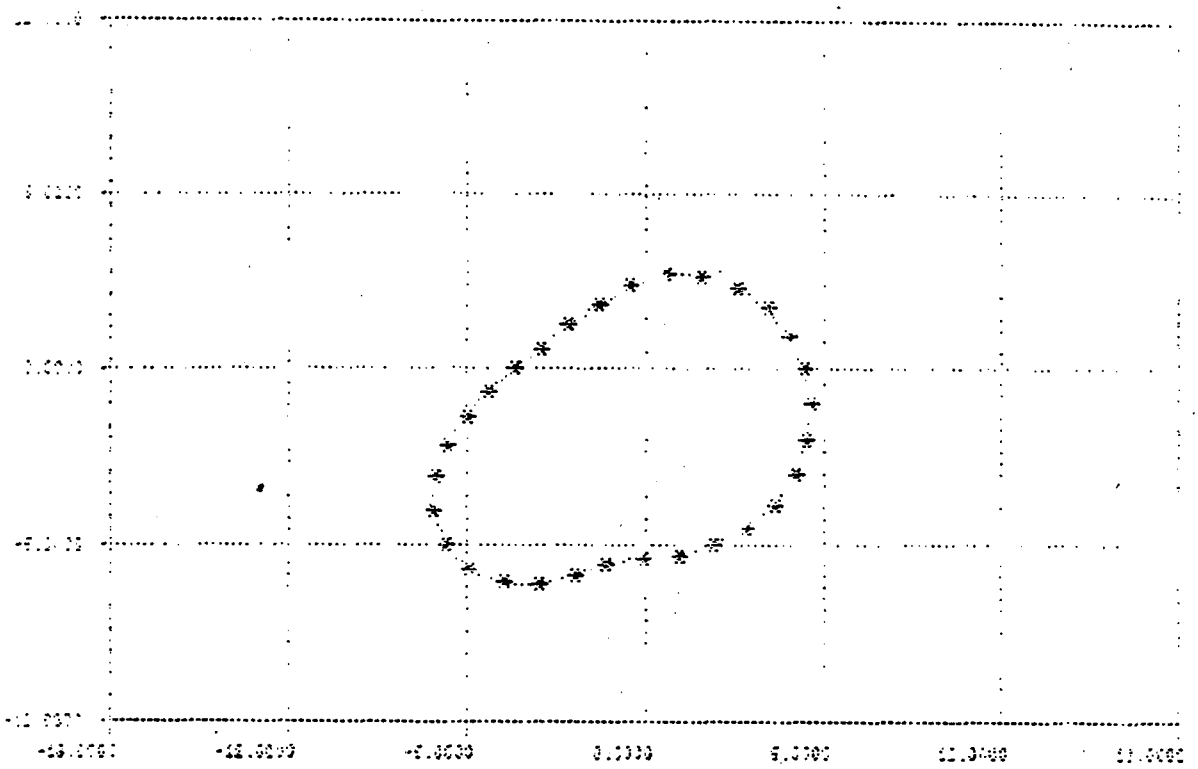

(a) Acceleration level: 0.01 m/s^2

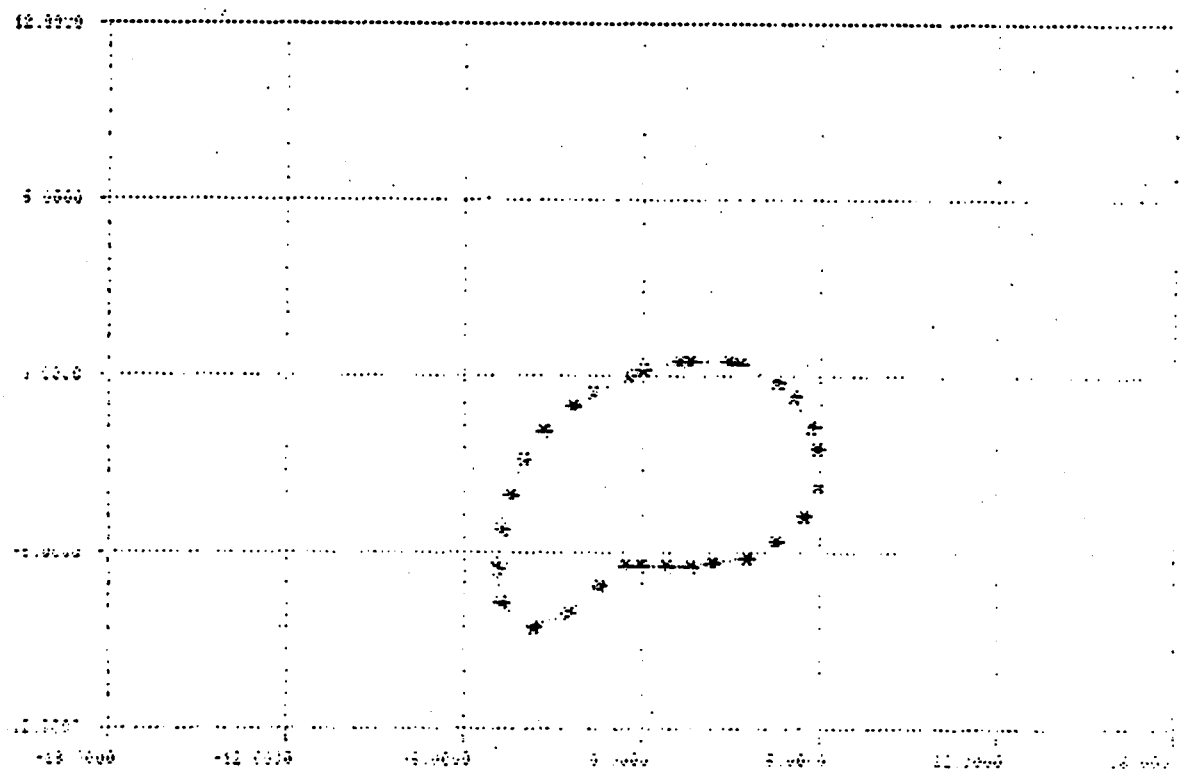

(b) Acceleration level: 0.1 m/s^2

Figure 27: The Effect of Increasing Bending Stiffness by a factor of 1,000 on the Belt Response to a Constant Acceleration in the Y Direction

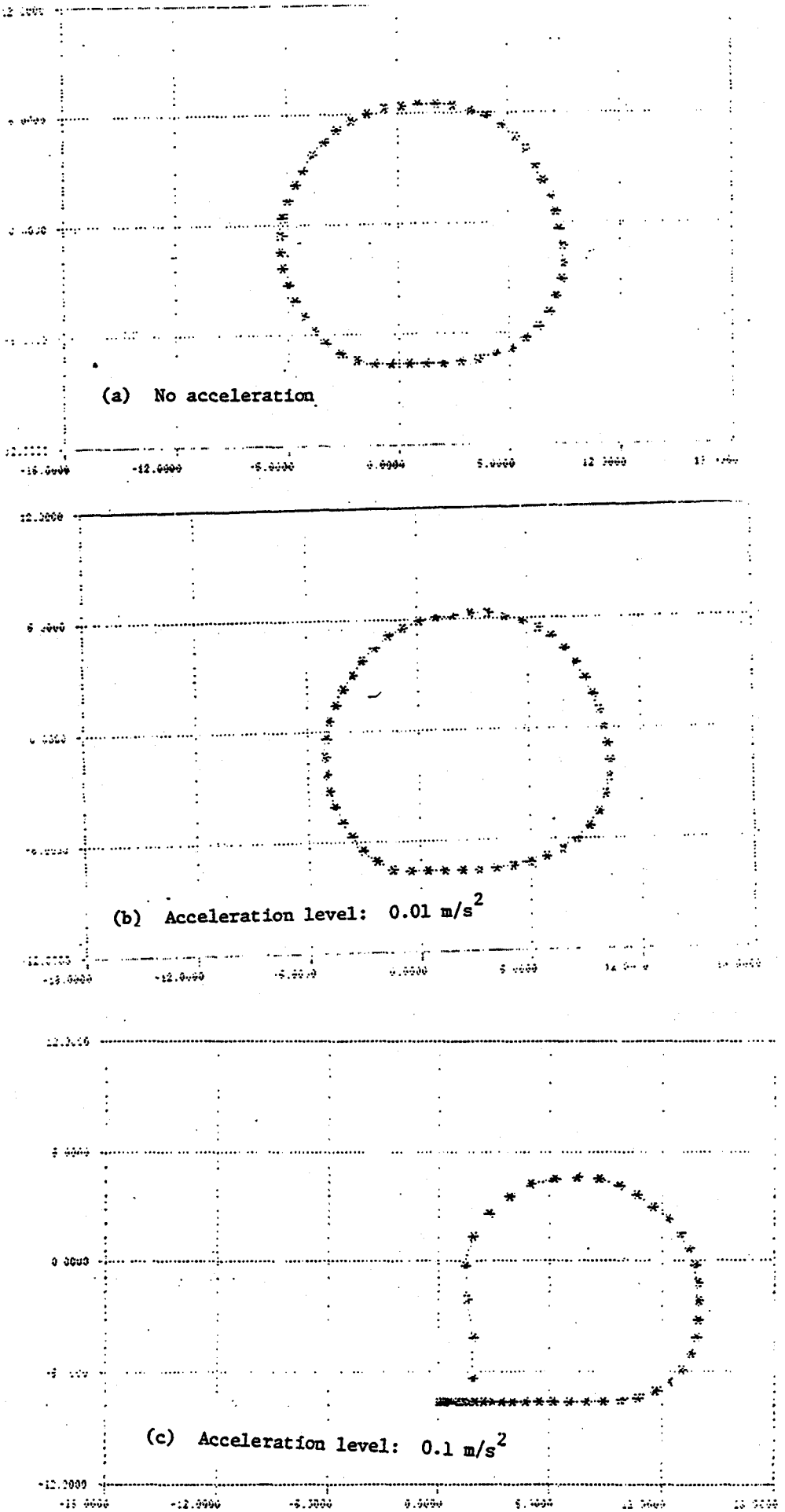

Figure 28: **The Effect of Increasing Belt Speed by a Factor of 10 on Belt Response to a Constant Acceleration in the Y Direction**

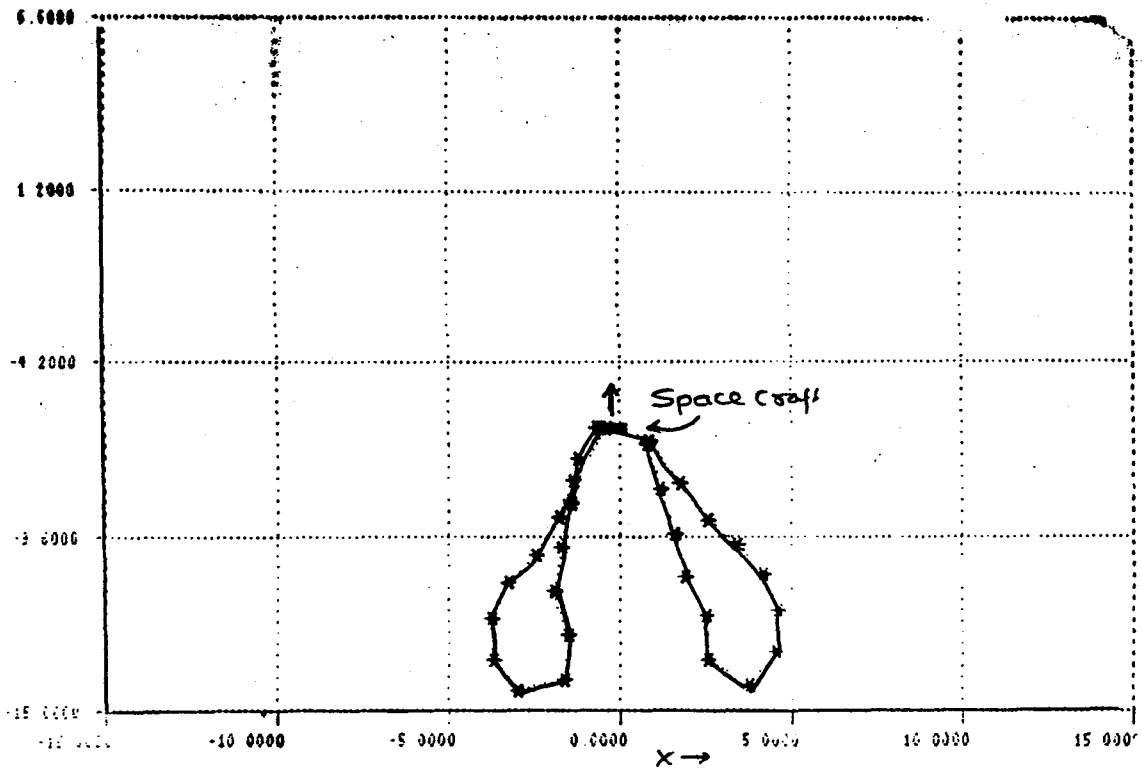

Acceleration level: 10 m/s^2

Figure 29: Belt Response to High Acceleration Level

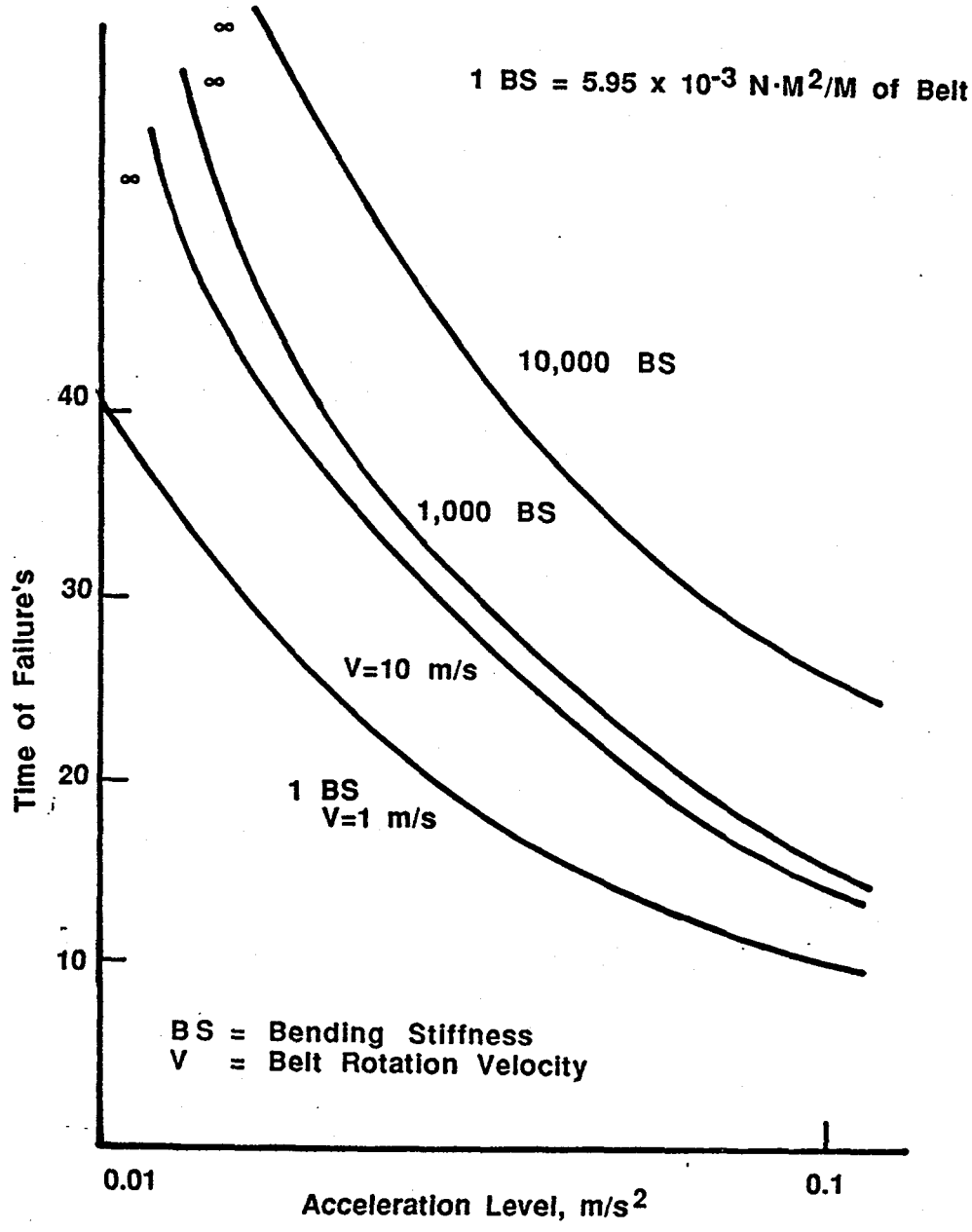

Figure 30: Belt Performance Envelope for Steady-State Y Direction Acceleration

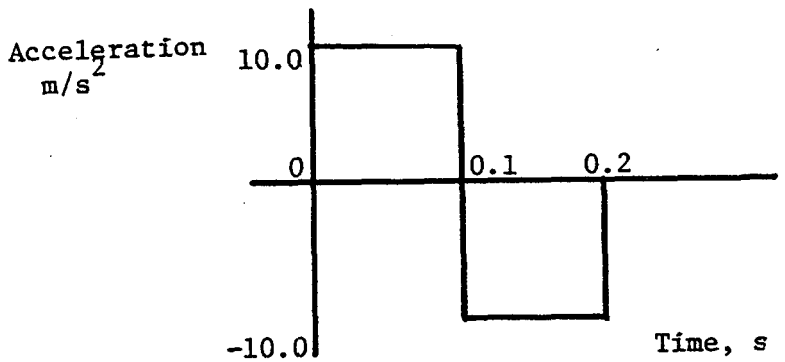

(a) The shape of the acceleration wave form

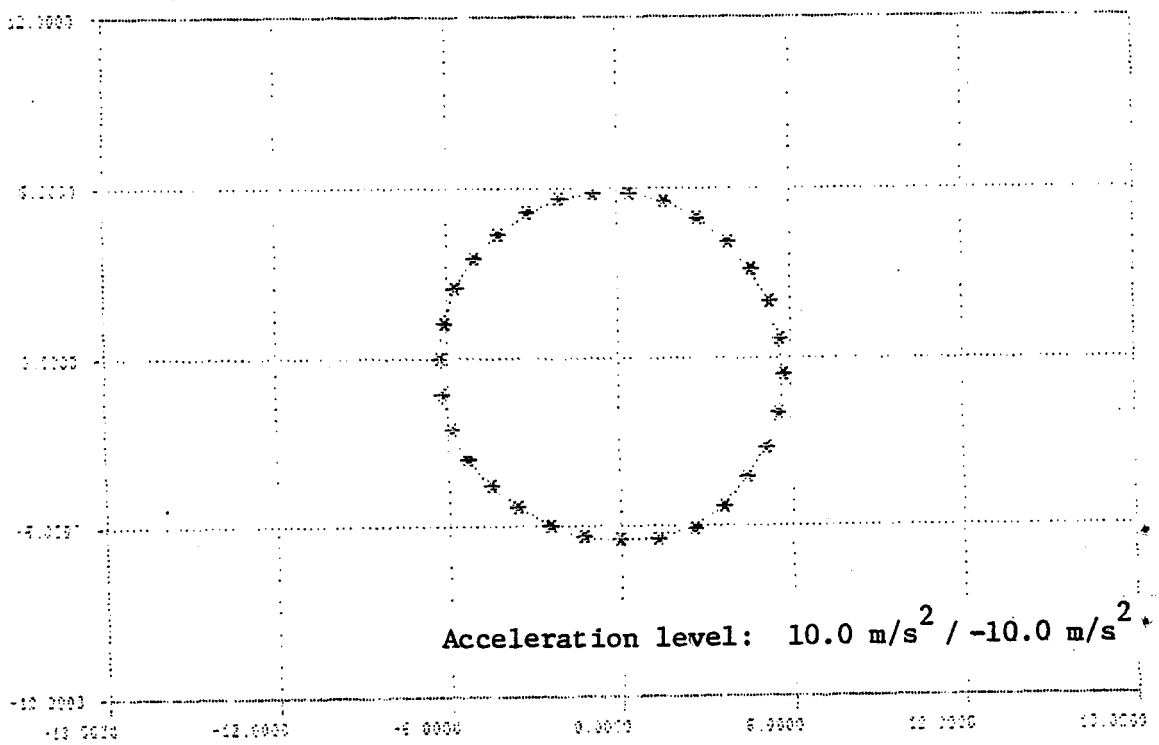

(b) The compliant belt shape after impulse

Figure 31: Belt Response to an Impulse in the Y Direction

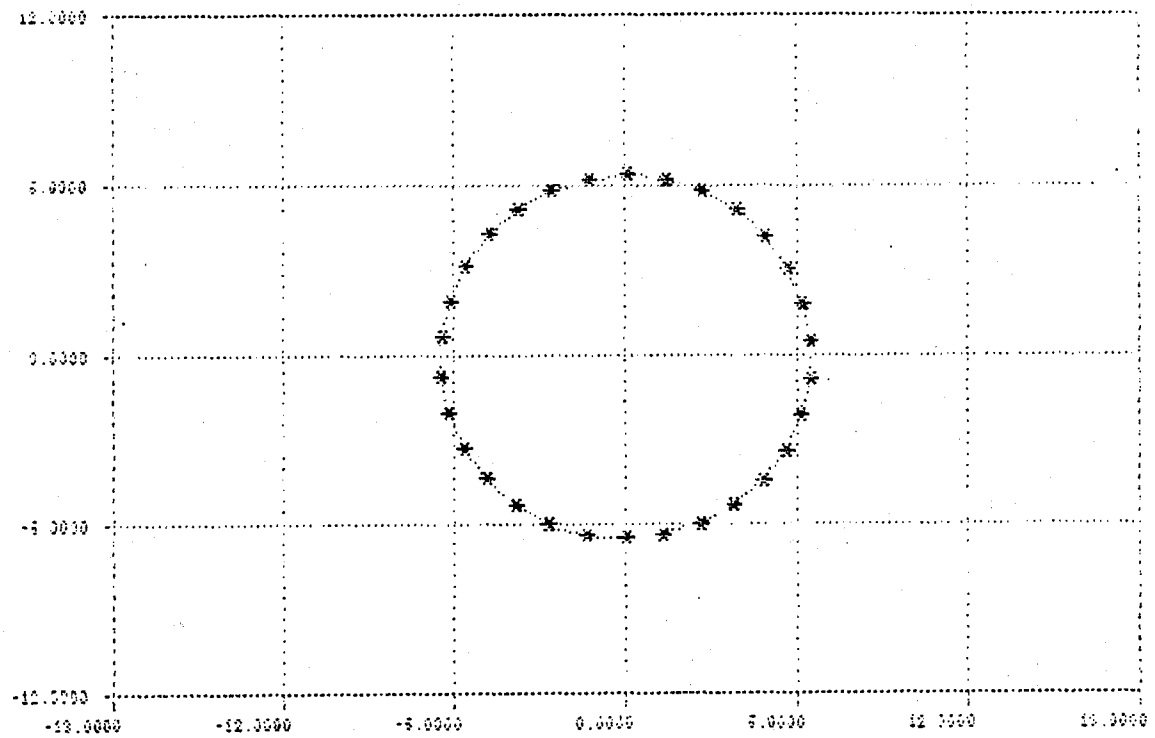

(c) The inelastic belt shape after the impulse

Acceleration level: 10 m/s^2 / -10 m/s^2

Figure 31: Belt Response to an Impulse in the Y Direction (Continued)

4.1.2.2 Belt Response to x-direction Motion

The belt turned out to be surprisingly weak in the x-direction. Also, we found that the elasticity of the belt does affect its ability to withstand motion in the x-direction.

Figure 32 shows the response of the compliant belt to a constant spacecraft acceleration of 0.01 m/s^2 in the x-direction. As can be seen, the belt seems to be able to withstand this relatively low level acceleration for at least 40 seconds.

The compliant belt is able to withstand an impulse type acceleration (of the type shown in Figure 33 (a)) of 1.0 m/s^2, as shown in Figure 31 (a). The inelastic belt, however, can withstand only 0.1 m/s^2 type acceleration, as shown in Figure 33 (b). Even increasing the bending stiffness by a factor of 10,000 did not help the inelastic belt withstand the 1.0 m/s^2 impulse. Thus, it seems that the level of acceleration that the belt is able to withstand in the x-direction is even lower than the level it can withstand in the y-direction. This applies to both constant and impulse type acceleration. Also, the bending stiffness does not seem to affect significantly the ability of the belt to withstand acceleration in this direction.

4.1.2.3 Belt Response to Rotation Around the z-axis

The objective of the computer runs simulating spacecraft rotation around z-axis was to get an estimate of how slow the rotation rate has to be for rotating the spacecraft by 180°.

We found that for rotational acceleration rates of 0.01 rad/s^2 the belt becomes entangled and thus fails. The belt shape just before this happens is shown in Figure 34 (a). Increasing the bending stiffness by a factor of 1000 does not help. Figure 34 (b) shows the belt shape for that case just prior to failure.

The belt seems to be able to withstand an acceleration of 0.0025 rad/s^2, as shown in Figure 34 (c), at least through a 90° rotation (beyond which the direction of acceleration will need to be reversed in order to ensure that the spacecraft stops rotating at 180°). At this acceleration level, the spacecraft will take about 50 seconds to rotate through 180°.

4.1.2.4 Summary of Dynamic Analysis

In this section, we have presented results of the dynamic analysis performed using the computer simulation developed for this purpose. The criteria for belt failure are:

- Belt touching itself;
- Belt touching the spacecraft.

Following are observations regarding belt dynamic performance:

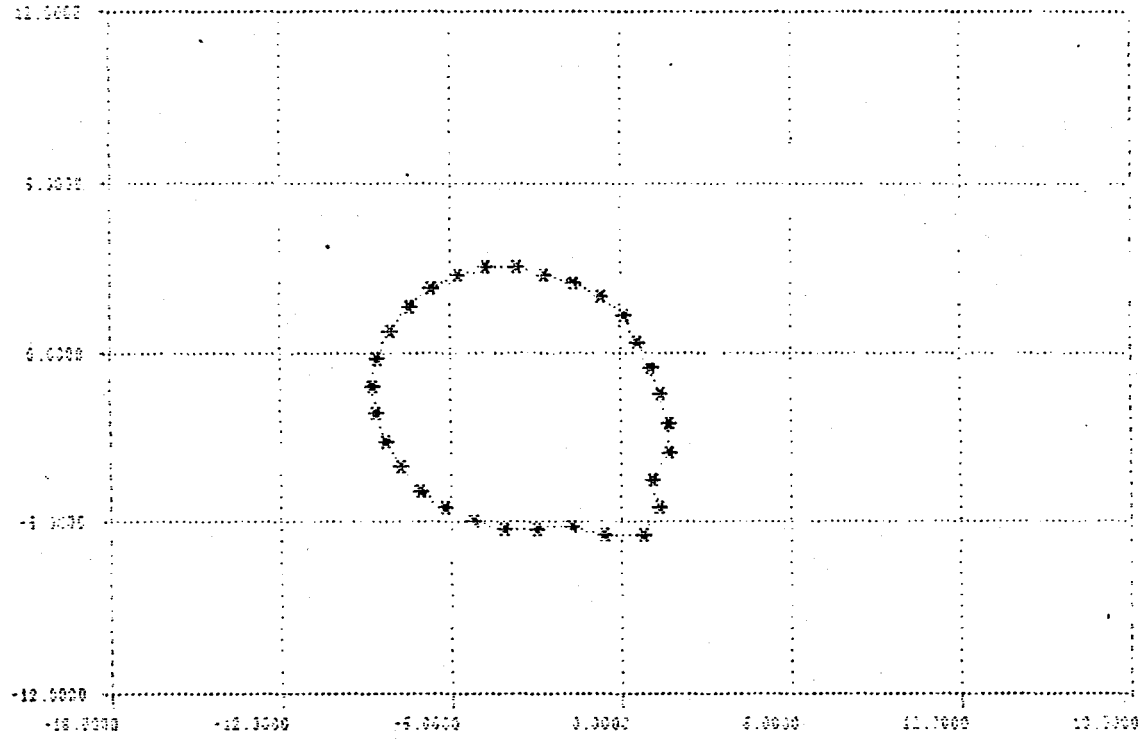

Acceleration level: 0.01 m/s^2

Figure 32: Belt Response to a Constant Acceleration in the X Direction

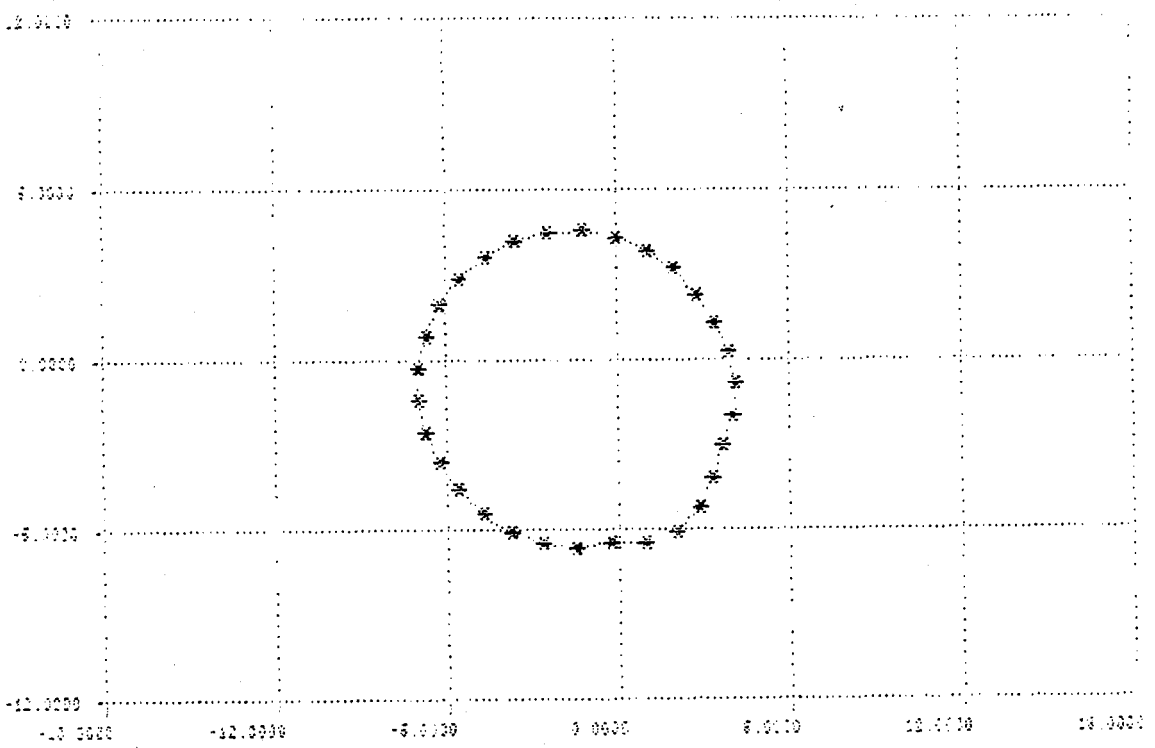

(a) The compliant belt shape after impulse

Acceleration level: 1.0 m/s^2 / -1.0 m/s^2

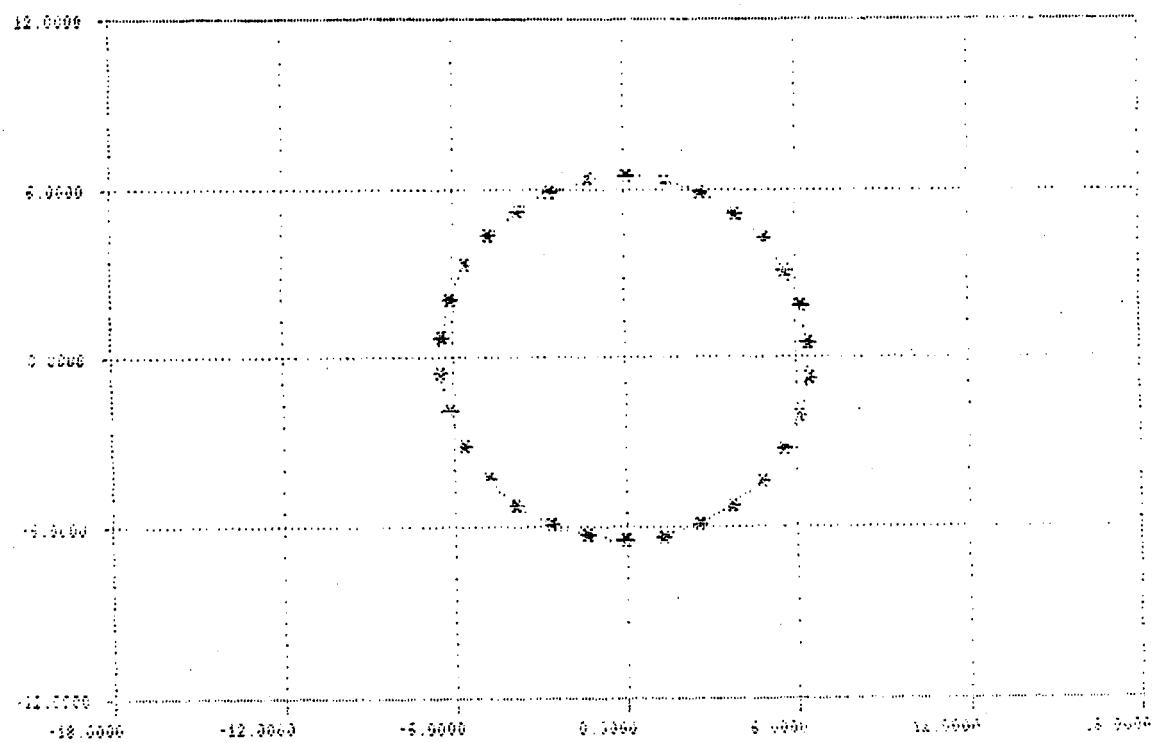

(b) The inelastic belt shape after impulse

Acceleration level: 0.1 m/s^2 / -0.1 m/s^2

Figure 33: Belt Response to an Impulse in the X Direction

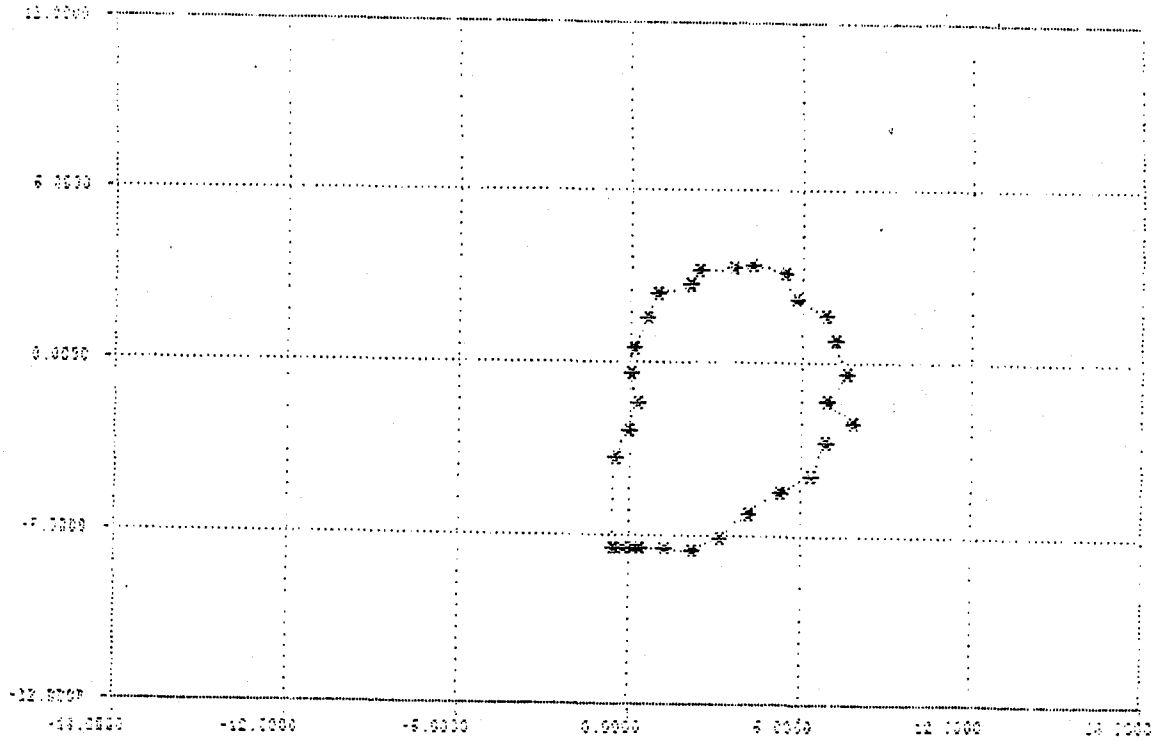

(a) Acceleration level: 0.01 rad/s^2

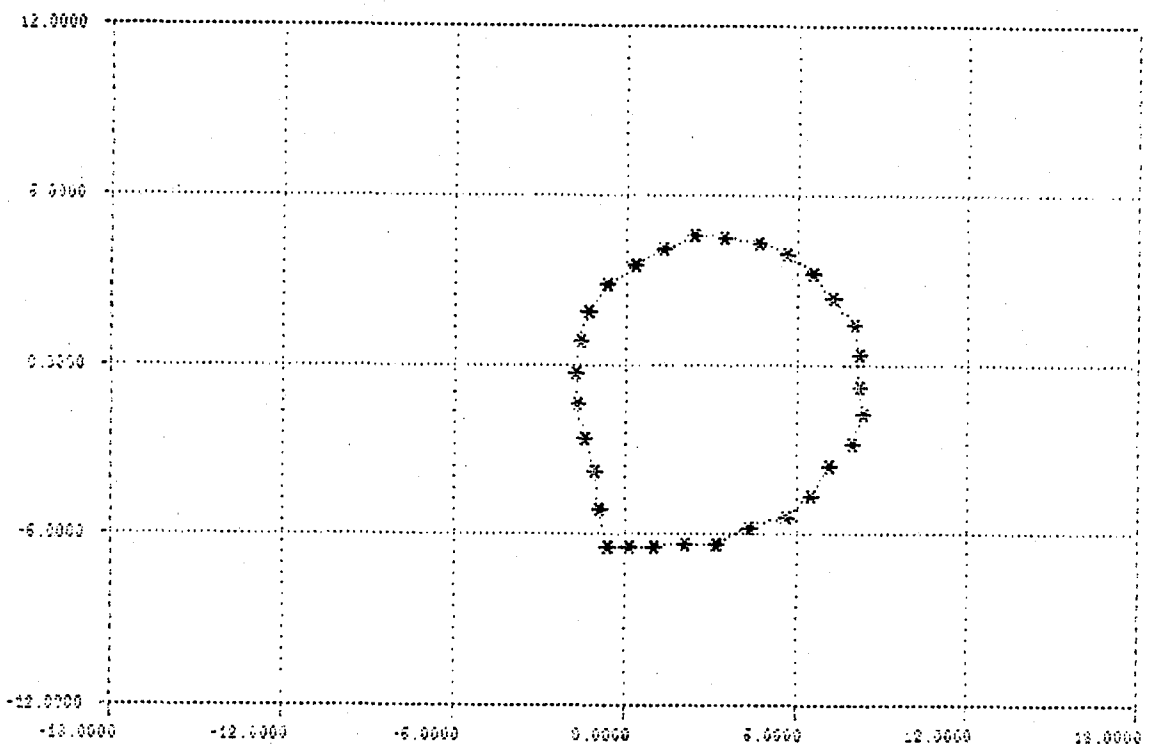

(b) Acceleration level: 0.01 rad/s^2

Figure 34: Belt Response to Rotation Around Z Axis

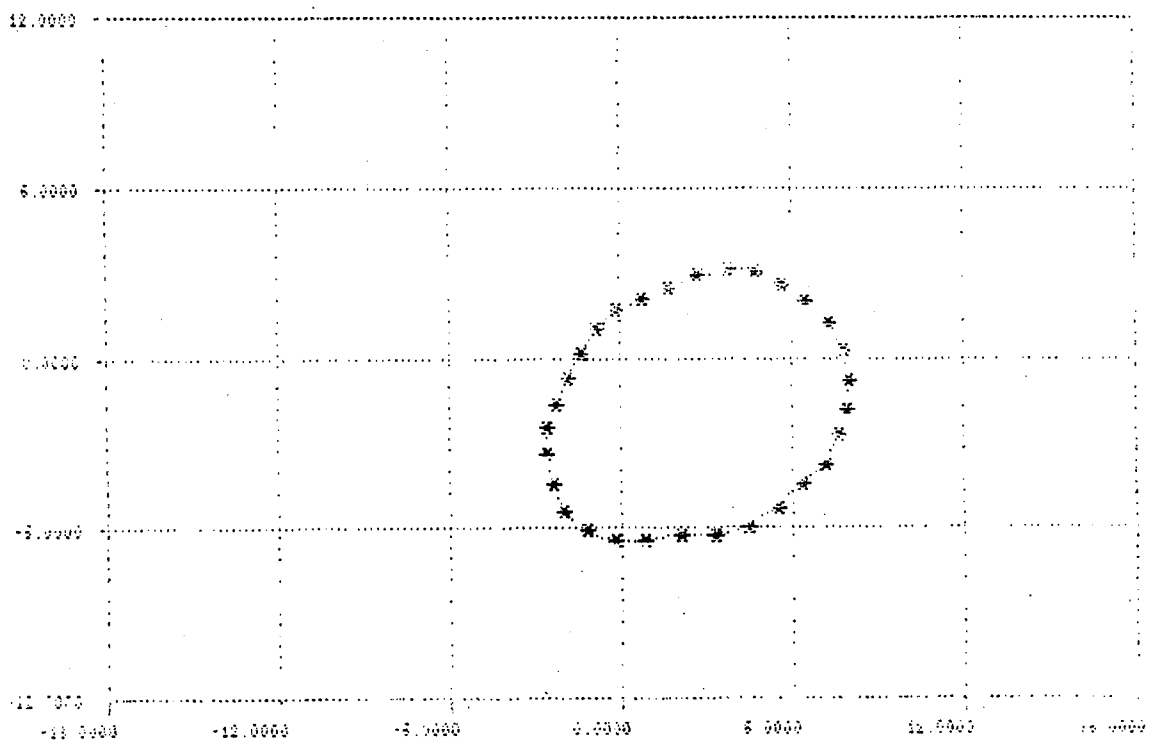

(c) Acceleration level: 0.0025 rad/s^2

Figure 34: Belt Response to Rotation Around Z Axis (Continued)

Translation along the Y-Direction[3]

- The "base case" belt can withstand only an acceleration level lower than 0.01 m/s^2 in this direction.
- Increasing the speed of the belt and/or its bending stiffness will make the belt able to withstand higher acceleration levels. However, even if the belt speed is raised by a factor of 10 or the bending stiffness is increased by a factor of 10,000, the belt will not be able to withstand an acceleration level of 0.1 m/s^2.
- The belt can, however, withstand substantially larger impulse type acceleration levels (e.g., 10 m/s^2 accelerations lasting 0.1 sec. followed by -10 m/s^2 acceleration lasting the same amount of time) even without any increase in speed or bending stiffness.
- The elasticity of the belt does not seem to affect its ability to withstand *Y*-direction acceleration.

Translation along x-direction

- The belt seems to be even less resilient in the *x-direction*; it can withstand an impulse type acceleration of only 0.1 m/s^2 without touching itself.
- The belt elasticity does affect its ability to withstand acceleration in the *x-direction.*
- The belt will be able to take very small constant acceleration in the *x-direction,* perhaps even less than 0.01 m/s^2.
- Increasing the bending stiffness does improve belt performance. However, it would have to increase more than 10,000 times to make the belt withstand 10 times the acceleration in the *x-direction.*

Rotation around the Z-Direction

- The spacecraft will have to rotate very slowly around the *Z*-axis in order to prevent the belt touching itself or the spacecraft.
- The belt withstands acceleration level of 0.0025 rad/s^2. At this level, it would take about a minute for the spacecraft to rotate through 180°.

4.1.3 Controls Analysis

In this section we briefly discuss options available to control the dynamic motion of the belt.

There are two major objectives in applying some form of control over belt behavior:

- To damp out undesirable vibratory motion;
- To increase the operating envelope of the belt.

Consistent with the thrust of the entire effort of Task 1, we have concentrated on improving the operating envelope of the belt rather than on damping undesirable vibrations.

---

[3] The Y-axis passes through the spacecraft and the belt center. The X-axis is perpendicular to that axis within the plane of belt rotation. Z-axis is perpendicular to the belt rotation plane.

Table 3 identifies control options available for increasing the ability of the belt to withstand accelerations in the plane of rotation. As can be seen, each option has associated advantages and disadvantages. From these options, we need to select the best option for a particular MBR design based on factors such as:

- Power availability;
- Types of spacecraft maneuvers;
- Probable warning time prior to maneuvers;
- Expected up-time for the radiator;
- Potential for design modifications required to reduce belt failures due to contact.

These factors will be considered further as the detailed designs of the MBR are developed.

Table 3: Control Options

Control Options	Advantages	Disadvantages
1. Design belt/spacecraft so the belt touching itself of belt touching spacecraft does not lead to a failure.	• No advanced warning of maneuver needed. • The belt can withstand substantially higher in-plane acceleration levels, since the failure mode will then be defined as tearing or creasing of belt or belt getting tangled, all of which need higher acceleration levels.	• May need design changes in belt and outer surface of spacecraft.
2. Stow the belt prior to a planned maneuver.	• The belt will be immune to almost any acceleration.	• Needs prior knowledge of impending maneuver. • Time consuming. • Will need a special mechanism to stow belt in space.
3. Align belt so that the acceleration acts on a stiffer axis of the belt (e.g., the out-of-plane z-axis.	• The belt does not need to be stowed. • The belt or spacecraft does not need to be designed to prevent contact type failures.	• Needs prior knowledge of impending maneuver. • Time consuming. • Will need a special mechanism to stow belt in space.
4. Increase belt rotation speed when the spacecraft is expected to accelerate.	• Simple in concept. • No basic changes in design required (except potential changes in power supply and drive mechanism). • The radiator continues to operate.	• Some prior warning of impending maneuver is required. • Needs additional power during maneuvers.
5. For two-phase belt -- stop rotating there so liquid metal solidifies increasing the bending stiffness during spacecraft maneuvers.	• Simple in concept. • Does not need additional power.	• The radiator stops operating during maneuvers. • May cause some problems while starting again.

4.1.4 Conclusions and Recommendations

This report presents the results of an initial study of belt dynamics and control. A major part of this initial effort was devoted to developing a computer program which can

simulate the response of the belt to the in-plane motion of the spacecraft. The program was then used to gain an understanding of the in-plane behavior of the belt and to develop performance envelopes.

From the simulation results we conclude that the belt is able to withstand only very small constant acceleration levels (in micro-g level) of the spacecraft before losing its tension and collapsing, or contacting the spacecraft. The belt can, however, withstand significantly higher levels of acceleration for a very short time, such as those generated by another spacecraft docking. The ability of the belt to withstand spacecraft motion improves as its bending stiffness or rotational speed are increased. However, substantial increases in these design variables are required (order-of-magnitude) to achieve any significant improvement in belt performance.

There are various options available to improve the performance envelope of the belt. Exercising these options will, however, mean either some design changes, increase in power consumption, or advanced warning of impending maneuver. The final selection of the best option can only be made after the MBR design is further defined.

The above conclusions are based on the results of an unverified computer simulation, and some preliminary analysis and measurements of belt properties. We plan to verify the computer program and obtain better estimates of belt properties in Task 4 of the effort.

4.2 Small Scale Table Top Testing

4.2.1 Rotating Loop Dynamics Tests

4.2.1.1 Test Objectives and Results

Rotating loop tests were performed with small-scale physical models to characterize both the dynamic properties of the rotating belt and the robustness of the rotating belt in the face of disturbances. The following tests were performed:

1. Spinning the belt about an axis perpendicular to gravity.
2. Spinning the belt about an axis parallel to gravity.

Test 1 simulated a one-G acceleration of the spacecraft away from the rotating belt. This is one of the cases addressed in the computer-based analysis of Task 1.

Test 2 verified that a flexible belt structure would deploy into a hoop shape when subjected to motion similar to that of a belt radiator. Test 2 also simulated the dynamic response of a rotating flexible hoop to perturbations. The effects of gravity were reduced by rotating the belt in a horizontal plane.

4.2.1.2 Test Revolving Perpendicular to Gravity

4.2.1.2.1 Physical Model Test

Two small-scale models of MBRs were assembled from tight-mesh fiberglass screen:

1. 2.54 cm wide by 64 cm long; and

2. 2.54 cm wide by 102 cm long.

The samples were formed into continuous belts and hung one at a time from an 8 cm diameter pulley as shown in Figure 35. The pulley was spun at angular velocities from 1.5 RPM up to 740 RPM. The belts did not form round loops while revolving at the planned rotation rate of 1.5 RPM or at much higher rotation rates. As shown in Figure 36, the static 64 cm belt forms an oblong loop. Revolving the belt does little to form a round loop, even at rotation rates much larger than planned. For instance, the belt is still not a round loop while revolving at 50 RPM. Even at 740 RPM the belt forms only an oblong loop as shown in Figure 37.

4.2.1.2.2 Computer Model Test

A computer simulation was run which modeled the dynamic response of an actual-sized belt during a 1-g spacecraft acceleration. The simulation conditions were analogous to the above test conditions of a belt revolving about an axis perpendicular to gravity. The modeled belt was 40.8 m in length, 3.3 m wide and revolved at 1.5 RPM. The simulation results indicate that a flexible belt will elongate into an oblong shape under the influence of a spacecraft accelerating away from the belt. The results of the computer simulation are consistent with the physical model test, which verifies the program's ability to predict gross rotating belt responses to spacecraft accelerations.

4.2.1.3 Test Revolving Parallel to Gravity

4.2.1.3.1 Test Apparatus

A small-scale 175 cm long by 15 cm wide rubber belt was used to model the MBR. Rubber was chosen to provide a belt with a high mass-to-stiffness ratio; this reduces the effects of wind resistance and decreases the influence of the hanging supports on the belt, since the belt mass is much greater than the support mass. A 16 cm square plate was connected at its center to a motor by a shaft. The motor and shaft hung vertically and the square plate was perpendicular to the shaft and thus parallel to the floor. To support the belt, four 1 cm wide by 90 cm long thin metal strips were hung from the corners of the square plate. Four 30 cm long pieces of nylon string were connected at one end to each of the four metal strips and at the other end to the rubber belt at four equidistant points along its edge.

4.2.1.3.2 Test Procedure

To test for hoop-forming potential, the test was started with the entire assembly at rest. The motor was started and its speed slowly increased until the belt began forming a round hoop. Once the belt formed a round hoop, it was struck with a rod to study its robustness in the face of a disturbance. When the round hoop survived a disturbance, the motor RPM was increased and the disturbance applied again. This was done a number of times to correlate belt stability with increasing RPM.

4.2.1.3.3 Test Results

The small-scale LBR belt formed a round hoop when started from rest and revolved about an axis parallel to gravity. The response of the belt to deployment and disturbances

Figure 35

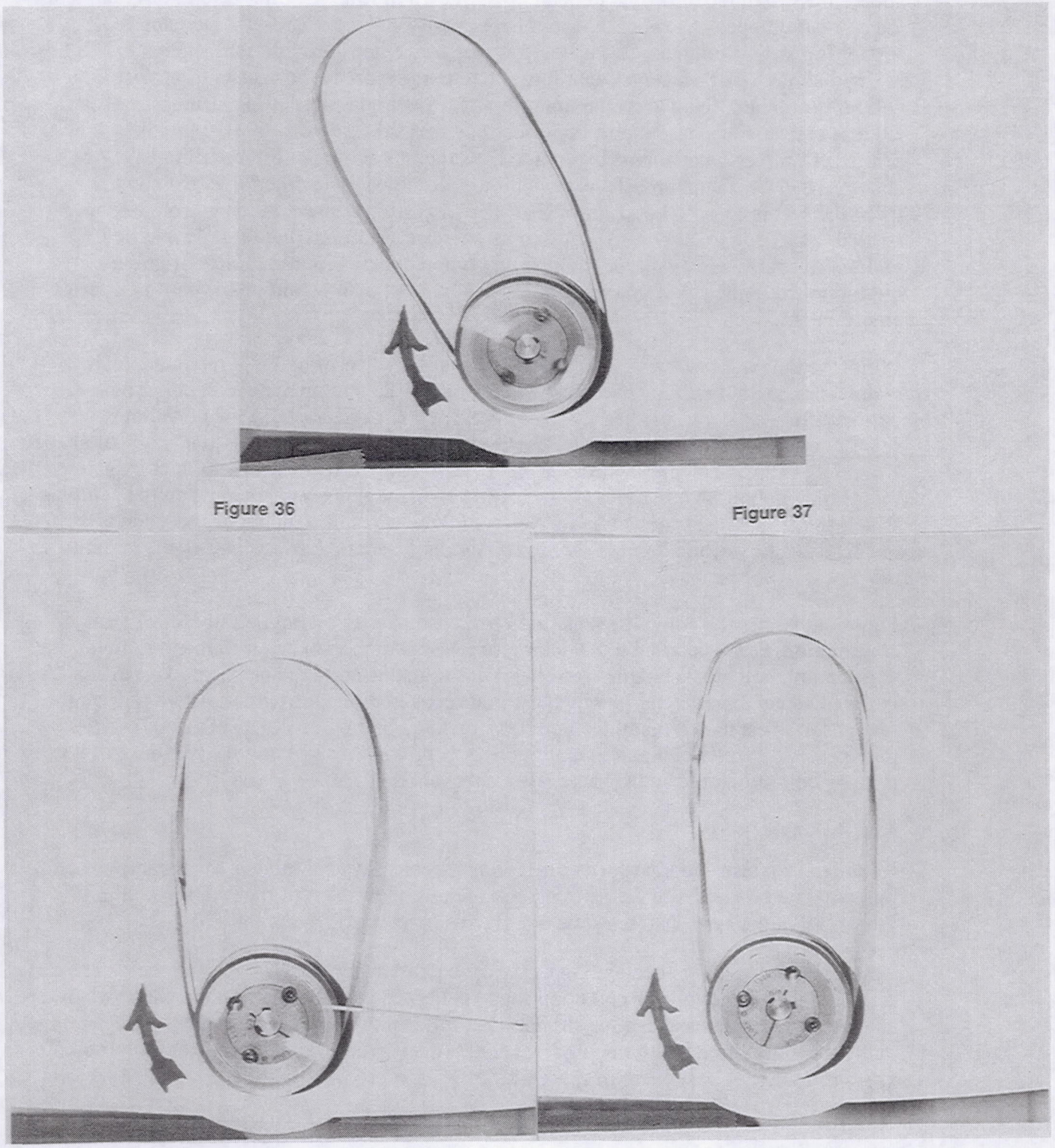

Figure 36

Figure 37

Figures 35, 36, and 37: Belt Revolving Perpendicular to Gravity

is shown in Figure 38 by frames 1 through 12. As shown in frame 1, the belt at rest hangs limp as it would before deployment in a space environment. While revolving at about 30 RPM, the belt begins to open up as shown in frame 2. In a zero-G environment the belt would open at lower RPM, but here gravity tends to distort the belt and the supporting strings tend to pull the belt towards the center of revolution. Once the belt has reached about 37 RPM, centrifugal forces overcome most of the effects of gravity and the belt pulls outward. However, the imperfections due to the supporting strings are still evident in frame 3. The support imperfections are still evident at 60 RPM, although belt centrifugal forces have almost overcome the support centripetal forces (frame 4). At about 96 RPM the support effects have almost disappeared (frame 5), and at about 150 RPM the belt is a round hoop (frame 6). The flexible belt structure goes from a limp (stored) condition to a hoop structure in an exercise similar to that of a moving belt radiator in space. However, in this simple ground experiment the effects of gravity require much higher rotational speeds for deployment than would be the case in a zero-G environment.

While the belt was revolving at 60 RPM, its shape was perturbed in a manner which simulated a short duration spacecraft acceleration -- docking maneuvers, etc. The perturbation was accomplished by striking the belt with a pole (frame 7). About two seconds after being struck, the belt hoop had almost fully recovered into its circular shape (frame 8). The belt was also struck while revolving at 96 RPM (frame 9) and it again recovered in about two seconds (frame 10). The same thing happened when the belt was struck at 150 RPM (frames 11 and 12). In all three cases, it took about six seconds for the disturbance to completely disappear. This shows that the round belt shape is robust in the face of disturbances.

Figure 39 shows the computer generated response of a revolving belt to a short term acceleration, corresponding to a docking or reorientation maneuver. Subject to final verification, belt characteristics are analogous to that used in the physical experiment. As in the physical experiment, in which the belt recovered in approximately two to four seconds, it is estimated that the computer simulated belt will recover in a comparable time period. Further computer simulations will provide insight into the response of a moving belt radiator to such spacecraft maneuvers.

4.2.1.4 Conclusions

Rotating loop tests were performed with small-scale physical models to characterize both the dynamic properties of the rotating belt and the robustness of the rotating belt in the face of disturbances. Two tests were performed.

Test 1 simulated a 1-g acceleration of the spacecraft away from the rotating belt. The test indicates that the revolving belt hoop shape collapses into an oblong hoop shape when the spacecraft accelerates at 1-g. A similar case was run on the Task 1 computer program and the results agreed with the physical test. This verifies the program's ability to predict gross rotating belt responses to spacecraft accelerations.

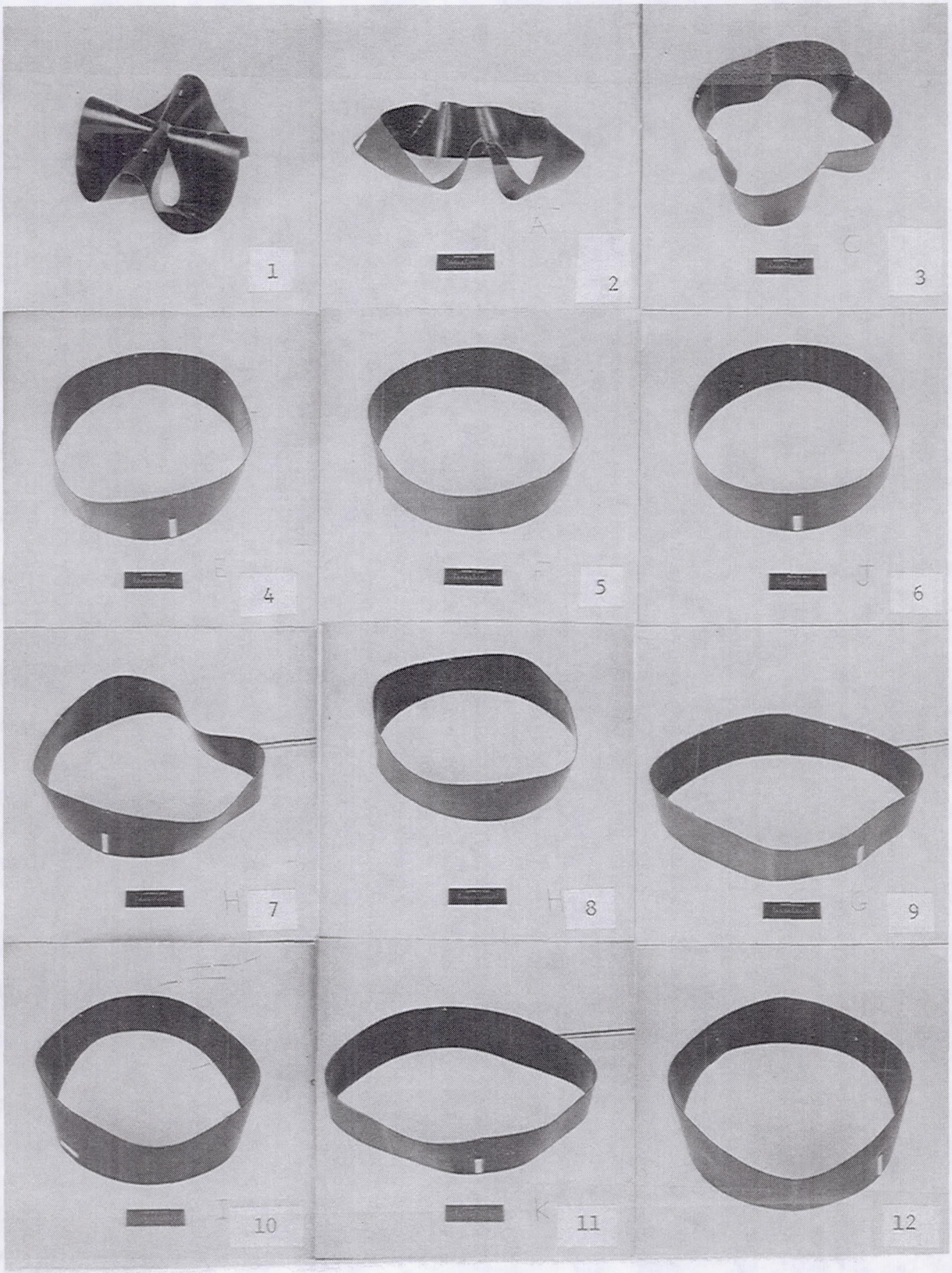

Figure 38: Belt Revolving Parallel to Gravity

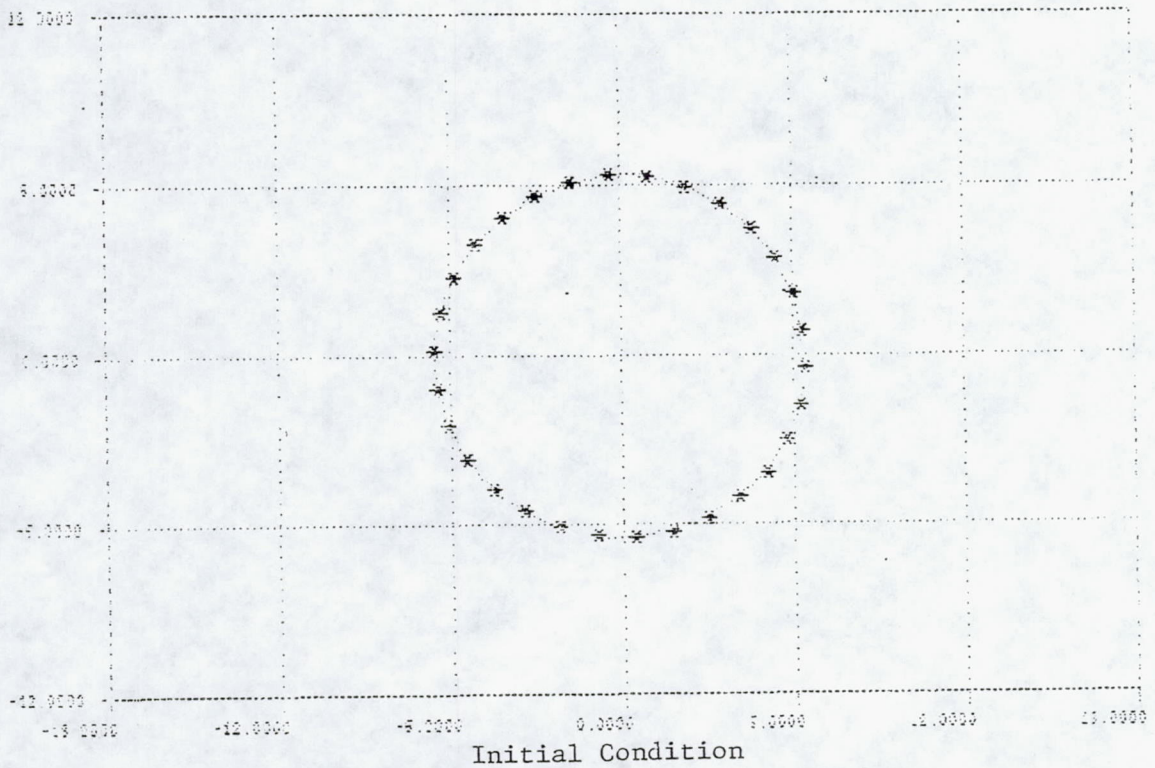

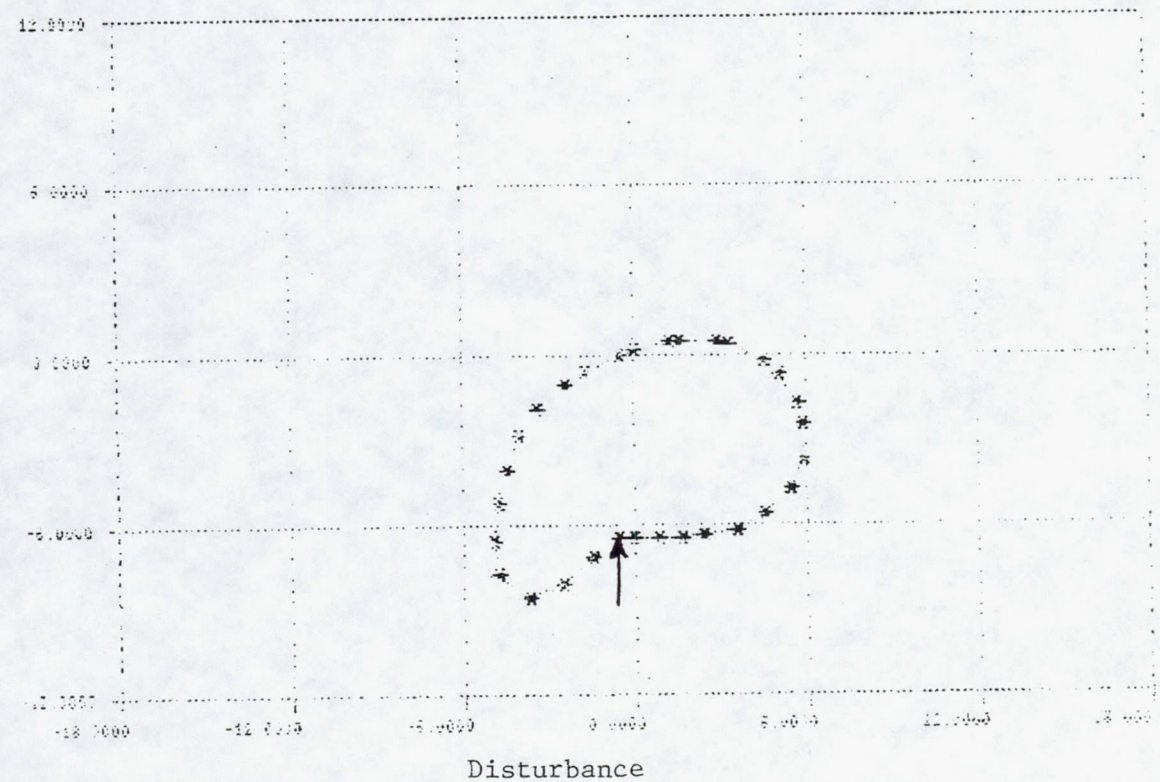

Figure 39: Computer Simulation

Test 2 simulated the case of a stored belt in space opening into a hoop shape when deployed under rotation. The test verified that a flexible belt structure would deploy into a hoop shape when subjected to motion similar to that of a belt radiator. Test 2 also simulated the dynamic response of a rotating flexible hoop to perturbations which model short duration spacecraft accelerations. The rotating belt hoop shape is robust in the face of such disturbances, recovering in two to six seconds. The test could not accurately model a free belt since the points of attachment on the belt corrupt the model and gravity distorts the belt shape at low RPM. Because the rotating belt loop had to be suspended in a 1-g field, more detailed damping and stiffness properties for the rotating belt were impossible to quantify. For these reasons, the hoop-forming test must be run in a zero-G environment to obtain more thorough and more reliable results. Further computer simulations will provide insight into the response of a moving belt radiator to such spacecraft maneuvers.

4.3 Conclusions and Recommendations

Rotating loop tests were performed with small-scale physical models to characterize both the dynamic properties of the rotating belt and the robustness of the rotating belt in the face of disturbances. Two tests were performed.

Test 1 simulated a 1-g acceleration of the spacecraft away from the rotating belt. The test indicates that the revolving belt hoop shape collapses into an oblong hoop shape when the spacecraft accelerates at 1-g. A similar case was run on the Task 1 computer program and the results agreed with the physical test. This verifies the program's ability to predict gross rotating belt responses to spacecraft accelerations.

Test 2 simulated the case of a stored belt in space opening into a hoop shape when deployed under rotation. The test verified that a flexible belt structure would deploy into a hoop shape when subjected to motion similar to that of a belt radiator. Test 2 also simulated the dynamic response of a rotating flexible hoop to perturbations which model short duration spacecraft accelerations. The rotating belt hoop shape is robust in the face of such disturbances, recovering in two to six seconds. The test could not accurately model a free belt since the points of attachment on the belt corrupt the model and gravity distorts the belt shape at low RPM. Because the rotating belt loop had to be suspended in a 1-g field, more detailed damping and stiffness properties for the rotating belt were impossible to quantify. For these reasons, the loop-forming test must be run in a zero-G environment to obtain more thorough and more reliable results. Also, further computer simulations will provide insight into the response of a moving belt radiator to such spacecraft maneuvers.

4.4 KC-135 Testing

The KC-135 experiment was designed to provide information on the dynamic behavior of a scaled down version of a MBR in a reduced gravity environment. No heat transfer tests were conducted. The tests were conducted aboard NASA's KC-135 out of Johnson Space Center. Five days of testing, with 25 to 35 parabolas each day, were completed. Each parabola provided approximately 20 seconds of reduced gravity. The types of tests which were conducted included:

- constant speed and no intentional perturbations;

- perturbations to the belt which simulated 1-g accelerations;
- perturbations to the belt by "tapping the belt";
- accelerations in the angular speed of the belt;
- decelerations in the angular speed of the belt;
- starting the belt once in reduced gravity;
- floating a belt in the cabin, i.e. not constrained by the drive system; and
- deployment sequences.

The tests were conducted on 18-19 April 1989 and 29-31 January 1990. During the first series of tests (April 1989) the primary goal was for a preliminary evaluation of belt dynamic performance and to verify the operation of the test apparatus. The second series of tests (January 1990) were designed to vary the test parameters from the first series of tests. Appendix B lists the schedules for each day.

4.4.1 Design of Apparatus

Figures 40 and 41 show the apparatus which was used in the reduced gravity tests. The apparatus consists of a frame, drive system, perturbation release/deployment storage system, and back drop. The frame was bolted down in the KC-135 and the remainder of the equipment was attached to the frame. In addition to this equipment, for the second series of flights, an instrument tape recorder (ITR) and a three axis accelerometer were included.

The perturbation system consisted of compressed springs and a release lever, (see Figure 42). During normal operation the release lever maintained the compression on the springs until zero-g was achieved. By pushing the lever the springs would expand, providing approximately 5 cm (2 in) of travel and an initial acceleration of 1-g.

The deployment system consisted of a storage box and retaining chains, (see Figure 43). The belt was folded up into the deployment box and held in place by the chains. While in zero-g the chains were removed and the belt was allowed to deploy using only the inherent belt stiffness and the centrifugal forces.

The design of the drive system for the reduced gravity testing incorporated the ability to change out the rollers used to drive the belt. Two types of rollers were used: a crowned roller and a flat roller. The rollers were made from tubes with a hard rubber coating. In the first series of tests, flat rollers were used to drive the belt. It was observed that a slight mismatch in roller pressure would pull the belt to the side with the higher load. Since the drive mechanism was suspended by springs, an adjustment could be made during the testing. Additionally, during the middle of a specific test, if required, the pressure could be varied manually. On the first day of testing, the belts tended to mistrack and could float out of the drive system. Therefore, on the second day a set of Delrin guides were added to help guide the belt through the drive system. The Delrin guides were placed at the ends of the rollers at the belt inlet side.

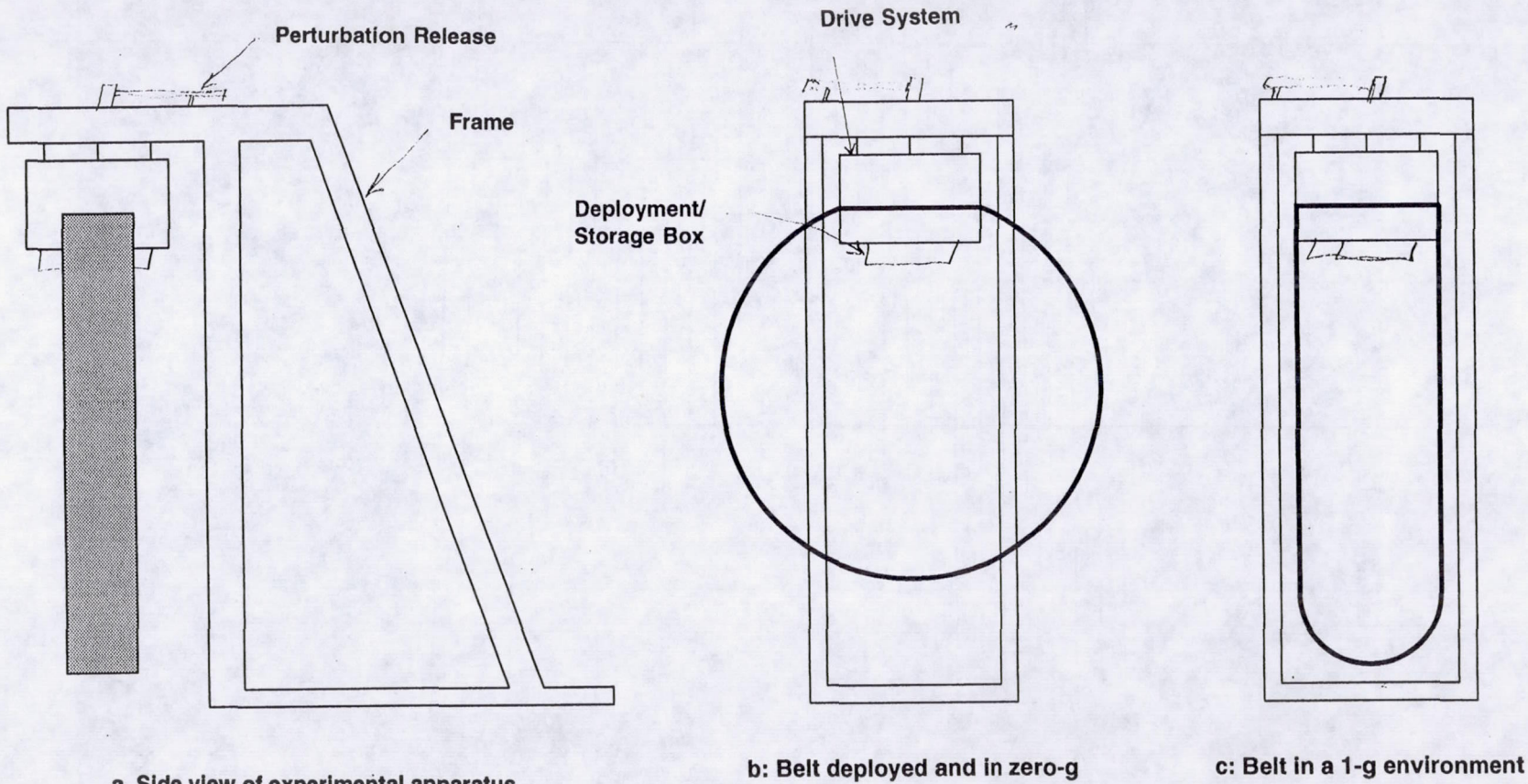

a. Side view of experimental apparatus

b: Belt deployed and in zero-g

c: Belt in a 1-g environment

Figure 40: Overall Experimental Apparatus Schematic

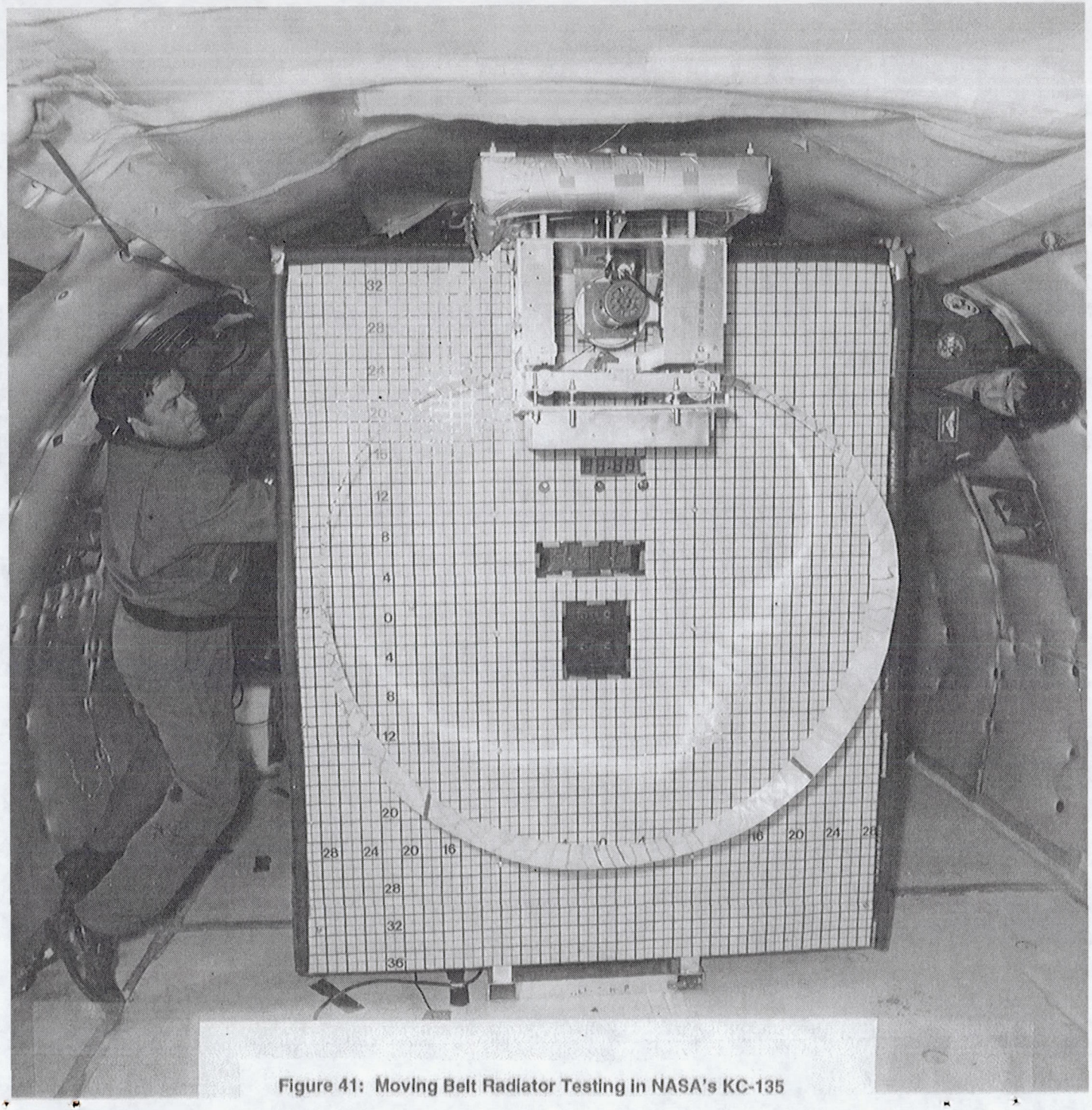

Figure 41: Moving Belt Radiator Testing in NASA's KC-135

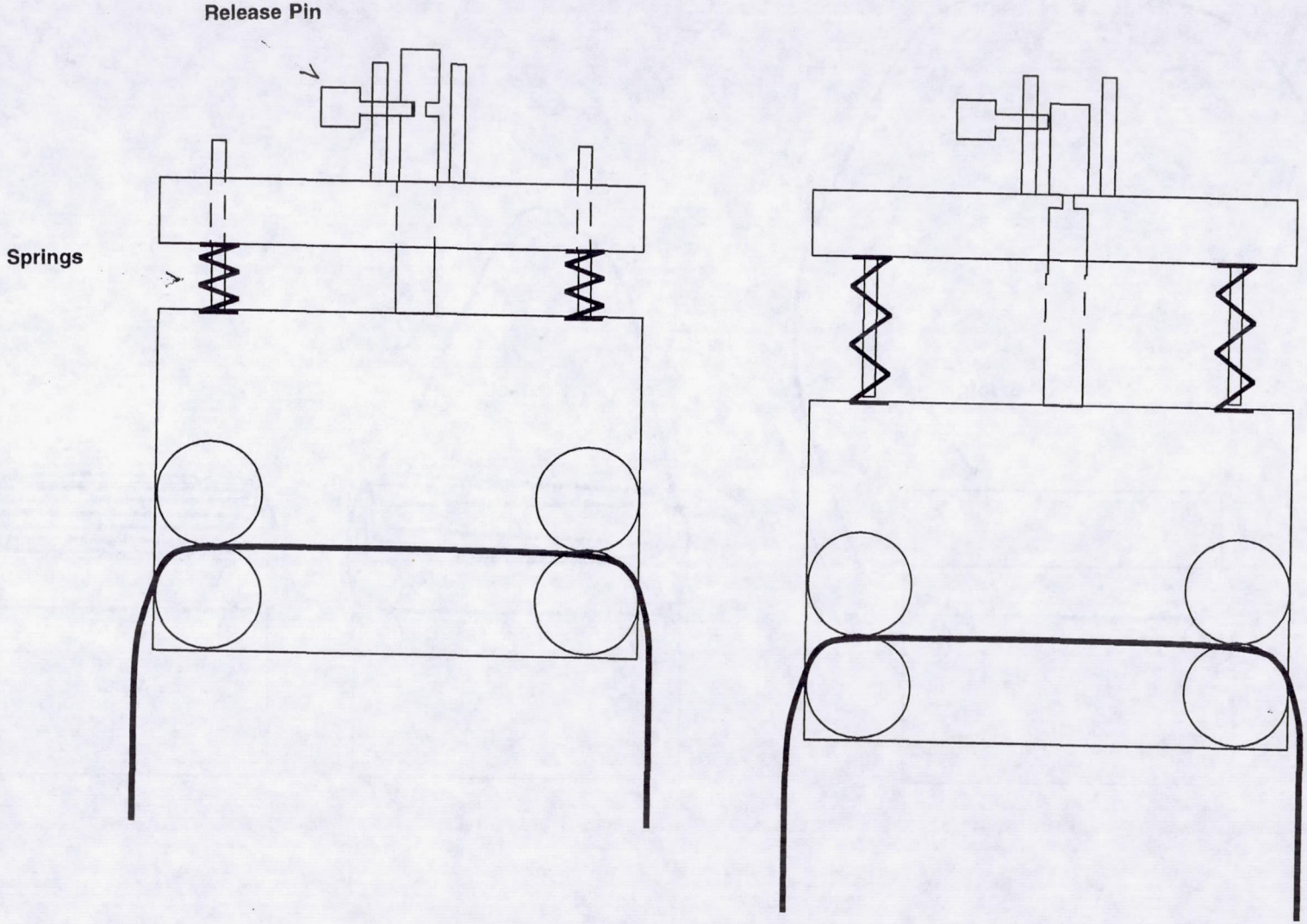

Figure 42: KC-135 MBR Perturbation System

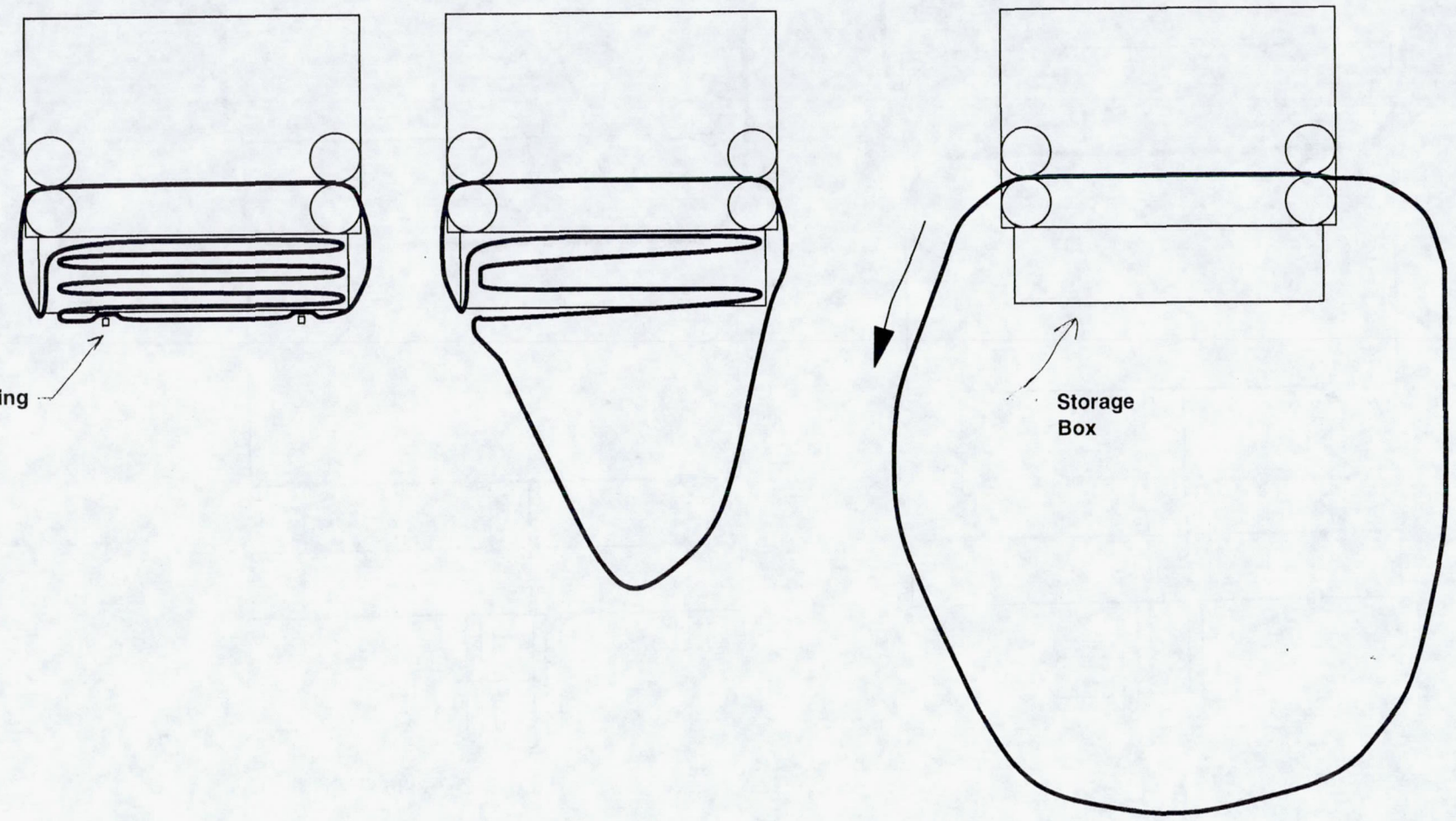

Figure 43: Storage/Deployment Apparatus for KC-135 MBR Experiment

For the second series of tests (January 1990), the rollers were crowned. Two types of crowns were fabricated. The first was a fully crowned roller and the second a partially crowned roller (i.e. a crowned roller with a short flat in the center). In ground tests combinations of rollers with no crown and crowned rollers were tried. It was observed that the best performance was when a flat roller and a partially crowned roller were used. This provided sufficient area for driving the belts while not allowing the main pressure point to vary to the roller ends.

4.4.2 Selection of Test Articles

The test articles were chosen so that a broad range of belts would be tested. The belt variables which were used as criteria included:

- Stiffness,
- Width,
- Diameter, and
- Belt material.

Table 4 shows the properties for a variety of belt materials. Those which were selected are highlighted in the table. These materials and the corresponding thickness were chosen to provide a range of test parameters. Appendix B lists the materials which were used during each parabola.

4.4.3 KC-135 Testing Schedule

Appendix B lists the schedules for each day's testing. Included in the schedules are comments from viewing films of the testing and those made during the testing. Indicated in the tables are the set speeds for the belt and measured speeds from the films.

4.4.4 Data Collection During Reduced Gravity

The data collection during the April 1989 flights consisted of:

- three fixed 16 mm cameras
- one roving video camera
- 70 mm still shots
- time display and speed indicators in the field of view

During the January 1990 flights the changes to the data systems included:

- three-axis accelerometer recorded on an instrument tape recorder (ITR)
- a larger time display;
- improved background for the belt; and
- elimination of one fixed 16 mm camera.

4.4.5 Results

Figures 44, 45, and 46 show typical shapes formed in reduced gravity. Appendix B includes comments on the performance of the various belts and Appendix C shows the acceleration traces. Some general observations are:

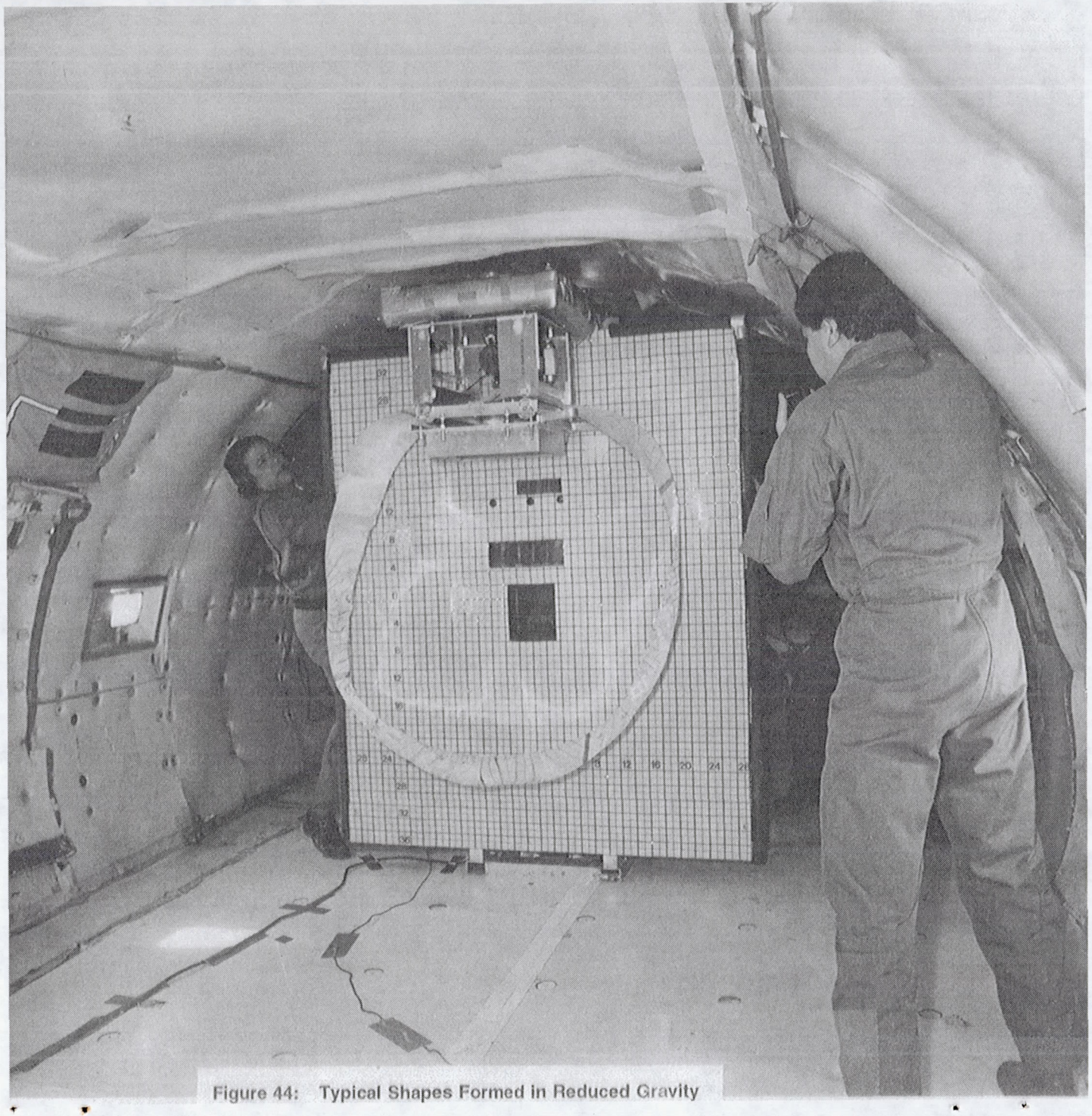

Figure 44: Typical Shapes Formed in Reduced Gravity

NASA
C-89-06409

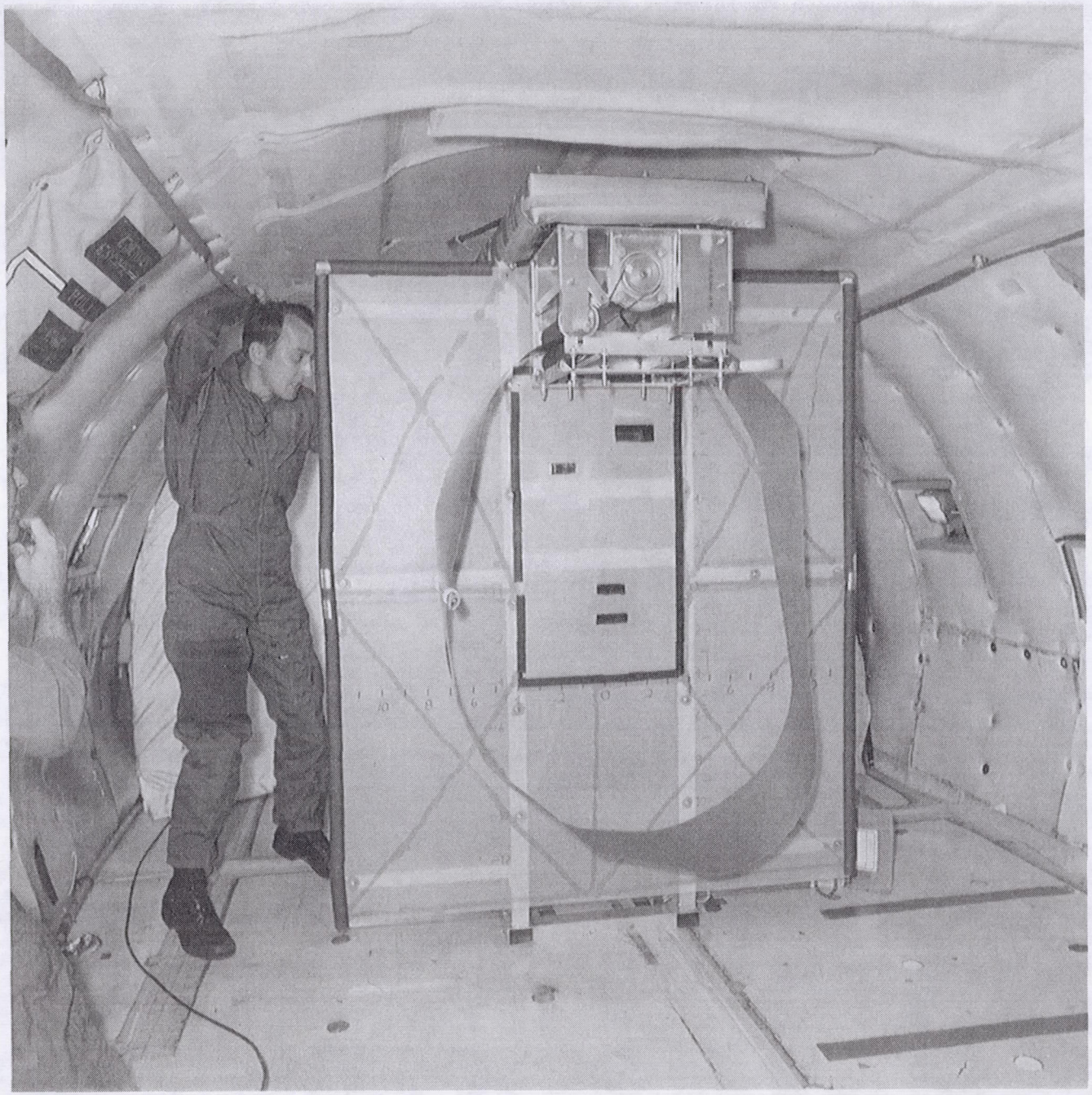

Figure 45: Typical Shapes Formed in Reduced Gravity

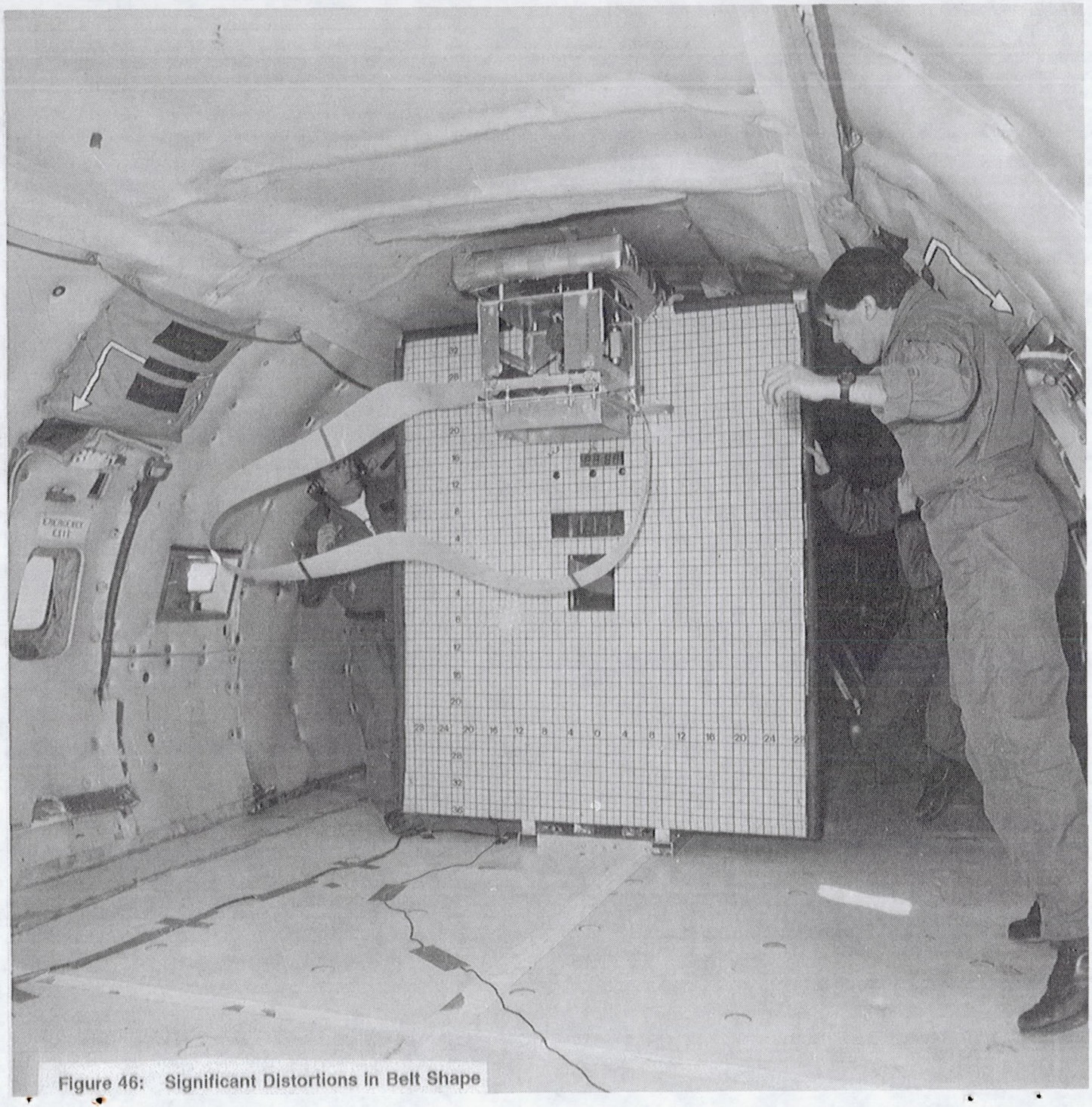

Figure 46: Significant Distortions in Belt Shape

- The stiffer metal belts worked very well for all cases except deployments (see Figure 41 and 44). The metal belts when used in the deployment tests maintained too much of a memory of the stowed configuration. As the distortions in the belt passed through the drive system, vibrations were generated throughout the test apparatus. The bends in the metal belts were flattened out after several rotations. This observation is in agreement with the analysis predicted by the BERS program.

- The soft Teflon belts did not perform well under any circumstances. The Teflon belts did not have sufficient bending stiffness to form a hoop and the test apparatus did not have the range to increase the speed to a sufficient level to induce a hoop form. Also, the Teflon belts retained the bends from the storage periods and did not smooth out.

- Accelerations parallel to the belt axis produced significant twist in the belt which tended to reduce the overall belt view factor. As the aircraft accelerated the belt would swing with the acceleration and the belt would twist and close down the hoop. As the belt closed down the interior surface of the belt reduced its view factor.

- Short-term accelerations of 1-g had minimal effect on belt performance and were either indistinguishable or damped out within a couple of revolutions. The short-term accelerations were generated by the experimental apparatus. Springs were used to generate the accelerations.

- The deployment of the belt without any sophisticated systems is possible providing the belt does not retain permanent folds. From these tests it was shown that a simple deployment system can work but it may be desirable to add more sophistication to the final design. The final design can have the capability of retracting the belt in the event of spacecraft maneuvers or hazards.

- Accelerating or decelerating the belt tends to produce significant distortions in the belt shape for a limited time. This is shown in Figure 46. The belt deviated from the near hoop shape to that shown in the figure. The belt did return to the same shape as was seen prior to the acceleration.

- Starting the belt from a cold start during zero-g typically does not result in any catastrophic results. Several belts were started from a cold start once in zero-g and the final shapes were the same as those that were started prior to entering zero-g. This allows options for stopping and starting a MBR as required in service.

Table 4: KC-135 Experiment Belts and Their Properties (1/3/89)

Material	Thickness (m)	S.G.	S.G. Ave.	Rho (kg/m**3)	Mu (kg/m**2)	Belt Mass (kg)	Et (N/m**2)	Et(mod) (N/m**2)	X-Sec Area (m**2)	I (m**4)	kt (N/m)	kb (N-m)	fn (Hz)	omega (sec)
Mylar (Pet)	7.620E-05	1.31-1.43	1.37	1370.2	1.044E-01	0.1219	1.930E+09	1.930E+06	2.323E-05	1.124E-14	1.171E+04	5.665E-06	49.32	3.227E-03
	1.270E-04		1.37	1370.2	1.740E-01	0.2032	1.930E+09	1.930E+06	3.871E-05	5.203E-14	1.951E+04	2.622E-05	49.32	3.227E-03
	1.778E-04		1.37	1370.2	2.436E-01	0.2844	1.930E+09	1.930E+06	5.419E-05	1.428E-13	2.731E+04	7.196E-05	49.32	3.227E-03
	3.302E-04		1.37	1370.2	4.524E-01	0.5282	1.930E+09	1.930E+06	1.006E-04	9.145E-13	5.072E+04	4.609E-04	49.32	3.227E-03
Teflon	7.620E-05	2.13-2.24	2.19	2010.6	1.532E-01	0.1789	3.447E+08	3.447E+05	2.323E-05	1.124E-14	2.090E+03	1.012E-06	17.21	9.250E-03
	2.540E-04		2.19	2010.6	5.107E-01	0.5962	3.447E+08	3.447E+05	7.742E-05	4.162E-13	6.968E+03	3.746E-05	17.21	9.250E-03
	3.810E-04		2.19	2010.6	7.660E-01	0.8943	3.447E+08	3.447E+05	1.161E-04	1.405E-12	1.045E+04	1.264E-04	17.21	9.250E-03
	4.826E-04		2.19	2010.6	9.703E-01	1.1328	3.447E+08	3.447E+05	1.471E-04	2.855E-12	2.855E-12	2.570E-04	17.21	9.250E-03
Aluminum	1.016E-04	1.14	2.70	2700.3	2.744E-01	0.3203	6.894E+10	6.894E+07	3.097E-05	2.664E-14	5.574E+05	4.795E-04	209.96	7.580E-04
Aluminum	2.032E-04	1.13	2.70	2700.3	5.487E-01	0.6406	6.894E+10	6.894E+07	6.194E-05	2.131E-13	1.115E+06	3.836E-03	209.96	7.580E-04
Vinyl	1.778E-04	1.20-1.70	1.45	1450.2	2.578E-01	0.3010	6.894E+08	6.894E+05	5.419E-05	1.428E-13	9.755E+03	2.570E-05	28.65	5.555E-03
Vinyl	2.540E-04	1.20-1.70	1.45	1450.2	3.683E-01	0.4300	6.894E+08	6.894E+05	7.742E-05	4.162E-13	1.394E+04	7.493E-05	28.65	5.555E-03
Vinyl	3.810E-04	1.20-1.70	1.45	1450.2	5.525E-01	0.6450	6.894E+08	6.894E+05	1.161E-04	1.405E-12	2.090E+04	2.529E-04	28.65	5.555E-03
Kapton HN	2.540E-04	1.42	1.42	1420.2	3.607E-01	0.4211	2.551E+09	2.551E+06	7.742E-05	4.162E-13	5.156E+04	2.772E-04	55.69	2.858E-03
Kapton VN	2.540E-04	1.42	1.42	1420.2	3.607E-01	0.4211	2.551E+09	2.551E+06	7.742E-05	4.162E-13	5.156E+04	2.772E-04	55.69	2.858E-03
Kapton VN	5.080E-04	1.52	1.42	1420.2	7.215E-01	0.8423	2.551E+09	2.551E+06	1.548E-04	3.330E-12	1.031E+05	2.218E-03	55.69	2.858E-03
Kapton FN	3.048E-05	1.52	1.53	1530.2	4.664E-02	0.0545	2.551E+09	2.551E+06	9.290E-06	7.193E-16	6.187E+03	4.791E-07	53.65	2.966E-03
Kapton FN	2.540E-04	1.53	1.53	1530.2	3.887E-01	0.4538	2.861E+09	2.861E+06	7.742E-05	4.162E-13	5.783E+04	3.110E-04	56.82	2.801E-03
ACLAR 88A	2.540E-04	2.10	2.10	2100.3	5.335E-01	0.6228	1.034E+09	1.034E+06	7.742E-05	4.162E-13	2.090E+04	1.124E-04	29.16	5.458E-03
ACLAR 22A	2.540E-04	2.10	2.10	2100.3	5.335E-01	0.6228	1.034E+09	1.034E+06	7.742E-05	4.162E-13	2.090E+04	1.124E-04	29.16	5.458E-03
ACLAR 22C	2.540E-04	2.11	2.11	2110.3	5.360E-01	0.6258	9.997E+08	9.997E+05	7.742E-05	4.162E-13	2.021E+04	1.086E-04	28.60	5.565E-03
ACLAR 33C	2.540E-04	2.12	2.12	2120.3	5.385E-01	0.6287	1.344E+09	1.344E+09	7.742E-05	4.162E-13	2.717E+04	1.461E-04	33.09	4.810E-03

5.0 Materials Evaluation

5.1 Materials Properties Tests

5.1.1 Test Objectives and Results

Materials property tests were conducted to determine stretching and bending characteristics of some possible belt materials, specifically:

1. Stiffness in stretching and bending, and
2. Damping in stretching and bending.

The accuracy of the analytical dynamics model described in Section 4.1 depends heavily upon using correct values for critical belt parameters such as the stiffness and damping in bending and stretching. The proposed belt materials include nylon, plastic, and fiberglass. Although the properties of these materials are tabulated in various publications, additional tests were necessary since the materials will be in the form of a screen mesh for the LBR. The damping and stiffness properties of a material change after it has been crimped, woven, and bonded into a screen mesh. In addition, the screen mesh properties are hard to determine analytically since the screen is complicated by stretching, sliding friction between fibers, and aligning of the mesh. For these reasons it was necessary to test the materials to arrive at accurate estimates of the damping and stiffness values.

The stiffness values found in the tests were used to improve the stiffness model in the Task 1 computer program. However, damping measurements made in the test indicated that the computer program's friction model had to be changed. Test results indicated that the damping force in a screen mesh sample is unchanged even when the deformation rate of the sample is changed. Thus the damping of the screen mesh sample resembles coulomb or sliding friction. Since the computer program modeled the belt with viscous friction, the computer friction model was changed to reflect the improved understanding of the damping mechanism in screen mesh materials.

5.1.2 Obtaining Materials Properties

Damping values for both stretching and bending of a sample were required. Following the assumptions made in the Task 1 computer model, we believed the damping to be caused by viscous friction. Thus, to quantify the damping, an "equivalent viscous damping" value was used. Equivalent viscous damping is based on equating the energy removed by an equivalent viscous damping mechanism with the energy removed by an unknown damping mechanism, such as a screen sample. Stiffness values for both stretching and bending of a sample were also required. To describe the stiffness, a linear spring constant was calculated for each sample.

Stiffness and damping values for stretching were obtained from tests on an Instron tensile test machine. By cyclically loading and unloading a material sample through a range of forces, a force vs displacement curve can be generated for the sample. The curve for one cycle forms a hysteresis loop as shown in Figure 47. The area inside this curve is the energy dissipated per cycle by the damping forces within the sample.

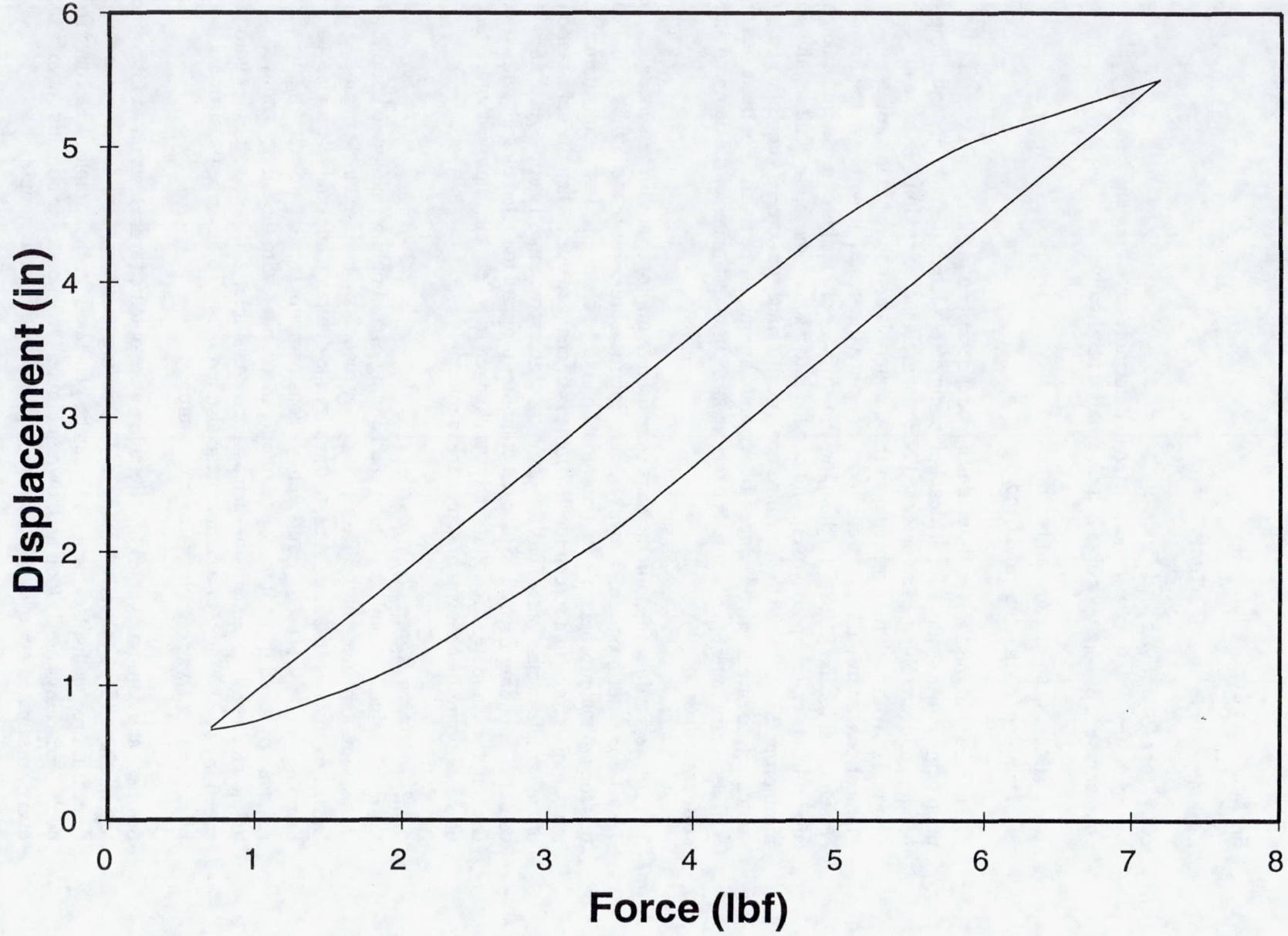

Figure 47: Hysteresis Curve for Rubber Belt

From a knowledge of this dissipated energy, an equivalent viscous damping value can be calculated for the sample in stretching. From the slope of the hysteresis loop, the linear stiffness value can also be calculated for the sample in stretching.

The bending stiffness and damping values can be calculated from the stretching stiffness and damping values. The conversion of the stretching values to the bending values is based on the assumption that the stiffness and damping forces act axially in the fibers being bent. An analytic derivation of bending stiffness and damping was preferred over direct measurement because of the great difficulty and inaccuracy associated with the measurement of these values. Table 5 lists the damping values and Table 6 the stiffness values for several materials at various deformation rates. Table 7 provides a comparison of the various materials and their properties.

Table 5: Damping Values

Material	Deformation Rate (in/min)	Force Range (lbf)	Damping Force (lbf)	Equivalent Viscous Damping Value (lbf/in/sec)	Energy Loss Per Cycle (lbf-in)
NY	0.5	1-10	0.370	44.27	0.166
NY	1.0	1-10	0.310	18.70	0.134
NY	2.0	1-10	0.280	8.57	0.120
TF	0.1	1-10	0.074	44.50	8.9×10^{-3}
TF	0.2	1-10	0.083	24.90	10.2×10^{-3}
TF	0.5	1-10	0.074	8.87	8.5×10^{-3}
TF	0.1	1-4	0.066	39.32	3.4×10^{-3}
TF	0.2	1-4	0.055	16.56	2.6×10^{-3}
TF	0.5	1-4	0.056	6.67	2.5×10^{-3}
LF	0.1	1-10	0.058	35.09	6.2×10^{-3}
LF	0.2	1-10	0.042	12.73	4.2×10^{-3}
LF	0.5	1-10	0.068	8.10	6.8×10^{-3}

LF is loose-woven fiberglass screen,
NY is nylon screen, and
TF is tight-woven fiberglass screen.
cm/min = 0.3937 in/min
N = 0.2248 lbf
N/cm/sec = 1.7513 lbf/in/s
N-cm = 11.2989 lbf-in

5.1.3 Test Results

For loose-woven fiberglass screen in the 1-4 lbf range there was not enough damping for accurate measurement by the tensile testing machine, and for Mylar plastic there was no measurable damping in either range. The nylon screen tests were run separately from the others, and so the deformation rates are different.

With viscous friction damping, the damping force is proportional to the deformation rate of the sample. However, for the samples considered, the damping force is practically constant as the deformation rate is varied; any change is probably due to measurement error. The fact that the damping force is constant indicates that the damping in the screen mesh is due to coulomb or dry friction damping and is not due to viscous friction damping, as was previously assumed.

Table 6: Stiffness Values

Material[3]	Deformation Rate[4] (in/min)	Force Range[5] (lbf)	Stiffness[6] (lbf/in)
NY	0.5	1-10	39.8
NY	1.0	1-10	40.6
NY	2.0	1-10	43.0
NY	0.5	1-4	50.3
NY	1.0	1-4	50.4
NY	2.0	1-4	51.7
PL	0.1	1-10	136.1
PL	0.2	1-10	135.7
PL	0.5	1-10	137.8
PL	0.1	1-4	114.7
TF	0.1	1-10	145.8
TF	0.2	1-10	142.2
TF	0.5	1-10	140.0
TF	0.1	1-4	112.7
TF	0.2	1-4	117.1
TF	0.5	1-4	116.9
LF	0.1	1-10	160.0
LF	0.2	1-10	161.5
LF	0.5	1-10	158.8
LF	0.1	1-4	148.3
LF	0.2	1-4	150.0
LF	0.5	1-4	150.5

Notes: The above damping and stiffness values are for a sample in stretching. To obtain the damping and stiffness values for a sample in bending, the materials must be subjected to bending tests. However, bending tests were found unnecessary for two primary reasons:

1. The bending values can be calculated from the stretching values to acceptable accuracy, and
2. More accurate values from testing would be time consuming and very expensive.
3. The damping and stiffness values for unit square samples -- one meter wide by one meter long -- are given in the Table 7.
   LF is loose-woven fiberglass screen,
   NY is nylon screen,
   TF is tight-woven fiberglass screen, and
   PL is Mylar plastic sheet.
4. cm/min = 0.3937 in/min
5. N = 0.2248 lbf
6. N/m = 1.7513 lbf/in

Table 7: Material Properties Comparison

Material	Stretching Stiffness	Bending Stiffness	Damping Force	Damping Moment	Belt Density
Computer Fiberglass (tight)	319261	1.72E03			0.61
1-4 lbf	485732	2.35E04	10.33	4.65E-04	0.135
Fiberglass (Tight) 1-10 lbf	599634	2.90E-04	13.48	6.06E-04	0.135
Fiberglass (Loose) 1-4 lbf	628775	5.41E-04			0.098
Fiberglass (Loose) 1-10 lbf	672907	5.79E-04	9.81	5.88E-04	0.098
Nylon 1-4 lbf	213515	3.47E-04			0.111
Nylon 1-10 lbf	171624	2.79E-04	56.04	4.62E-03	0.111
Mylar Plastic 1-4 lbf	482089	1.87E-03			0.312
Mylar Plastic 1-10 lbf	573856	2.23E-03			0.312

5.1.4 Comparison with the Computer Model

The parameters used in the Task 1 computer simulation are shown as "computer" in Table 7. Comparing stiffness values, the measured stretching stiffness values for all tested materials are of the same order of magnitude as the stretching stiffness value used in the computer program. The bending stiffness values for all materials are either close to the computer bending stiffness value or differ from the computer program values by only a factor of ten. Since bending stiffness has less influence than stretching stiffness, these differences are relatively small. These results confirm the modeling assumptions that were made in estimating the stretching and bending stiffness in the Task 1 computer program. The test results will be used to improve the computer stiffness models and to allow different materials to be simulated using known stiffness properties.

There are no damping values shown for the computer program since the program assumed viscous friction damping for screen mesh while the test results indicate that the damping is actually dry friction or coulomb friction damping. Since the amount of energy removed from the system by viscous damping depends upon the rate of deformation, and the energy removed by coulomb damping depends on the total deformation, comparisons between the computer viscous damping values and the measured coulomb damping values cannot be easily made. The test results will be used to alter the computer program so that it more accurately models the stretching and bending damping of the proposed belt materials.

5.1.5 Conclusions

These tests were run to quantify the damping and stiffness properties of several candidate LBR belt materials. Samples tested were made of nylon screen, fiberglass screen, and Mylar plastic sheet.

Test results indicate that the damping of the screen mesh samples resembles coulomb or sliding friction. Since the Task 1 computer program modeled the belt with viscous friction, the computer friction model must be changed to reflect our improved understanding of the damping mechanism in screen mesh materials.

The stiffness values obtained from the materials tests confirm the modeling assumptions which were made in estimating the stretching and bending stiffness in the Task 1 computer program. The test results will be used to improve the computer stiffness models and to allow different materials to be simulated using known stiffness properties.

As described in Section 5.1, stretching and bending properties of MBR materials were measured to characterize the dynamic properties of the MBR belt. This information is necessary to revise and improve the dynamic belt model of Task 1. The Task 1 computer model will be modified with the knowledge gained from the materials tests of this task. In addition to studying LBR materials, Task 4 analyzed the response of a revolving belt to various inputs using a physical model of the LBR. This was done primarily to verify the results of the Task 1 computer simulation.

We ran materials properties tests to determine stretching and bending characteristics of proposed belt materials, specifically:

1. Stiffness in stretching and bending, and
2. Damping in stretching and bending.

Samples tested were made of nylon screen, fiberglass screen, and Mylar plastic sheet.

Test results indicate that the damping of the screen mesh samples resembles coulomb or sliding friction. Since the Task 1 computer program modelled the belt with viscous friction, the computer friction model must be changed to reflect our improved understanding of the damping mechanism in screen mesh materials.

The stiffness values obtained from the materials tests confirm the modeling assumptions which were made in estimating the stretching and bending stiffness in the Task 1 computer program. The test results will be used to improve the computer stiffness models and to allow different materials to be simulated using known stiffness properties.

6.0 Interface Heat Exchanger Testing

6.1 Heat Transfer Tests

6.1.1 Task Objectives

The objectives of this task were to:

- Determine if a continuous Teflon belt could be transported through a gallium bath and reject heat while suffering negligible mass transfer of gallium through the bath seals.

- Verify the heat transfer and viscous drag characteristics of the interface heat exchanger using gallium as a thermal transfer fluid and compare the measured characteristics with those assumed in the system performance models described in Section 3.1
- Undertake preliminary experiments in the fabrication and thermal characteristics of hybrid belt structures, which incorporate thermal phase change materials.
- Assess the potential impact of the mechanical properties (stiffness, weight, thickness, etc.) of hybrid belt structures on belt stowability and deployment.

6.1.2 Moving Belt/Interface Heat Exchanger Tests

6.1.2.1 Test Apparatus

As indicated in previous reports (Reference 4), gallium is the preferred heat transfer fluid for use in a hybrid belt radiator. The favorable properties of gallium include its high thermal conductivity, low vapor pressure, and non-wetting properties.

Figures 48 and 49 show drawings of the experimental apparatus used for the MBR heat transfer/drag tests, and Figures 50 and 51 are photographs of the apparatus. The apparatus was that used in the Task 2 seal tests modified for continuous belt operation and to allow for heat transfer measurements. The essential features of the apparatus include:

- A bench top size interface heat exchanger (IHX) unit having electric mats mounted top and bottom to provide accurately measured heat inputs into the system. The combined power capability of the heating mats was 0.8 kW with a power density of 15.5 kW/m^2.
- Gallium containment is accomplished by the sponge wiper seals located at the bath entrance and exit. Seal loading could be adjusted over a range of 0 to 2.3 kg to assess the effect of seal loading on leakage and drag forces. Seal loadings and velocities are very low which should result in long life. For example, unlubricated seals in Stirling engines which have demonstrated life in excess of 10,000 hours, are subjected to velocities 10 - 30 times those in the MBR system.
- A speed controlled DC motor with gear box reduction drives the power roller to produce a constant belt velocity. The adjustable tension roller provides enough pressure to keep the belt from slipping on the roller drive. Belt velocity could be adjusted over a wide range to assess impacts on seal performance and viscous drag losses.
- A set of eight thermocouples were used to measure IHX surface temperatures and the entrance and exit temperatures of the moving belt. This allowed for measuring temperature drops across the gallium bath as a function of belt operating parameters including temperature level velocity and heat transfer rates. Multiple thermocouples were used to verify measurement accuracy.
- A continuous, etched Teflon belt. Teflon was selected due to its:
  - Excellent chemical resistance to gallium
  - Low coefficient of friction for minimum belt wear.
  - Low (negligible) wetting with liquid gallium.

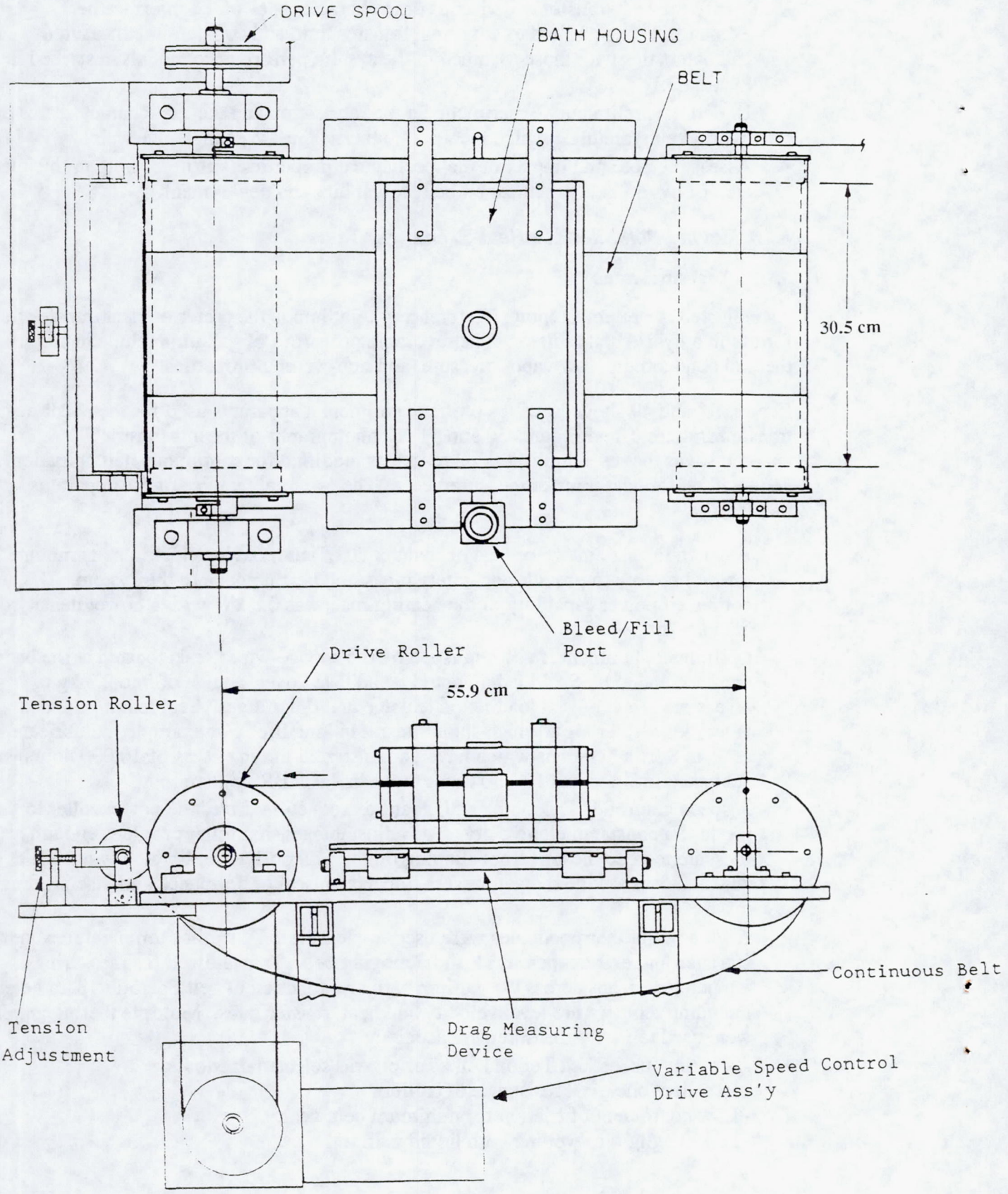

Figure 48: Overview Heat Transfer/Viscous Drag Test Apparatus Drawing

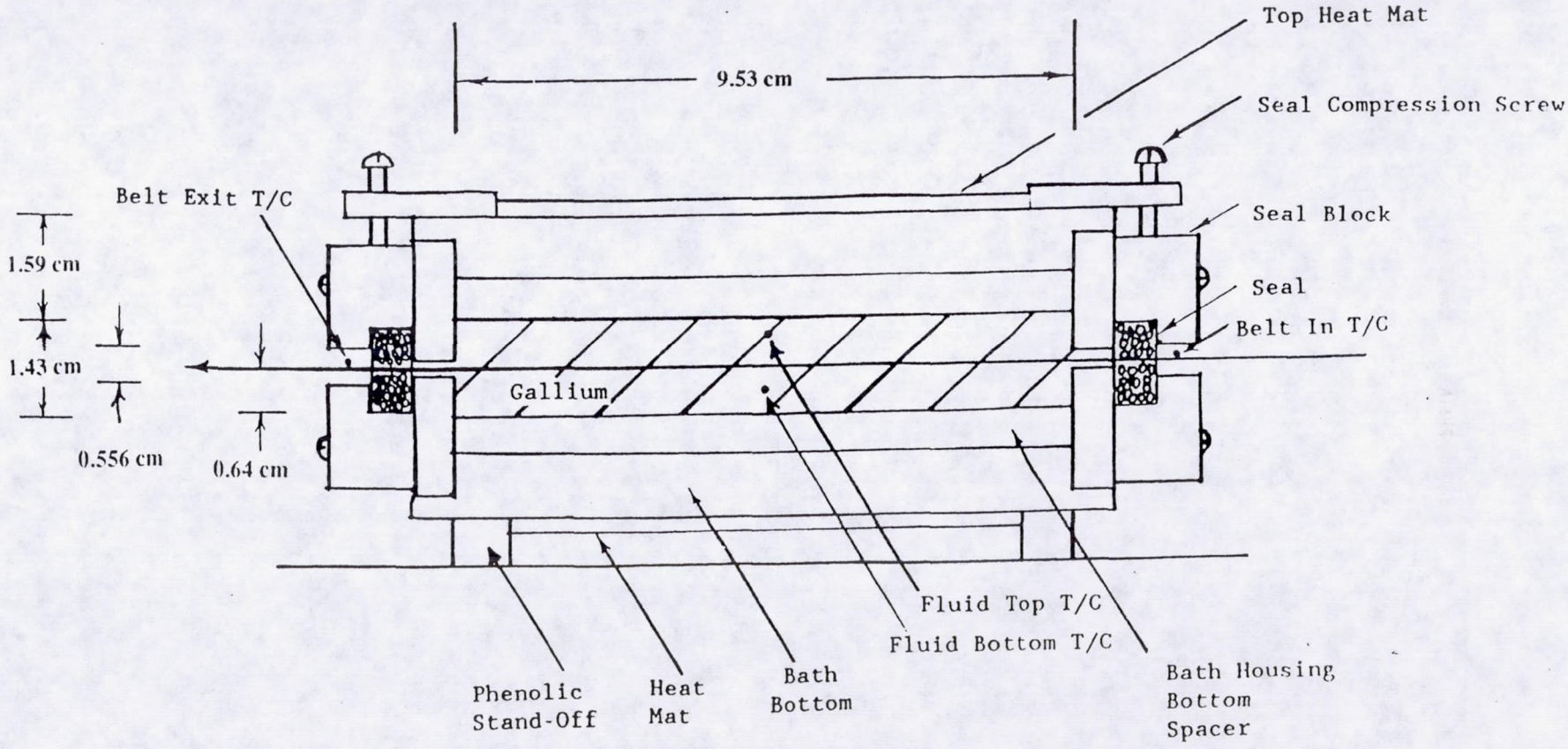

Figure 49: Interface Heat Exchanger Layout

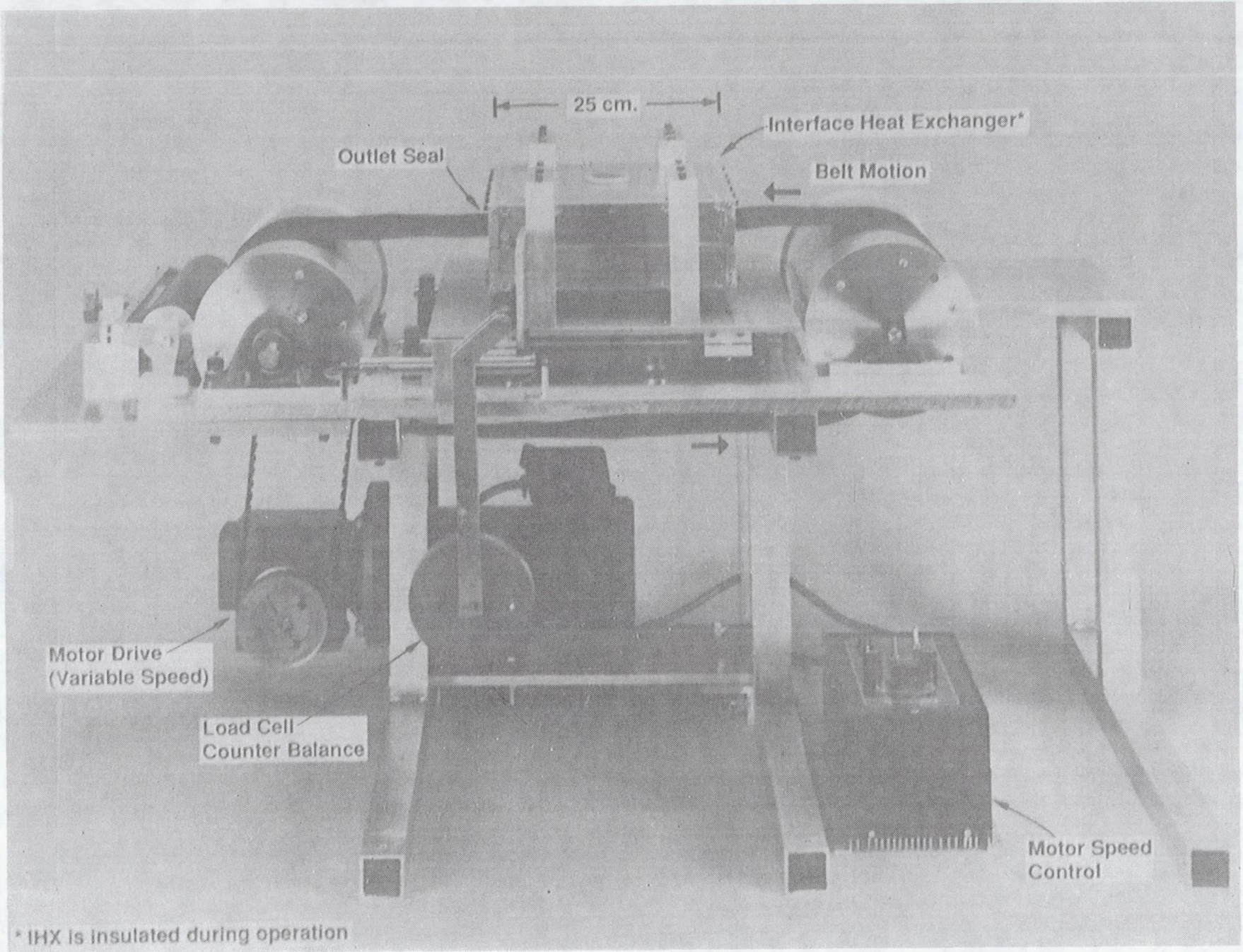

Figure 50: Interface Heat Exchanger Test apparatus - Overall View

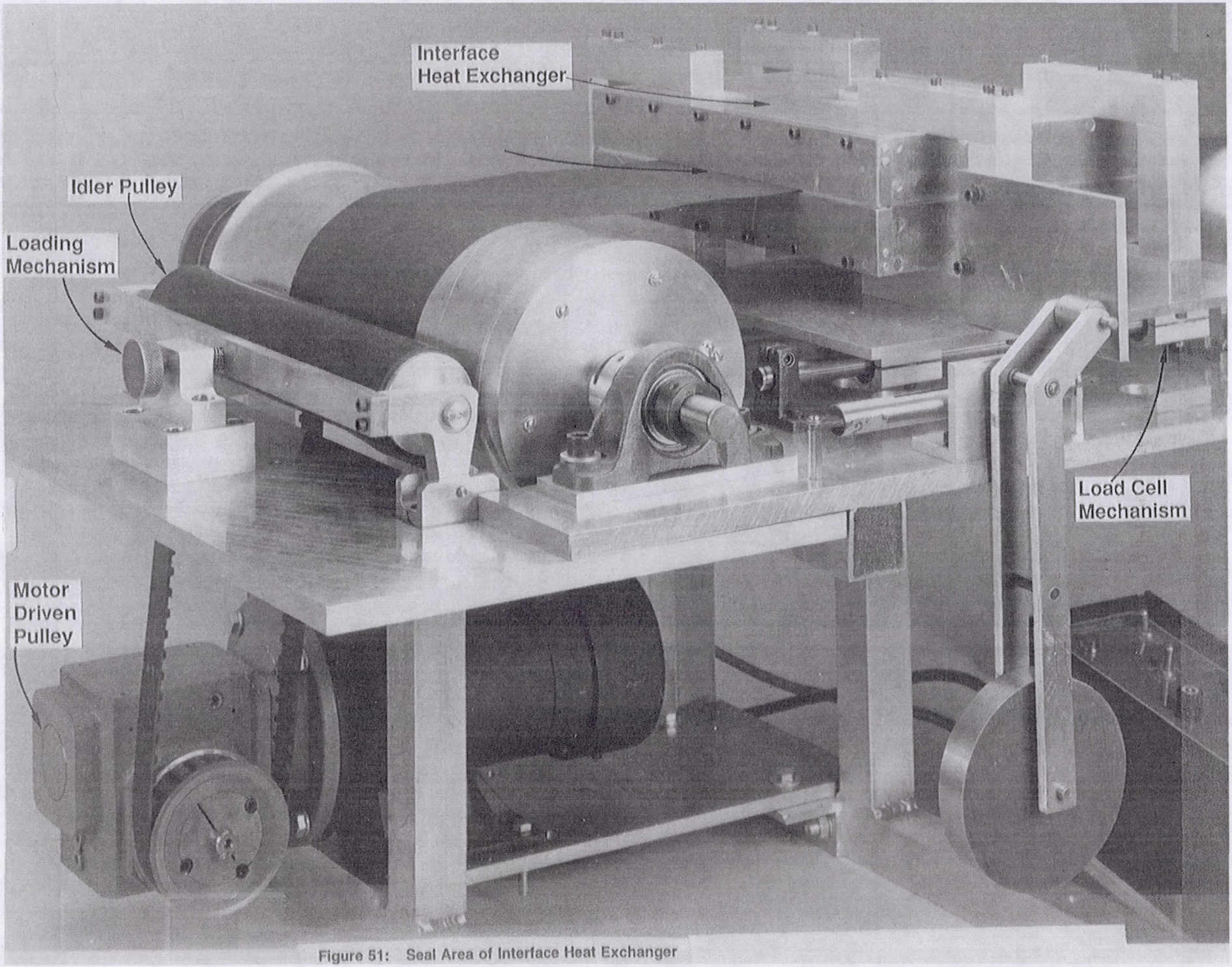

Figure 51: Seal Area of Interface Heat Exchanger

A belt strip measuring 167.6 cm long by 15.25 cm wide by 0.0127 cm thick (66 in by 6 in by 0.005 in) was made into a continuous belt. Figure 52 shows the physical arrangement of various seam configurations and Table 8 the characteristics of the seam. For test purposes, seam configuration D was chosen for superior strength. In all cases the adhesive was applied to the seam such that shoveling due to the belt seam discontinuity would be prevented at the bath seal inlet and exit.

Table 8:Belt Seams Characteristics

Seam	Description	Strength	Thickness[2]	Comments
(A)	Butt Joined Normal to Belt Direction	3.63	0.018	Good continuity, relies solely on adhesive in tension
(B)	Butt Joined 35° to Belt Direction	11.79	0.018	Good continuity, relies solely on adhesive in tension, provides a lead into seals
(C)	Lap Joined (1") Normal to Belt Direction	18.14	0.031	Excellent strength in shear but may shovel entrance seal
(D)	Lap Joined (1") 35° to Belt Direction	18.14	0.031	Excellent strength, provides a lead in to seals
(E)	Multi-Angle	4.31	0.018	
(F)	V-Shape	10.89	0.020	

[1] All seals used 3M DP-190 adhesive
[2] As measured across seam

6.1.2.2 Heat Transfer Tests

The test apparatus functions as a calorimeter where the power input to the heat pads equals the heat transfer to the moving belt plus extraneous heat losses. Due to the insulation package surrounding the IHX test section, heat losses as measured without belt motion were less than 3 Watts.

Heat rejection for the MBR is quantified by applying a first law (of thermodynamics) approach to the Teflon belt where:

$$Q = (\rho t w)\, v\, C_p\, (T_e - T_i)$$

and:

ρ :	Density of Teflon	= 2200.56 kg/m^3
t :	Belt thickness	= 0.0127 cm
w :	Belt width	= 15.24 cm
v :	Belt velocity	= 1.524 - 3.81 cm/sec.
C_p :	Specific heat of Teflon	= 4.1865 kJ/kg-K
T_e :	Belt exit temperature (K)	
T_i :	Belt inlet temperature (K)	

Table 9 indicates the results of heat transfer tests for a range of belt velocities from 1.27 cm (0.5 in) to 7.62 cm/sec (3.0 in/sec) and bath temperatures of 310.9 K to 330.4 K. These tests indicated that:

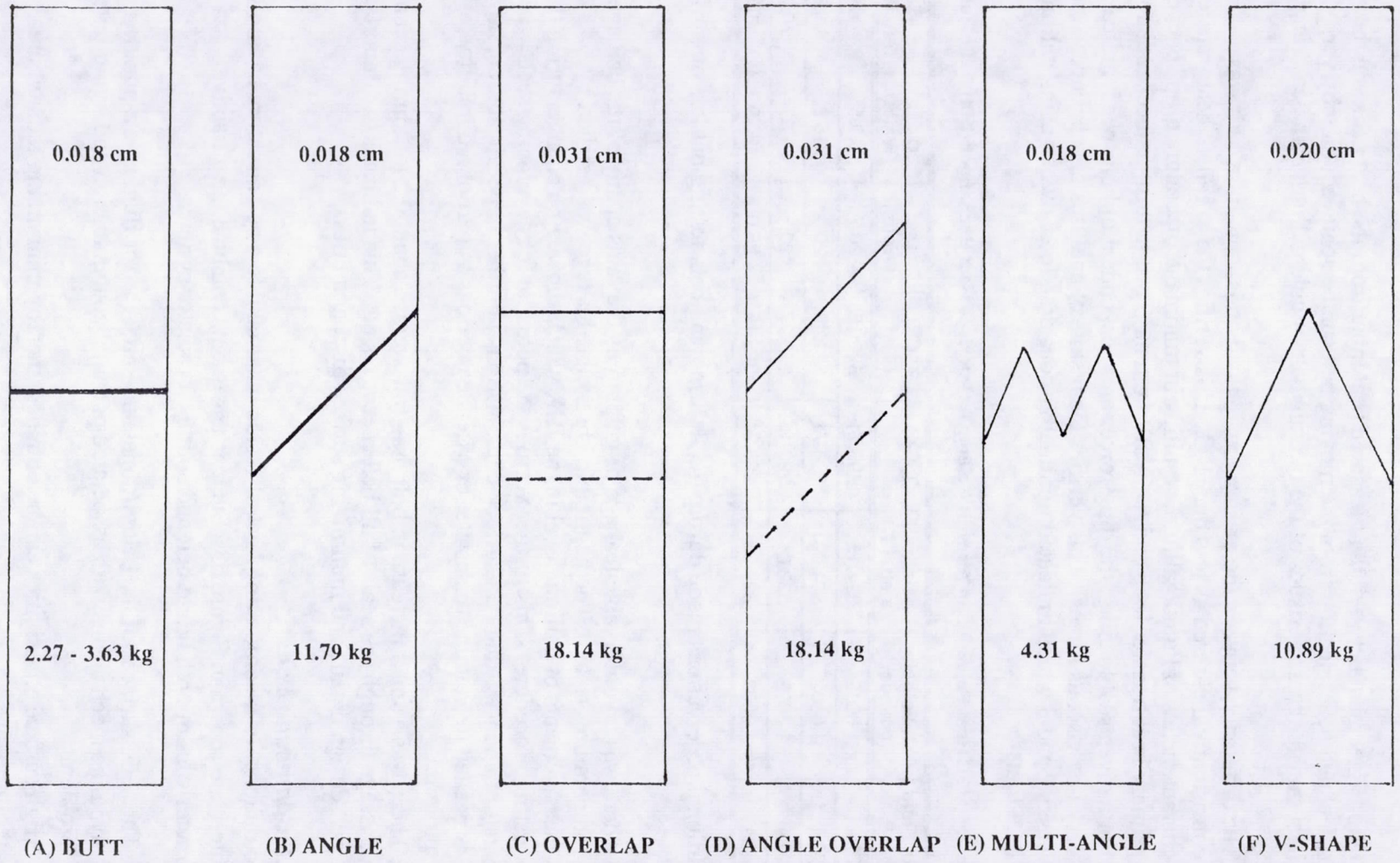

Figure 52: Continuous Belt Seam Configurations

- Good agreement between the measured heat input from the heat pads and the calculated heat rejection from the moving belt can be achieved, thereby verifying the heat transfer characteristics of the moving belt - liquid gallium bath heat transfer system.
- The difference between the exiting moving belt and the gallium bath was consistently measured as less than 1°C. This verifies the excellent heat transfer characteristics of liquid gallium, resulting in minimal temperature drops between the primary heat transfer loop and the MBR system. This, in turn, reduces radiator area.
- For a given seal loading, the drag forces are independent of belt speed, indicating very low viscous forces. This verifies the results of analyses of references 1, and Tasks 2 and 3 which indicated minimal viscous drag forces when using gallium as a heat transfer fluid.

Table 9: MBR Heat Rejection in Air with Gallium as Interface Heat Exchanger (IHX) Bath Fluid

Bath Fluid	Belt Velocity (cm/sec)	Bath Temp. (°K)	T_i (°K)	T_e (°K)	Q_{in} (Watts)	Q_{reject} (Watts)	Belt Tension [kg]
Ga	1.6002	324.15	298.71	323.15	20.7	19.5	1.134
Ga	1.6002	324.09	298.71	321.48	20.4	18.2	1.2701
Ga	1.6002	322.04	298.15	320.37	20.2	17.7	0.9072
Ga	1.6002	329.82	298.71	328.15	25.0	23.9	1.3608

Additional observations made during the IHX/moving belt, testing but less quantifiable, were:

- There was no observable leakage of gallium by the seals at any of the belt speeds or temperatures tested. The negligible observable leakage was verified by measurements of gallium level in the IHX which showed no change during the testing procedure. This further verifies the potential for developing seals when using gallium/non-wetting belt surface combinations. Further experimentation, however, is needed to examine this issue for extended periods as part of a durability testing program.
- There was a small increase in belt drag (on average about 0.2 kg) during seam passage through the seals of all belt speeds tested. This indicates the importance of belt design details and minimizing surface discontinuities.

6.1.3 Composite Belts

Two options for incorporating heat of fusion material into a belt structure having solid surfaces are shown in Figure 53. Such arrangements combine the attractive characteristics of both liquid belt and solid belt radiator systems.

- The solid surfaces of the belt eliminate potential loss of fluid by evaporation or dynamic mechanisms with associated potential contamination and liquid inventory problems.
- High surface emissivities can be obtained, thereby minimizing radiator area requirements.

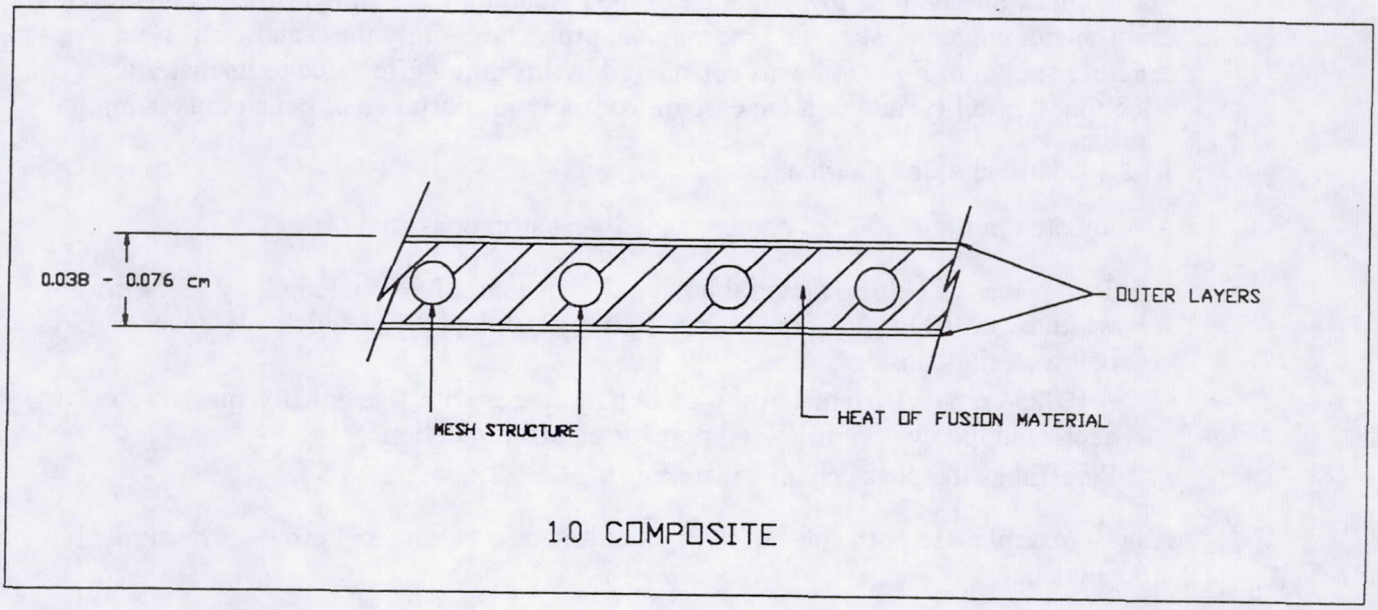

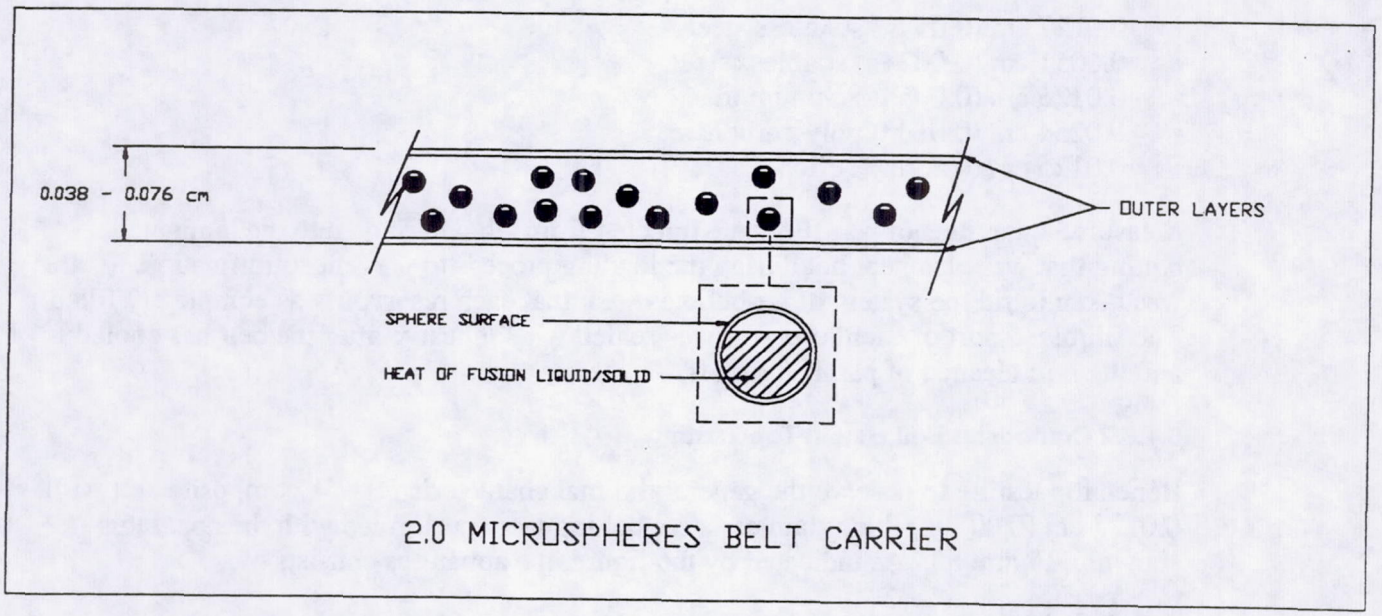

Figure 53: Hybrid Belt Design Concepts

- The incorporation of heat of fusion material lowers the required belt speeds for a given belt thickness (and unit mass) thereby reducing IHX sealing and dynamic issues.

This subtask initiated the investigation of the potential modes of hybrid belt construction, heat transfer characteristics, and mechanical properties. Only the "sandwich" type structure shown in Figure 53 was considered in this initial effort due to its material selection, flexibility, and relative ease of assembly for purposes of bench top testing.

6.1.3.1 Composite Belt Fabrication

As indicated in Figure 54 the composite belt test strip consisted of:

- Two pieces of belting material having dimensions 27.94 cm length by 15.24 cm width by 0.0127-0.254 cm (11 in by 6 in by 0.005 to 0.1 in) thickness depending on belt material chosen.
- A 0.0254 cm (0.1 in) thick poly-carbonate spacer with five equally spaced reservoirs each equipped with a fill/bleed port for paraffin injection.
- Paraffin as the phase change material (M.P. = 322.04 ± 2.78 K).

Adhesive applied to both sides of the spacer joins the belting and provides reservoir independence.

The overall belt thickness is dependent upon the belting chosen. The material used for the test sections were:

- 0.0127 cm (0.05 in) stainless steel.
- 0.0051 cm (0.002 in) stainless steel.
- 0.0125 cm (0.005 in) aluminum.
- 0.0254 cm (0.01 in) poly-carbonate.
- 0.0125 cm (0.05 in) Teflon.

Measured quantities of paraffin were injected from a hot syringe into the laminated belting that was also kept hot during the loading process to prevent solidification. (Care was taken to rid the system of air bubbles such that each reservoir was completely filled.) The fill/bleed port of each reservoir was sealed with adhesive after the belt has cooled and the port cleaned of paraffin runoff.

6.1.3.2 Composite Belt Bench Top Testing

Bench top testing to observe the general thermal characteristics of a composite belt with 0.0127 cm (0.005 in) thick stainless steel belting were performed with the apparatus shown in Figure 55. As indicated by the figure, the apparatus consists of:

- A 250 Watt radiant heat source.
- A heavily insulated enclosure with temperature measurement instrumentation on both the front and back surface of the hybrid belt test sections.
- Fast reaction thermocouples monitored by a Datalogger 3000 System interfaced with personal computer.

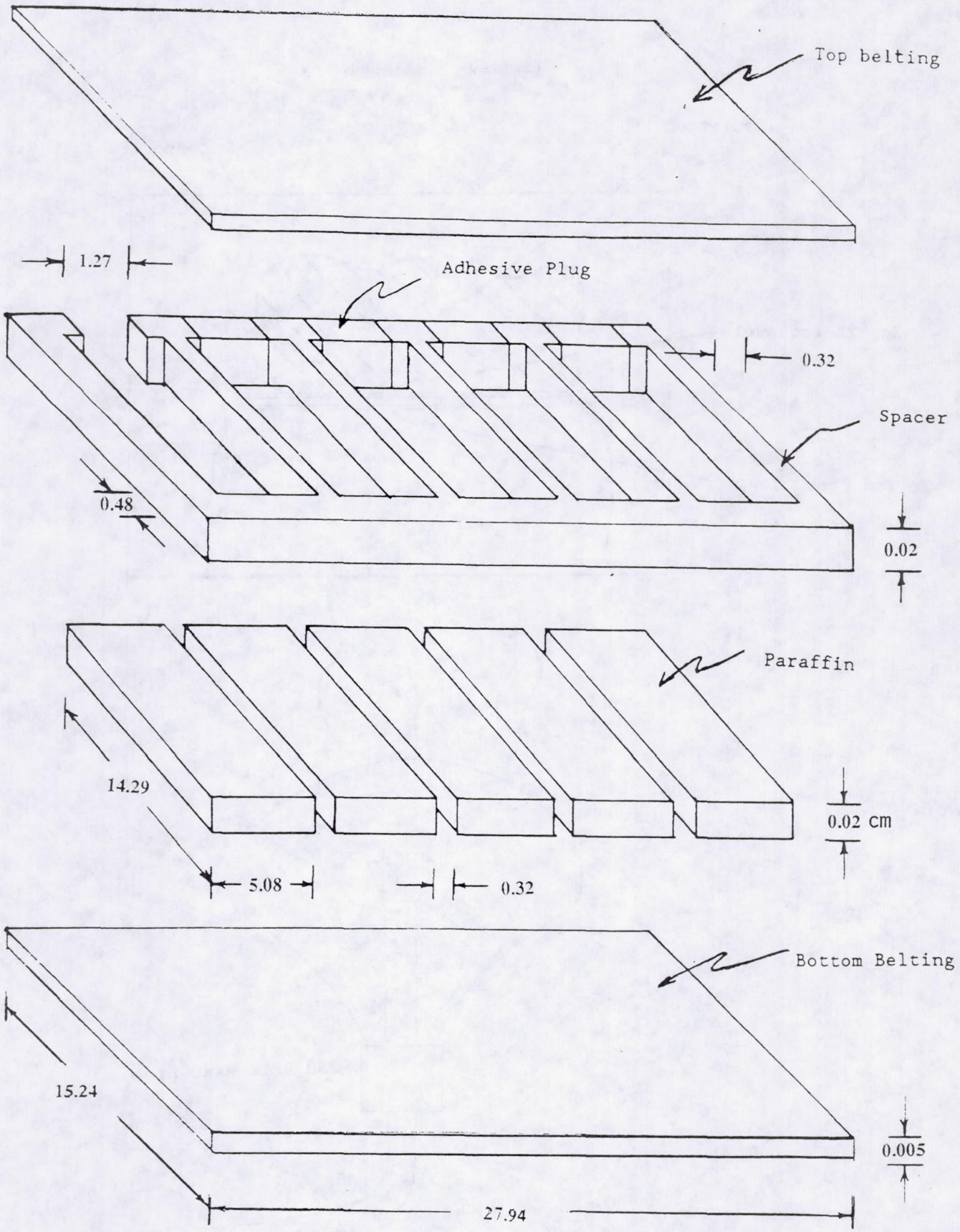

Figure 54: Construction of Hybrid Belt Test Sections

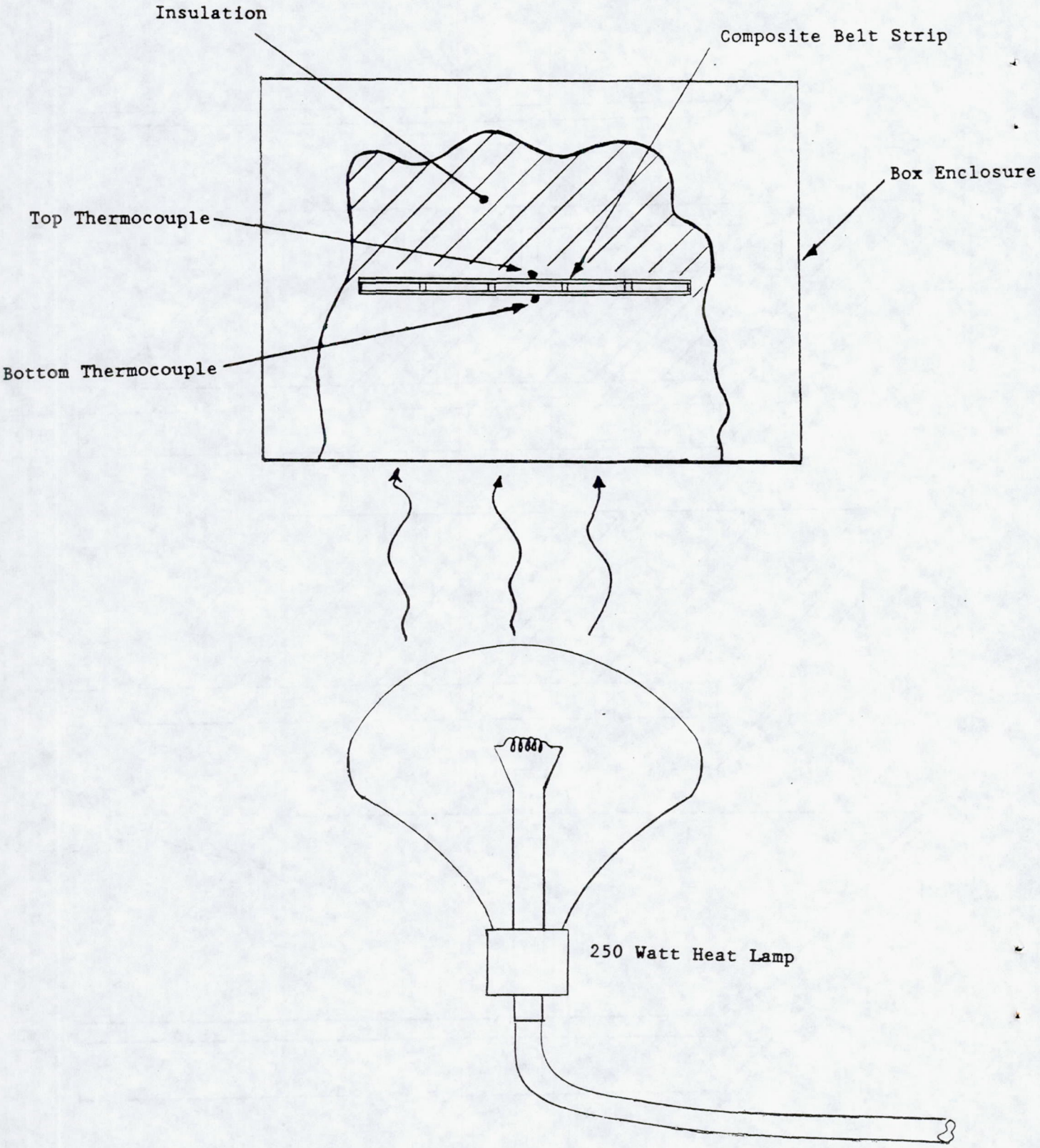

Figure 55: Bench Top Apparatus for Observing Hybrid Belt Segment Thermal Characteristics

The thermocouple location was in the center of each reservoir on the heat source side.

Figures 56 and 57 show the plots of temperature as a function of time for the stainless steel composite with paraffin and without paraffin. Figure 57 clearly displays the effect of the heat of fusion material on the composite belt thermal properties and, in particular, the large amounts of heat transfer at nearly constant temperature conditions during the melting of the paraffin. The thermal capacity of the paraffin during melting was 14 times the sensible heat of the belt structure for a 5.56 K temperature change.

The composite structures, with Teflon outer surfaces, had flexibility properties consistent with being rolled in a compact shape for launch. The structures using metal outer surfaces were rather stiff - only about 30% less than a solid piece of material (aluminum, steel) of the same overall thickness since the structure is of I-beam construction. The stiffness of hybrid belts with metallic outer surfaces will, therefore, be a consideration in future design studies and in selecting appropriate belt speed vs belt thickness tradeoffs.

6.1.4 Conclusions And Recommendations

The simple bench top testing described in this topical report has helped verify the potential for successfully addressing several of the key technical issues associated with the MBR concept. Specific observations resulting from this work include:

- A moving belt can be moved through an interface heat exchanger containing Gallium as the heat transfer fluid without loss of fluid through the seals. This capability was projected based on the physical characteristics of Gallium - most importantly the fact that it is non-wetting to virtually all common materials.
- The viscous drag forces associated with the belt movement through a liquid Gallium heat exchanger bath are negligible which is consistent with the very low viscosity of this material.
- Due to the very high heat transfer coefficients associated with all liquid metals, including Gallium, the temperature drops between the IHX surface and the moving belt (i.e. across the Gallium gap) are very low which would result in minimizing radiator area for a given heat rejection temperature from the spacecraft.
- A hybrid belt using a "sandwich" structure can achieve most of the advantage associated with using a heat of fusion effect to allow large levels of heat rejection over a narrow temperature range. As previously stated, this is important for reducing belt weights and speeds as compared to using a sensible heat capacity effect only.

As indicated above, the benchtop experiments provided preliminary verification of several of the key technical performance characteristics of the HBR system including IHX sealing, low viscous drag forces leading to low parasitic power inputs, excellent heat transfer capabilities, and the potential for hybrid belt structures. Much more analytical and experimental work will have to be done, however, to verify the potential of this concept for use in long term space missions including durability testing of bath - seal systems, long term mechanical testing of belt structures subject to flexure and seal loadings, development of hybrid belt structures with required mechanical/thermal characteristics for long term operation, and extension of temperature capabilities to those associated with high temperature power cycles.

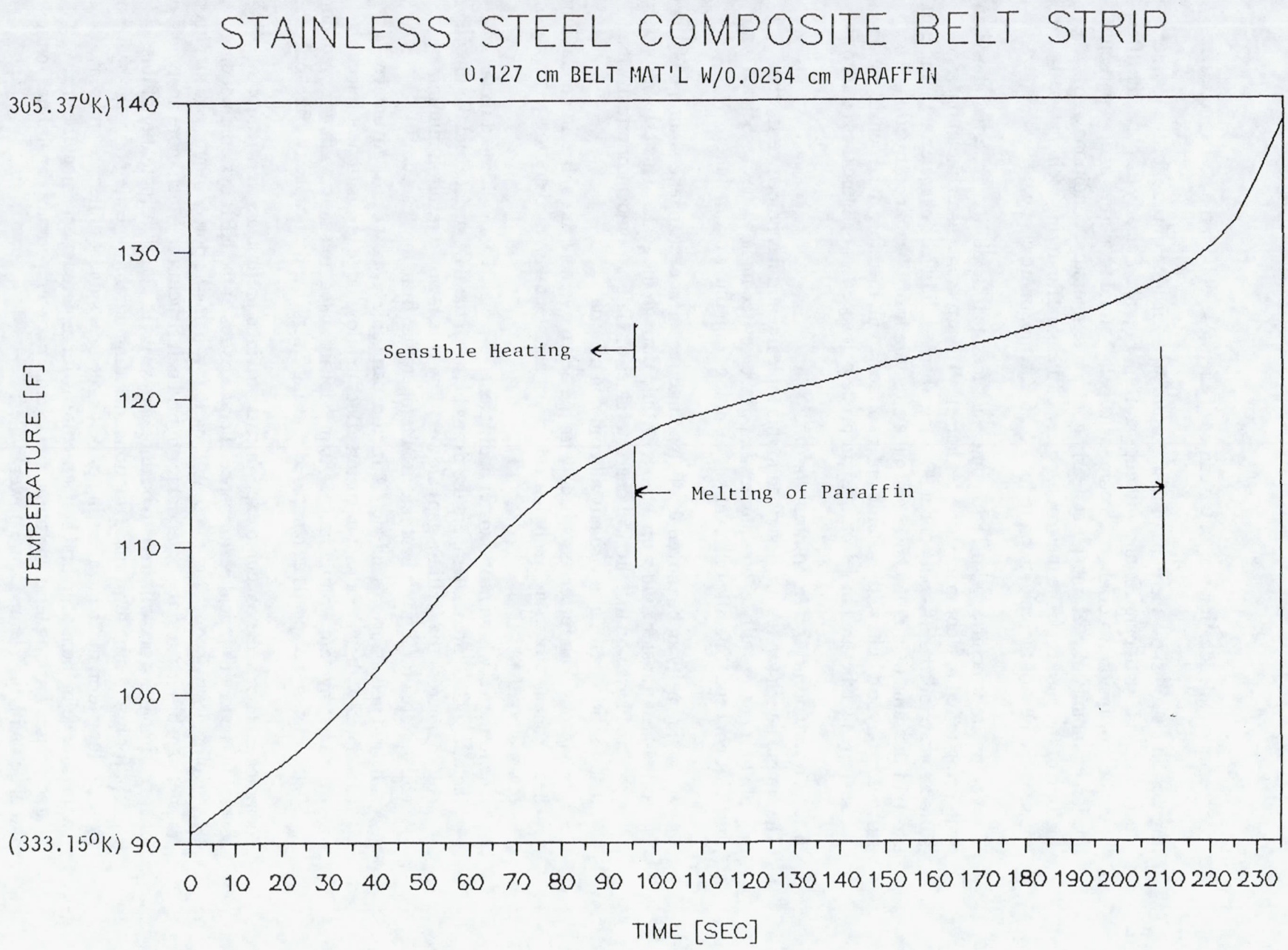

Figure 56: Temperature vs Time Plot of Hybrid Belt Structure

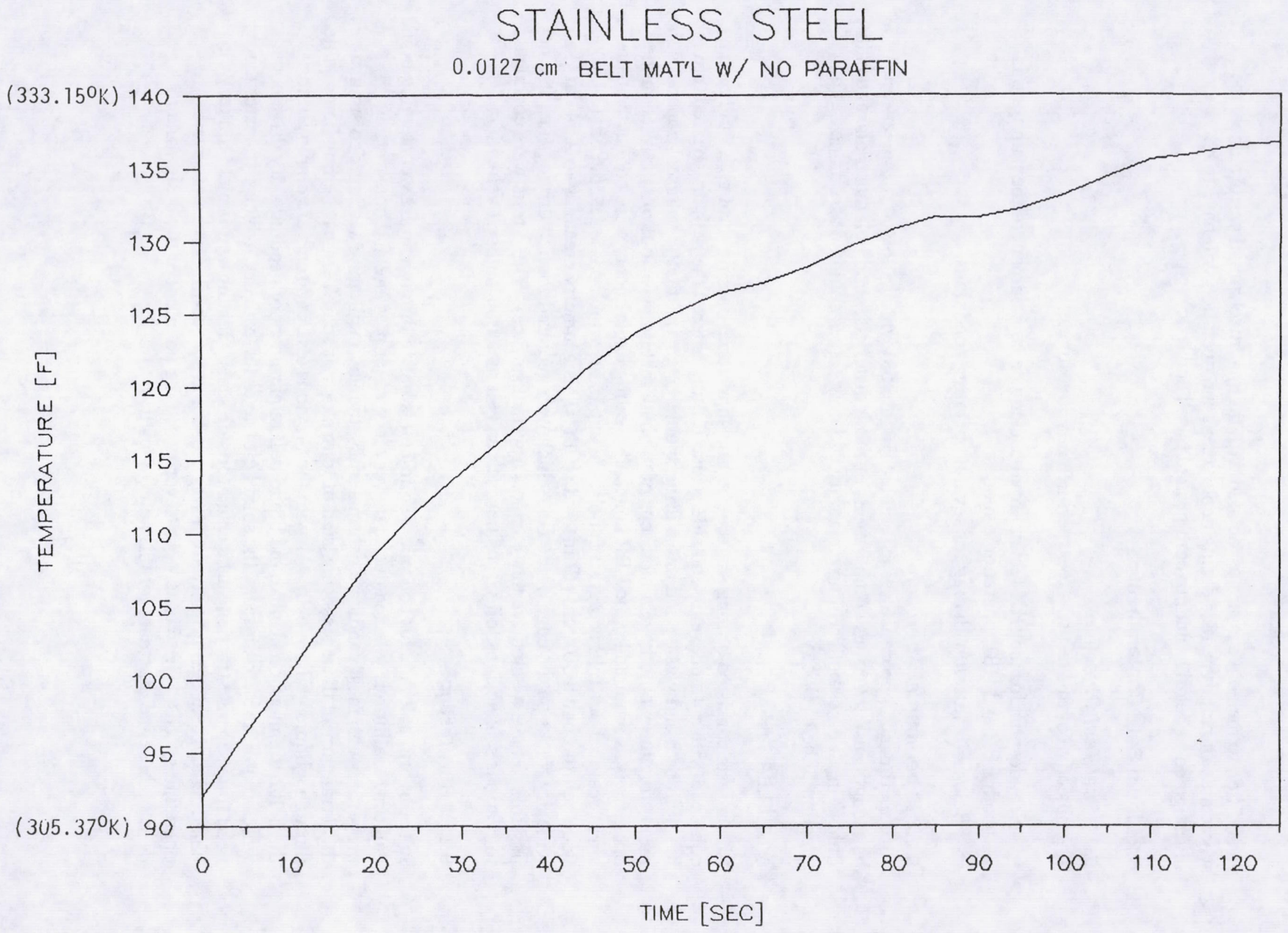

Figure 57: Temperature vs Time Plot of Solid Belt Structure

In addition to the above issues associated with thermal/mechanical performance, the whole area of belt dynamics during deployment and operation will have to be investigated in detail including both ground based and space experiments.

6.2 Liquid Bath Containment

6.2.1 Seal Test Objective

The objective of this test was to experimentally investigate:

- Seal designs for the IHX which provide adequate containment of the bath fluid in both LBR and HBR operational modes;
- Belt/seal and belt/bath drag for several operating conditions.

6.2.2 Experimental Approach

An experimental apparatus was assembled (Figure 58) which allowed for linear tests of belt lengths using various combinations of mesh materials, solid belt materials, and bath fluids. In all cases both sealing capability and drag forces could be ascertained as a function of belt velocity.

6.2.2.1 LBR Testing

Linear tests consisted of long strips of belt mesh material passing through a fluid bath equipped with entrance, exit, and side seals. Belting entered the bath dry, passed through the fluid bath and was wound into a drive spool. Upon exiting the bath/seal apparatus the mesh structure would have a meniscus of the bath material (various oils) formed in the open areas as required by the LBR concept. Sealing experiments were conducted using a small scale (about 1/10 actual size) belt/seal apparatus which passed a 35.6 cm (14 in) wide belt through a 30.4 cm (12 in) wide bath. This geometry created two 2.54 cm (1 in) wide dry tracks on the edge of the belt which were required for belt driving (i.e., it is not possible to have a belt drive that contacts a wetted surface). These tests were conducted for various seal designs, oil viscosities, screen belt materials and belt velocities.

6.2.2.2 HBR Testing

In the hybrid belt radiator concept, a solid belt is pulled through an IHX containing liquid gallium. Gallium is selected due to its very low vapor pressure and non-wetting properties with most candidate belt materials, thereby facilitating sealing. To simulate this arrangement these tests consisted of long strips of solid Teflon® belting being pulled through a liquid gallium bath. As with the previous test, end seals are employed to seal the belt/bath interface. Unlike the liquid belt requirement of needing a dry drive edge which requires side bath seals, the solid belt leaves the bath dry, which eliminates the need for a separate traction surface and for side seals. Testing was limited to measuring belt drag and seal performance for a single belt and seal configuration at several operating speeds. These tests were to verify sealing potential of the design and to develop baseline drag data for this new geometry.

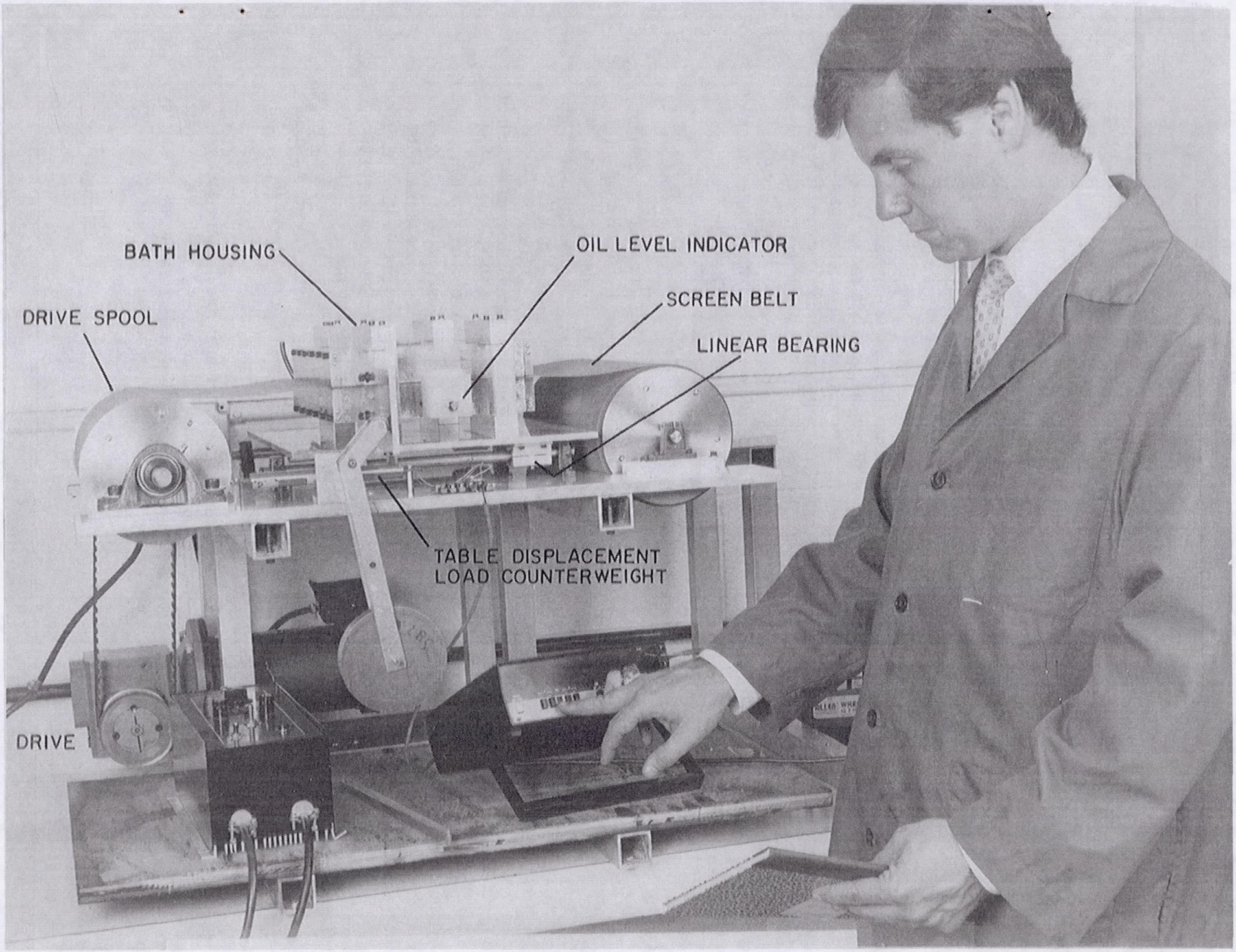

Figure 58: Seal Test Apparatus

6.2.2.3 Experimental Apparatus

The seal test apparatus constructed for seal test experiments is shown in Figure 58. The device consisted of belt drive subassembly, a load cell for determining belt/bath/drag, and liquid bath with seals.

The apparatus power spools the belt material stored on the right hand spool through the bath and bath seals and around the driven left hand spool. To produce a constant belt velocity, the power spool was driven by speed controlled D.C. motor with a gear box reduction before the timing belt drive to the spool. The storage spool was supported on instrument quality bearings to minimize belt drag not related to seal or bath interactions. The fluid bath was supported on a low friction linear bearing subassembly, which permitted the use of dead weight load to measure the reaction force generated by belt drag. Figure 59 presents the free body of the bath and load cell, and the load cell geometry. By measuring the displacement of the dead weight by means of linear potentiometers (with its wiper attached to dead weight pivot arm), the combined seal/belt and belt/fluid drag was determined. The friction in the linear bearing unit was measured at 0.76 N (0.17 lbf). The bath was constructed such that the upper bath housing was supported and the belt could slice through the entire bath. This bath support system was required since a LBR concept required a belt with a liquid wet region and dry edges for belt driving. Figure 60 shows the unit configured for liquid belt testing.

6.2.3 Test Conditions

The liquid belt seal tests used the test apparatus described in Section 6.2.2.3. Sealing performance and drag load measurements were made for various combinations of working fluids, screen types and seal geometry. Tests were conducted for several belt speeds and seal preloads. Working fluid characteristics, screen geometry, and belt speeds were selected to match potential geometries to be used in a space system.

The liquid belt concept relies on a very low vapor pressure organic material as the heat transfer fluid. Fluid such as SANTOVAC-6 diffusion pump oil has been suggested as a likely choice for this radiator concept. This diffusion pump oil is very expensive and not practical for bench top seal experiments where leakage and fluid loss were likely. To simulate these products, gear oil of the appropriate weight was chosen to match the viscosity of SANTOVAC-6 like materials in the space environment. It was determined that 80W SAE oil was appropriate for fluids with 200 to 400 cSt kinematic viscosity and STP oil treatment was reasonable for the very viscous fluid choices.

Using oils with similar densities and viscosities as compared to the more exotic flight candidates maintained the necessary Reynolds number similarity between the test conditions and likely space configurations.

Screen materials were chosen to simulate the 90% or greater void requirement for a LBR. Void space is defined as a ratio of open space to total area. The 8 mesh fiberglass screen has a void percentage of about 95% and the 16 mesh screen has a void ratio of roughly 0.9. The 8 mesh screen was labeled Type 1 belt and the 16 mesh belt was called Type 2.

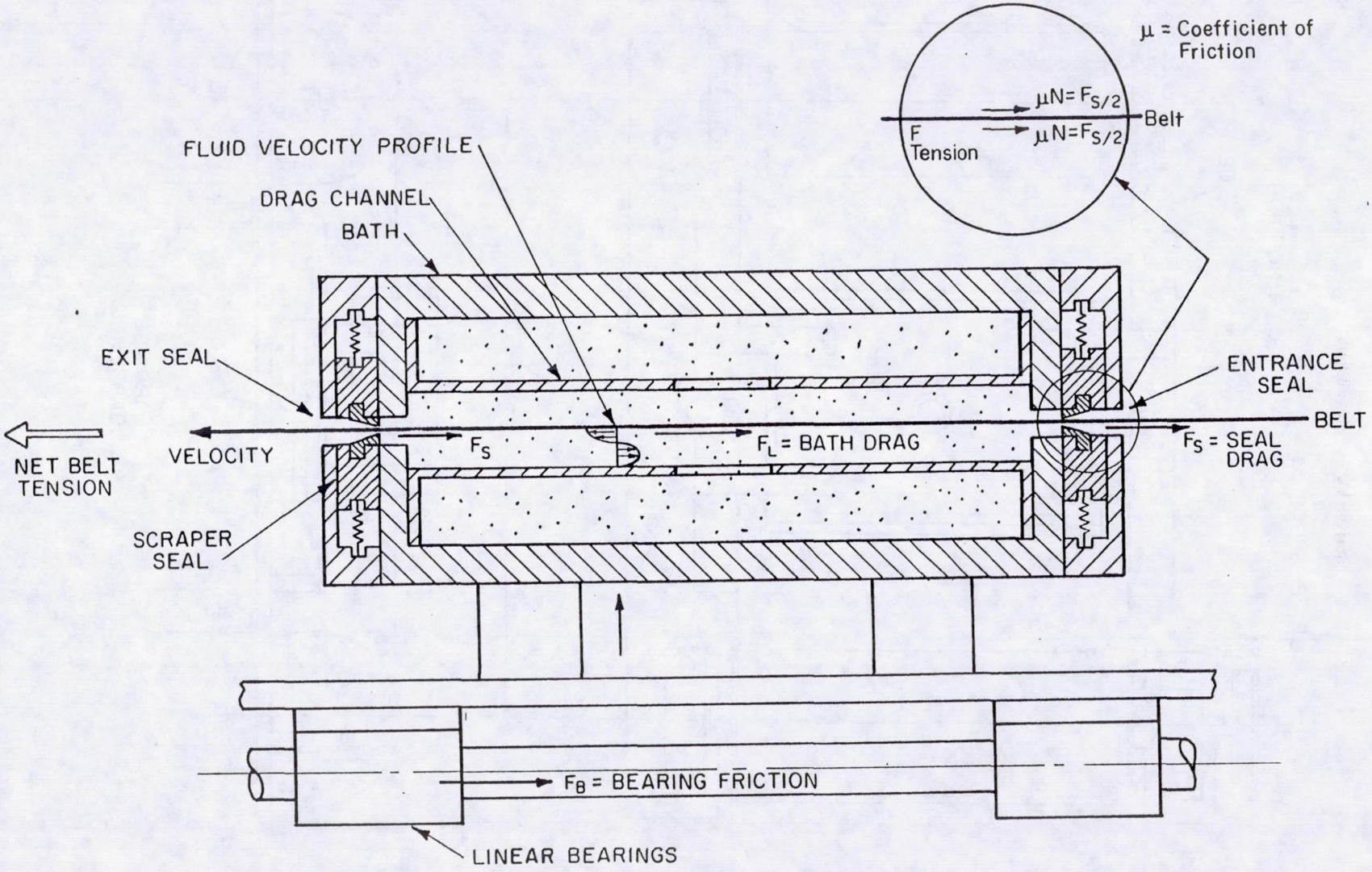

Figure 59: Schematic Belt/Bath Geometry with Drag Loads Noted

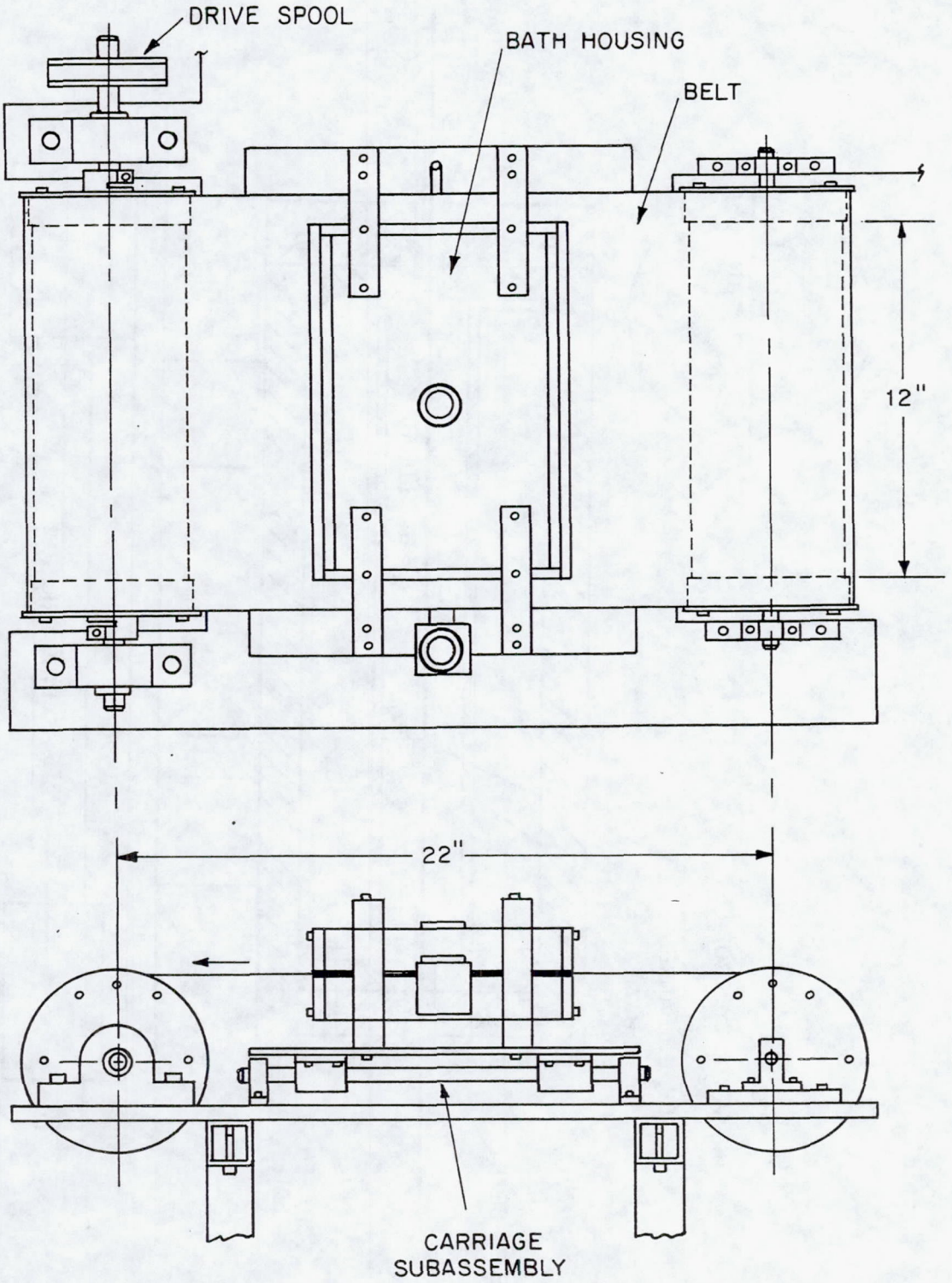

Figure 60: Seal Test Rig in Liquid Belt Configuration

In addition to the void ratio difference between the test screens, the two screens presented a different contact area to the end seals, which results in a larger belt/seal drag for a given belt velocity, seal design and preload.

Seal designs selected for testing were as follows:

- Side seals - clearance seals;
- End seals - scraper seals;
- End seals - scraper seal and clearance seal.

Figures 61 and 62 show the bath container with the various seal configuration. Cross-sections of the seal choices are presented in Figure 63.

6.2.3.1 Liquid Belt Test Results

The liquid belt tests were conducted for several seal designs, fluids, and belt materials. A summary of the test data are presented in Table 10. Seal leakage performance was characterized as very good with end seals controlling fluid deposition onto the belt to a thin layer, and the side seals preventing oil flow to the belt edges. Figure 64 shows initial liquid deposition on the belt with a thin, nearly transparent oil film created. Figure 65 shows steady state seal operation with both side and end seals controlling oil wetting of the belt.

Table 10: Test Results for Liquid Belt Tests

Test Condition (Fluid and Belt)	End Seal Type	(per Seal) Seal Preload (End)	Side Seal	Ave Drag Load (lbf)		
				0.638 ft/sec	1.300 ft/sec	2.000 ft/sec
STP on Belt Type 1	Teflon Scraper	2.28 lbf 0.014 wire	Clearance 1/8 in Teflon®	6.8	--	9.3
80W on Belt Type 1	Teflon Scraper	2.28 lbf 0.014 wire	Clearance 1/8 in Teflon®	2.6	--	4.5
STP on Belt Type 2	Teflon Scraper	2.28 lbf 0.014 wire	Clearance 1/8 in Teflon®	5.6	--	9.1
80W on Belt Type 2	Teflon Scraper	2.28 lbf 0.014 wire	Clearance 7/8 in Teflon®	3.1	3.9	5.1
80W on Belt Type 2	Teflon Scraper	4.92 lbf 0.018 wire	Clearance 1/8 in Teflon®	4.8	5.5	6.2
80W on Belt Type 2	Teflon Scraper and Teflon Rod	4.921 lbf (0.018 wire)	Clearance 1/8 in Teflon®	4.85	5.5	6.5
Dry on Belt Type 2	Teflon Scraper and Teflon Rod-Clear	4.92 lbf (0.018 wire)	Clearance 1/8 in Teflon®	4.5	4.5	4.8
STP on Belt Type 2	Teflon Scraper and Teflon Rod	4.92 lbf (0.018 wire)	Clearance 1/8 in Teflon®	9.1	>10.0	>10.0

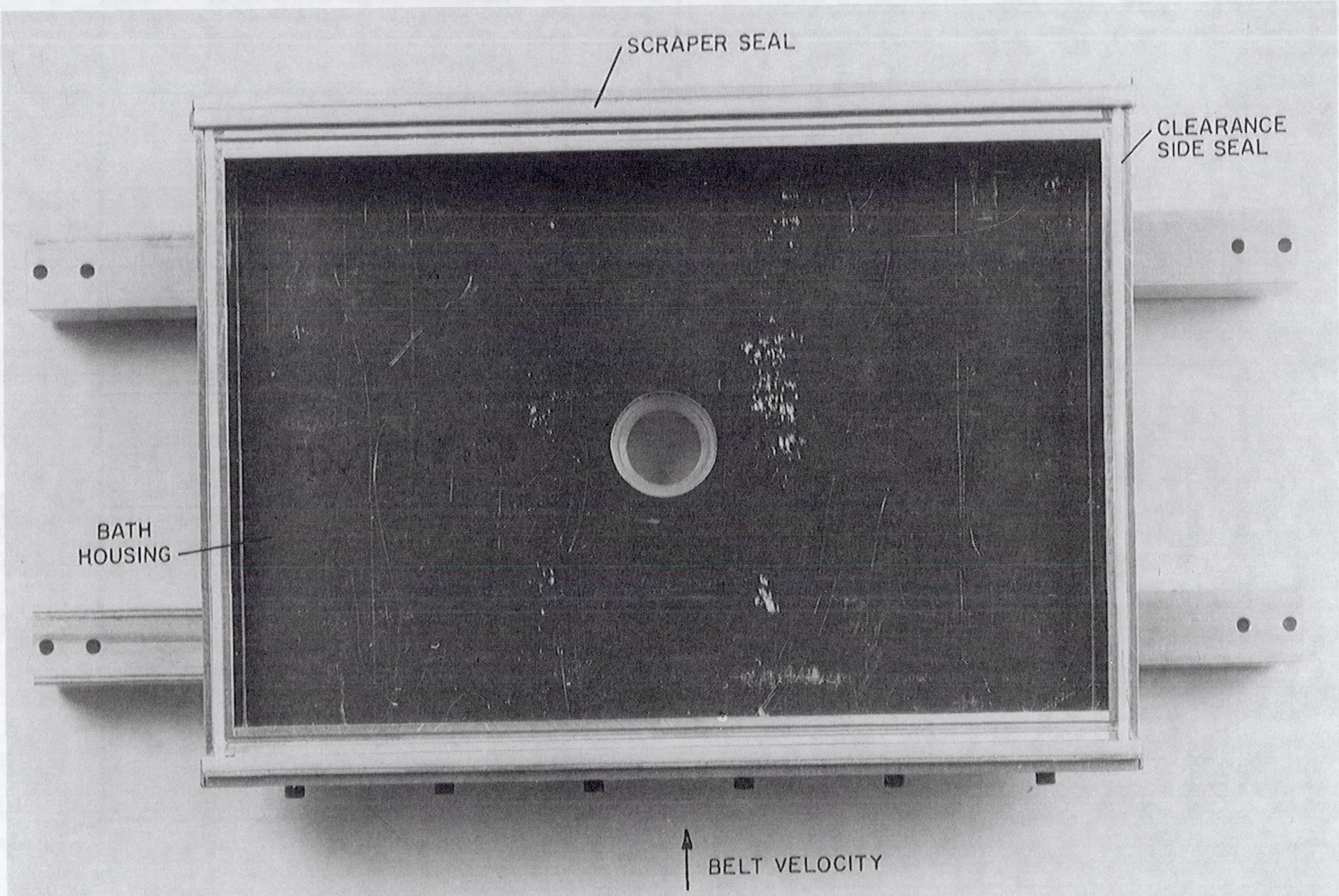

Figure 61: Liquid Belt Bath Sealing Geometry Using Scraper and Clearance Side Seals

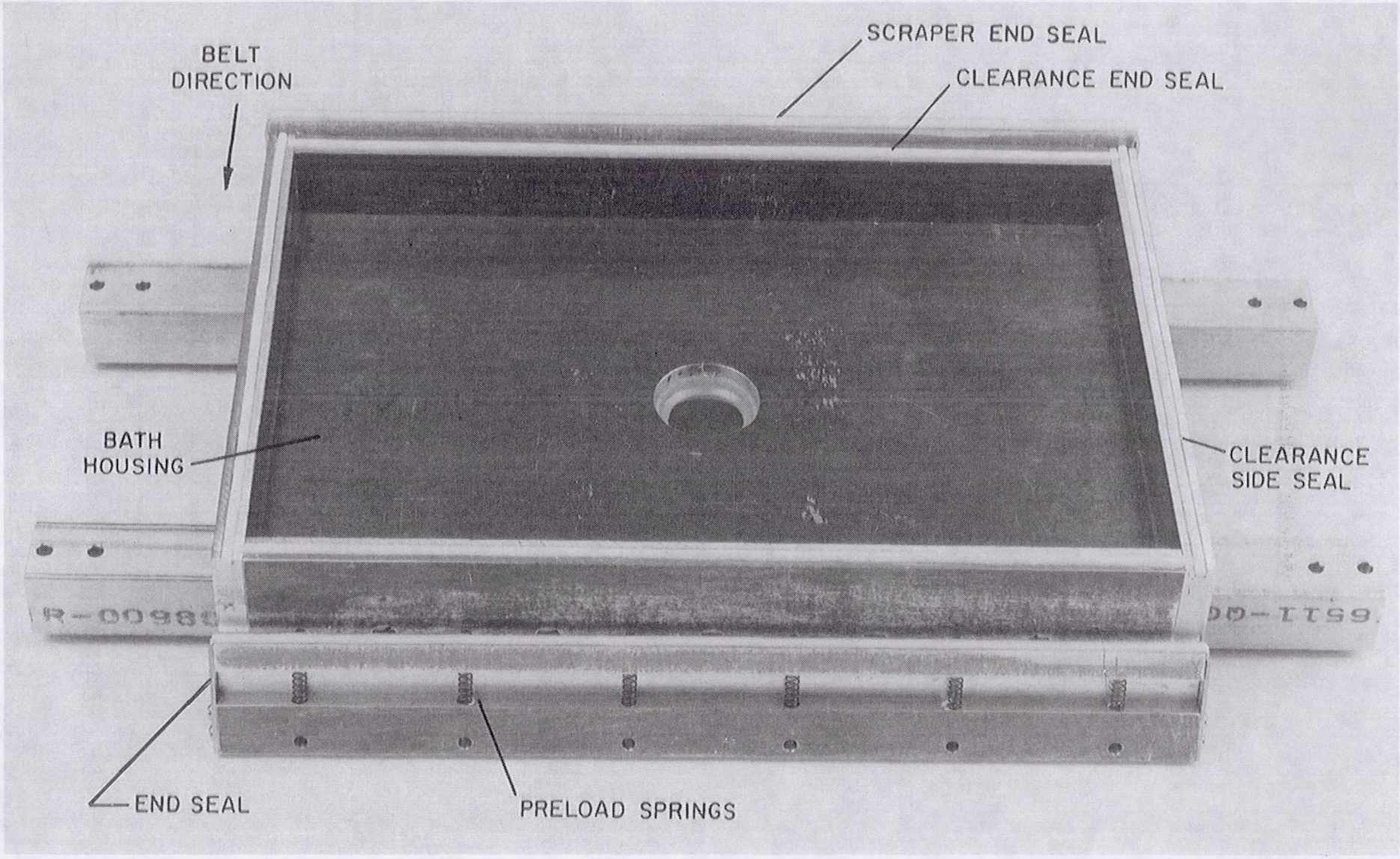

Figure 62: Scraper and Clearance End Seals with Seal Rod Preload Load Subassembly

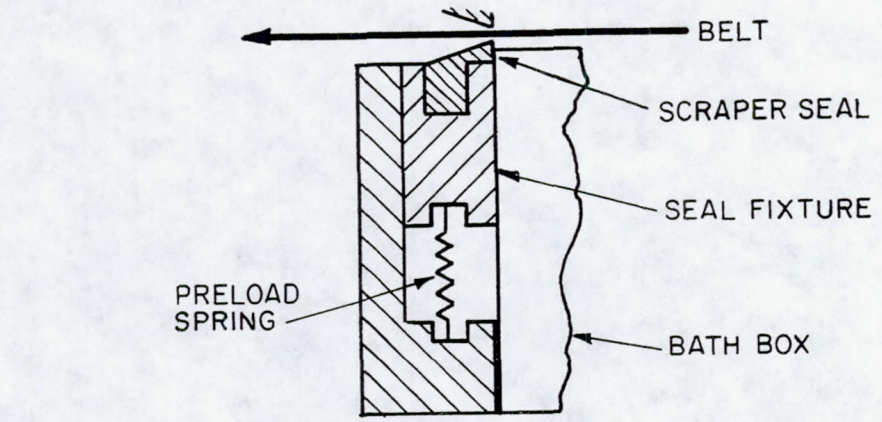

(a) SCRAPER END SEAL

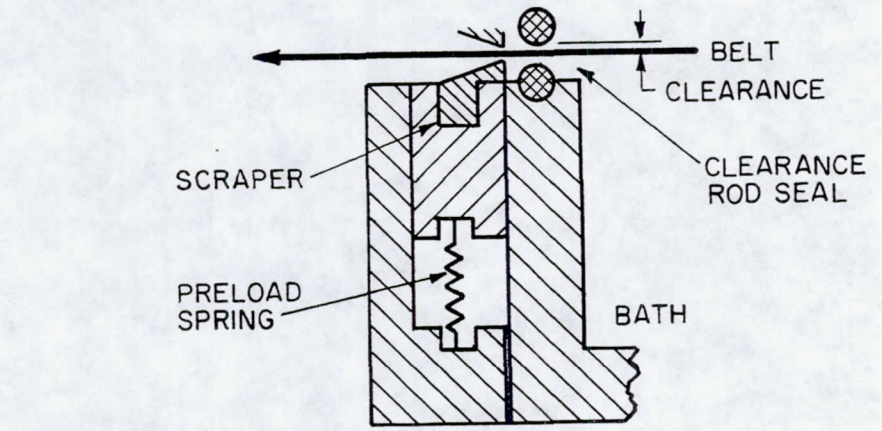

(b) SCRAPER AND CLEARANCE END SEAL

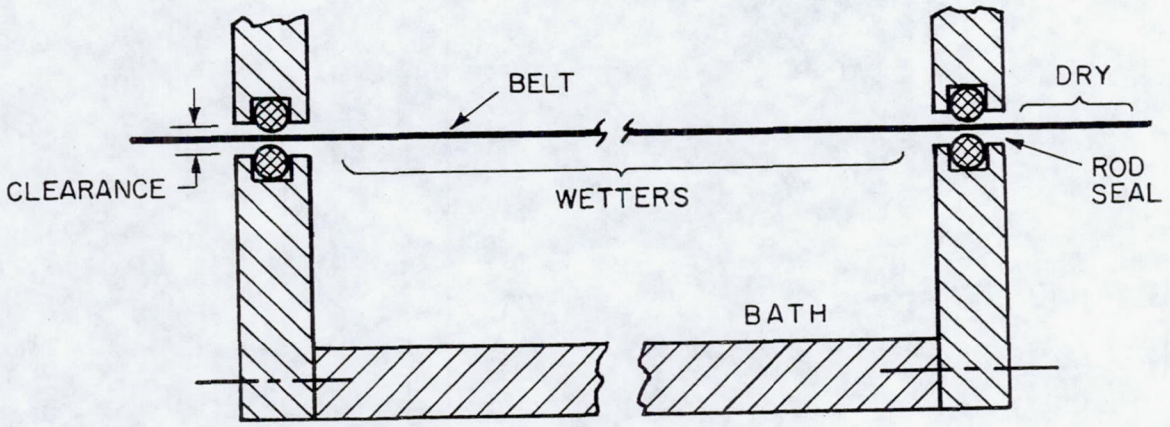

(c) CLEARANCE SIDE SEAL (End View)

Figure 63: Cross Sections of Liquid Belt Seals

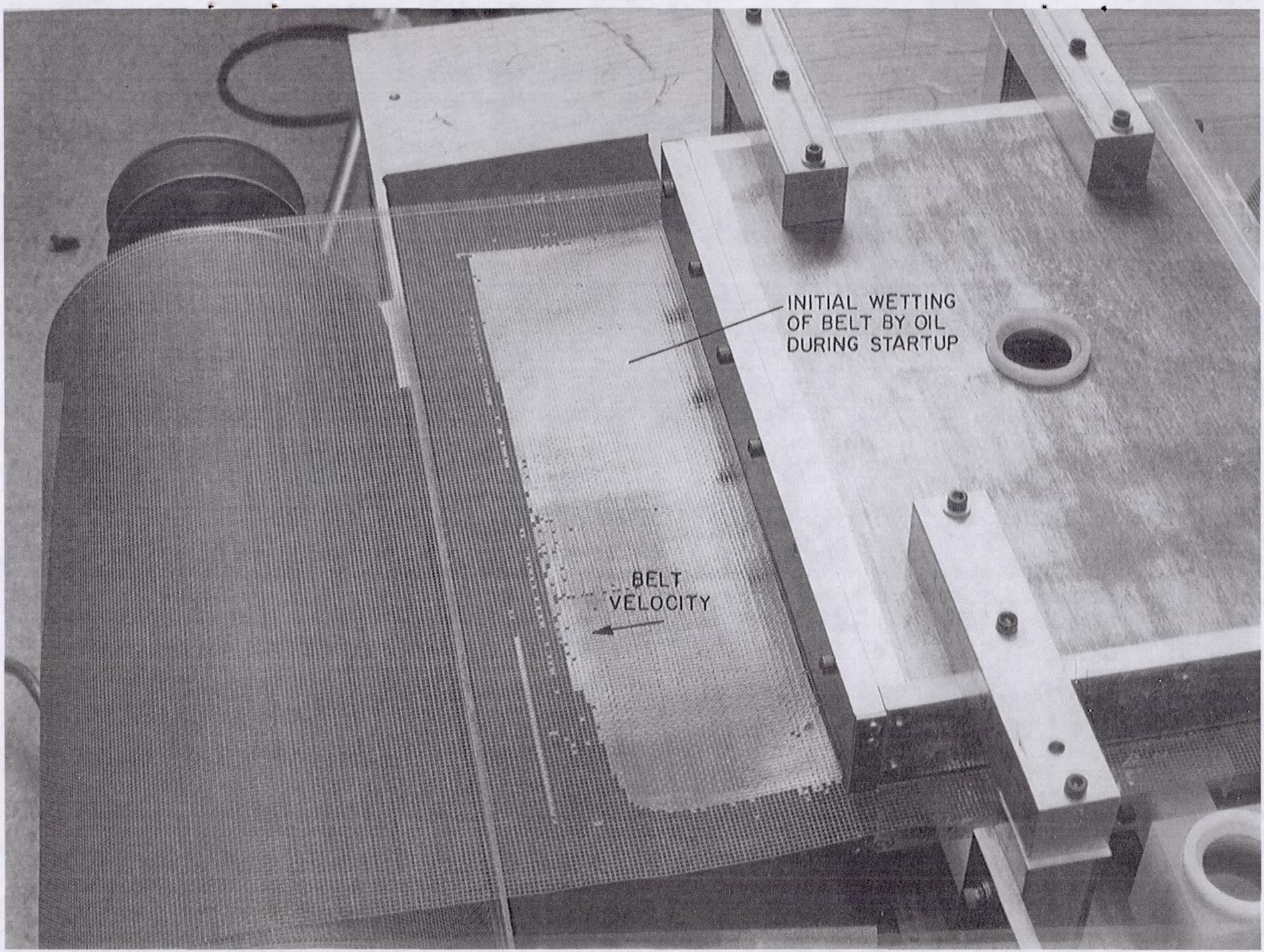

Figure 64: Liquid Belt Seal Test - Start-Up Condition Using Scraper End Seal

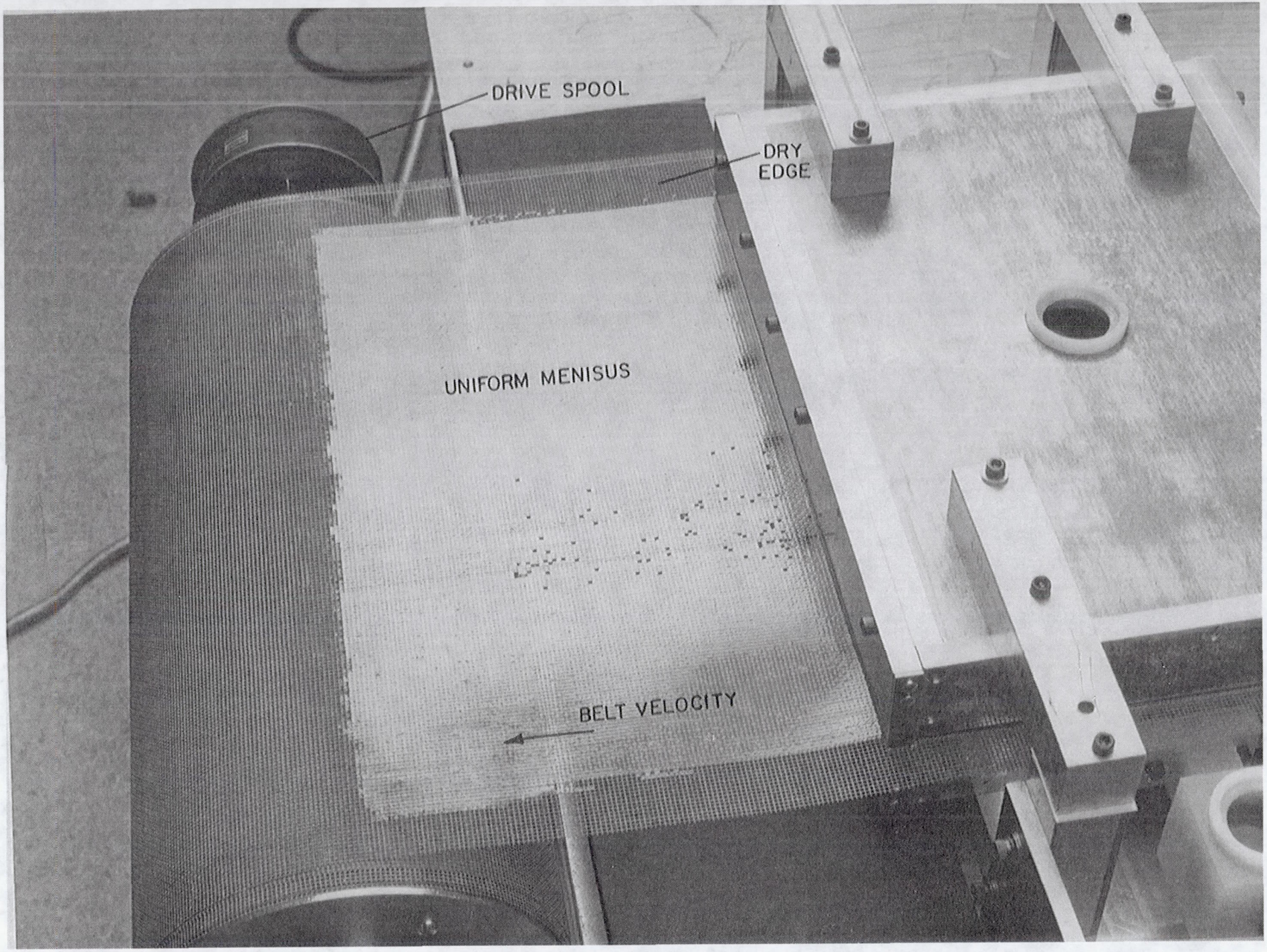

Figure 65: Steady State Wetting of Screen Belt Material (Note: Dry Edge Belt Edge)

*Type 1 (8 mesh fiberglass screen); Type 2 (16 mesh fiberglass)

Test observations were as follows:

1. Scraper seal design works very well;
2. Oil menisci tend to droop under 1-g loading preventing laboratory continuous belt testing with oils on screen belts;
3. Clearance side seals work very well given that leakage path was normal to the bath flow direction;
4. Scraper seal preloads loads must be at least 0.7 N/cm (0.4 lbf/in) of seal length to maintain solid contact between belt and seal;
5. The combination of scraper and clearance end seals did not perform better than the single scraper seal;
6. Drag load is dominated by seal friction at these modest velocities;
7. The large mesh belt, Type 1, produced slightly lower drag results as compared to the finer mesh (Type 2) belt.

6.2.3.2 Correlation With Seal Drag Model

A schematic of a simplified belt/bath drag model is shown in Figure 59. This model lumps all belt and bath interactions into coulomb seal/belt friction and a viscous belt/fluid drag. As indicated by the free body diagram shown in Figure 59, the total drag force can be expressed as:

$$F_{drag} = (\mu_s \eta_s N_s)_{seal} + \left(\mu_l \eta_l \frac{V}{A}\right)_{liquid}$$

where:

μ_s = coefficient of friction between belt and seal
η_s = number of seals
N_s = normal seal load
η_l = number of sides in contact with liquid
μ_l = liquid viscosity
V = belt viscosity
η = liquid depth
A = wetted surface area

For the liquid belt analysis, the side seals are neglected since these are clearance seals with very small wetted areas and they contribute little to the drag. The accuracy of analysis is dependent on the assumed coefficient of friction between contact seal and belt as well as the assumed oil viscosity.

This analysis does predict the correct trends and magnitudes of seal drag. Table 11 compares experimental data for 80W oil on Type 2 belt with predicted drag loads based on experimental geometry. In one case the predicted loads are less than the experimental

values, and for the higher preload case, the analysis predicts a slightly larger load. These differences are likely due to a difference in oil viscosities between experimental and an assumed average oil viscosity used in the analysis.

Table 11: Comparison of Experimental Belt/Bath Data to Model Prediction

	Seal Preload (lbf)	Belt Velocity (ft/sec)	Drag (lbf)	
			Experimental	Predicted
1. 80W oil with Type 2 Belt with Scraper Seal	2.3	0.64	3.1	2.9
		1.3	3.9	3.5
		2.0	5.1	4.1
2. 80W oil with Type 2 Belt With Scraper Seal	4.9	0.64	4.9	5.6
		1.3	5.5	6.1
		2.0	6.5	6.8

Analysis Assumptions:
Oil viscosity = 0.638 lbf/ft-sec
Coefficient of friction = 0.25 Teflon scraper on fiberglass screen
Bath depth = 0.94 cm (0.031 ft)
Wetted area = 0.06 m^2 (0.66 ft^2) (one side)

Conversions
m/sec = 0.3 ft/sec
N = 0.22 LVD

6.2.4 Hybrid Belt Sealing Tests

The hybrid belt radiator concept uses a liquid metal bath to transfer heat to a solid radiator belt which moves through the fluid. In this approach, the hot belt must be dry as it leaves the bath which requires a belt/bath sealing system that completely confines the fluid to the bath. To explore the solid belt/liquid metal sealing requirements, two groups of experiments were performed:

- Bench top experiments;
- Solid belt tests using the seal test apparatus.

Bench top experiments were screening tests which evaluated several different seal designs. The most promising approach found in the bench top work was incorporated into formal tests conducted with the seal test apparatus.

6.2.4.1 Bench Top Experiments

These experiments have the primary objective of quickly evaluating seals for the gallium solid belt concept. As such, these were hand operated experiments where a belt was pulled through a small gallium bath which was fitted with different seals. The outcome of this work was to determine the most promising seal technique by visual inspection for gallium leaks past the prototype seals.

A typical setup is shown in Figure 66, where a Teflon® belt roughly 6.34 cm (2.5 in) wide is pulled through a gallium bath heated to roughly 38°C, and past a single set of seals.

Three types of seals were investigated:

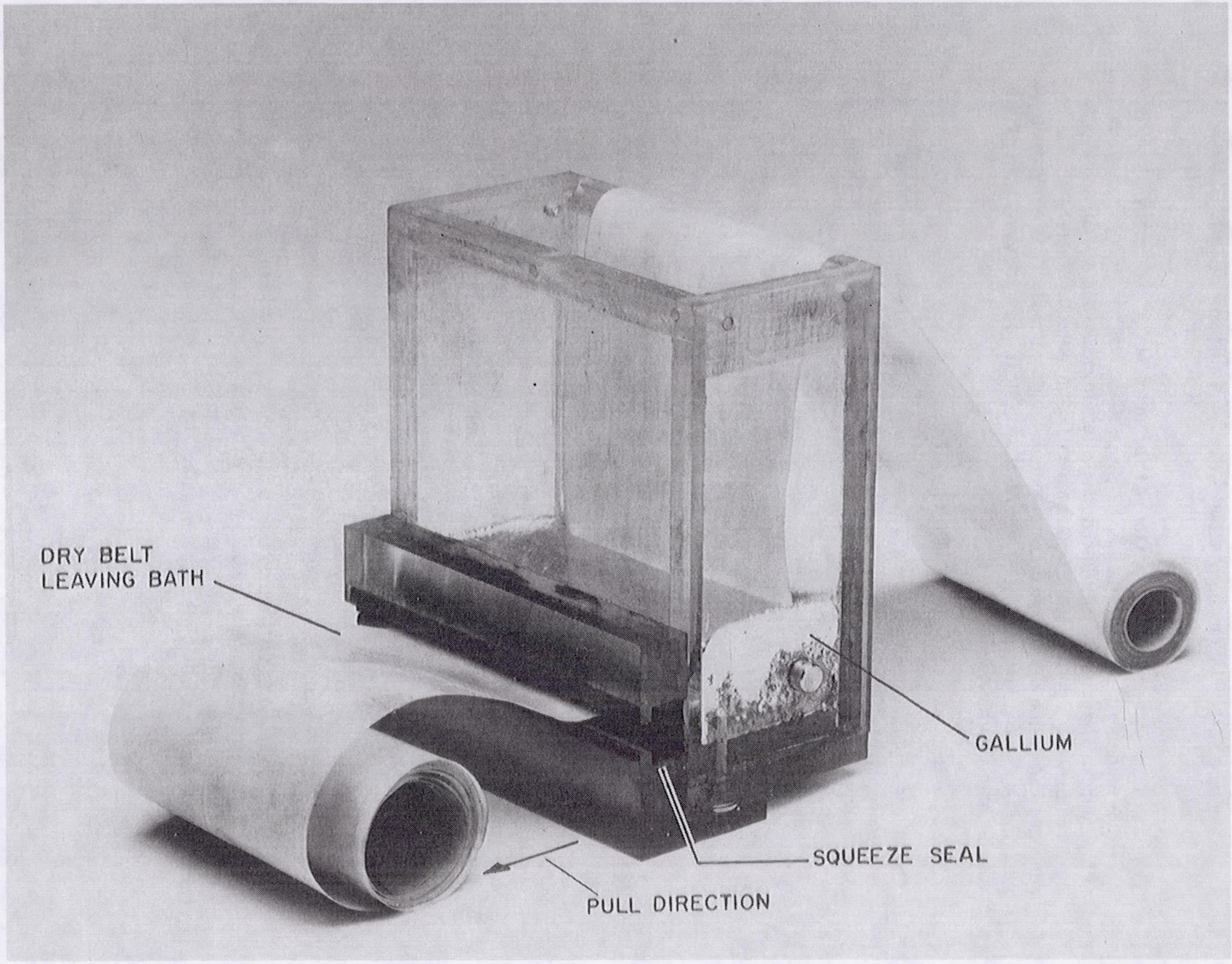

Figure 66: Solid Belt/Gallium Bench Top Test Set-Up

- Scraper Seal - Teflon® material with 20° chisel point
- Clearance Seal - 0.005 inch gap created by a 1/6 inch diameter Teflon® rod seal.
- Squeegee Seal - Closed cell foam strips.

The scraper and clearance seals were found to be unacceptable in that they allowed small quantities of the nearly inviscid gallium to escape as the belt was pulled through the bath at low speeds. The scraper seal allowed the gallium release when a small gap was produced between a portion of the seal and the 0.005 inch thick Teflon® belt. The squeegee seal design showed excellent potential. This seal consisted of a 0.95 by 0.64 cm (0.375 by 0.25 in) cross section closed cell foam strips (a 3M product) with its skin coat in contact with the belt.

6.2.4.2 Solid Belt Tests Using Seal Test Apparatus

The squeegee seal design was selected from solid belt/gallium tests using the modified seal test apparatus. The test rig was modified to hold a plexiglass gallium bath fitted with pairs of squeegee seals as shown in Figure 67. Both dimensions were as follows:

- Belt width of 15.9 cm (6.25 in);
- Wetted surface of belt 15.9 by 10.2 cm (6.25 by 4 in);
- Gallium depth above and below belt of 0.43 cm (0.17 in);
- Seal length of 17.8 cm (7 in); and
- Seal compression of 0.25 mm (0.010 in).

As indicated in Figure 68, the solid belt approach does not require side seals since the belt exits the bath dry and it could be driven by a system that contacts the heat transfer surface of the belt radiator. The end seals are wider than the belt and squeeze together at the belt edges to form the necessary side seal.

As with the liquid belt experiments, the gallium/solid belt tests were conducted as linear tests which passed long strips of the Teflon® belt through the apparatus. Since this was a dry belt design, the entrance and exit bath seals see the same conditions for a linear run and a continuous belt run. These tests were conducted as follows:

- Entire apparatus heated to roughly 41°C (105°F);
- The belt pulled through the bath at different speeds for single bath seal preload;
- The drag force recorded for belt velocity; and
- Leakage seal performance noted.

Results of the seal drag tests are presented in Table 12. The seal preload was 13.8 N (3.1 lbf) for foam strip compressed by 0.25 mm (0.010 in) from its free height. The sealing performance was excellent with no leakage past the seals for the speeds tested. Figure 69 shows the clean belt leaving the gallium bath.

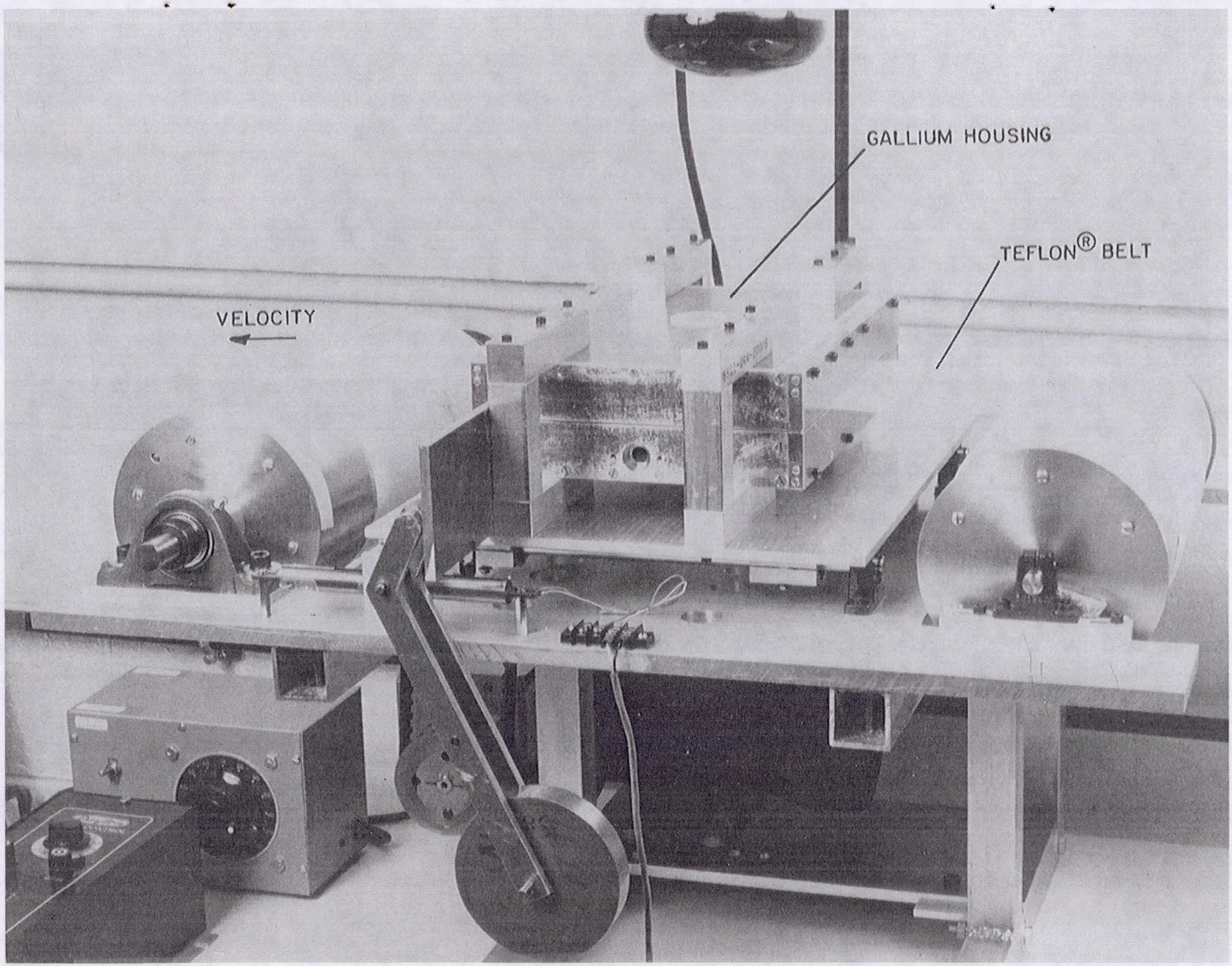

Figure 67: Solid Belt And Gallium Bath Test Apparatus

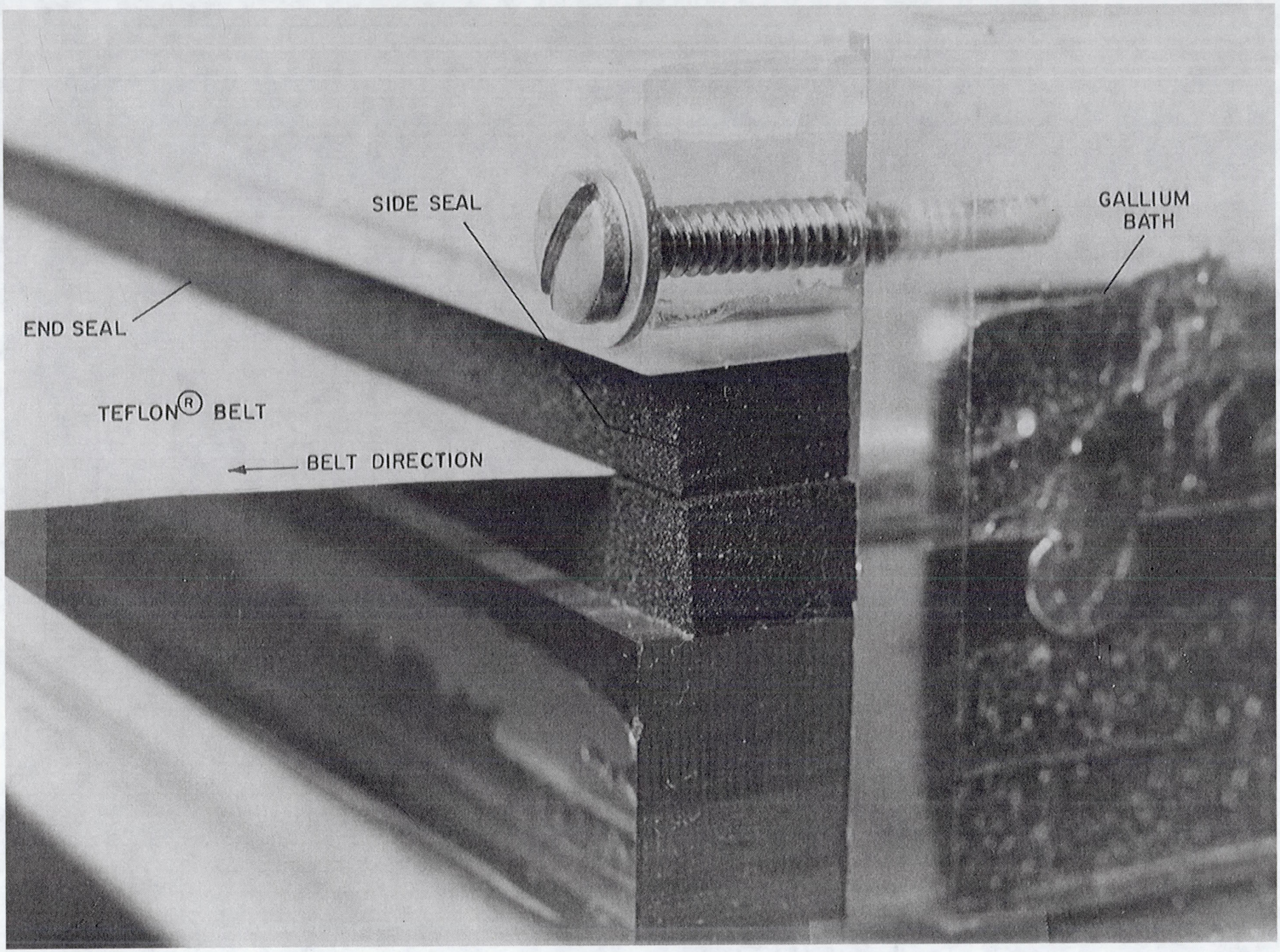

Figure 68: Solid Belt End and Side Seal

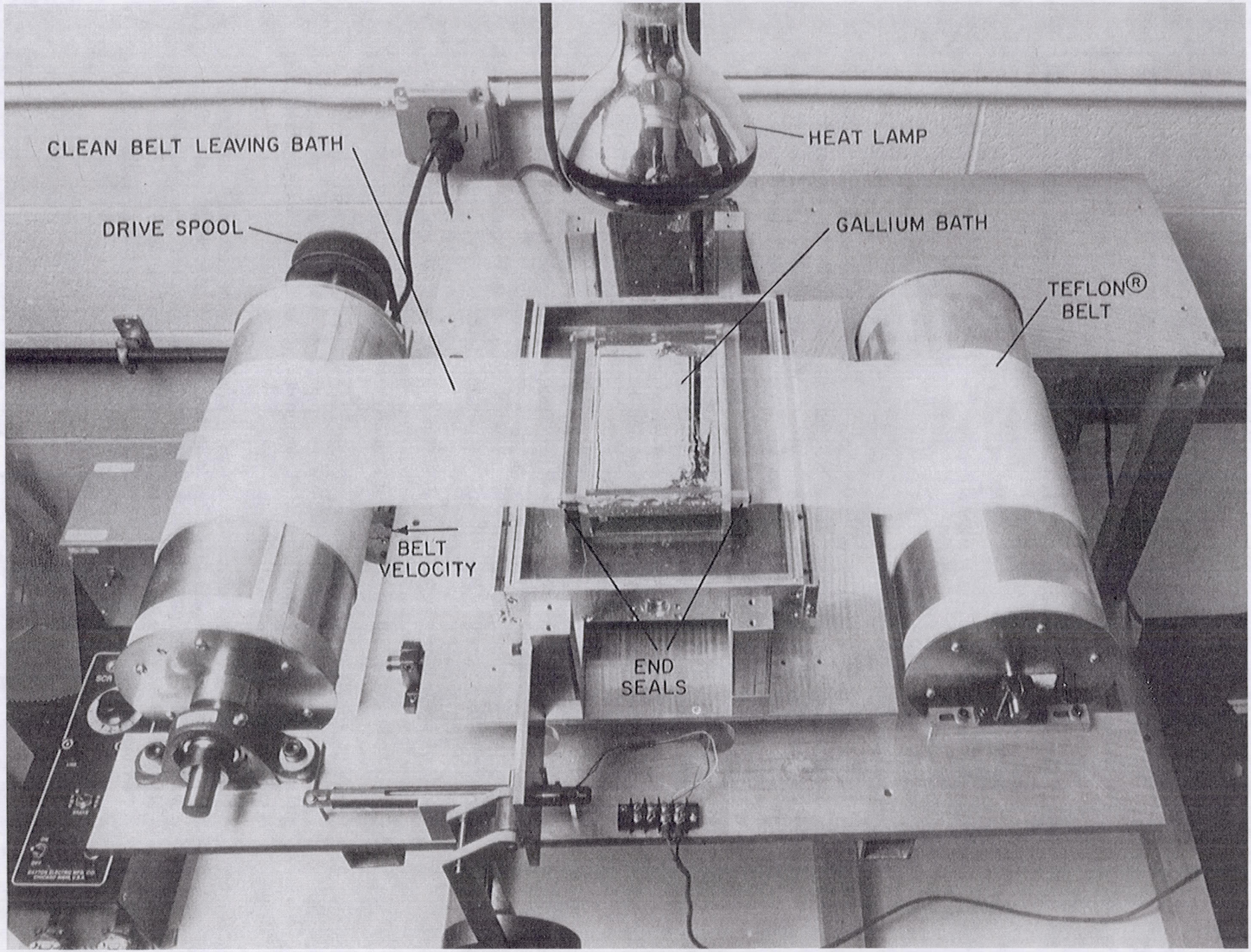

Figure 69: **Belt Passing Through Gallium Bath and Seals with a Clean Belt Exiting Bath Subassembly**

Table 12: Drag Loads for Gallium and Solid Belt Tests

Belt Velocity (ft/sec)	Seal Preload (lbf)	Ave Drag (lbf)
0.64	3.1	1.4
1.3	3.1	1.7
2.0	3.1	2.5

Wetted area of belt - 2.0 x 0.173 ft^2
Bath depth - 0.17 ft
Temperature - 105°F
Seal Stiffness - ≈52 lbf/inch of seal per inch of deflection

Conversions: m/sec = 0.3 ft/sec
N = 0.22 Lbf

6.2.4.3 Correlation with Model

The drag model presented earlier was compared to solid belt/gallium results. This model assumed coulomb friction between the belt and seals and viscous drag between belt and bath fluid. Since liquid gallium is nearly inviscid with a viscosity of 5.5×10^{-4} N-sec/m (1.8 CP), the model reduces to a seal friction model with a constant seal induced drag of 5.3 N (1.2 lbf) for all velocities tested. This analysis assumed a coefficient of friction between belt and seal of 0.10 which is typical for a smooth dry Teflon® surface in contact with another smooth polymer surface. The model does predict the correct magnitude of drag but not the appropriate trend with velocity. The experimental results show an increasing drag load with velocity which implies that the drag model for the seal should be a combination of viscous and coulomb friction.

6.2.5 Conclusions

Task 2 results indicate that both the liquid belt and solid belt radiator configurations can be appropriately sealed. The liquid belt bath sealing system produced the desired belt wetting while creating dry belt edges necessary for belt traction. The solid belt/liquid metal bath seals required to implement the hybrid belt concept produced excellent results by completely containing the gallium within the interface exchanger bath as the belt passed through the bath at speeds up to 0.6 m/sec (2 ft/sec). Drag loads induced by the seal/belt and belt/bath were very small with maximum drag loads that would scale up to 268 W power requirement for a 3 m (10 ft) wide liquid belt operating at 0.6 m/sec (2 ft/sec) and 134 W belt drive power for similarly scaled solid belt/gallium system.

Drag loads were found to be a strong function of belt velocity, fluid viscosity, seal preload, and belt/seal contact conditions. A simple drag model was developed and it predicted correct drag loads in terms of magnitude and trends for different belt materials, fluids, belt speed and seal preloads.

Task 2 results indicate that reasonable sealing systems for the different belt radiator designs are possible and that these belt/bath seals can produce excellent seal performance with low drag. This work does not represent an optimum solution to belt/bath containment but rather was the first experimental look at this issue. These results indicate that the potential for an effective seal for a full scale radiator is high.

7.0 Conclusions

All of the results and conclusions are detailed throughout this report in the specific sections that describe the various tasks. Following are the results that are of the most significance for future MBR development. These include:

- The scalability of a MBR is largely a function of the IHX working fluid. This is due to the emissivity (in the case of a LBR) and the performance of the working fluid in the IHX. In the case of a SBR or HBR the emissivity of the belt itself plays a large part of the scalability of the system. Tin and liquid metals demonstrated preferred working fluids characteristics. The ability of the metals to transfer heat to the belt were superior to the organics that were tested. When the system was examined as a whole these metals allowed the design of a MBR system with superior performance. The organics did, however, have higher emissivities but this characteristic was offset by the lower performance as an IHX working fluid.

- Hybrid systems that use phase change materials would likely be the most effective and provide the highest specific heat. A HBR could benefit from the metals in the IHX and would not have the losses associated with a LBR. In addition, the use of a phase change material in the belt would increase its heat capacity and would allow for a smaller belt and a slower speed. The fabrication of a hybrid belt was demonstrated in this series of tests.

- Increasing speed or belt stiffness improves belts resistance to failure modes. Based on the dynamic analysis using BERS, a belt that has a higher stiffness will be able to withstand perturbations and maneuvers. Two methods were identified to achieve the higher stiffness: 1) use a belt with inherently higher stiffness (thicker belt materials, higher modulus of elasticity, etc.); 2) increase the belts rotational speed.

- Based on the table top dynamic testing and the BERS analysis, a 1-g acceleration perpendicular to the axis of the belt forces the belt into an oblong shape. This provides a limiting acceleration for all the belts that were tested. The limits at which a belt would deviate from the optimum circular shape were examined for a limited number of belt configurations.

- It was demonstrated on the KC-135 that a belt can be deployed from the stowed configuration into a circular shape. The belt must be made of a material that has no memory of the stowed shape. If the belt does maintain a memory, the drive system must be designed to accommodate the shape.

- Perturbations have minimal affect on belts in reduced gravity. Several types of perturbations were imposed on rotating belts during the table top dynamics testing and in the KC-135 testing. It was observed that if a belt is perturbed it will return to its original shape within a couple of revolutions. Starting in reduced gravity is possible as demonstrated in the KC-135 testing.

- An IHX using gallium as the working fluid can be designed such that no gallium will be lost from the IHX. The use of scraper and clearance seals on the IHX will contain the gallium.

- The parasitic losses resulting from the IHX drag forces are minimal. Also, the parasitic losses are not proportional to the belt speed. This allows the design of MBR systems with faster moving belts to improve the belt stiffness and to control the heat dissipation without affecting the parasitic losses.

Based on the results of the testing and analysis that was conducted, no obvious technology hurdles are apparent. All of the components that were tested performed as expected.

Additional tests could further prove the performance of the MBR systems. This additional testing should include further KC-135 testing, larger scale benchtop tests that includes several components together, and a longer term shuttle or space station testing. A full MBR system should be tested and the only way to fully test the systems is in microgravity.

8.0 References

1. Liquid Belt Radiator Design Study, NASA Contractor Report 174901, January 1986
2. Buch, R.R., and Hantress, A.R., Organo Siloxane Workiong fluids for the liquid Droplet Radiator, NASA CR-175033, December 1985.
3. Lallman, F.J., "Vibration Characteristics of a Steadily Rotating Slender Ring," NASA Technical Paper 1775, NASA, December 1980.
4. Performance Characteristics of Moving Belt Radiators, D. McFadden and W.P. Teagan, Arthur D. Little, Inc. IECEC 1987, Paper No. 879285.

Appendix A

April 1990 Day 1									
Parabola No.	Roller Speed (rpm)	Belt Speed (m/s)	Measured Speed (m/s)	Belt Material	Belt Thickness (mils)	Clock Start Time	Clock End Time	Test Objective	Comments
1	120	0.4		Mylar	5	--	--	initial system check	mistracked
2	120	0.4		tef-glass	5	--	--		mistracked; belt twisted prior to getting tangled
3	120	0.4		tef-glass	5	--	--		belt formed wobbly hoop, not stable; during > 1-g belt did not move, needed stiffer preload springs; belt hit separator hoop minor effects
4	120	0.4		tef-glass	5	--	--		hoop not stable; "floats around;" goes from flat vertical oval to flat horizontal oval; belt twists during motion
5	120	0.4		tef-glass	5	--	--	pert.	attempted perturbation (perturbation system did not work); belt formed wobbly unstable hoop
6	120	0.4		tef-glass	5	--	--	pert.	during perturbation slow accel. due to mechanism; belt not noticeably affected; belt had short periods of very good hoops then went unstable
7	120	0.4		tef-glass	19	--	--		belt swaying and appears as if initial up acceleration deforms belt; not stable hoop
8	120	0.4		tef-glass	19	--	--	pert.	belt swaying fore and aft; perturbation had no visible effect on belt; belt shape unchanged; belt shape not fully stable
9	240	0.8		tef-glass	19	--	--	accel.	belt shape tends to form an oblong shape but with twisting in the belt; during acceleration belt swings from left to right
10	240	0.8		tef-glass	19	--	--		forward sway in belt which causes twisting, continuously hitting guide
11	240	0.8		tef-glass	19	--	--	pert.	belt formed decent hoop and maintained it ≈13.5 sec although belt did have a twist in it; perturbation did not work

Parabola No.	Roller Speed (rpm)	Belt Speed (m/s)	Measured Speed (m/s)	Belt Material	Belt Thickness (mils)	Clock Start Time	Clock End Time	Test Objective	Comments
12	240	0.8		tef-glass	19	--	--	pert.	perturbation coincided with a disruption of the hoop which was followed by an upward acceleration lifting the belt above the drive on the right side; belt did form a hoop for a short period
13				tef-glass	19	--	--		twist in belt; started off with a good hoop although it had a twist then shifted to the left side but did not collapse the hoop
14				tef-glass	19	--	--	pert.	perturbation did not work; belt formed hoop with a twist and stabilized for most of the parabola
15				Mylar	13	--	--		belt formed a hoop but kept swaying left to right and did not stop
16				Mylar	13	--	--		belt more stable some left-right sway and twist; belt hit by crew member first time belt recovered was a mild hit, second time belt did not recover fully to original shape, third hit was late in the parabola and belt did not have a chance to stabilize; during parabola loose items in cabin floated up which would indicate an upward acceleration
17				Mylar	13	--	--		forms good hoop approximately 10 sec; mild twist then moves to left side for a couple of seconds and regains shape
18				Mylar	13	--	--		forms good hoop; test director taps belt on left side, approximately 4.8 sec to recover
19				Mylar	13	--	--		forms oval shape; test director taps belt on left side, approximately 0.7 sec to recover; second tap on stable hoop recovers almost immediately
20				Mylar	13	--	--		had items float up as did belt; formed horizontal oval then stabilized into hoop; test director tapped approximately 1.2 sec to recover; second tap approximately 0.5 sec to recover
21			1.56	Mylar	13	--	--	deploy	deployment approximately 14.2 sec; went to left side then formed good hoop and swung to right side

Parabola No.	Roller Speed (rpm)	Belt Speed (m/s)	Measured Speed (m/s)	Belt Material	Belt Thic kness (mils)	Clock Start Time	Clock End Time	Test Objective	Comments
22			1.55	Mylar	13	--	--	deploy	deployment approximately 14.4 sec; formed good hoop similar to parabola 21
23			0.78	Mylar	13	--	--	deploy	deployment approximately 9.59 sec; drive started prior to deployment; formed oval and fluctuated
24			0.77	Mylar	13	--	--	deploy	deployment approximately 10.56 sec; belt twisted then formed good hoop and stabilized
25			0.48	Mylar	13	--	--	deploy	deployment approximately 10.96 sec; formed good hoop but swayed left-right
26			0.49	Mylar	13	--	--	deploy	deployment approximately 11.84 sec; no steady state; twist in belt; hoop minor effects

April 1990 Day 2									
Parabola No.	Roller Speed (rpm)	Belt Speed (m/s)	Measured Speed (m/s)	Belt Material	Belt Thic kness (mils)	Clock Start Time	Clock End Time	Test Objective	Comments
1	302	1.00	0.99	Mylar	7	--	--		belt mistracked
2	302	1.00	1.03	Mylar	7	--	--		belt mistracked; went under pulley
3	302	1.00	1.02	Mylar	7	--	--		belt formed oval slanting to the left
4	302	1.00	1.06	Mylar	7	--	--		belt still moving forward; belt pressure adjusted; twist in belt; floating pen in FOV indicates good zero-g; belt formed slanted oval
5	302	1.00		Mylar	7	--	--		belt formed slanted oval
6	302	1.00		Mylar	7	--	--		belt mistracked
7	302	1.00	1.07	Mylar	7	--	--		slanted oval; belt steady; floating pen does not indicate ideal zero-g
8	302	1.00	1.05	Mylar	7	--	--		belt formed peanut shape with a twist; floating pen kept falling during reduced gravity
9	302	1.00	1.07	Mylar	7	--	--	pert.	belt formed peanut shape; perturbation with small springs produced waves in belt but overall shape of belt was not changed; near end of parabola belt at the exit went above drive system (i.e. belt exited drive went up and formed small loop then formed large arc to drive entrance)
10	607	2.02	2.15	Mylar	7	--	--		steady shape with slight twist in belt; belt formed decent oval but slanted to left; belt drifting toward the aircraft aft end
11	607	2.02	2.22	Mylar	7	--	--	pert.	perturbation produced no noticeable effects; steady oval shape which is slanted
12	1207	4.01		Mylar	7	--	--		steady shape; belt drifts to the left
13	1207	4.01		Mylar	7	--	--	pert.	flipped belt inside out to determine if belt is coned; perturbation has no effect on belt; belt has twist; started out with a peanut shape then swung out and hit left wall of aircraft

Parabola No.	Roller Speed (rpm)	Belt Speed (m/s)	Measured Speed (m/s)	Belt Material	Belt Thickness (mils)	Clock Start Time	Clock End Time	Test Objective	Comments
14	1200	3.99		Mylar	7	--	--	deploy	deployment approximately 5.11 sec; after deployment belt hit left side of aircraft; shape of belt not good since view factors would be much smaller than one for the interior area of the belt
15	410	1.36		Mylar	7	--	--	deploy	no film
16	203 to 680	0.67 to 2.26	--	Mylar	7	--	--	deploy and accel.	no film
17	203	0.67		Mylar	7	--	--		no film
18	203	0.67	0.63	Mylar	5	--	--		belt twisted; never formed a hoop; just hung almost as if in 1-g
19	203	0.67		Mylar	5	--	--		belt not tracking; adjusted spring load
20	305	1.01	1.15	Mylar	5	--	--		adjusted belt during zero-g; belt formed peanut shape; shape not too different than in 1-g (NOTE: Post-It in FOV incorrect)
21	305	1.01	1.12	Mylar	5	--	--	pert.	perturbation had no effect on belt; test director tapped belt, 3.33 sec to recover; during zero-g adjusted belt pressure; shape similar to parabola 20
22	603	2.00		Mylar	5	--	--		belt had twist but not much change from 1-g
23	603	2.00	2.21	Mylar	5	--	--	pert.	perturbation had no effect on belt; belt almost touched left wall; belt comes out of drive straight, then loops up and follows aircraft wall contour, then forms remainder of hoop to drive entrance
24	603	2.00	2.21	Mylar	5	--	--	pert.	perturbation does not affect belt; peanut shape due to twist
25	1220	4.06		Mylar	5	--	--	pert.	perturbation has no effect on belt; stable shape but no a hoop (kidney shape)
26	401	1.33		tef-glass	3	--	--	cold start	belt tangled up in drive
27	401	1.33		tef-glass	3	--	--		belt mistracked
28	410	1.36	1.40	Mylar	7	--	--	deploy	deployment approximately 15.89 sec; belt did not form a hoop; belt exited drive and went up formed a small loop came back around to the drive entrance

Parabola No.	Roller Speed (rpm)	Belt Speed (m/s)	Measured Speed (m/s)	Belt Material	Belt Thic kness (mils)	Clock Start Time	Clock End Time	Test Objective	Comments
29	203	0.67	0.67	Mylar	7	--	--	deploy and accel.	deployment approximately 28.23 sec; initially belt sticking (static electricity) together; oval shape formed; acceleration drives belt to left side
30	203	0.67	0.70	Mylar	7	--	--	deploy	deployment approximately 23.70 sec; belt forms good hoop with some sway to right
31	415	1.38	1.32	Mylar	7	--	--	deploy	belt hit wall of aircraft during deployment and never fully deployed
32	415	1.38		tef-glass	3	--	--	deploy	no stable shape; belt went from a fluctuating loop which was high on the left side ultimately hitting the ceiling and crawling over the drive system
33	215	0.71		tef-glass	10	--	--	deploy	belt hit wall and climbed up the side over the drive system
34	415	1.38		tef-glass	10	--	--	cold start	hit the side of the aircraft
35	615	2.04		tef-glass	10	--	--		hit wall, tangled up, and floated away from the drive

29 Jan 1990 Day 3									
Parabola No.	Roller Speed (rpm)	Belt Speed (m/s)	Measured Speed (m/s)	Belt Material	Belt Thickness (mils)	Clock Start Time	Clock End Time	Test Objective	Comments
1	864	2.84		Mylar	13	0:00	0:00		initially a slanted oval, slanted to the left; stabilized into good hoop with some fluctuation and a slight twist
2	1559	5.12		Mylar	13	0:33	0:55		started with a large kidney shape; at end of the parabola the shape was a horizontal oval; objects in the FOV were floating up indicating an upward acceleration
3	1559	5.12		Mylar	13	1:53	2:11	cold start	belt hit wall; upward acceleration indicated by objects floating up
4	369	1.21		Mylar	13	3:01	3:25		decent shape but not stiff; many small fluctuations
5	369	1.21		Mylar	13	6:59	7:31	deploy	deployment approximately 12.45 sec; decent shape but wavy
6	(369)	1.21		tef-glass	19	13:17	13:42		Belt did not track properly
7				tef-glass	19	14:35	14:42		Belt did not track properly
8				tef-glass	19				Belt did not track, no film
9				tef-glass	19				Belt did not track, tried perturbation system which worked, no film
10				Teflon	15	22:42	22:52	cold start	belt mistracked
11	864	2.84		Teflon	15	24:10	24:26		shoots off to the left hits wall; belt is stable but wavy; tracking decent
12	1559	5.12		Teflon	15	25:22	25:48		oval shape with extreme twist; belt hitting backdrop; ± 0.01 g level
13	369	1.21		Teflon	15	26:46	27:11	decel.	no oval formed; belt not very stiff; belt is very wavy; deceleration drives belt to the right side
14	(864)	2.84		Teflon	15	30:40	30:59	deploy	deployment approximately 13.92 sec; belt goes straight out and hits wall; virtually no stiffness in belt

Parabola No.	Roller Speed (rpm)	Belt Speed (m/s)	Measured Speed (m/s)	Belt Material	Belt Thickness (mils)	Clock Start Time	Clock End Time	Test Objective	Comments
15	(1559)	5.12		Teflon	15	34:04	34:23	deploy	deployment approximately 16.0 sec; belt not stable; very wavy; sways to the left and hits wall
16	369	1.21		alum	8	39:22	39:45		decent parabola; no guide system; good hoop some fluctuation; nearly round hoop; stiffest belts seem to be best
17	864	2.84		alum	8	40:40	40:57		tracked to the back and hit guide; back edge of belt is damaged; nice hoop; walked off front of drive
18	369	1.21		alum	8	41:56	42:20	cold start	takes awhile to stabilize; good hoop with some fluctuation
19	369	1.21		alum	8	43:15	43:38	pert.	good hoop formed; very little effect from perturbation
20	369	1.21		alum	8	47:21	47:38	deploy	belt gets stuck on folds during deployment, needs help to unfold belt; folds straighten out after a couple of revolutions; forms decent hoop; some inidication of folds remain
21	369	1.21		alum	4	52:16	52:28		belt not moving, jammed, aluminum belt damaged
22				alum	4	52:39	54:01		good hoop
23				alum	4	55:01	55:28		ITR tape ran out; drive not working; belt getting stuck due to damage; belt forms a hoop with no motion
24				alum	4	56:24	56;49		belt not moving easily, hitting on the pulley; decent hoop formed
25	369	1.21		Mylar 6 in	10	1:10	1:39		a lot of twist in belt; forms vertical oval which turns into horizontal oval
26	369	1.21		Mylar 6 in	10	2:05	3:00	cold start	forms hoop before drive engaged; pretty good oval until approximately 0.02-g
27	864	2.84		Mylar 6 in	10	5:44	6:06		forms oval which is slanted to the left; belt has significant twist

Parabola No.	Roller Speed (rpm)	Belt Speed (m/s)	Measured Speed (m/s)	Belt Material	Belt Thic kness (mils)	Clock Start Time	Clock End Time	Test Objective	Comments
28	864	2.84		Mylar 6 in	10	7:02	7:22	cold start	forms a hoop before drive system started; mistracked
29	369	1.21		Mylar 6 in	10	10:46	11:06	deploy	deployment approximately 16.67 sec; fluctuates; does not form a hoop but does stay open (would have a relatively high view factor)

30 Jan 1990 Day 4									
Parabola No.	Roller Speed (rpm)	Belt Speed (m/s)	Measured Speed (m/s)	Belt Material	Belt Thickness (mils)	Clock Start Time	Clock End Time	Test Objective	Comments
1	369	1.21	1.19	alum	8	0:00	0:00		fluctuation in belt; belt swings out from back drop which forms twist in belt
2	369	1.21	1.18	alum	8	0:40	0:55	cold start	twist in belt, same as parabola 1; able to track using Delrin; good zero-g good shape on belt
3	864	2.84	2.83	alum	8	1:47	2:09		swings out from back drop and produces twisting but decent shape; tracking decently; Delrin popped out went thru aluminum belt
4	864	2.84	2.09	alum	8	3:50	4:11	cold start	no guidance on back end of belt; belt starts into hoop before started motor also swings out prior to drive start; belt forms horizontal oval; tracked to the back and hit pulley
5	369	1.21	--	alum	4	10:01	10:23		has problem in high g load; pretty good parabola, 0.001 and 0.03 g; stable good hoop with some lateral sway; prior to end of parabola belt swings out
6	369	1.21	--	alum	4	11:21	11:41	cold start	forms decent hoop prior to start; belt swings to the right and up due to initial upwards acceleration; after start extends out to left hand side, horizontal oval; 0.03 to .002 shape not too good
7	864	2.84	--	alum	4	12:38	13:01		springs are weak in 2-g; heavy twist; not quite touching screen; belt swings out and twists; stabilizes into decent shape, slightly horizontal oval
8	864	2.84	--	alum	4	14:05	14:13	cold start	prior to start had decent shape; belt jammed after start
9	369	1.21	--	alum	4	17:27	17:40	deploy	aluminum belt gets stuck under drive system due to folds must help along several times, did not work very good; belt did form horizontal oval for a short period
10	369	1.21	--	6 in alum	8	22:05	22:27		Delrin is guiding on center; very good belt shape, near zero-g; some slight fluctuation and lateral swing

Parabola No.	Roller Speed (rpm)	Belt Speed (m/s)	Measured Speed (m/s)	Belt Material	Belt Thic kness (mils)	Clock Start Time	Clock End Time	Test Objective	Comments
11	864	2.84	--	6 in alum	8	23:26	23:47		some twist at 0.03-g; as approach zero-g get good shape; there is some forward swing to belt which is producing the twist; belt sways laterally
12	1559	5.12	--	6 in alum	8	24:49	25;13		belt swings out and stabilizes into good shape; good zero-g; banging noise from apparatus
13	369	1.21	--	6 in alum	8	29:00	29;21	cold start	belt swings out and curls up prior to start; not much running time
14	369 to 1559	1.21 to 5.12	--	6 in alum	8	30:17	30:41	accel.	belt swing out (twists); during acceleration belt loses shape, drives to left side, and forms a horizontal oval
15	1559 to 369	5.12 to 1.21	--	6 in alum	8	31:38	33:00	decel.	making clicking noise from drive system; initially swings out (twists) and forms slanted oval; during deceleration belt swings to the right; belt begins to drop and forms a good hoop; pretty good g-level
16	369	1.21	1.11	Mylar mobius	10	36:02	36:24		hard time with driving system; weird shape not a cylinder; decent g-level; mobius twist forces fluctuations in belt
17	864	2.84	2.81	Mylar mobius	10	37:23	37:47		belt hitting backdrop; mobius twist tends to stay at bottom of oval
18	864	2.84	2.73	6 in Mylar mobius	7	41:08	41:32		belts are running very good; problem with static electricity; belt does not open up completely; lateral swinging in belt
19	1559	5.12	4.93	6 in Mylar mobius	7	46:27	46:47		belt shape is stable but does not open up completely; swings up towards left hand side; had to switch out ITR tape t=53:10
20	369	1.21	1.10	Teflon	15	54:46	55:10		belt has many permanent folds; flapping around a lot; floats up to the left side; pretty good parabola

Parabola No.	Roller Speed (rpm)	Belt Speed (m/s)	Measured Speed (m/s)	Belt Material	Belt Thickness (mils)	Clock Start Time	Clock End Time	Test Objective	Comments
21	864	2.84	2.52	Teflon	15	56:26	56:36		adjusted incoming rollers to help with flapping; folds are leveling out; shape more stable than in previous parabola; belt riding over rear guide, drive stopped
22	369	1.21	1.10	Teflon	15	58:06	58:24	cold start	a lot of bends in belt; folds causing problems and control motion; prior to start forms horizontal oval; after start hits wall on left side
23	369	1.21	1.13	Teflon	15	0:01	0:26	pert.	belt tends to ride over back side; shape not too bad after perturbation; perturbation has little effect, folds provide dominant disturbance
24	369	1.21	1.09	Teflon	15	2:55	3:08	deploy	jerky motion due to folds; belt is opening and closing
25	369	1.21	1.08	6 in Mylar	7	5:52	6:17		picking up debris on belt; some twist in belt; possibly some aft drift; belt drifts way out getting twisted up; belt exits drive loops around to return to drive but has a small loop on returning leg which is higher than belt on exiting; floating objects indicate good parabola
26	864	2.84	--	6 in Mylar	7	7:32	7:55	cold start	prior to start belt forms horizontal oval, decent hoop; after start belt hits wall on left side
27	1559	5.12	--	6 in Mylar	7	11:41	12:05		big twist in belt, belt swings out and up; hits backdrop; looks like mobius strip
28	864	2.84	2.65	6 in Mylar	7	13:05	13:27	pert.	good parabola into third digit, did vary up to ±0.03-g; belt swung out; perturbation produces ripples for approximately 2 revolutions
29	864	2.84	2.76	6 in Mylar	7	16:06	16:36	deploy	very good parabola; belt hit wall on left side
30	369	1.21	1.09	6 in Mylar	5	19;26	19:46		belt has a twist and as twist leaves belt it swings out to the left wall; acceleration level varying between 0.02 0.01-g
31	864	2.84	2.85	6 in Mylar	5	20:50	21:15	cold start	prior to start belt forms oval; after start belt swings out to the left side and forms horizontal oval with most of the belt to the left of the drive system

Parabola No.	Roller Speed (rpm)	Belt Speed (m/s)	Measured Speed (m/s)	Belt Material	Belt Thic kness (mils)	Clock Start Time	Clock End Time	Test Objective	Comments
32	1559	5.12	--	6 in Mylar	5	25:23	25:50		belt starts swings out to left side and hits wall; initially belt formed a slanted oval
33	864	2.84	2.70	6 in Mylar	5	26:52	27:17	pert.	good parabola; belt swings out (forms a twist which is almost 90°; perturbation produces some ripples but no other effects
34	864	2.84	2.66	6 in Mylar	5	31:32	32:03	deploy	good parabola; belt hits left wall and stays stable

31 Jan 1990 Day 5									
Parabola No.	Roller Speed (rpm)	Belt Speed (m/s)	Measured Speed (m/s)	Belt Material	Belt Thic kness (mils)	Clock Start Time	Clock End Time	Test Objective	Comments
1	369 to 1559	1.21 to 5.12	--	6 in alum	8	0:29	0:58	accel	starts with a large twist which distorts belt (could be benificial in improving view factor); during acceleration belt swings to left and settles to oval after acceleration
2	1559 to 369	5.12 to 1.21	1.38	6 in alum	8	1:43	2:06	decel	initially belt swinging to left; during deceleration belt swings to the right then settles to hoop; hoop is wavy
3	864	2.84	1.36	6 in alum	8	3:09	3:40	pert	large twist in belt; belt fluctuated some, from horizontal oval to vertical oval; perturbation had little effect
4	864	2.84	1.31	6 in alum	8	4:47	5:11	cold start	prior to start belt formed decent hoop but did have a twist; after start had decent shape with but fluctuating
5	369	1.21	1.33	6 in Mylar	10	8;09	8:34	pert	belt in a left slanted oval with some twist; perturbation produced some ripples which damped out in less than one revolution
6	864	2.84	2.45	6 in Mylar	10	9:33	9:59	pert	belt started as left slanted oval; belt developed bump on exiting side of drive due to perturbation; belt settled to a good hoop
7	--	--	--	6 in Mylar	10	10:56	11:17	floated belt	belt opens to hoop and falls to the floor
8	--	--	--	6 in Mylar	10	12:11	12:31	floated belt	tighter hold on belt at release; belt opens to good hoop; fluctuates in a bending mode (perpendicular to belt axis)
9	--	--	--	6 in Mylar	10	15:59	16:21	floated belt	tight hold; opens to good hoop and falls to floor
10	--	--	--	6 in Mylar mobius	10	17:21	17:37	floated belt	mobius strip opens then curls up and falls to the floor
11	--	--	--	6 in Mylar mobius	10	18:30	18:53	floated belt	belt stays curled up and falls to the floor
12	--	--	--	6 in Mylar mobius	10	19:46	20:11	floated belt	belt stays curled up
13	369	1.21	1.55	Mylar 3 ft dia	7	23:11	23:35		decent shape, some fluctuations

Parabola No.	Roller Speed (rpm)	Belt Speed (m/s)	Measured Speed (m/s)	Belt Material	Belt Thickness (mils)	Clock Start Time	Clock End Time	Test Objective	Comments
14	864	2.84	3.83	Mylar 3 ft dia	7	24:32	24:57		not circular at first but does form a good hoop prior to end of parabola; not as good a parabola 0.01-g
15	1559	5.12	--	Mylar 3 ft dia	7	25:55	26:21	pert.	good zero-g; belt does not form a good shape at high speeds; belt has a twist; belt vibrates due to perturbation and damps out in less than two revolutions
16	1559	5.12	--	Mylar 3 ft dia	7	27:14	--	cold start	no film
17	864	2.84	3.48	Mylar 3 ft dia	7	30:07	30:16	deploy	initially belt sticks together then swings up to the left side and stabilizes as a horizontal oval
18	369	1.21	1.08	Mylar	7	33:54	34:16		crease in belt; bouncing above Delrin spacer; belt leans to the front; crease due to storage; belt does stay open
19	864	2.84	2.62	Mylar	7	35:18	35:41		belt swings out from backdrop which creates a twist
20	1559	5.12	5.61	Mylar	7	36:35	36:58	pert.	belt swings out and creates the twist; perturbation has no effect
21	864	2.84	2.57	Mylar	7	38:01	38:22	cold start	prior to start belt tries to form hoop; might enter good circular shape without motion; belt hits backboard; after start shoots off to left side; ITR tape ends at 43:00; 25 revolutions of calibration signal
22	369	1.21	1.17	tef-glass	19	43:40	44:02	pert	belt never stabilizes; always fluctuating and twisting; starts in a vertical oval and finishes in a horizontal oval; perturbation has little effect; does not form a good shape
23	864	2.84	2.47	tef-glass	19	45:02	45:24	pert	belt rode up on rear c-clamp; belt fluctuates and generates twist; belt is tapped to help the tracking which may contribute to fluctuations; perturbation had little effect
24	369 to 1559	1.21 to 5.12	--	tef-glass	19	46:22	46:25	accel	belt came out of drive system
25	369	1.21	--	tef-glass	10	50:22	50:25		belt came out of drive system

Parabola No.	Roller Speed (rpm)	Belt Speed (m/s)	Measured Speed (m/s)	Belt Material	Belt Thic kness (mils)	Clock Start Time	Clock End Time	Test Objective	Comments
26	--	--	--	tef-glass	10	51:43	52:06		no test
27	--	--	--	Mylar mobius	10	54:34	54:45	floated belt	mobius fell to floor and stayed curled up
28	369	1.21	--	Mylar	13	58:16	58:22		belt jammed
29	369	1.21	1.18	Mylar	13	59:32	59:54		belt requires constant adjustment; belt fluctuating but stays close to a hoop
30	--	--	--	Mylar	13	0:56	1:16	cold start	requires constant adjustment; belt hits operator; adjustments not fast enough belt jams; belt stayed close to cylinder
31	--	--	--	Mylar	13	2:10	2:14		hitting backboard, belt jams
32	369	1.21	0.98	Teflon	?	6:11	6:35		belt has many folds/wavy; belt hits left wall; objects in cabin are floating up
33	864	2.84	2.67	Teflon	?	7:32	7:56		belt stays stable; does not open up completely; belt has a twist
34	1559	5.12	4.62	Teflon	?	8:48	9:12	pert.	belt tended to hit backdrop; similar to previous parabola, more twist; belt floats out; perturbation produces waves but overall shape stable
35	864	2.84	2.67	Teflon	?	10:05	10:30	cold start	belt hits left wall; belt fluctuating

Page intentionally left blank

Appendix B

Task 1: Belt Dynamics and Dynamic Control

- Conduct a vibrations analysis of the LBR;
- Conduct a vibrations analysis of the belt alone;
- Estimate belt stiffness and damping coefficients as functions of belt geometry and working fluid properties;
- Model the deployed LBR as a dynamic system;
- Develop equations governing dynamic response of LBR;
- Develop equations governing dynamic response of belt alone;
- Identify normal mode vibrations of the system and of the belt;
- Conduct controls analysis of the LBR and the belt alone;
- Develop engineering block diagrams;
- Define desired response of system (milestone for NASA approval);
- Identify type of controller and/or modifications to design; and
- Present with equations and graphs.

Task 2: Liquid Bath Containment

- Define, design and test candidate bath containment seals;
- Minimize gravity effect during testing;
- Design, procure, and fabricate hardware to test;
- Measure force to pull belt through seals;
- Quantify losses in LBR;
- Submit experimental test plan for approval; and
- Provide design prints for seals tested.

Task 3: System Size Limitation

- Investigate changes in operating point or design as heat load increases;
- Investigate multiple belt deployment;
- Analyze and develop conceptual designs for heat rejection rates - 150 kWth, 500 kWth, 10 MWth, 50 MWth.

Option Block A

Task 4: Experimental Hardware for Testing Dynamic Model

- Design, procure and fabricate hardware for ground testing of dynamics;
- Test at least two forcing functions;
- Recommend forcing functions to be tested;
- Submit experimental test plan to NASA for approval; and
- Use results of testing to modify transfer function and/or engineering block diagram developed in Task 1.

Task 5: Power System Optimization

- Address impact of radiator mass on power system optimization for closed cycle Brayton engines, organic Rankine engines, and Stirling engines power cycles for Space Station and SP-100/MMW; and

- Investigate impact of LBR on system mass and/or performance for power systems using thermoelectric and thermionic conversion.

Task 6: Heat Transfer Tests

- Design, procure, and fabricate hardware to test heat transfer from surface of moving belt;
- Submit experimental test plan for NASA approval; and
- Include test variable, ranges, number of tests, test sequence, analyses to reduce/evaluate data, method of evaluation, expected functional relationships, and test hardware design in test plan.

Option Block B

Task 7: Liquid Metal Studies

- Conduct literature surveys and analyses to examine wettability and emissivity of working fluids, lithium, and tin;
- Identify alloys which modify heat rejection temperature;
- Identify alloys which increase value of surface emissivity;
- Identify potential stable impurities in Tin and Lithium;
- Assess effect of impurities on surface tension and wettability; and
- Define chemically compatible belt-fluid combinations with required wettability.

Task 8: Lithium emittance Measurements

- Measure emissivity of lithium at melting point using Fourier Transfor infra-red spectrophotometer;
- Measure emissivity on pure lithium and lithium with impurities;
- Submit letter outlining changes/rational for modifying spectrophotometer (for NASA approval); and
- Provide original graphs and/or magnetic tape of emissivity spectrum.

Task 9: Tin Emittance Measurements

- Measure emissivity of tim at melting point using Fourier Transform infra-red spectrophotometer;
- Measure emissivity on pure tin and tin alloys or tin with impurities;
- Submit letter outlining changes/rational for modifying spectrophotometer (for NASA approval); and

Option Block C

Task 10: Hardware for Bath Containment Tests in Zero-Gravity

- Develop hardware to test bath containment seals in zero-gravity (at NASA ZGR);
- Design and fabricate hardware compatible with drop package used in ZGF;
- Coordinate with NASA to ensure suitability of design;
- Consult manager of ZGF for input to design; and
- Provide complete set of mechanical and electrical design prints of hardware.

Task 11: Hardware for Belt Dynamics Tests in Zero-Gravity

- Develop hardware to test dynamics of belt in Zero-gravity (at NASA ZGF);
- Design and fabricate hardware compatible with drop package used in ZGF;
- Coordinate with NASA to ensure suitability of design;
- Consult manager of ZGF for input to design; and
- Provide complete set of mechanical and electrical design prints of hardware.

Task 12: Space Environment Experiment Definition

- Assess cost and develop preliminary experimental designs procedures, and schedules for testing candidate belt materials, fluids, and belt-fluid combinations for: ground based ionized vacuum chamber; Space Shuttle payload bay; and NASA's Long Duration Exposure Facility; and
- Recommend best test environment.

Task 13: Fluid Charging

- Define mechanisms for fluid charging; and
- Define extent mechanisms impact performance of LBR.

Task 14: Reporting of Results

- Submit monthly reports;
- Distribute copies to persons identified by NASA;
- Prepare and submit final report to NASA for approval;
- Print copies of report (up to 150 copies);
- Distribute reports as directed by NASA;
- Submit one (1) set of glossy continuous tone prints of all photographs;
- Prepare brief summary reports of tasks;
- Submit summary task report to NASA within (30) days after task completion; and
- Follow "Reports of Work" as identified in Section J of RFP3-161000

Appendix C

Parabola No. 1, Day 3

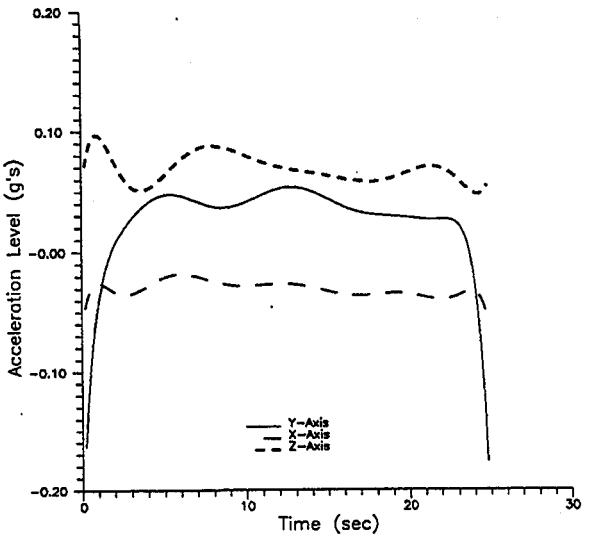

Parabola No. 2, Day 3

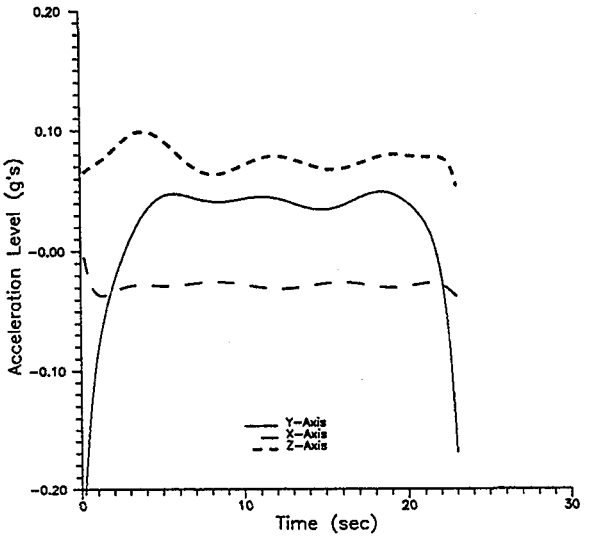

Parabola No. 3, Day 3

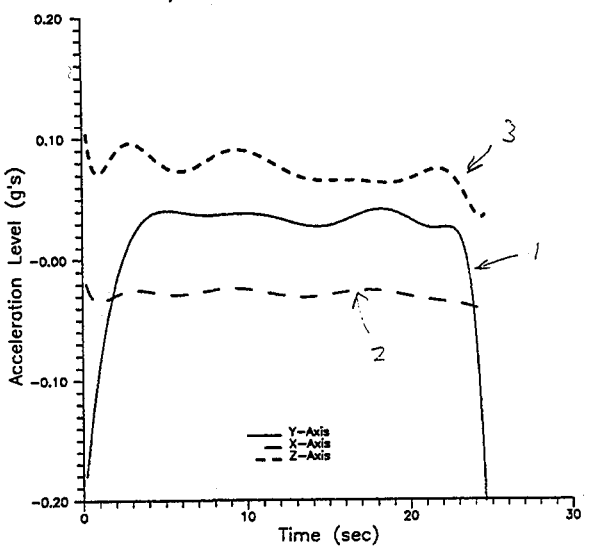

Parabola No. 4, Day 3

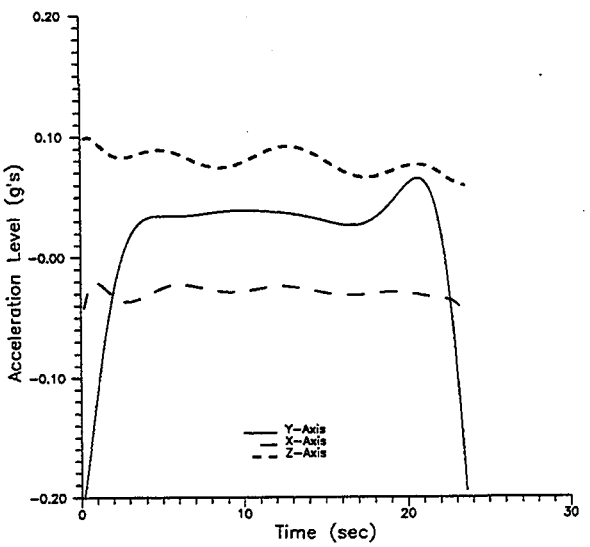

Parabola No. 5, Day 3

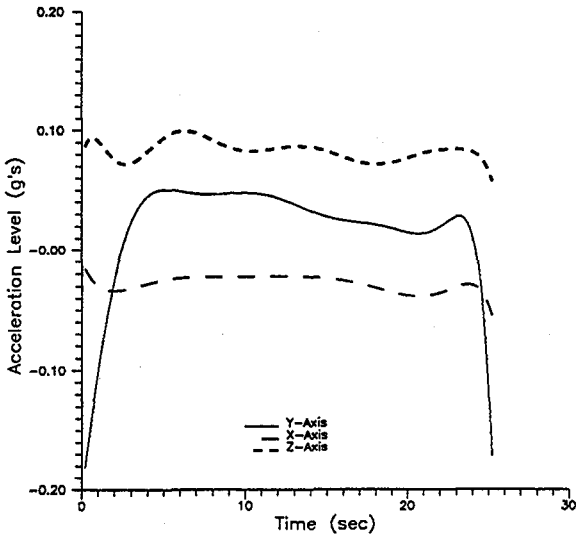

Parabola No. 6, Day 3

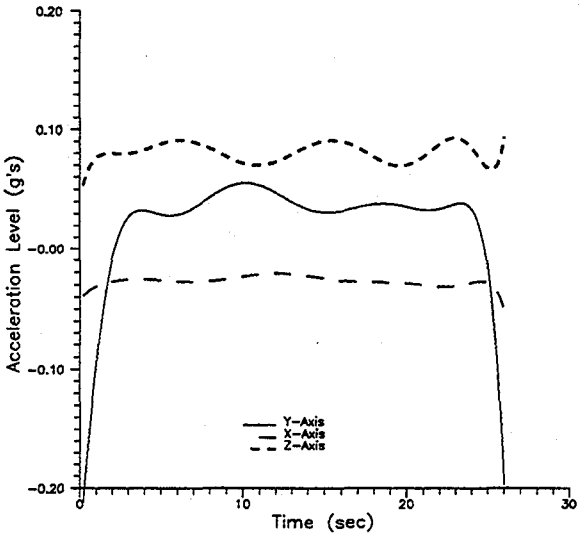

Parabola No. 7, Day 3

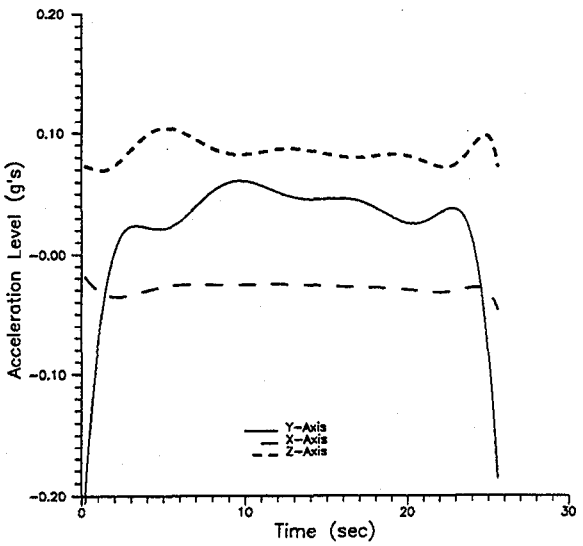

Parabola No. 8, Day 3

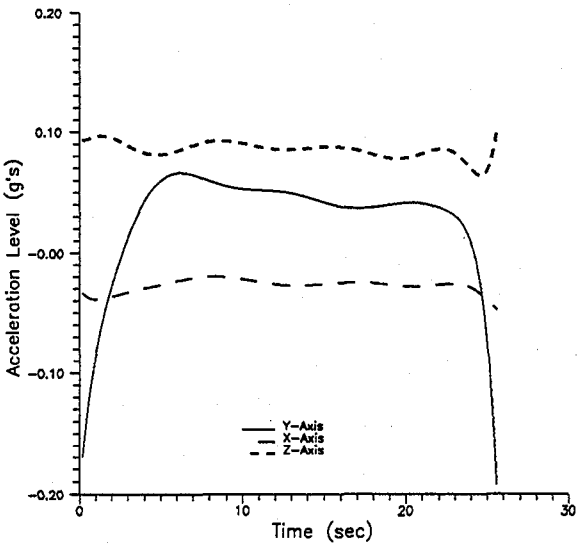

Parabola No. 9, Day 3

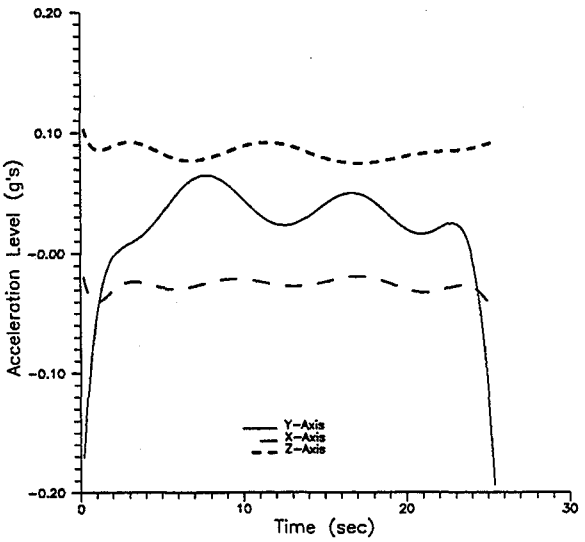

Parabola No. 10, Day 3

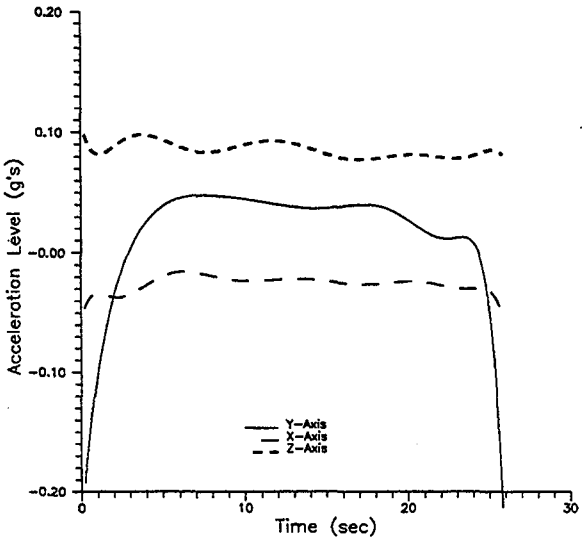

Parabola No. 11, Day 3

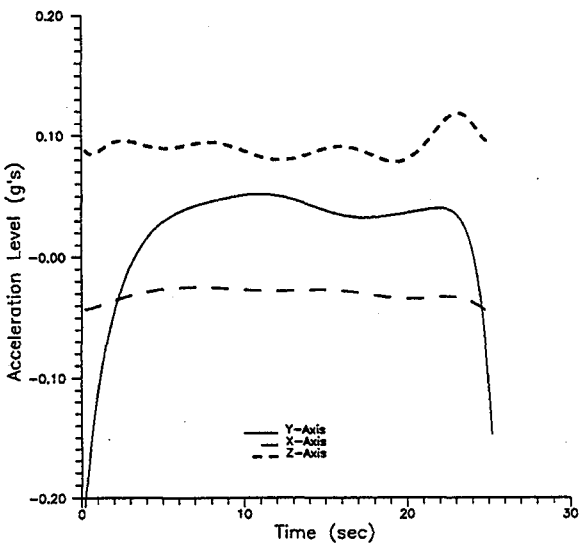

Parabola No. 12, Day 3

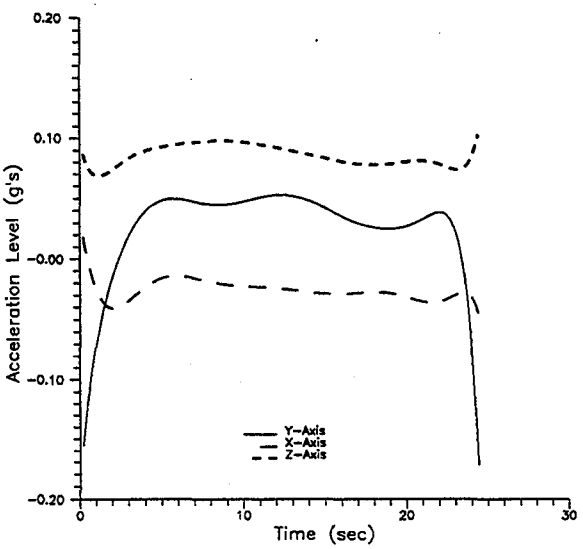

Parabola No. 13, Day 3

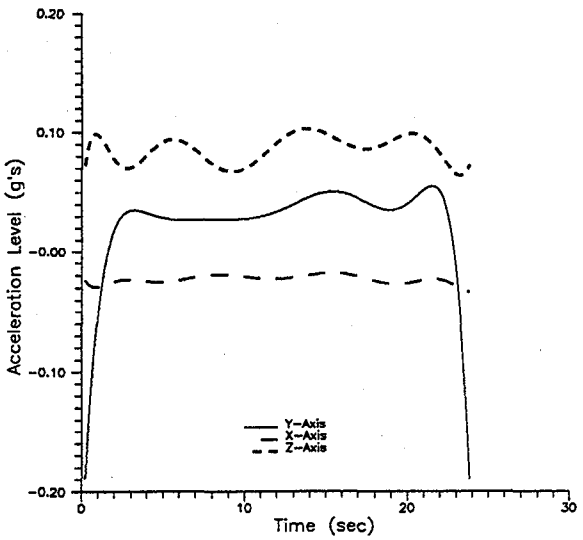

Parabola No. 14, Day 3

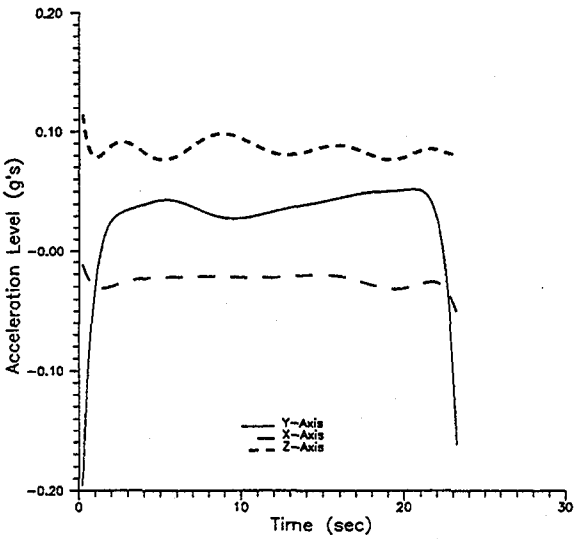

Parabola No. 15, Day 3

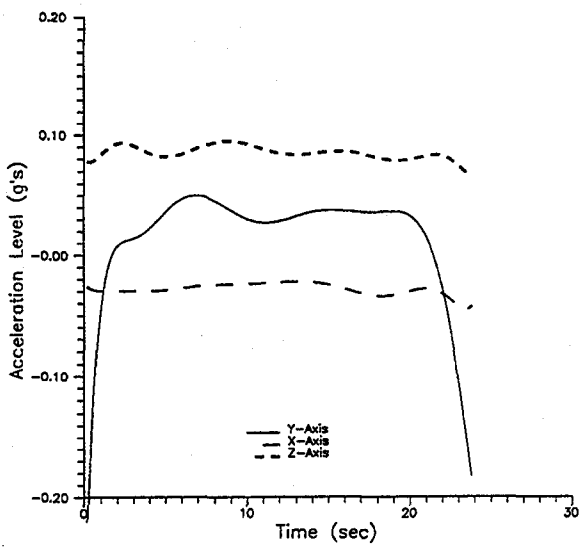

Parabola No. 16, Day 3

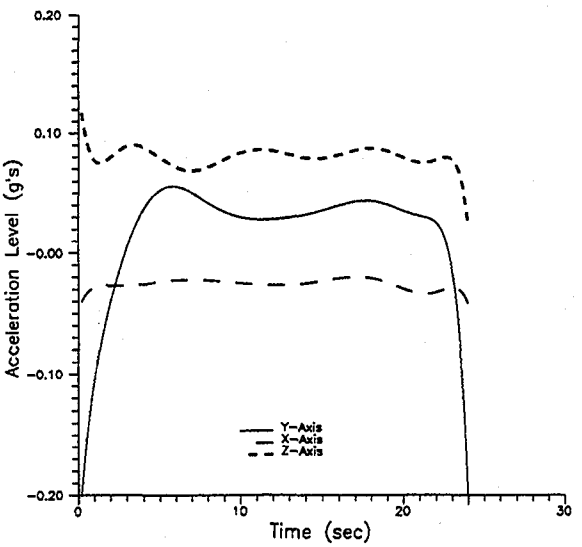

Parabola No. 17, Day 3

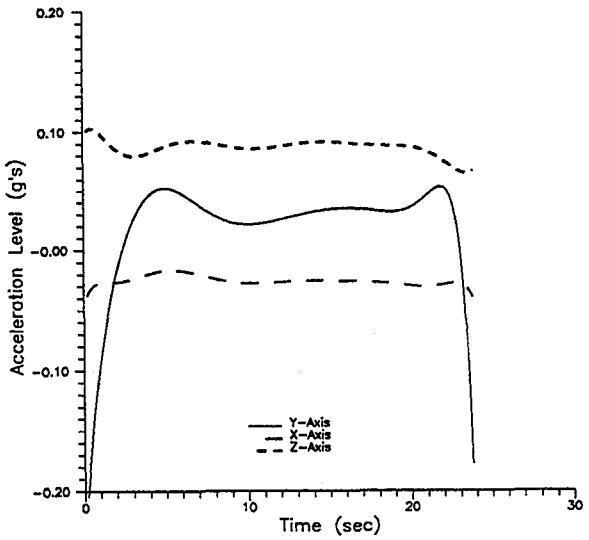

Parabola No. 18, Day 3

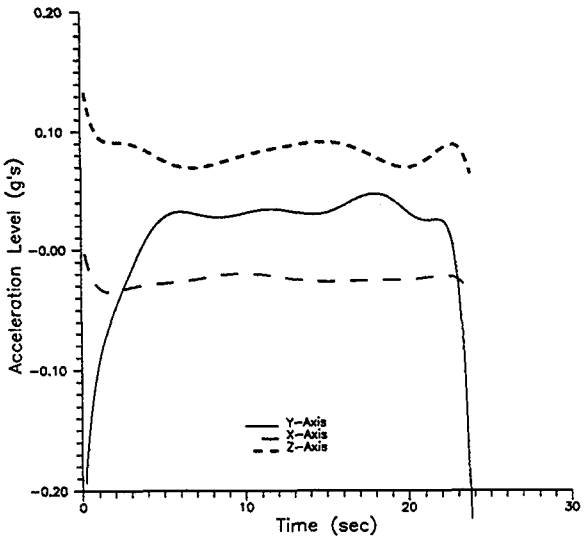

Parabola No. 19, Day 3

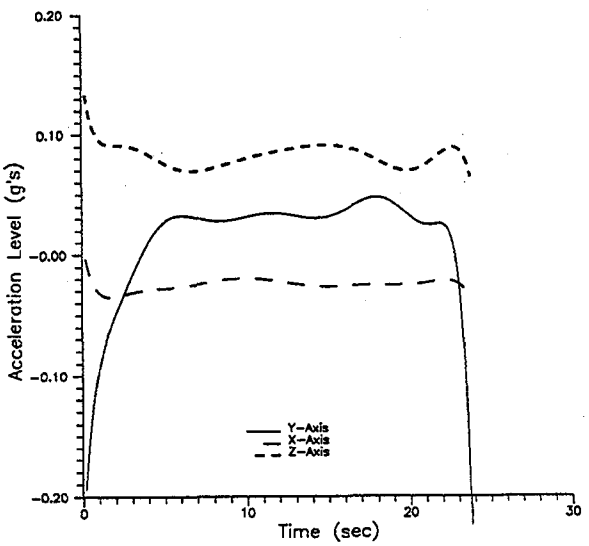

Parabola No. 1, Day 4

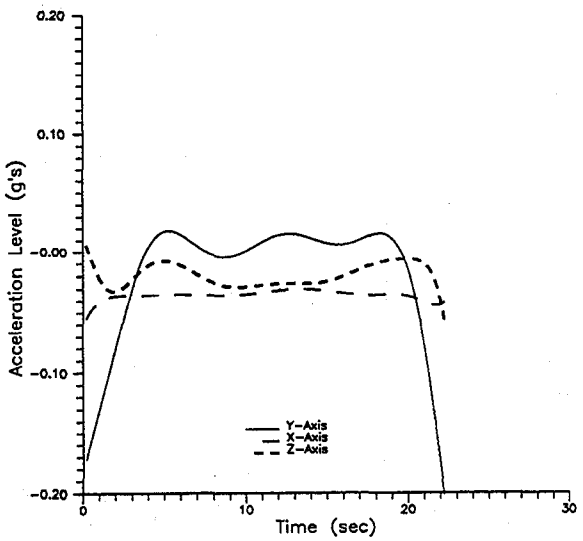

Parabola No. 2, Day 4

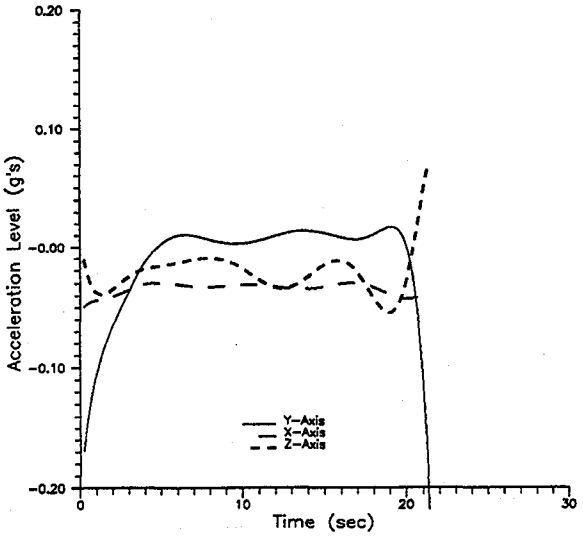

Parabola No. 3, Day 4

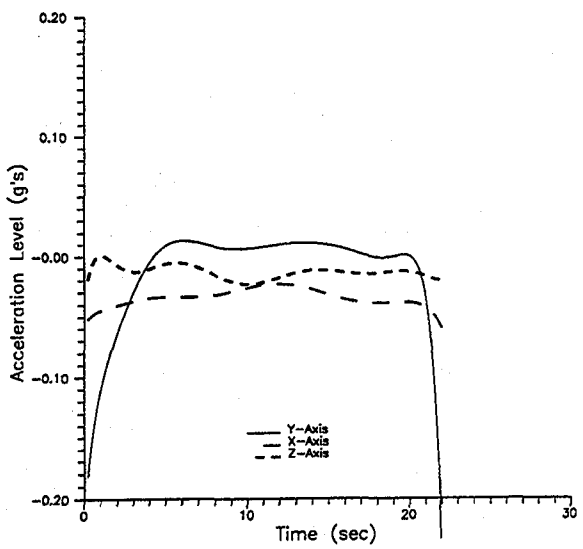

Parabola No. 4, Day 4

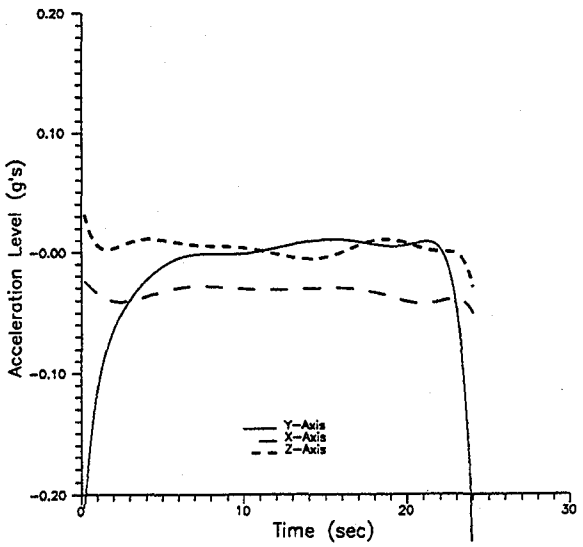

Parabola No. 5, Day 4

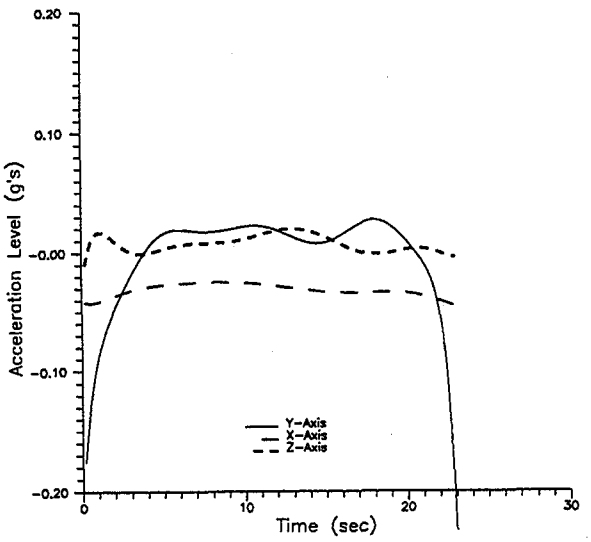

Parabola No. 6, Day 4

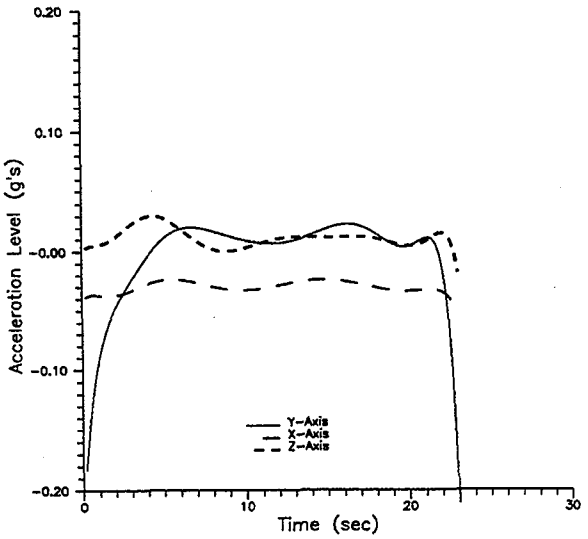

Parabola No. 7, Day 4

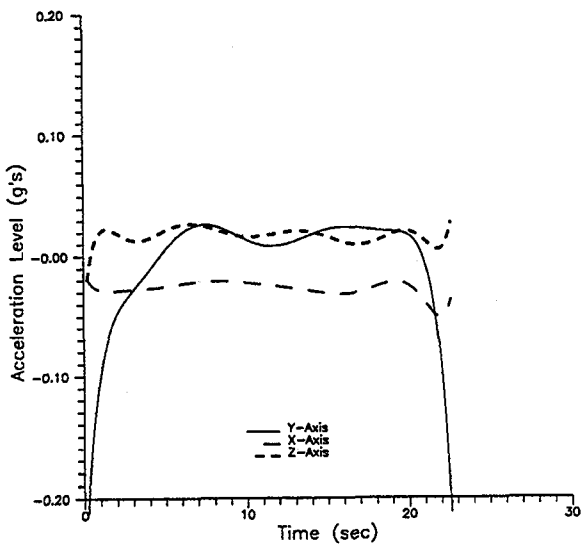

Parabola No. 8, Day 4

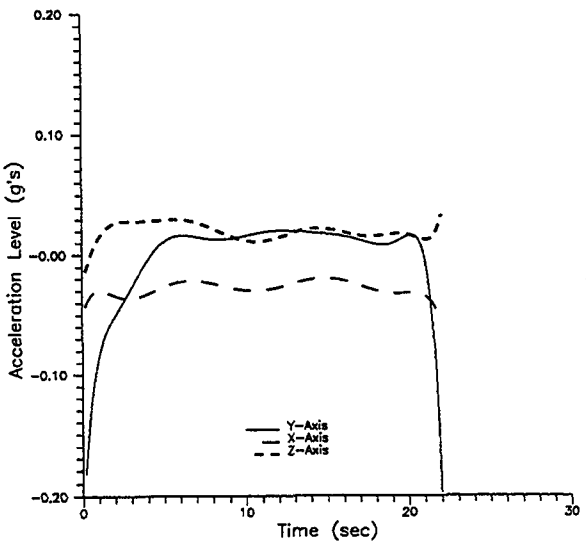

Parabola No. 9, Day 4

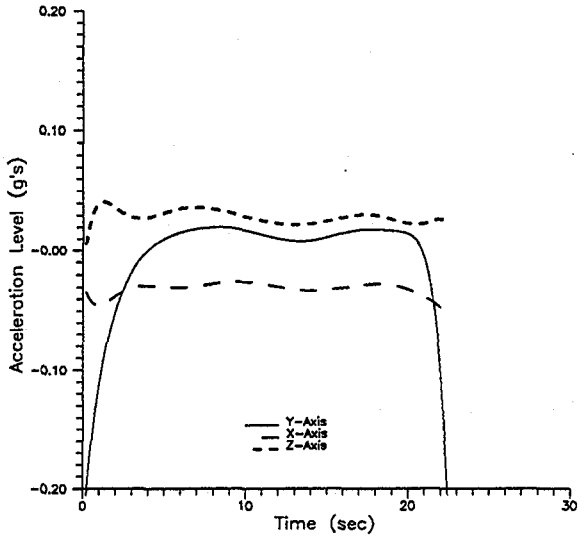

Parabola No. 10, Day 4

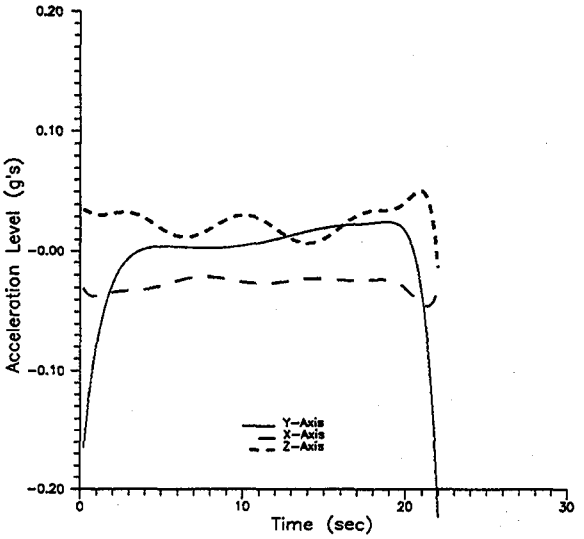

Parabola No. 11, Day 4

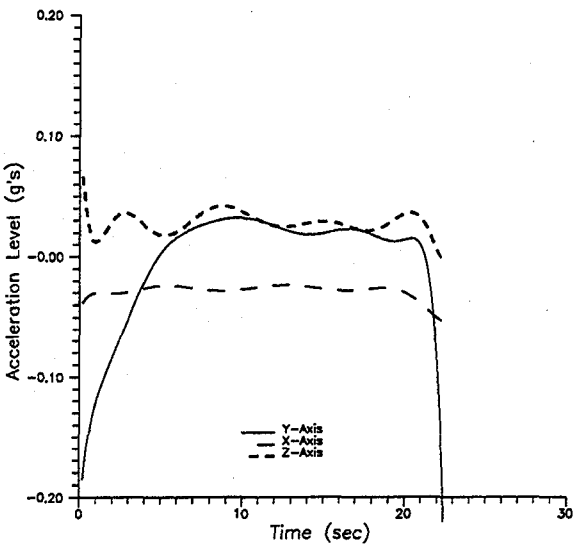

Parabola No. 12, Day 4

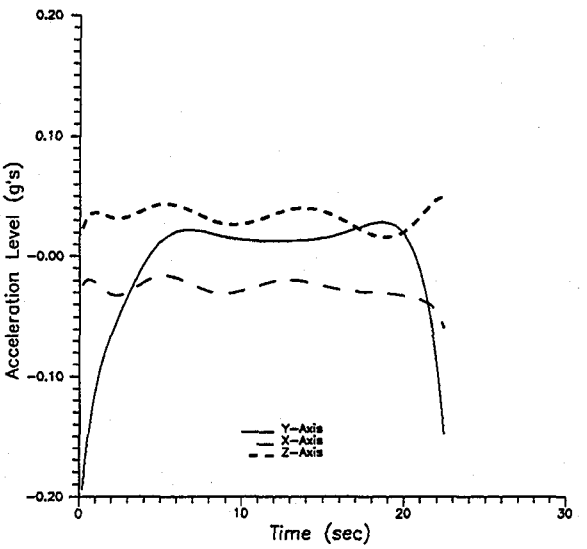

Parabola No. 13, Day 4

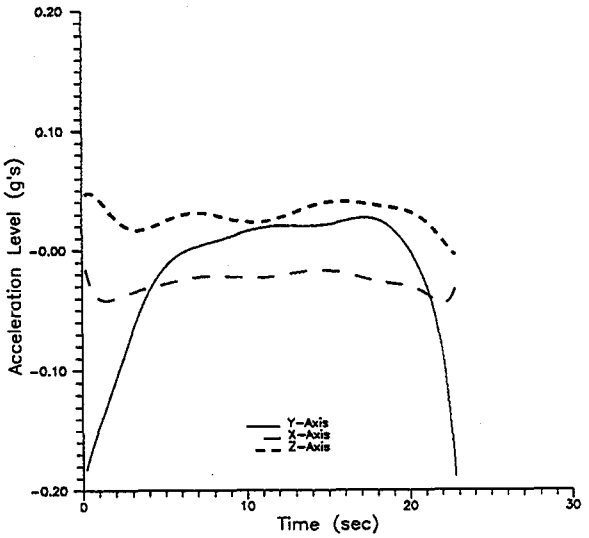

Parabola No. 14, Day 4

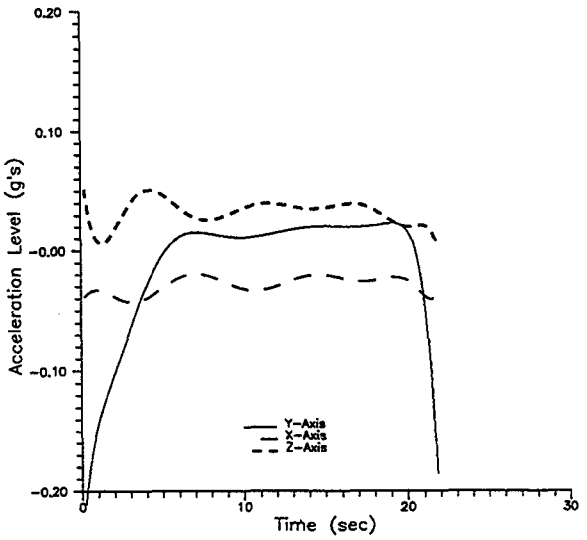

Parabola No. 15, Day 4

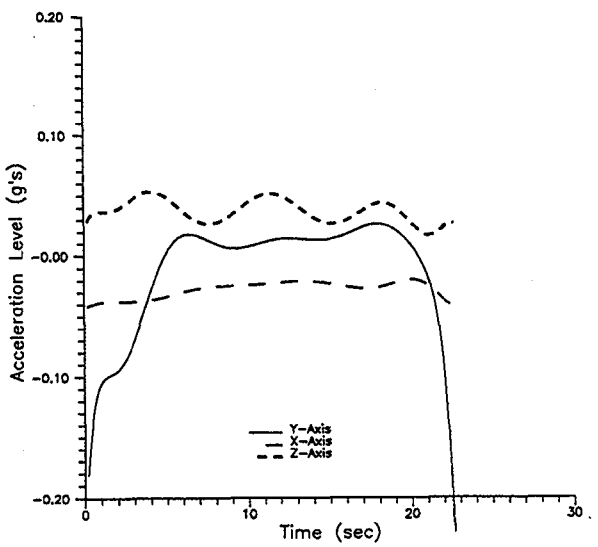

Parabola No. 16, Day 4

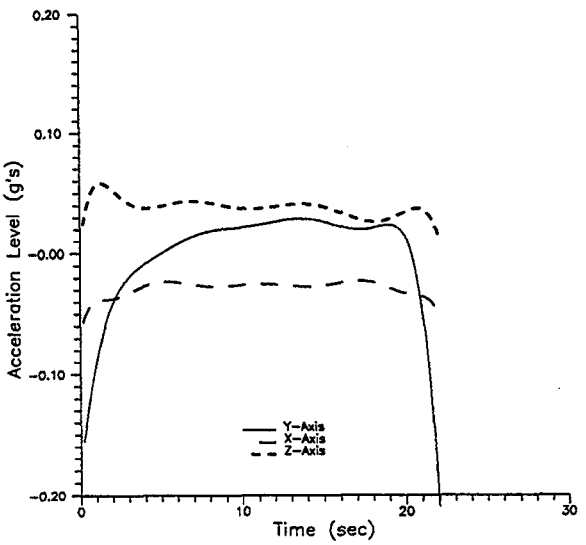

Parabola No. 17, Day 4

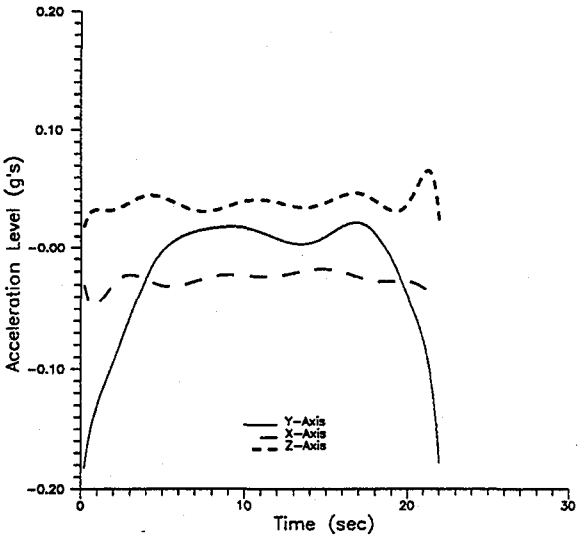

Parabola No. 18, Day 4

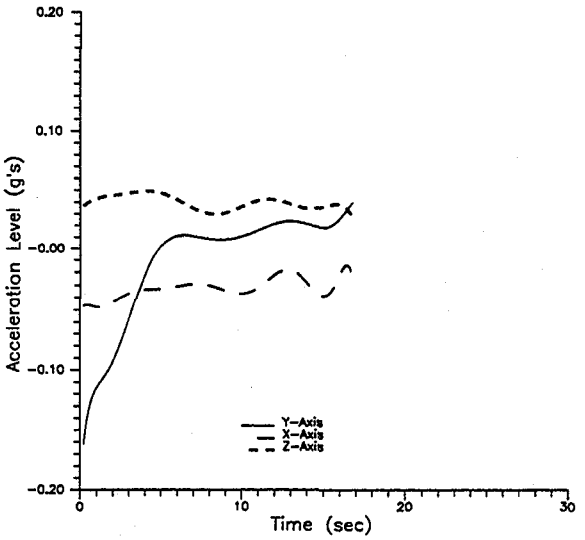

Parabola No. 20, Day 4

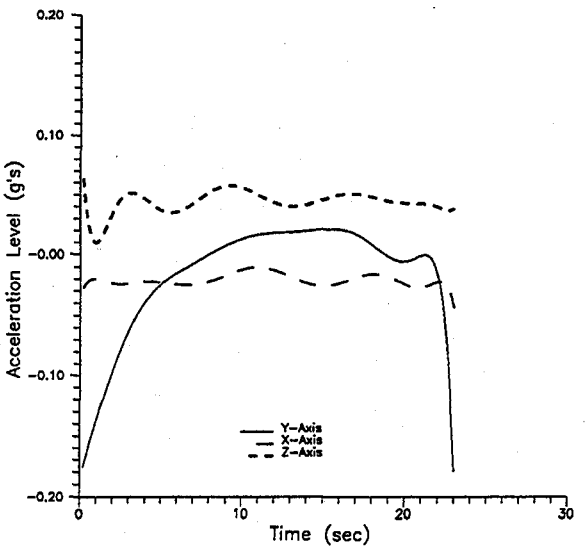

Parabola No. 21, Day 4

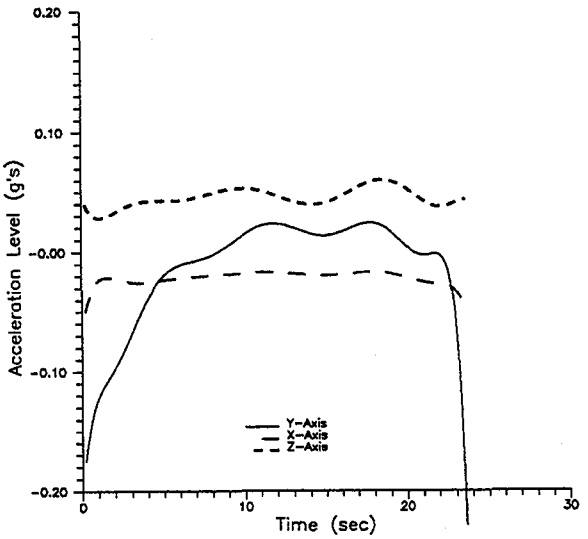

Parabola No. 22, Day 4

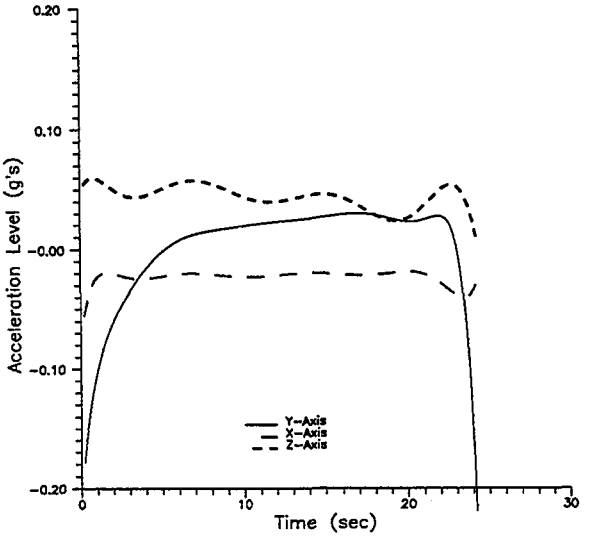

Parabola No. 23, Day 4

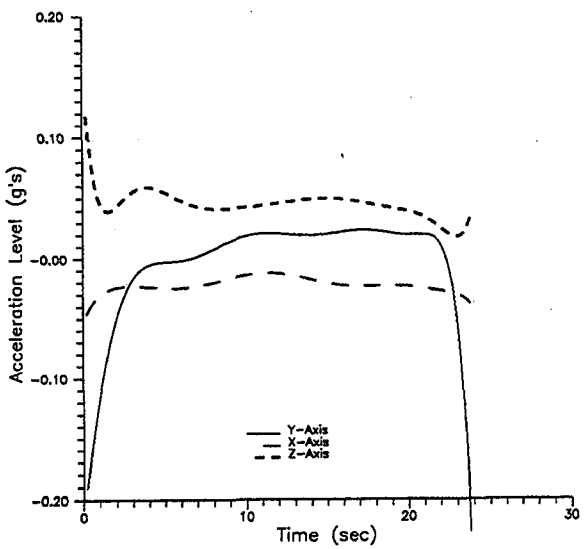

Parabola No. 24, Day 4

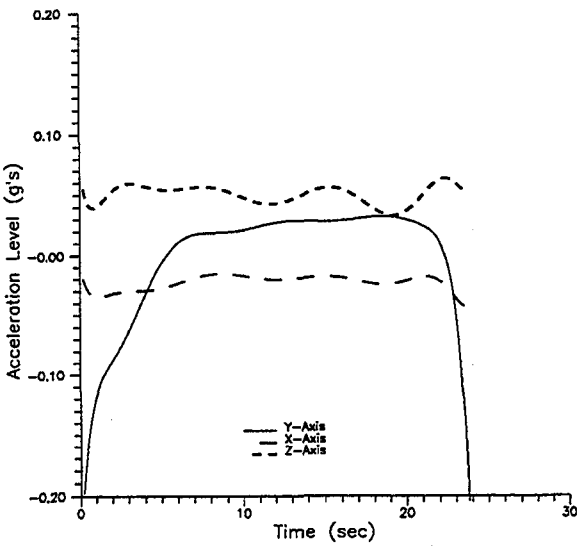

Parabola No. 25, Day 4

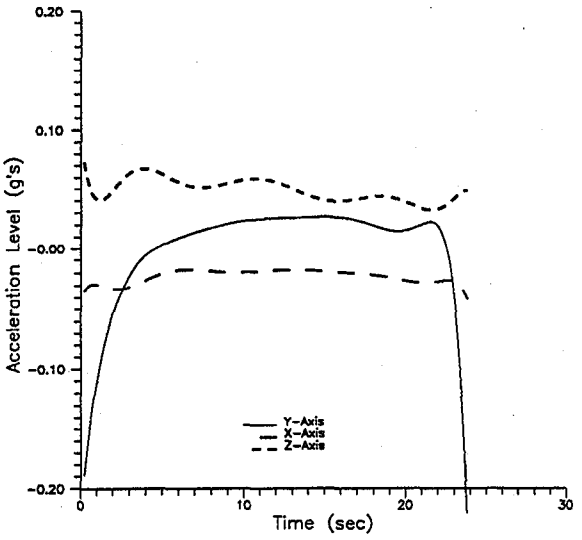

Parabola No. 26, Day 4

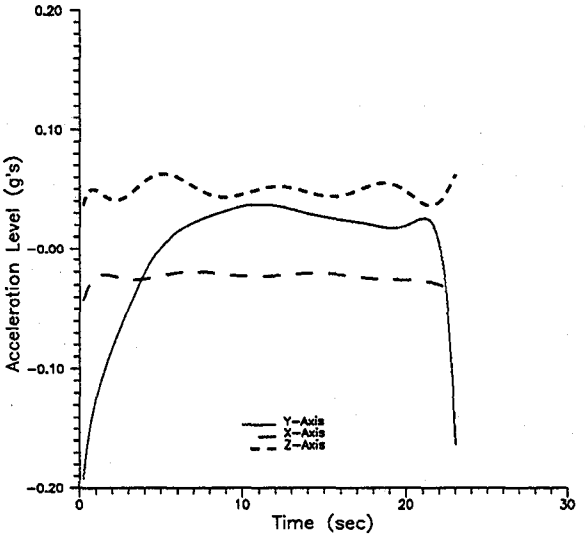

Parabola No. 27, Day 4

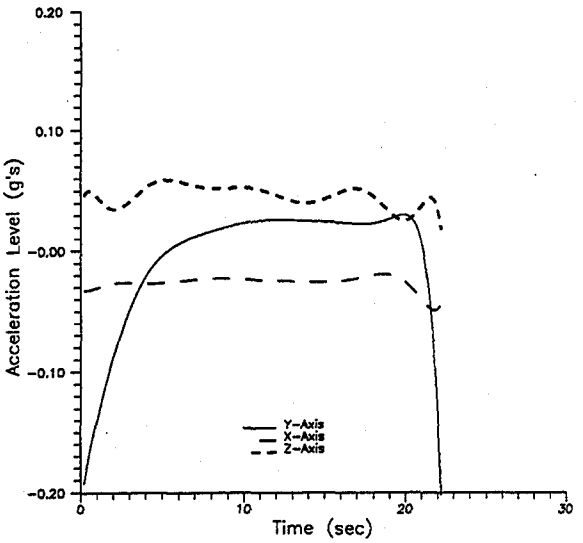

Parabola No. 28, Day 4

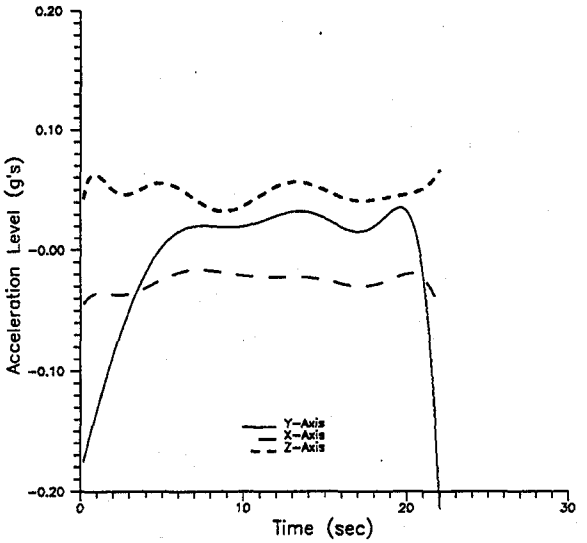

Parabola No. 29, Day 4

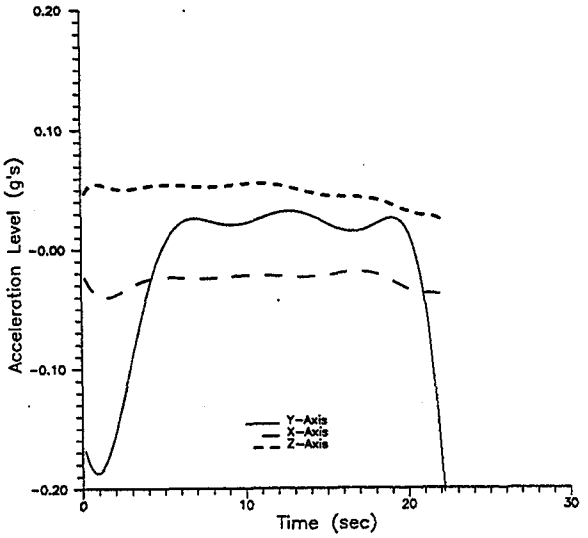

Parabola No. 30, Day 4

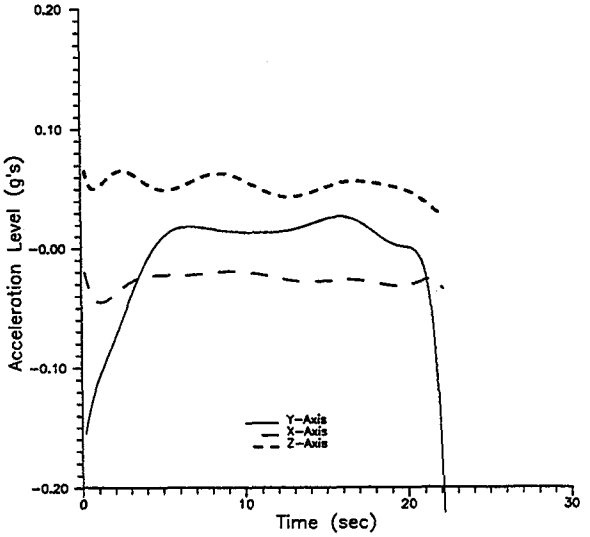

Parabola No. 31, Day 4

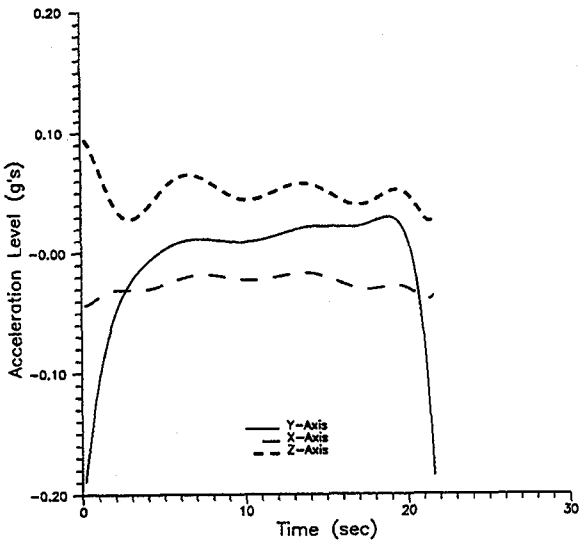

Parabola No. 32, Day 4

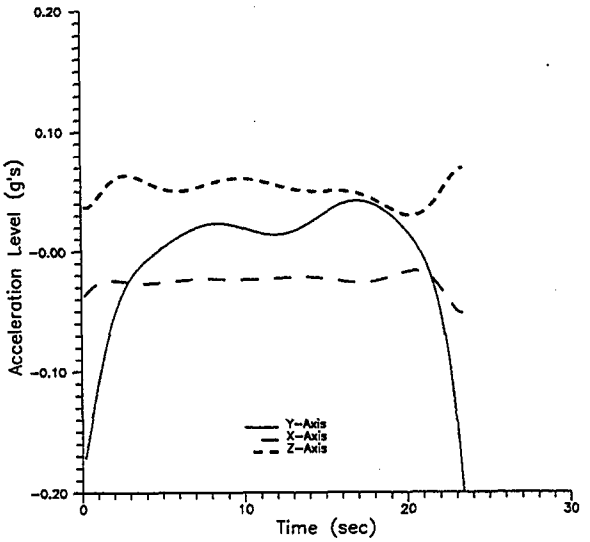

Parabola No. 33, Day 4

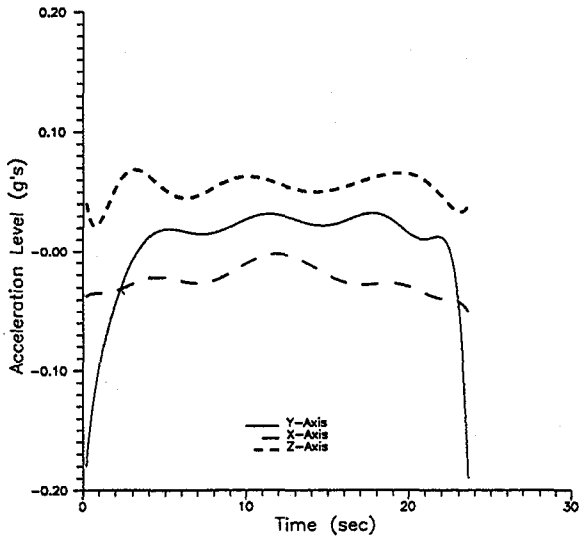

Parabola No. 34, Day 4

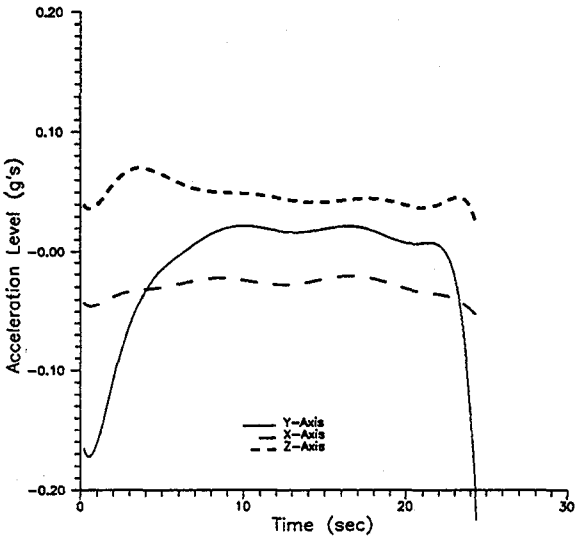

Parabola No. 1, Day 5

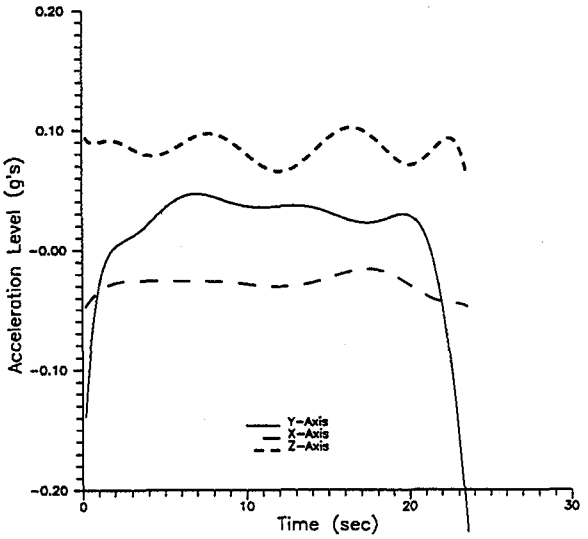

Parabola No. 2, Day 5

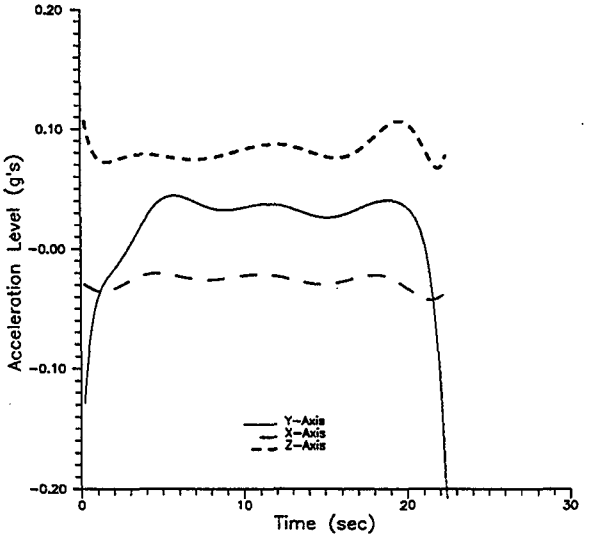

Parabola No. 3, Day 5

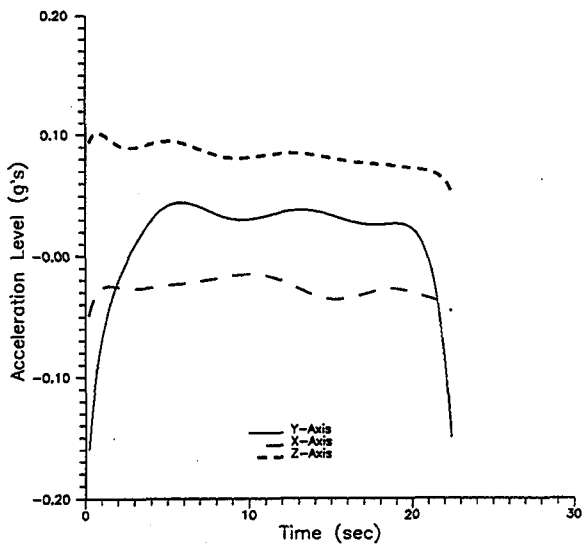

Parabola No. 4, Day 5

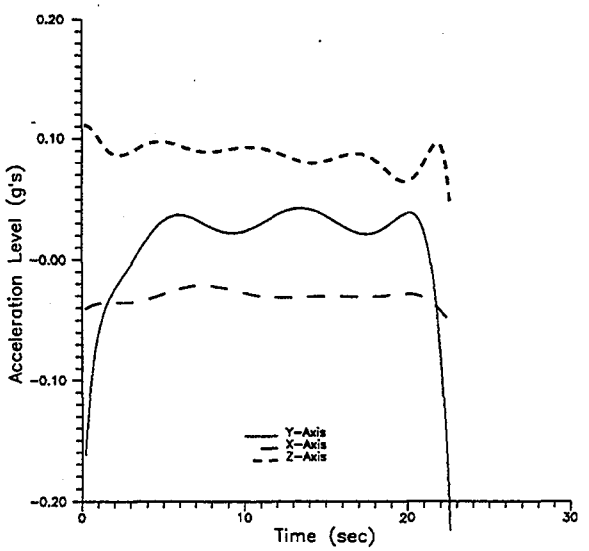

Parabola No. 5, Day 5

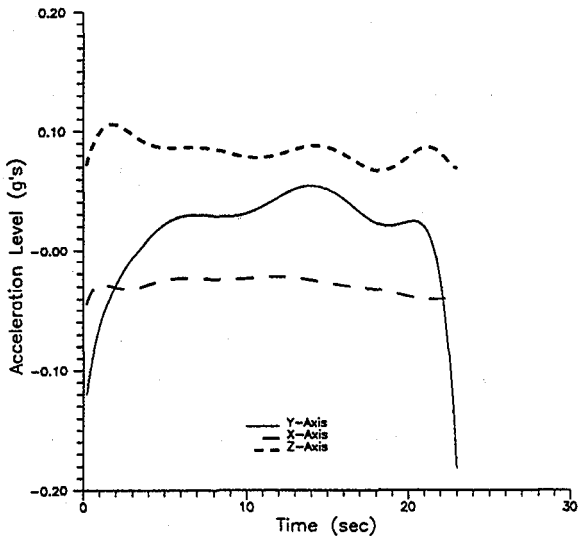

Parabola No. 6, Day 5

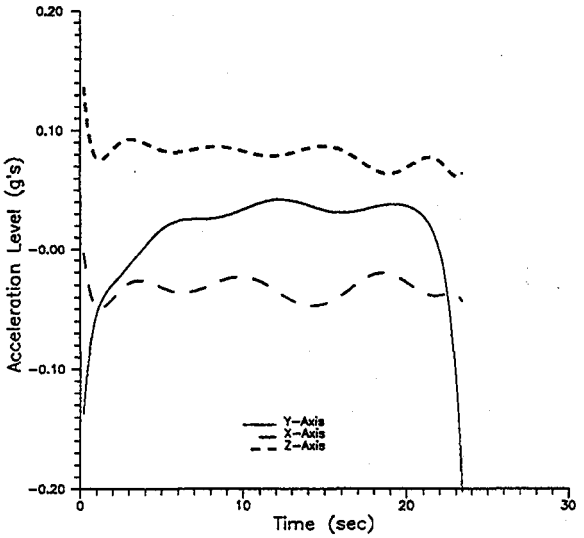

Parabola No. 7, Day 5

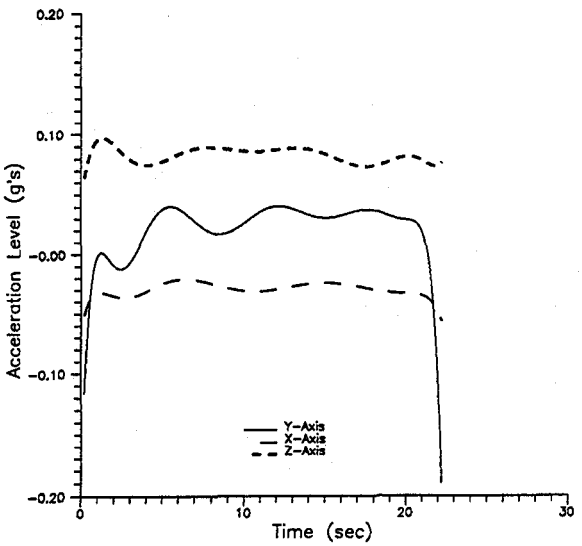

Parabola No. 8, Day 5

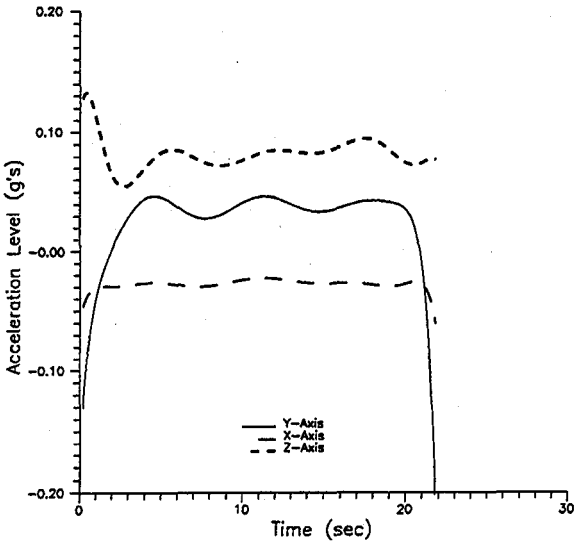

Parabola No. 9, Day 5

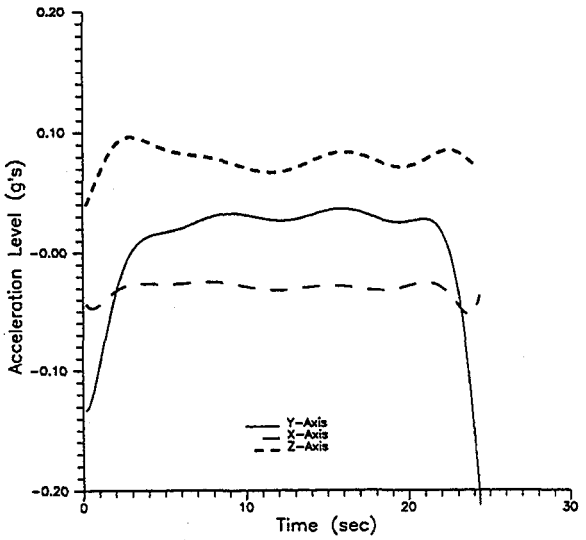

Parabola No. 10, Day 5

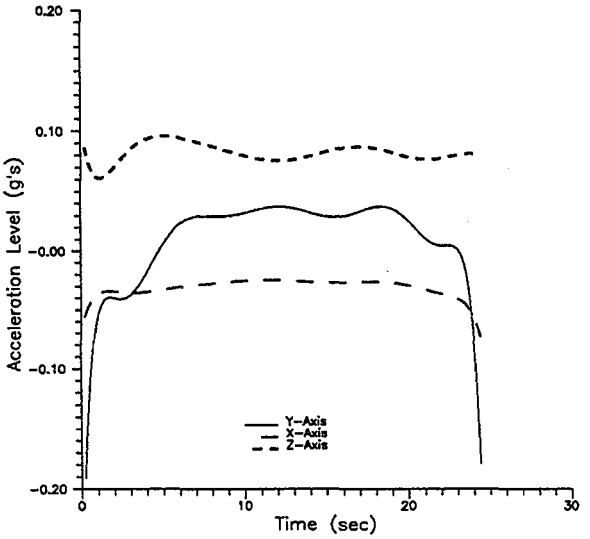

Parabola No. 11, Day 5

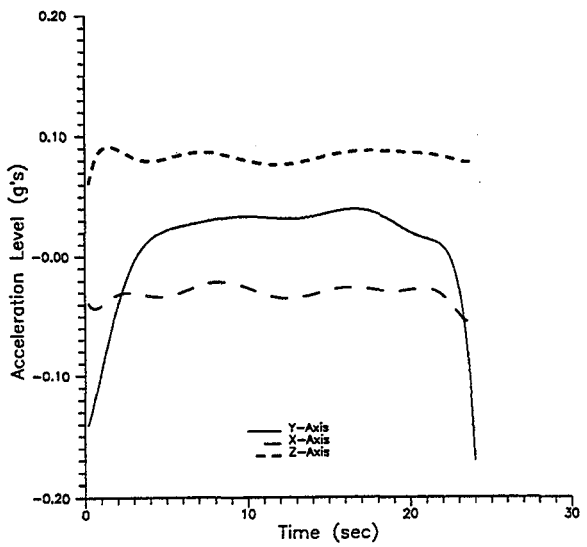

Parabola No. 12, Day 5

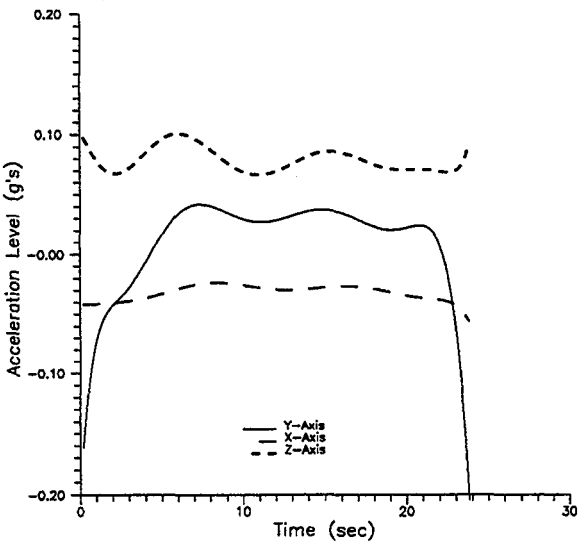

Parabola No. 13, Day 5

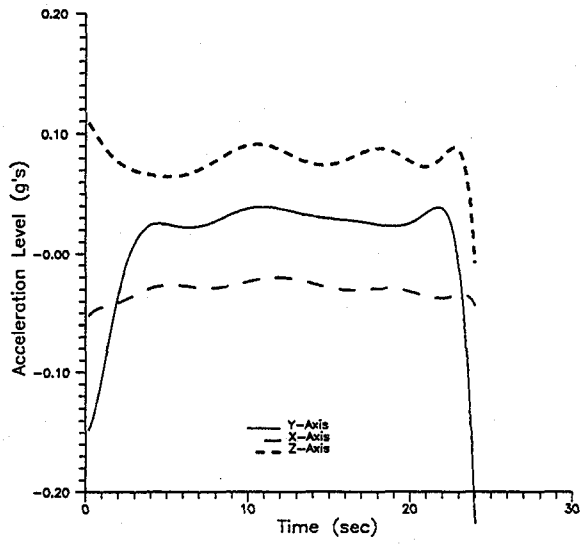

Parabola No. 14, Day 5

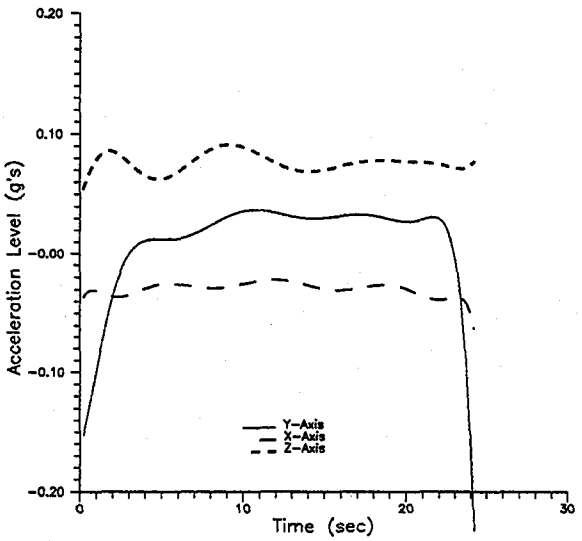

Parabola No. 15, Day 5

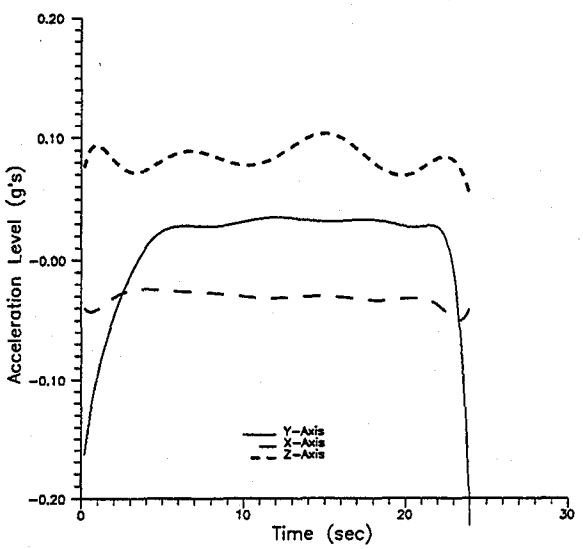

Parabola No. 16, Day 5

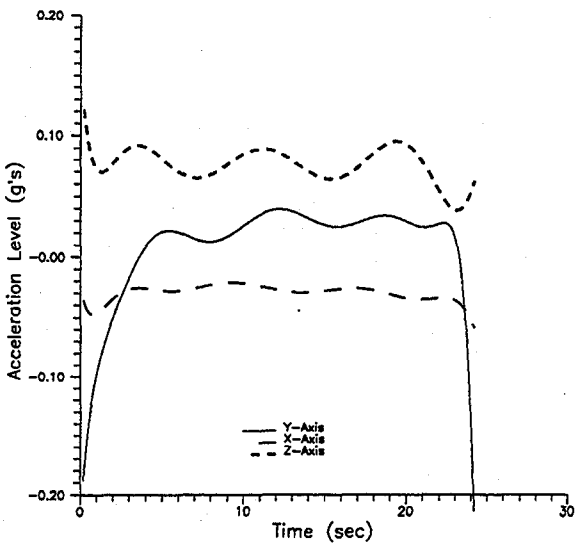

Parabola No. 17, Day 5

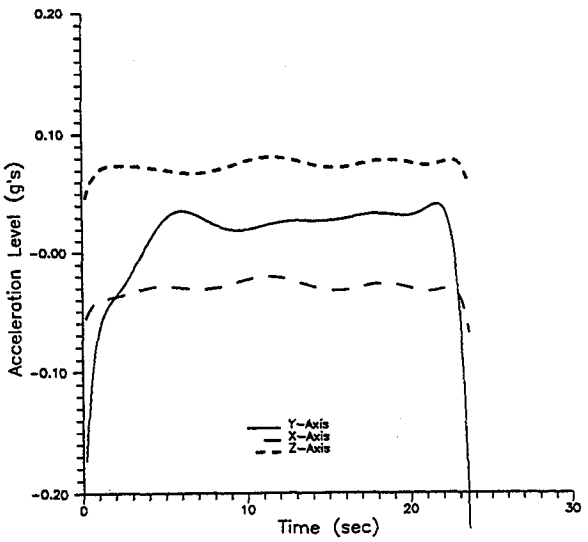

Parabola No. 18, Day 5

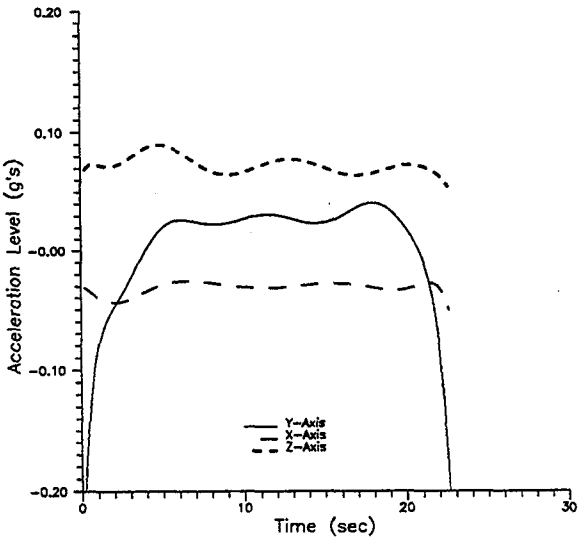

Parabola No. 19, Day 5

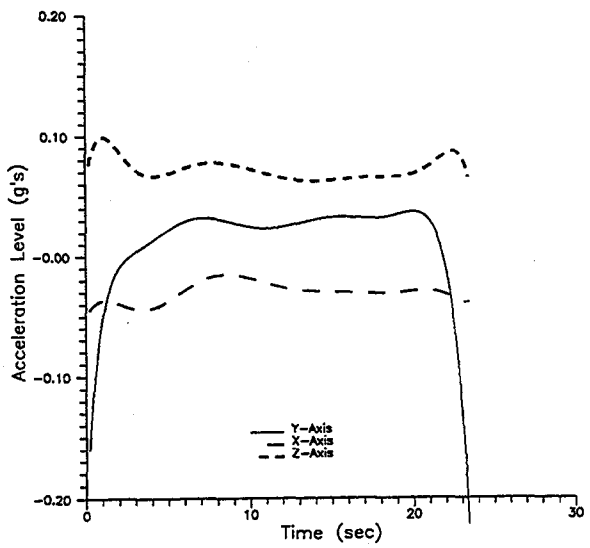

Parabola No. 20, Day 5

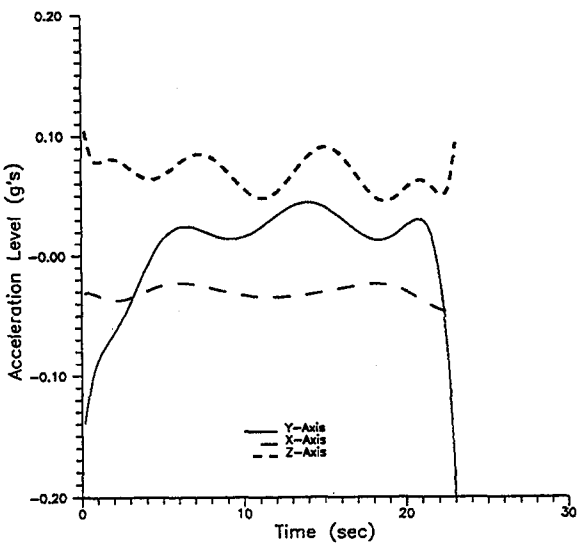

Parabola No. 21, Day 5

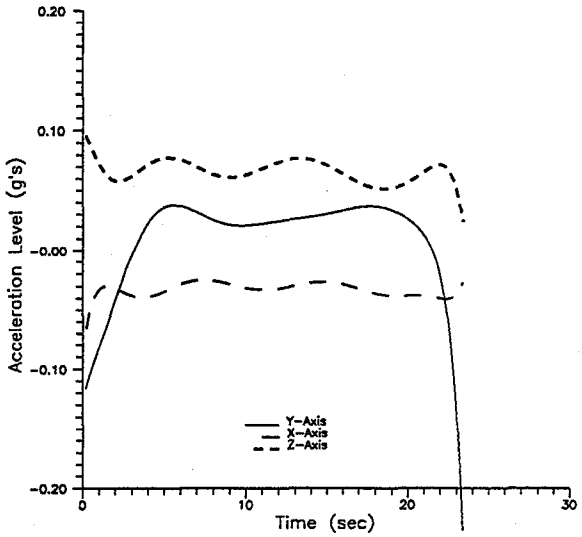

Parabola No. 22, Day 5

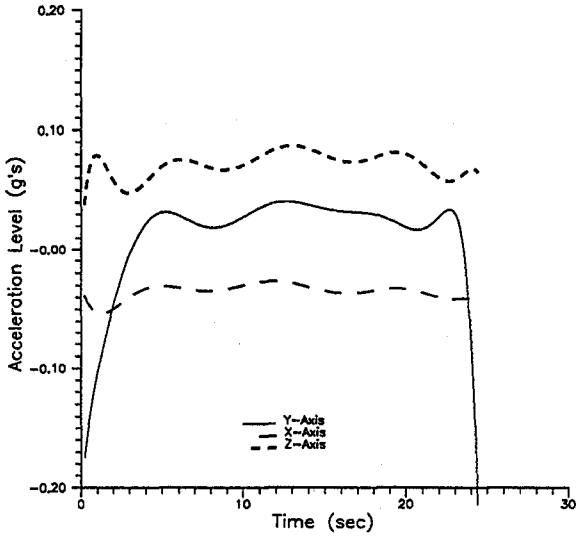

Parabola No. 23, Day 5

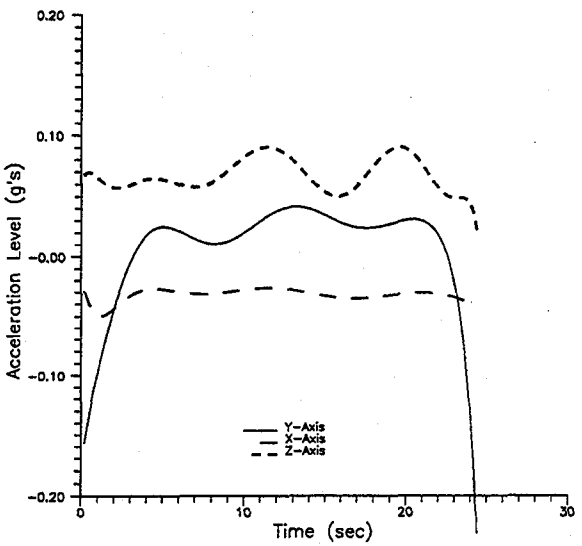

Parabola No. 24, Day 5

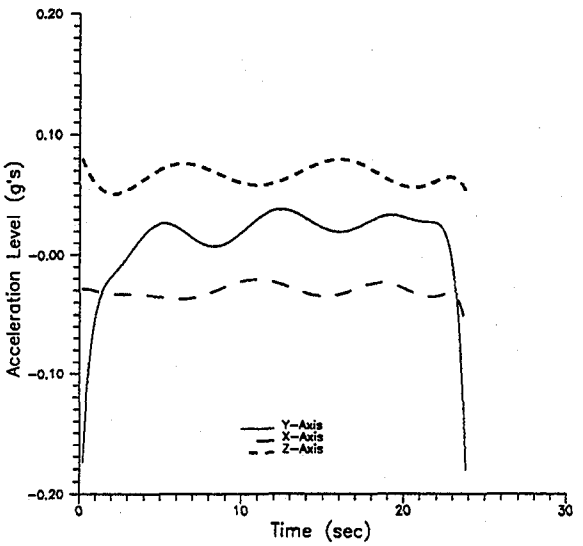

Parabola No. 25, Day 5

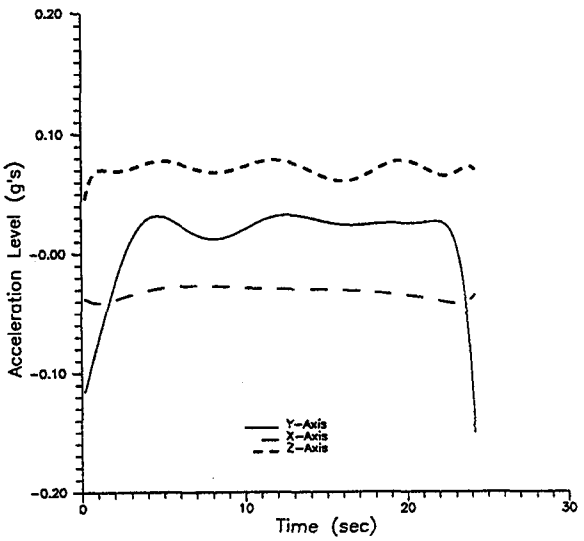

Parabola No. 26, Day 5

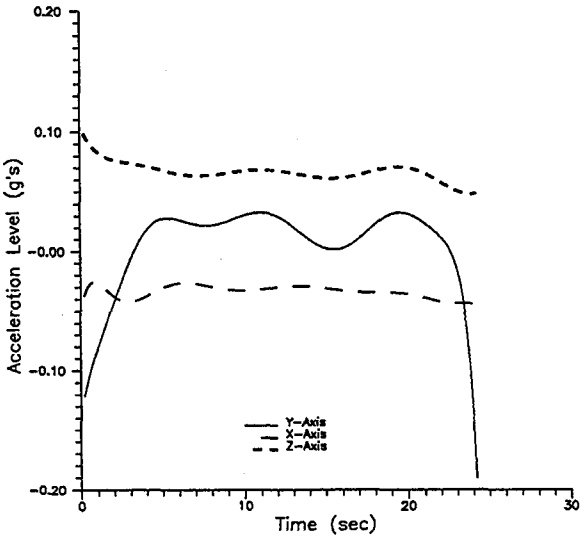

Parabola No. 27, Day 5

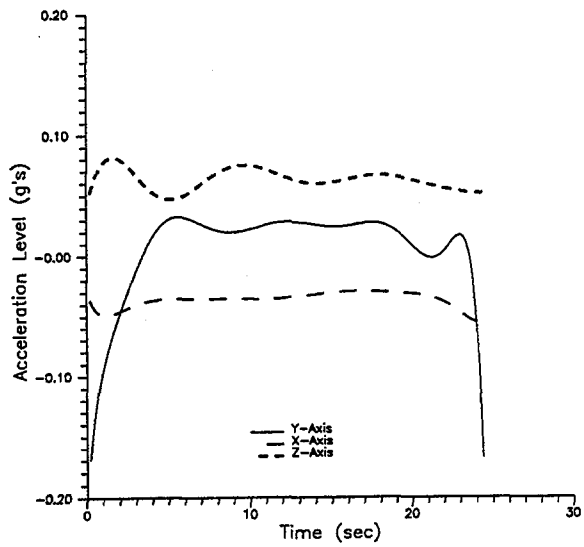

Parabola No. 28, Day 5

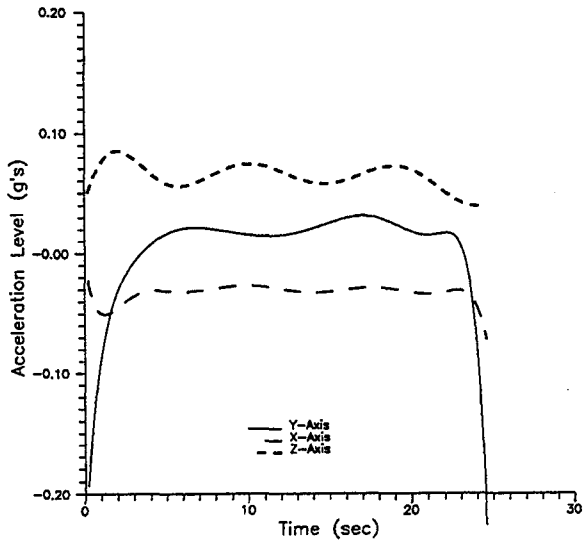

Parabola No. 29, Day 5

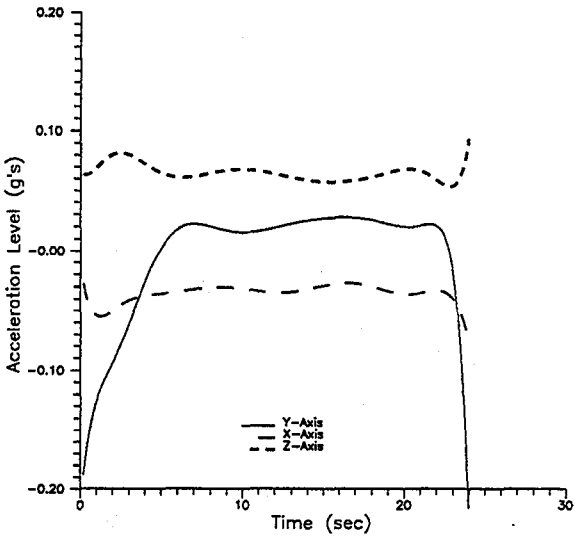

Parabola No. 30, Day 5

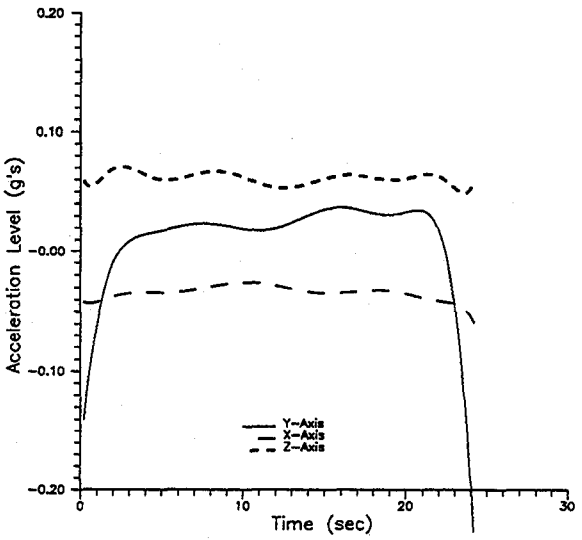

Parabola No. 31, Day 5

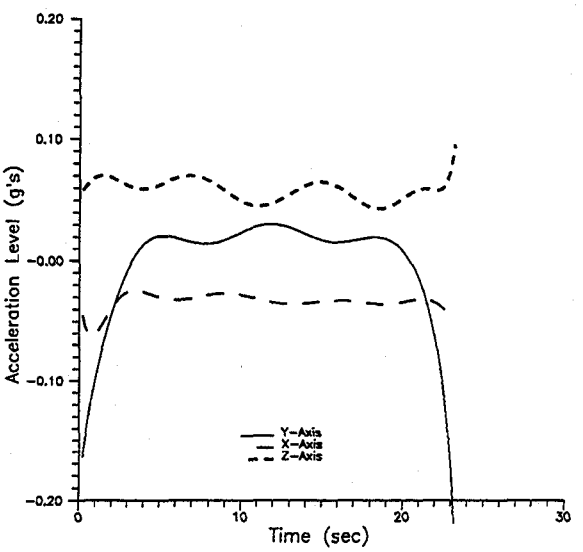

Parabola No. 32, Day 5

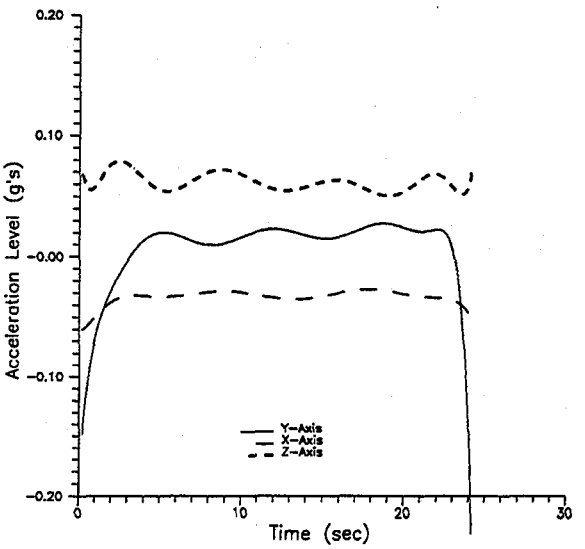

Parabola No. 33, Day 5

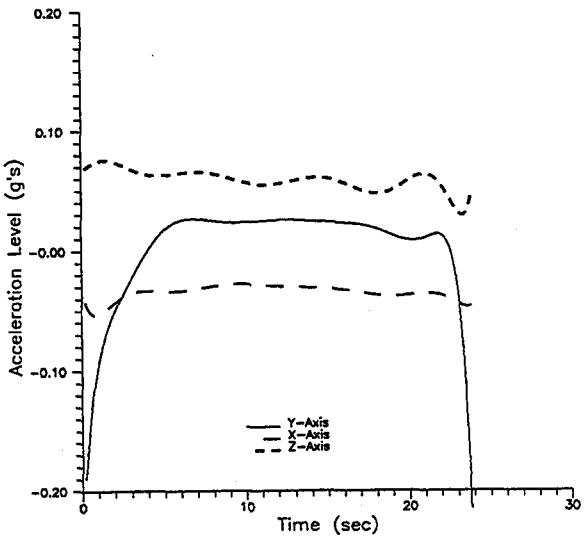

Parabola No. 34, Day 5

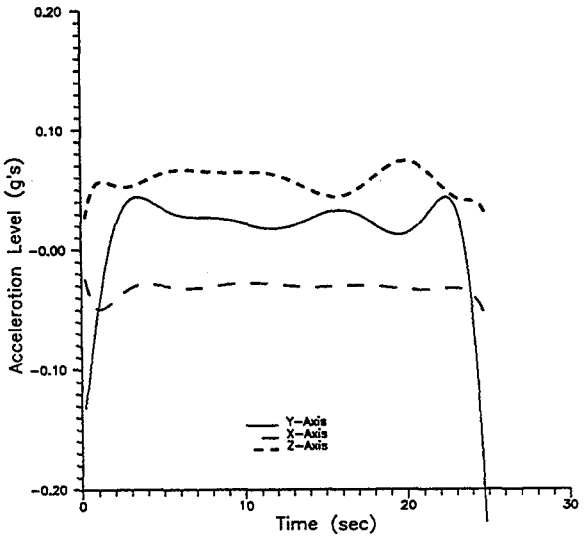

Parabola No. 35, Day 5

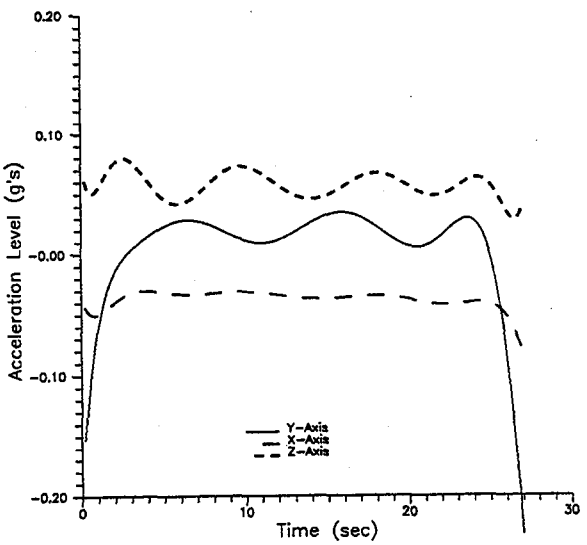

REPORT DOCUMENTATION PAGE

Form Approved
OMB No. 0704-0188

1. AGENCY USE ONLY (Leave blank)	2. REPORT DATE	3. REPORT TYPE AND DATES COVERED
	June 1994	Final Contractor Report

4. TITLE AND SUBTITLE

Investigation of Moving Belt Radiator Technology Issues

5. FUNDING NUMBERS

WU-233-01-0D
C-NAS3-24650

6. AUTHOR(S)

W. Peter Teagan and Jerry L. Aguilar

7. PERFORMING ORGANIZATION NAME(S) AND ADDRESS(ES)

Arthur D. Little, Inc.
20 Acorn Park
Cambridge, Massachusetts 02140-2390

8. PERFORMING ORGANIZATION REPORT NUMBER

E-8904

9. SPONSORING/MONITORING AGENCY NAME(S) AND ADDRESS(ES)

National Aeronautics and Space Administration
Lewis Research Center
Cleveland, Ohio 44135-3191

10. SPONSORING/MONITORING AGENCY REPORT NUMBER

NASA CR-195340

11. SUPPLEMENTARY NOTES

Project Manager, K. Alan White, Power Technology Division, NASA Lewis Research Center, organization code 6711, (216) 433-6563.

12a. DISTRIBUTION/AVAILABILITY STATEMENT

Unclassified - Unlimited
Subject Categories 20 and 31

12b. DISTRIBUTION CODE

13. ABSTRACT *(Maximum 200 words)*

The development of an advanced spacecraft radiator technology is reported. The moving belt radiator is a thermal radiator concept with the promise of lower specific mass (per kW rejected) than that afforded by existing technologies. The results of a parametric study to estimate radiator mass for future space power systems is presented. It is shown that this technology can be scaled up to 200 MW for higher rejection temperatures. Several aspects of the design concept are discussed, including the dynamics of a large rotating belt in microgravity. The results of a computer code developed to model the belt dynamics are presented. A series of one-g experiments to investigate the dynamics of small belts is described. A comprehensive test program to investigate belt dynamics in microgravity aboard the NASA KC-135 aircraft is discussed. It was found that the desired circular shape can readily be achieved in microgravity. It is also shown that a rotating belt is stable when subjected to simulated attitude control maneuvers. Heat exchanger design is also investigated. Several sealing concepts were examined experimentally, and are discussed. Overall heat transfer coefficients to the rotating belt are presented. Material properties for various belt materials, including screen meshes, are also presented. The results presented in this report indicate that the moving belt radiator concept is technically feasible.

14. SUBJECT TERMS	15. NUMBER OF PAGES
Space radiator; Nuclear power; Moving belt radiator; Belt dynamics	174
	16. PRICE CODE: A08

17. SECURITY CLASSIFICATION OF REPORT	18. SECURITY CLASSIFICATION OF THIS PAGE	19. SECURITY CLASSIFICATION OF ABSTRACT	20. LIMITATION OF ABSTRACT
Unclassified	Unclassified	Unclassified	